The metagalactic UV background at $z < 3$

Dissertation
zur Erlangung des Doktorgrades
des Fachbereichs Physik
der Universität Hamburg

vorgelegt von

Cora Fechner

aus Hamburg

Hamburg
2005

Gutachter der Dissertation:	Prof. Dr. D. Reimers Prof. Dr. L. Wisotzki
Gutachter der Disputation:	Prof. Dr. D. Reimers Prof. Dr. P. H. Hauschildt
Datum der Disputation:	16. 12. 2005
Vorsitzender des Prüfungsausschusses:	PD Dr. F.-J. Zickgraf
Vorsitzender des Promotionsausschusses:	Prof. Dr. G. Huber
Dekan des Fachbereichs Physik:	Prof. Dr. G. Huber

Abstract

The high ionization state of the intergalactic medium (IGM) is maintained by the metagalactic UV background radiation. This ionizing radiation field is supposed to be the integrated radiation of quasars and young star-forming galaxies, which is reprocessed and attenuated by the intergalactic gas. Since the UV background is inaccessible to direct observations, it is impossible to test theoretical predictions of its spectral energy distribution in great detail. However, constraints can be derived from studies of metal absorption systems, the H I Lyα opacity, or the He II Lyα forest, respectively. Observations of the He II/H I column density ratio η particularly probe the variations of the UV background. Since unobscured quasars permitting observation of He II absorption are rare, there are only two lines of sight, towards the quasars HE 2347-4342 and HS 1700+6416, where the He II Lyα forest can be resolved.

This work presents a study of the UV background at redshifts $z < 3$ investigating the He II absorption towards the quasars HS 1700+6416 ($z_{\rm em} = 2.72$), which provides the second line of sight where the He II Lyα forest is resolved. The numerous metal line systems detected in the spectra of this QSO are studied in order to avoid biases due to unrecognized metal line absorption in the He II forest. In this connection, several shapes of the ionizing radiation are tested for each system. The majority of the considered systems, in particular those at $z \gtrsim 2$, is best reproduced with an ionizing radiation similar to the UV background of Haardt & Madau (2001), where the He II break, formally located at 4 Ryd, is shifted to lower energies (~ 3 Ryd), probably due to the opacity of the higher He II Lyman series lines.

The He II/H I ratio η is estimated using two different methodical approaches. The expected metal line absorption in the far-UV is taken into account as well as molecular absorption of galactic H_2. About 16 % of the η values are significantly affected by metal line absorption. In order to investigate the applicability of the analysis methods, simple artificial spectra are created, based on the statistical properties of the H I Lyα forest. The analysis of the artificial data shows that both procedures lead to confident results for restricted data samples due to line saturation and thermal line broadening. For the restricted data samples a scatter of $10 - 15$ % in η would be expected even if the underlying value is constant. The observed scatter is significantly larger, indicating that the intergalactic radiation background is indeed fluctuating. In the redshift range $2.58 < z < 2.72$, where the data quality is best, we find $\eta \sim 130$ suggesting a contribution of soft sources like galaxies to the UV background.

Finally, an alternative analysis method is introduced and applied to the data of the quasars HS 1700+6416 and HE 2347-4342. The new procedure fits the high quality, optical H I data directly to the He II spectrum, and permits to derive redshift scales that characterize the fluctuations of the He II/H I ratio. A smooth change of η with redshift on typical scales of $\Delta z \sim 0.01 - 0.03$ (corresponding to $8 - 24\,h^{-1}$ Mpc comoving) or even larger is found. The data reveals an apparent correlation between low η regions and strong H I absorption. Thermal line broadening is suggested as a probable explanation for this apparent correlation, since the fit methods would severely underestimate η for absorber with $N_{\rm H\,I} \gtrsim 10^{13}$ cm^{-2} if the line width was dominated by thermal broadening. Indeed, lines located close to the cut-off of the $b(N)$ distribution exhibit lower column density ratios compared to the whole sample, in particular if high density absorbers are considered. Therefore, the apparent correlation of η with the strength of the H I absorption is probably caused by the insufficient consideration of thermal broadened lines in the framework of the analysis.

Zusammenfassung

Der hohe Ionisationsgrad des intergalaktischen Mediums (IGM) wird durch den metagalaktischen UV Strahlungshintergrund erzeugt. Das ionisierende Strahlungsfeld setzt sich aus der beim Durchgang durch das intergalaktische Gas gefilterten Strahlung von Quasaren und jungen Galaxien zusammen. Da der UV-Hintergrund direkten Beobachtungen unzugänglich ist, ist eine detaillierte Überprüfung theoretischer Modelle für die spektrale Energieverteilung nicht möglich. Allerdings können durch die Untersuchung von Metallabsorptionssystemen, der H I Lyα-Opazität oder des He II Lyα-Waldes gewisse Einschränkungen abgeleitet werden. Insbesondere ist das He II/H I-Säulendichteverhältnis η sensitiv für Fluktuationen des UV-Hintergrundes. Da nur wenige Quasare die Beobachtung von He II Absorption erlauben, gibt es bisher nur zwei Sehlinien, für die der He II Lyα Wald aufgelöst werden kann, nämlich die Quasare HE 2347-4342 und HS 1700+6416.

In dieser Arbeit wird der UV-Hintergrund bei Rotverschiebungen $z < 3$ anhand der He II-Absorption im Spektrum des Quasars HS 1700+6416 ($z_{\rm em} = 2.72$) untersucht. Dabei handelt es sich um die zweite Sehlinie, für die der He II Lyα-Wald aufgelöst werden kann. Die zahlreichen Metallsysteme im Spektrum dieses Quasars werden analysiert, um systematische Fehler aufgrund unerkannter Metallabsorption im He II Lyα-Wald zu vermeiden. Für jedes System werden dabei verschiedene spektrale Energieverteilungen getestet. Die meisten der betrachteten Systeme, insbesondere die bei $z \gtrsim 2$, lassen sich am besten mit einem Strahlungsfeld ähnlich dem von Haardt & Madau (2001) modellieren, bei dem die He II-Kante bei 4 Ryd zu kleineren Energien (~ 3 Ryd) hin verschoben ist. Ein möglicher Grund für diese Verschiebung ist die Opazität der Linien höherer Ordnung der He II Lyman Serie.

Die Bestimmung des He II/H I-Verhältnisses η erfolgt mit Hilfe von zwei verschiedenen methodischen Ansätzen. Dabei wird die im fernen UV erwartete Metallabsorption ebenso berücksichtigt wie die Absorption durch galaktische H_2-Moleküle. Etwa 16 % der η-Werte werden durch Metallabsorption signifikant beeinflusst. Um die Anwendbarkeit der Analysemethoden abzuschätzen, werden einfache, synthetische Spektren auf der Basis der statistischen Eigenschaften des H I Lyα-Waldes erzeugt. Die Untersuchung der künstlichen Daten ergibt, dass beide Prozeduren aufgrund von Sättigungseffekten und thermischer Linienverbreiterung nur für eingeschränkte Datensätze zu glaubwürdigen Ergebnissen führen. Für derartige Datensätze ist eine Streuung von $10 - 15$ % in η zu erwarten, auch wenn der zugrunde liegende Wert konstant ist. Die beobachtete, signifikant größere Streuung deutet darauf hin, dass der intergalaktische Strahlungshintergrund tatsächlich fluktuiert. Im Rotverschiebungsbereich mit der besten Datenqualität, d.h. $2.58 < z < 2.72$, ergibt sich $\eta \sim 130$, was einen Beitrag weicher Strahlungsquellen wie Galaxien zum UV-Hintergrund nahelegt.

Schließlich wird eine alternative Analysemethode vorgestellt und auf die Daten der Quasare HS 1700+6416 und HE 2347-4342 angewendet. Die neue Prozedur passt die optischen H I-Daten direkt an das He II-Spektrum an und erlaubt die Bestimmung von Rotverschiebungsskalen zur Charakterisierung der Fluktuationen des He II/H I-Verhältnisses. Es ergibt sich ein glatter Verlauf für $\eta(z)$ auf Skalen von $\Delta z \sim 0.01 - 0.03$ oder größer, was mitbewegten $8 - 24\,h^{-1}$ Mpc entspricht. Anscheinend besteht eine Korrelation zwischen starker H I Absorption und Regionen mit niedrigem η. Eine mögliche Erklärung ist die Vernachlässigung thermischer Linienverbreiterung, da die verwendeten Analysemethoden die η-Werte für primär thermisch verbreiterte Absorptionslinien mit $N_{\rm H\,I} \gtrsim 10^{13}\,{\rm cm}^{-2}$ stark unterschätzen würden. Tatsächlich ergeben sich für Linien nahe der Untergrenze der $b(N)$ Verteilung niedrigere Säulendichteverhältnisse als für die gesamte Linienauswahl, insbesondere bei der Betrachtung von Absorbern mit hoher Dichte. Deshalb wird die scheinbare Korrelation zwischen η und der Stärke der H I Absorption vermutlich durch die unzureichende Berücksichtigung thermisch verbreiterter Linien verursacht.

Contents

1 Introduction **3**

2 The ionization state of the intergalactic medium **5**
2.1 The epoch of reionization . . . 5
2.1.1 Hydrogen . . . 5
2.1.2 Helium . . . 6
2.2 The intergalactic UV background . . . 7
2.3 Probing the IGM by quasar absorption lines . . . 11

3 Effects of unrecognized metal lines in the HeII Lyα forest **13**
3.1 Creating artificial datasets . . . 13
3.2 Analysis of the simulated spectra . . . 13
3.3 Conclusions . . . 15

4 Metal line systems in the spectrum of HS 1700+6416 **16**
4.1 Observations . . . 17
4.2 Modelling procedure . . . 17
4.3 Limitations . . . 19
4.4 Observed systems . . . 19
4.4.1 System $z = 0.2140$ . . . 20
4.4.2 System $z = 0.7222$ . . . 21
4.4.3 System $z = 0.8643$ . . . 22
4.4.4 System $z = 1.1573$ . . . 22
4.4.5 System $z = 1.4941$ . . . 23
4.4.6 System $z = 1.7241$ . . . 24
4.4.7 System $z = 1.8450$ . . . 25
4.4.8 System $z = 2.1680$ . . . 28
4.4.9 System $z = 2.2896$ . . . 29
4.4.10 System $z = 2.3155$ . . . 29
4.4.11 System $z = 2.3799$ . . . 32
4.4.12 Systems $z = 2.4321$ and $z = 2.4331$ . . . 33
4.4.13 Systems $z = 2.4386$ and $z = 2.4405$ . . . 34
4.4.14 System $z = 2.4965$ . . . 37
4.4.15 System $z = 2.5683$ . . . 37
4.4.16 System $z = 2.5785$ . . . 38
4.5 Discussion . . . 39
4.5.1 Implications on the He II/H I ratio . . . 44
4.5.2 Correlation with galaxies . . . 45
4.5.3 Prediction of metal lines in the FUSE spectral range . . . 46
4.6 Conclusions . . . 47

5 The He II Lyα forest towards HS 1700+6416 **49**
5.1 Observations . . . 50
5.2 Continuum definition . . . 50
5.3 Metal line absorption . . . 52
5.4 Simulations . . . 54
5.4.1 Methods . . . 55
5.4.2 Creating artificial datasets . . . 55

5.4.3 Profile fitting analysis . . . 55
5.4.4 Apparent optical depth method . . . 56
5.4.5 Comparing profile fitting and apparent optical depth . . . 58
5.5 Results and discussion . . . 59
5.5.1 Profile fitting analysis . . . 59
5.5.2 Apparent optical depth method . . . 60
5.5.3 The ionizing background . . . 61
5.5.4 Redshift evolution of the He II optical depth . . . 62
5.6 Summary and conclusions . . . 63

6 Fluctuations of the UV background towards HS 1700+6416 and HE 2347-4342 64
6.1 Data . . . 64
6.2 Method . . . 65
6.3 Results . . . 66
6.3.1 The Lyα forest towards HE 2347-4342 . . . 66
6.3.2 The patchy zone towards HE 2347-4342 . . . 69
6.3.3 HS 1700+6416 . . . 70
6.4 Discussion . . . 72
6.4.1 Methodical uncertainties . . . 73
6.4.2 Thermal broadening . . . 73
6.4.3 Physical implications . . . 75
6.5 Summary and conclusions . . . 75

7 Conclusions 77
7.1 Summary . . . 77
7.2 Outlook . . . 78

A Line parameters 79
A.1 Observed metal line systems towards HS 1700+6416 . . . 79
A.2 Predicted metal lines . . . 83
A.3 H_2 lines towards HS 1700+6416 . . . 104
A.4 Observed Lyα lines towards HS 1700+6416 . . . 105
A.5 Observed Lyα lines towards HE 2347-4342 . . . 110

References 119

1. Introduction

The intergalactic medium (IGM) can be well described as a fluctuating distribution of baryons, organized by the gravitational forces of dark matter and photoionized by the radiation of quasars and starburst galaxies. According to numerical studies of structure formation the gaseous IGM traces the mass distribution of the cold dark matter resulting a sheet-like structure of filaments and voids, where in the densest portions stars and galaxies can be formed (for a review see Davé 2003). Since the sight-lines of QSOs intersect this cosmic web, the distribution and the physical properties of the absorbing gas can be studied in the spectra of quasars.

Observations exhibit the IGM to be highly photoionized. Instead of continuous absorption due to neutral gas (Gunn & Peterson 1965) a forest-like structure of distinct absorption features, arising from clumps of neutral hydrogen, is detected in the spectra of QSOs. Since the universe recombines at $z \sim 1000$, there has to be a phase of reionization. Hydrogen reionization is supposed to be completed at $z \sim 6$ according to the observation of Gunn-Peterson troughs in the spectra of very high redshift quasars (e.g. Becker et al. 2001). Regarding helium, there is evidence that its reionization phase ends at $z \sim 3$ (e.g. Reimers et al. 1997a). The sources responsible for reionization and the details of the processes are still a matter of debate. Chapter 2 includes a summary of the main suggestions discussed so far.

The IGM is kept photoionized by the metagalactic UV background. As a first approximation, the ionizing background originates from the radiation of quasars, which is reprocessed by the intergalactic absorbers, resulting in a characteristic spectral energy distribution (Haardt & Madau 1996; Fardal et al. 1998). The main features are sharp breaks at the ionization thresholds of H I and He II, 1 Ryd and 4 Ryd, respectively (shown e.g. in Fig. 2.1). A comparison of observational results to theoretical studies indicates that galaxies have to contribute to the UV background as well (e.g. Sokasian et al. 2003; Aguirre et al. 2004) resulting in a softer spectral energy distribution (Bianchi et al. 2001; Haardt & Madau 2001).

The true shape of the UV background, however, is inaccessible to direct observations. Photoionization models of observed metal line systems are required to derive constraints for the shape of the ionizing radiation (performed e.g. by Vogel & Reimers 1993; Savaglio et al. 1997; Agafonova et al. 2005). Systems showing a sufficient number of features from different ions are normally complex, i.e. they have a multi-phase structure and only part of the lines arises from the same gas volume. Furthermore, the absorber metallicity is a priori unknown and deviations from the solar abundance pattern are likely. Indeed, constraining the shape of the UV background from metal line systems depends on numerous free parameters.

Alternatively, observations of He II absorption in combination with the H I Lyα forest also probe the ionizing radiation. The column density ratio $\eta = N_{\mathrm{He\,II}}/N_{\mathrm{H\,I}}$ depends on the intensity and the slope of the UV background at the ionization edges of H I and He II (e.g. Fardal et al. 1998). Fluctuations in the column density ratio therefore indicate variations of the UV background. Low η values (~ 10) represent hard ionizing radiation like that emitted by quasars, while high η values ($\sim 100 - 1000$) indicate a significant contribution from soft sources like starburst galaxies.

Since the UV flux of most QSOs is obscured by intervening Lyman limit or damped Lyα systems (Picard & Jakobsen 1993), until now only two quasars have been discovered, which are bright enough for high resolution spectroscopy with the Far Ultraviolet Spectroscopic Explorer (FUSE). The He II Lyα forest towards HE 2347-4342 has been investigated extensively by Kriss et al. (2001), Shull et al. (2004), and Zheng et al. (2004b) using line profile fits or an apparent optical depth method. All studies find that the column density ratio η strongly fluctuates on small scales. Values from $\eta \lesssim 10$ up to $\gtrsim 1000$ are measured varying within ~ 1 Mpc. Since this scale is less than the typical distance between quasars (~ 30 Mpc), the results are not completely understood (Shull et al. 2004). Bolton et al. (2005) present a first approach to explain the observational results using hydrodynamical simulations. According to the authors, the fluctuations are due to the small number of QSOs that contribute to the He II photoionization rate at any given point in the IGM. Furthermore, an apparent correlation between the strength of the H I absorption and the inferred η value has been measured (Shull et al. 2004; Reimers et al. 2004).

With HS 1700+6416 the second line of sight resolving the He II Lyα forest is observed (Reimers et al. 2004). It will be presented in detail in this work. At first glance, the HS 1700+6416 data seem to confirm the previous results. However, as will be pointed out in this study, part of the observed fluctuations can be related to simplifications made by the analysis methods and are obviously artifacts.

Using new far-UV data of HS 1700+6416 taken with FUSE, the He II Lyα forest is analyzed, and the redshift distribution of the column density ratio η is determined. Since the spectrum of HS 1700+6416 shows plenty of metal lines including seven Lyman limit systems, metal line absorption is expected to be present in the He II Lyα forest. As will be demonstrated in Chapter 3 by analyzing artificial spectra, absorption from unrecognized metal lines leads to a bias in the estimated η values. In order to avoid systematic errors due to unrecognized metal line absorption, photoionization models are computed on the basis of the observed optical

and UV spectra of HS 1700+6416 (Chapter 4). These models depend on the assumed shape of the ionizing energy distribution. Therefore, they are investigated with two different aims: First, to predict the metal line spectrum in the FUSE spectral range and, secondly, to gain constraints of the shape of the intergalactic UV background.

The resulting metal line prediction is included into the study of the He II Lyα forest (Chapter 5). Since the investigation of the artificial data presented in Chapter 3 indicates additional systematic errors and statistical uncertainties, the simulated data are studied in more detail. The artificial spectra exhibit constraints and limitations that have to be considered when analyzing the observed data with standard methods. These points are taken into account for the analysis of the observed He II Lyα forest presented in Chapter 5.

An alternative method to estimate the He II/H I ratio is introduced in Chapter 6. The spectrum fitting method intends to avoid the disadvantages of the standard procedures fitting the H I Lyα forest directly to the He II spectrum. At the same time it provides the first step to derive the scale characterizing the fluctuations of the ionizing background directly from the data. This new method is applied to the observations of HE 2347-4342 and HS 1700+6416; limitations and consequences are discussed.

An important aspect, that will be figured out in this study, is the questionableness of one of the basic assumption made in the analysis. All methods presume turbulent line broadening, i.e. H I and He II features are supposed to have the same line widths. However, as it is known from Lyα forest statistics, there are absorbers with line widths dominated by thermal broadening, which are usually considered statistically to estimate the temperature of the IGM (e.g. Schaye et al. 1999). For these lines, all methods produce systematically too low η values. This systematic effect will lead to incorrect conclusions, if considered improperly. Line profile fitting is the only method providing the potential to avoid this bias. Possible modifications of the analysis and future prospects will be pointed out in Chapter 7.

Remarks on the organization of this work

This work is organized into Chapters, which are prepared to be stand-alone articles (Chapters 3, 4, 5, and 6). Partly the have already been submitted to "Astronomy & Astrophysics" (Chapter 4). Therefore, each Chapter has an independent introduction, which may be redundant in some aspects. Slight modifications have been made to each Chapter to outline the relation between the individual parts of this work. Various aspects have been added to Chapter 4 in comparison to the submitted article. Chapter 3 is based on a poster contribution to the conference "Astrophysics in the Far Ultraviolet – Five Years of discovery with FUSE" held in Victoria, BC, Canada in August 2004. The text has been revised to point out the connections to the following Chapters.

The data reduction of the FUSE observations presented in Chapter 5 has been performed by Dr. G. A. Kriss. He has contributed the paragraphs in Section 5.1 describing the reduction of the FUSE data.

2. The ionization state of the intergalactic medium

2.1. The epoch of reionization

The evolution of the universe from the Big Bang until now can be classified into several epochs, which are characterized each by the dominant physical processes. The atomic nuclei formed during early nucleosynthesis recombine with the electrons to a neutral medium at redshift $\sim$ 1000. As a relic of this recombination epoch, when radiation and matter decoupled, the cosmic microwave background (CMB) is observed. The neutral universe mainly consisting of hydrogen then undergoes further expansion during the Dark Ages ($z \gtrsim 30$). The Cosmic Dawn rises, when the first luminous objects form ($30 \gtrsim z \gtrsim 15$). These first radiation sources start to reionize the neutral medium. According to observations of the most distant quasars known, the epoch of reionization[1] is completed at $z \approx 6$. Helium, which is harder to ionize than hydrogen, completes its reionization phase about 1.4 Gyr later at $z \approx 3$.

2.1.1. Hydrogen

Observations of the CMB by the Wilkinson Microwave Anisotropy Probe (WMAP) reveal a Thomson scattering optical depth of $\tau_e = 0.17 \pm 0.04$ (Spergel et al. 2003; Kogut et al. 2003) indicating that the reionization occurs early at $z \approx 15$. However, the uncertainties are large depending on the analysis technique employed. On the other hand, the Gunn Peterson troughs (Gunn & Peterson 1965) observed in the spectra of very high redshifted quasars (Becker et al. 2001; Fan et al. 2002; White et al. 2003) suggest that the epoch of reionization is completed at $z \sim 6$ (see also Songaila 2004). Further constraints are given by the value of the IGM temperature from the Lyα forest at $z \approx 2 - 4$ (e.g. Ricotti et al. 2000; Schaye et al. 2000), which depends on the reionization history (e.g. Wyithe & Loeb 2003b).

One of the most important issues to develop a consistent scenario for the reionization history concerns the possible sources of ionizing radiation. Probable candidates are early galaxies, active galactic nuclei (AGN), PopIII stars, but even black holes, sterile neutrinos (Hansen & Haiman 2004; Mapelli & Ferrara 2005), annihilating dark matter particles (Padmanabhan & Finkbeiner 2005), or other kinds of decaying particles (Chen & Kamionkowski 2004). The required amount of radiation is roughly six ionizing photons per baryon, which could be provided if only a fraction of 1/10 000 of the baryons was incorporated into O stars.

[1] The term 'epoch of reionization' refers to the reionization of hydrogen unless noted otherwise.

Even though there are quasars at high redshift, their density declines rapidly for $z > 2.5$ (e.g. Schmidt et al. 1991; Warren et al. 1994) and there is no evidence for an upturn of the faint end of the AGN luminosity function at $z \gtrsim 3$ (e.g. Fan et al. 2001; Hunt et al. 2004). Thus, QSOs most likely contribute only a minor fraction of the ionizing photons. According to Meiksin (2005) quasars alone could not reionize the IGM prior to $z \sim 4$ (see also Willott et al. 2005). However, their hard non-thermal radiation becomes important to reionize helium.

Observations of star-forming galaxies at high redshifts indicate that the star formation rate at $z \sim 6$ is less than required by the theoretical calculations of Madau et al. (1999), and is, therefore, insufficient to reionize the universe (e.g. Lehnert & Bremer 2003; Bunker et al. 2004). Due to the small number of investigated fields so far, this might be an effect of cosmic variance. Other ideas, that might solve this discrepancy, refer to star formation at even earlier epochs or differences in the initial mass function. Probably, fainter galaxies cannot be reached with recent techniques.

It is still uncertain whether ionizing photons can escape from galaxies efficiently. Steidel et al. (2001) claim to measure a significant escape fraction of ionizing photons from galaxies at $z \sim 3$, while Giallongo et al. (2002), Malkan et al. (2003), Fernández-Soto et al. (2003), and Inoue et al. (2005) report on non-detections at several epochs. Also theoretical calculations do not come to a clear prediction so far (e.g. Ricotti & Shull 2000; Clarke & Oey 2002; Fujita et al. 2003). Observations and theoretical studies agree that the escape fraction has to be $f_{\rm esc} \leq 15\,\%$.

The first stars, formed during the epoch of Cosmic Dawn, are metal-free (PopIII). The first heavy metals are created by nuclear burning and super nova explosions of the PopIII stars themselves. In order to form stars out of metal-free gas, cooling due to atomic and, in particular, molecular hydrogen is needed, where the cooling time has to be shorter than the Hubble time and the dynamical heating time. These pre-conditions constrain the epoch of first star formation to $z \lesssim 50$ (reviews on this topic can be found e.g. in Miralda-Escudé (2003) and Schneider (2004); Ciardi & Ferrara (2005) give a review on PopIII stars in the context of structure formation). Furthermore, the first stars have to be very massive ($\gg 100\,M_\odot$; Abel et al. 2002; Bromm et al. 2002). Less massive stars can only form if the proto-stellar gas is enriched by metals or dust (e.g. Schneider et al. 2002, 2003).

Due to their high mass, the majority of the PopIII stars collapse in a black hole at the end of their life (Woosley & Weaver 1995; Heger & Woosley 2002). The black holes

grow via accretion and mergers and may radiate as miniquasars (Haiman & Loeb 1998; Madau et al. 2004; Ricotti & Ostriker 2004a). Their radiation contributes to the infrared and X-ray background today, which constrain the importance of miniquasars for reionization (Cooray & Yoshida 2004; Dijkstra et al. 2004), even though they cannot be the only sources (Salvaterra et al. 2005).

Theoretical scenarios of the formation of PopIII stars are supported by observations of the amplitude and anisotropy of the near-infrared background (Magliocchetti et al. 2003; Salvaterra & Ferrara 2003). Additionally, an important property of PopIII stars is their intrinsically harder spectrum in comparison to low-metallicity PopII stars, which makes them suitable to reionize helium as well (e.g. Schaerer 2002; Tumlinson et al. 2003; Venkatesan et al. 2003). Models predicting early reionization by PopIII stars are consistent with the WMAP electron scattering optical depth (e.g. Wyithe & Loeb 2003b; Choudhury & Ferrara 2005). However, as indicated by observations, the reionization history must be complex (e.g. Hui & Haiman 2003). Effects of reionization will influence the formation of the sources that provide the ionizing photons. The formation of dwarf galaxies, e.g., is suppressed by reionization (Benson et al. 2002, 2003). They may be more abundant in rich clusters if they are formed before the epoch of reionization.

The complexity of reionization is described in three stages introduced by Gnedin (2000). During the pre-overlap phase, isolated bubbles grow around radiation sources. The emerging H II regions merge rapidly during the overlap stage and reionize the low-density, diffuse intergalactic gas. Since during the overlap phase the sources begin to "see" each other and the contributions from different sources combine, this phase is characterized by a sharp rise in the level of the ionizing background and the photon mean free path. The remaining high-density regions are gradually reionized during the post-overlap stage (Miralda-Escudé et al. 2000). Thereby, overdensities start earlier to be reionized, since the sources are formed preferentially in overdense regions, but complete later due to a higher recombination rate. Because of the clumpiness of the IGM and the distribution of the radiation sources, the reionization process is inhomogeneous (Ciardi et al. 2003; Barkana & Loeb 2004; Furlanetto & Oh 2005), and the propagation of the ionization fronts depends on the small-scale structure (Iliev et al. 2005).

Despite the CMB, observations of the H I 21 cm line would be an important probe of the epoch of reionization (e.g. Loeb & Zaldarriaga 2004). The fluctuations of the brightness temperature of the 21 cm radiation trace the variations of the gas density. Since the observed wavelength scales with redshift, measuring the signal of the 21 cm radiation can be used to create a 3D map of the universe (e.g. Madau et al. 1997; Zaldarriaga et al. 2004; Bharadwaj & Ali 2005). First instruments with the purpose to detect these fluctuations are recently under construction (e.g. the Low Frequency Array (LOFAR) in the Netherlands; Kassim et al. 2004). However, due to various foreground effects (Shaver et al. 1999; Di Matteo et al. 2002; Oh & Mack 2003), the data analysis will be very challenging (e.g. Morales & Hewitt 2004; Bowman et al. 2005).

2.1.2. Helium

The reionization of helium is delayed by 1.4 Gyr with respect to H I. This is due to the harder photons ($h\nu > 54.5\,\mathrm{eV} = 4.0\,\mathrm{Ryd}$) required in comparison to reionization of hydrogen ($h\nu > 13.6\,\mathrm{eV} = 1.0\,\mathrm{Ryd}$). These photons are believed to be provided by quasars (e.g. Madau et al. 1999; Miralda-Escudé et al. 2000; Sokasian et al. 2002; Gleser et al. 2005). Furthermore, also massive PopIII stars may provide He II reionizing photons (Venkatesan et al. 2003). Including the stellar contribution into models, helium may undergo two phases of reionization (e.g. Oh et al. 2001; Wyithe & Loeb 2003a) with a recombination phase in between. According to Ricotti & Ostriker (2004b) a similar reionization history is also conceivable considering only the X-ray background due to primordial black holes.

An alternative approach is presented by Miniati et al. (2004). The authors calculate the contribution of thermal emission from gas, which has been shock heated during cosmic structure formation. They find that haloes with temperatures of 10^6–10^7 K, corresponding to masses 10^{11}–$10^{13}\,M_\odot$, i.e. large galaxies and small groups, produce thermal radiation well above the H I and He II ionization thresholds. Their results predict that structure formation alone provides enough photons to reionize He II at $z \sim 6$ and keep it reionized thereafter.

According to observations the reionization of helium is completed at $z \approx 3$. At this redshift the He II Lyα absorption in the spectra of quasars changes from completely saturated absorption troughs to a Lyα forest structure (Reimers et al. 1997a; Heap et al. 2000; Zheng et al. 2004b; Reimers et al. 2005a). In addition to the direct observation of He II absorption features, there are several observational results providing supplementary evidence for the reionization of helium at this epoch. All of those studies find a sudden change in the thermal and/or ionizing conditions of the IGM, which plausibly can be attributed to the helium reionization. Prior to complete reionization, the hard UV radiation emitted by the quasars is softened due to absorption and re-emission by intergalactic He II. This effect decreases significantly, when nearly all He II is ionized to He III. However, there is still an ongoing controversy about the significance of the observed results, and other possible explanations are discussed as well.

Songaila (1998) finds an abrupt change of the ratio Si IV/C IV at $z \sim 3$, indicating a significant change in the ionization balance of metal absorbers in the Lyα forest. At higher redshifts high values of Si IV/C IV imply that the ionizing radiation must be soft with a large break at the He II ionization edge (4 Ryd). Since the IGM contains less He II filtering the quasars' hard UV radiation after helium reionization is completed, the observed change should occur at the redshift at which He II completely ionizes to He III. Other authors (Kim et al. 2002b; Boksenberg et al. 2003; Aguirre

Table 2.1: Known quasars with observable He II absorption.

QSO	z_{em}	V	references
HS 1700+6414	2.72	16.1	Davidsen et al. (1996); Reimers et al. (2004)
HE 2347-4342	2.885	16.1	Reimers et al. (1997a); Kriss et al. (2001); Smette et al. (2002); Shull et al. (2004); Zheng et al. (2004b)
CSO 118[a]	2.97	17.0	Reimers et al. (2005a)
PKS 1935-692	3.17	18.8	Anderson et al. (1999)
Q 0302-003	3.286	17.8	Jakobsen et al. (1994); Hogan et al. (1997); Heap et al. (2000); Jakobsen et al. (2003)
SDSS J2346-0016	3.50	18.6	Zheng et al. (2004a)

[a] also known as HS 1157+3143 or Q 1157+3143

et al. 2004) find no discontinuity of Si IV/C IV around $z \approx 3$ arguing that it might not be a good indicator of helium reionization.

Ricotti et al. (2000) derived an effective equation of state of the IGM from the Doppler parameters of low-density Lyα forest lines. Their results indicate a second reheating of the IGM at $z \sim 3$, which they identify as the He II reionization occurring at this epoch. Theuns et al. (2002a) and also Bernardi et al. (2003) find a deviation of the effective optical depth of the H I Lyα forest from a smooth distribution in the redshift range $3.4 \gtrsim z \gtrsim 3.0$. The authors relate this decrease of absorption to the temperature dependence of the hydrogen recombination coefficient. The corresponding temperature change at the measured redshift is supposed to be caused by the He II reionization. Further estimations of the temperature of the Lyα forest are done by Schaye et al. (2000) and Theuns et al. (2002b). Both studies find a relatively sudden increase in the widths of Lyα forest lines, and thus in the temperature of the IGM at $z \approx 3.0$. They associate this finding with an increase of entropy resulting from the reionization of He II. This is consistent with theoretical studies predicting an increase of the temperature of the Lyα forest due to He II reionization (e.g. Haehnelt & Steinmetz 1998).

Direct observations of He II absorption in the spectra of quasars are difficult. Its Lyα transition occurs at a rest wavelength of 303.7822 Å, which is in the extreme UV. A redshift of $z \gtrsim 3$ is needed to observe the He II Lyα forest with the Space Telescope Imaging Spectrograph (STIS) onboard the Hubble Space Telescope (HST), and $z \gtrsim 2$ for observations with FUSE. Even though the quasar luminosity function has its maximum at $z \approx 2$, there are only few quasars providing enough unabsorbed UV flux to be suitable for observations with sufficiently high S/N. The reason is the large number of high density H I absorbers towards high redshift quasars. Damped Lyman alpha (DLA) and Lyman limit systems (LLS) obscure the UV brightness of the background QSOs due to Lyman continuum absorption (Møller & Jakobsen 1990; Picard & Jakobsen 1993).

Until today, six quasars at $z \sim 3$ with observable He II absorption are known. Their redshifts and visual magnitudes are summarized in Table 2.1. Only two of them, HE 2347-4342 and HS 1700+6416, are bright enough to obtain high resolution ($R \approx 20\,000$) spectra with fairly sufficient signal-to-noise with FUSE (Kriss et al. 2001; Shull et al. 2004; Zheng et al. 2004b; Reimers et al. 2004). These high resolution data resolve the He II Lyα forest and a direct comparison between the H I and He II absorption features is possible.

He II Lyα absorption is, in general, stronger than the H I Lyα absorption by a factor of

$$\eta = \frac{N_{\mathrm{He\,II}}}{N_{\mathrm{H\,I}}}\,, \tag{2.1}$$

due to lower fluxes and cross sections at its ionizing threshold. Additionally, He III recombines ~ 5.5 times faster than H II and He II. Due to its larger strength, He II absorption is also a good diagnostic of low-density regions in the IGM (e.g. Croft et al. 1997). For optically thin lines, Eq. 2.1 can be written as

$$\eta \approx 4 \cdot \frac{\tau_{\mathrm{He\,II}}}{\tau_{\mathrm{H\,I}}} \tag{2.2}$$

(Miralda-Escudé 1993), where the factor 4 is actually the ratio of the Lyα rest wavelengths 1215.6701 Å/303.7822 Å $\approx$ 4.0017819.

Measurements of η probe the shape of the intergalactic radiation field (e.g. Haardt & Madau 1996; Fardal et al. 1998). The relation between the column density ratio and the UV background will be presented and discussed in the next Section.

2.2. The intergalactic UV background

The radiation of the cosmic sources is propagated through the IGM through absorption and re-emission by intergalactic matter. These radiative processes filter the radiation in a way depending on the properties like density and distribution of the absorbing material, i.e. the IGM itself. Finally, the absorbers located far from any source are exposed to a mean metagalactic background radiation. The shape of the intergalactic ionizing background is inferred theoretically by numerical calculations (Haardt & Madau 1996, 2001; Madau et al. 1999; Fardal et al. 1998; Bianchi et al. 2001). These calculations are based on observational quantities like the quasar luminosity function, the spectral energy distribution of quasars (Zheng et al. 1997; Telfer et al. 2002; Scott et al. 2004), and the distribution of Lyα absorbers in the IGM (e.g.

Cristiani et al. 1995; Hu et al. 1995; Lu et al. 1996; Kirkman & Tytler 1997; Kim et al. 2001).

The mean intensity J_ν of the background radiation at the H I Lyman limit, i.e. at 912 Å (J_{ν_0} or $J_{\rm H\,I}$, respectively), can be estimated exploiting the proximity effect (Bajtlik et al. 1988). Due to enhanced ionization of hydrogen in the vicinity of the QSO by the quasar's radiation, the number of Lyα absorbers in the proximity zone is decreased. Comparing the number of observed lines to the number of lines expected if the quasar were absent, the mean intensity of the UV background at the H I ionizing threshold can be estimated. Such estimate has been performed by several authors (e.g. Williger et al. 1994; Giallongo et al. 1996; Cooke et al. 1997; Scott et al. 2000, 2002; Liske & Williger 2001). The derived values are in the range $J_{\rm H\,I} \approx 10^{-22} - 10^{-21}$ erg s^{-1} cm^{-2} Hz^{-1} sr^{-1} (a compilation of the results is presented in Liske & Williger 2001). Scott et al. (2000) find $\log J_{\rm H\,I} = -21.1^{+0.15}_{-0.27}$ from a sample of 74 QSOs at redshifts $1.7 - 4.1$, roughly consistent with the result from Liske & Williger (2001), who estimate $\log J_{\rm H\,I} = -21.45^{+0.4}_{-0.3}$ from a sample of 10 QSOs at $z \approx 2.9$ using a technique based on the statistics of the transmitted flux. However, the UV background is expected to evolve with redshift. Since quasar radiation is supposed to provide the main contribution, the evolution of the mean intensity should be governed by the space density of QSOs. According to theoretical calculations of Haardt & Madau (1996), $J_{\rm H\,I}$ increases from $\log J_{\rm H\,I} \sim -23$ at $z = 0$ to $\log J_{\rm H\,I} \approx -21.3$ at $z \approx 2.5$, where the space density of quasars reaches its maximum, and decreases again at higher redshifts. Indeed, this prediction is supported by observational results (Scott et al. 2002).

Knowledge of the mean intensity of the UV background is required to study numerous the physical processes in the IGM. For example J_ν is needed to estimate the total mass content of the IGM since the gas in the Lyα forest is highly photoionized (e.g. Rauch et al. 1997). However, most of the studies like estimating the metallicity of the IGM and/or deviations from the solar abundance pattern require not only the mean intensity of the UV background but also its spectral energy distribution. In the following paragraphs, several standard energy distributions will be presented. We will point out the importance of the shape of the ionizing radiation in the context of quasar absorption line studies, and will present possible approaches to constrain the shape of the UV background from observational data.

Fig. 2.1 presents several standard energy distributions. In the simplest model the ionizing radiation is assumed to be a simple power law[2] ν^α. Telfer et al. (2002) created a composite spectrum of 184 QSOs and find that the overall composite continuum can be described by a power law with the spectral index $\alpha = -1.76 \pm 0.12$ between 500 and 1200 Å, which corresponds to 1.825 and 0.76 Ryd. They also find that the spectral energy distribution of a single AGN can dramatically differ from the average. Recently, Scott et al. (2004) estimated the spectral index with a composite spectrum of low redshift AGN ($z \leq 0.67$) and find a significantly harder slope ($\alpha = -0.56^{+0.38}_{-0.28}$). In comparison to the results of Telfer et al. (2002), who investigated AGN in the redshift range $0.33 < z < 3.6$, these results may indicate a redshift evolution of quasars concerning their spectral index.

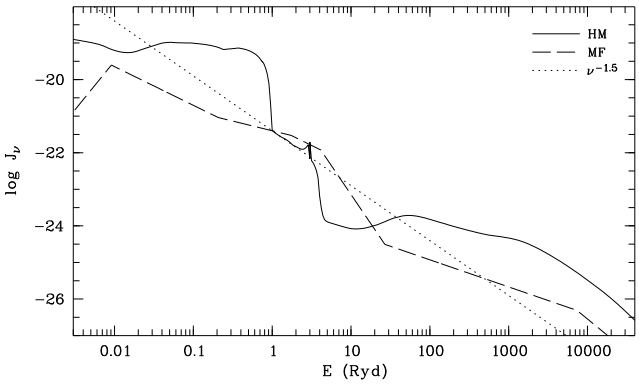

Fig. 2.1: The spectral shape of several radiation fields. The solid line represents the UV background of Haardt & Madau (2001, HM) at $z \approx 3$, the long-dashed line shows the AGN-like spectral energy distribution derived by Mathews & Ferland (1987, MF), and the dotted line indicates the simple power law $J_\nu \propto \nu^{-1.5}$.

The energy distribution given by Mathews & Ferland (1987) represents a semi-empirical description of the spectrum of AGN. The low energy part of this spectrum is to describe part of the Big Blue Bump, a characteristic feature in the spectral energy distribution of AGN (a review of the continuum emission of AGN can be found e.g. in Koratkar & Blaes 1999).

The UV background from Haardt & Madau (1996, HM) is based on the emitted spectrum of quasars ($\alpha = -1.5$ above 1 Ryd) whose radiation is attenuated while propagating through the IGM. Since H I and He II are the most abundant intergalactic absorbers, the two breaks at the ionization edges of H I and He II, respectively, are characteristic features of the HM background. In a more recent version (Haardt & Madau 2001, shown in Fig. 2.1 for $z \approx 3$), a contribution of the radiation of starburst galaxies is included assuming an escape fraction of $f_{\rm esc} = 0.1$. There is indeed growing evidenc, that galaxies contribute significantly to the UV background. For example, Sokasian et al. (2003) derived from numerical simulations that at $z \sim 3$ the contribution of galaxies must be equal to that of quasars to match the observed H I Lyα opacity. A model of an UV background dominated by massive stars can be found in Haehnelt et al. (2001). The authors argue, however, that at $z < 3$ measurements of the H I and He II opacity indicate a UV background dominated by quasars.

The shape of the intergalactic UV background plays an important role for studies of the IGM's metallicity. Since usually only few ions of an element are observed, inferring metal abundances from observed absorption features requires knowledge of the ionization fractions and thus of the ionizing radiation. DLA absorption systems provide a

[2] In this work the spectral index α of a power law energy distribution is always given in the positive way ν^α. Note, that in literature some authors define the spectral index by its negative $\nu^{-\alpha}$.

suitable tool to derive metallicities independently of the ionizing radiation (for a recent review see Wolfe et al. 2005). Since nearly all elements are in a neutral state (Prochaska & Wolfe 1996), the estimation of elemental abundances is unbiased by assumptions about ionization corrections. Instead, dust corrections are usually required. However, DLA systems are believed to arise from the inner part of galaxies or protogalaxies. As a consequence, they actually do not probe the common IGM properties.

The metallicity of the IGM is found to be much more sensitive to the density (Schaye et al. 2003; Aracil et al. 2004) than to time, i.e. redshift (Songaila 2001; Pettini et al. 2003). According to Schaye et al. (2003), the carbon abundance at the mean cosmic density is [C/H] ≈ -2.80 (see also Simcoe et al. 2004). Silicon appears to be enhanced with respect to carbon by [Si/C] ≈ 0.7 (Aguirre et al. 2004; Simcoe et al. 2005). However, the exact numbers depend on the presumed UV background (Aguirre et al. 2004, see also Chapter 4). Schaye et al. (2003) found unphysical results for the metallicity of the IGM if the ionizing radiation is too hard. Further complications may be caused by local sources close to intergalactic absorbers, whose importance is pointed out by Schaye (2004) and Miralda-Escudé (2005).

Since the measurement of the metallicity depends on the UV background, it is essential to consider the production processes of elements in order to evaluate the observational results. Theoretical studies of supernovae yields adopting various progenitor properties predict [Si/C] $\approx 0.0 - 1.0$ (Woosley & Weaver 1995; Heger & Woosley 2002; Chieffi & Limongi 2004; Umeda & Nomoto 2002, 2005). But Qian & Wasserburg (2005) predict that [Si/C] can be as high as ~ 1.3 if the metals are produced by very massive stars ($> 100\,M_\odot$) adopting a model of Umeda & Nomoto (2002).

The evidence of no redshift evolution of the metallicity suggests that the metal enrichment of the IGM has to occur very early. Since metals can only be produced in stars, they have to be distributed into the IGM by some mechanism. Adelberger et al. (2003) proposed that galactic supernovae driven winds expel metal enriched interstellar gas into the IGM at high redshift, providing simultaneously an explanation for the apparent correlation between C IV absorption and Lyman break galaxies at $z = 2 - 3$ (also Adelberger et al. 2005; Simcoe et al. 2005; Songaila 2005). Spectroscopic signatures of metal-rich outflows are indeed seen in galaxies at $z \gtrsim 3$ (Franx et al. 1997; Pettini et al. 2001). However, Porciani & Madau (2005) showed that also pregalactic enrichment from dwarf galaxies at $6 < z < 12$ are consistent with the observations.

Despite its importance for the interpretation of observations, there is no possibility to observe the shape of the ionizing background directly. The only approach to derive an unobserved spectral energy distribution in the most direct way from observed quantities is based on the measurement of metal absorption systems (efforts are made by Levshakov et al. 2003; Fechner et al. 2004; Agafonova et al. 2005). The basic idea is that the shape of the ionizing radiation can be, in principle, restored from the observed column densities using photoionization calculations (e.g. using CLOUDY; Ferland 1997; Ferland et al. 1998). Since the ionization fractions depend on the flux level of the radiation near the ionization threshold, the observation of different ions of an absorber scans the energy distribution of the ionizing radiation. The position of the ionization edges of several important ions are shown in Fig. 2.2. The corresponding numbers can be found in Table 2.2.

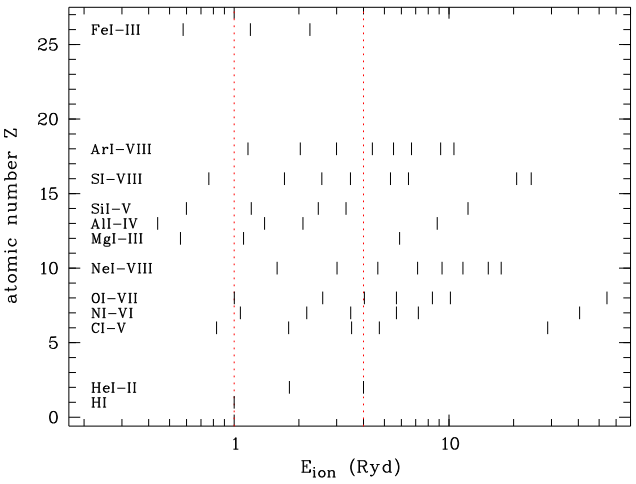

Fig. 2.2: Ionization potentials of important ions. The ionization energies versus the atomic numbers of the ions are indicated (see also Table 2.2). The ionization edges of H I (1 Ryd) and He II (4 Ryd) are marked as dashed lines.

The results are the more reliable the more different ions are observed, provided that all transitions are produced in the same volume. Unfortunately, most absorption systems have a multi-phase structure, i.e. high ionization transition do not originate from the same gas as low ionization stages. General speaking, low ionization lines arise from cold, dense gas, while highly ionized material traces a thinner, more extended region (e.g. Lopez et al. 1999). In order to avoid uncertainties because of unknown elemental abundances, systems showing different ions of the same element (e.g. C II, C III, and C IV or Si II, Si III, and Si IV, respectively), are especially appropriate. Nevertheless, in the case of C II and C IV most likely only part of the observed C IV absorption will be physically connected to C II, while the other portion will arise from a different phase. This problem also emerges in the standard analysis of absorption systems on the basis of a presumed ionizing background. Examples of well studied low redshift, multi-phase absorption systems can be found e.g. in Ding et al. (2003); Zonak et al. (2004); Masiero et al. (2005).

The column density ratio $\eta = N_{\mathrm{He\,II}}/N_{\mathrm{H\,I}}$ depends on the ionizing background. In photoionization equilibrium the density of hydrogen and helium is

$$n_{\mathrm{H\,I}} = \frac{n_e n_{\mathrm{H\,II}} \alpha^{(A)}_{\mathrm{H\,I}}}{\Gamma_{\mathrm{H\,I}}} \quad \text{and} \quad n_{\mathrm{He\,II}} = \frac{n_e n_{\mathrm{He\,III}} \alpha^{(A)}_{\mathrm{He\,II}}}{\Gamma_{\mathrm{He\,II}}}, \tag{2.3}$$

respectively, with the case A recombination rate coefficients $\alpha^{(A)}_{\mathrm{H\,I}} = 2.51 \cdot 10^{-13}\, T_{4.3}^{-0.755}\,\mathrm{cm^3\,s^{-1}}$ and $\alpha^{(A)}_{\mathrm{He\,II}} = 1.36 \cdot$

Table 2.2: Ionization edges of important ions. The ionization potentials are given in eV and Ryd (Verner et al. 1994), as well as the corresponding rest wavelength of the ionization edge, the atomic number Z, and the number of electrons N.

ion	E (eV)	E (Ryd)	λ (Å)	Z	N	ion	E (eV)	E (Ryd)	λ (Å)	Z	N
H I	13.60	1.00	912.9	1	1	Mg II	15.04	1.11	825.8	12	11
He I	24.59	1.81	505.0	2	2	Mg III	80.14	5.89	154.9	12	10
He II	54.42	4.00	228.2	2	1	Al I	5.99	0.44	2074.1	13	13
C I	11.26	0.83	1102.6	6	6	Al II	18.83	1.38	659.4	13	12
C II	24.38	1.79	509.2	6	5	Al III	28.45	2.09	436.4	13	11
C III	47.89	3.52	259.3	6	4	Al IV	119.99	8.82	103.5	13	10
C IV	64.49	4.74	192.5	6	3	Si I	8.15	0.60	1523.0	14	14
C V	392.09	28.82	31.7	6	2	Si II	16.35	1.20	759.6	14	13
N I	14.53	1.07	854.3	7	7	Si III	33.49	2.46	370.7	14	12
N II	29.60	2.18	419.4	7	6	Si IV	45.14	3.32	275.0	14	11
N III	47.45	3.49	261.7	7	5	Si V	166.77	12.28	74.5	14	10
N IV	77.47	5.69	160.3	7	4	S I	10.36	0.76	1198.4	16	16
N V	97.89	7.20	126.8	7	3	S II	23.33	1.72	532.2	16	15
N VI	552.07	40.58	22.5	7	2	S III	34.83	2.56	356.5	16	14
O I	13.62	1.00	911.7	8	8	S IV	47.31	3.48	262.5	16	13
O II	35.12	2.58	353.5	8	7	S V	72.68	5.34	170.8	16	12
O III	54.94	4.04	226.0	8	6	S VI	88.05	6.47	141.0	16	11
O IV	77.41	5.69	160.4	8	5	S VII	280.94	20.65	44.2	16	10
O V	113.90	8.37	109.0	8	4	S VIII	328.24	24.13	37.8	16	9
O VI	138.12	10.15	89.9	8	3	Ar I	15.76	1.16	787.8	18	18
O VII	739.34	54.34	16.8	8	2	Ar II	27.63	2.03	449.4	18	17
Ne I	21.57	1.59	575.7	10	10	Ar III	40.74	2.99	304.8	18	16
Ne II	40.96	3.01	303.1	10	9	Ar IV	59.81	4.40	207.6	18	15
Ne III	63.46	4.66	195.7	10	8	Ar V	75.02	5.51	165.5	18	14
Ne IV	97.12	7.14	127.8	10	7	Ar VI	91.01	6.69	136.4	18	13
Ne V	126.22	9.28	98.4	10	6	Ar VII	124.32	9.14	99.9	18	12
Ne VI	157.93	11.61	78.6	10	5	Ar VIII	143.46	10.54	86.6	18	11
Ne VII	207.28	15.24	59.9	10	4	Fe I	7.87	0.58	1577.6	26	26
Ne VIII	238.10	17.50	52.2	10	3	Fe II	16.19	1.19	767.0	26	25
Mg I	7.65	0.56	1623.8	12	12	Fe III	30.65	2.25	405.1	26	24

$10^{-12}\, T_{4.3}^{-0.70}\,\mathrm{cm^3\,s^{-1}}$. The photoionization rates Γ are

$$\Gamma_{\mathrm{H\,I}} = 4\pi \int_{\nu_{\mathrm{LL,H\,I}}}^{\infty} \frac{J_\nu}{h\nu}\, \sigma_{\mathrm{H\,I}}(\nu)\, d\nu\,, \tag{2.4}$$

in case of hydrogen and equivalent in case of He II. ν_{LL} denotes the ionizing threshold for H I (1 Ryd) or He II (4 Ryd), respectively. The He II/H I ratio is

$$\eta = \frac{\alpha^{(A)}_{\mathrm{He\,II}}}{\alpha^{(A)}_{\mathrm{H\,I}}}\, \frac{n_{\mathrm{He\,III}}}{n_{\mathrm{H\,II}}}\, \frac{\Gamma_{\mathrm{H\,I}}}{\Gamma_{\mathrm{He\,II}}}\,. \tag{2.5}$$

The photoionization rates can be approximated, since J_ν is dominated by its value near the ionizing threshold ν_{LL} due to the ν^{-3}-dependence of the photoionization cross section. Assuming that the gas is almost fully ionized and adopting primordial helium abundance ($Y = 0.244 \pm 0.002$; Burles et al. 2001), it is

$$\eta \approx 1.7 \cdot \frac{J_{\mathrm{H\,I}}}{J_{\mathrm{He\,II}}}\, \frac{3-\alpha_4}{3-\alpha_1}\, T_{4.3}^{0.055}\,, \tag{2.6}$$

where α_1 and α_4 are the slopes of J_ν at 1 and 4 Ryd, respectively (see Fardal et al. (1998), Shull (2004), or Chapter 4 for a more detailed presentation).

Alternatively, one can consider the softness parameter

$$S = \frac{\Gamma_{\mathrm{H\,I}}}{\Gamma_{\mathrm{He\,II}}} \approx 2.4 \cdot \eta\,, \tag{2.7}$$

which is defined as the ratio of the intergalactic H I and He II photoionization rates (applied in the context of He II absorption e.g. by Heap et al. 2000; Smette et al. 2002; Bolton et al. 2005). The approximate relation to the column density ratio η given in Eq. 2.7 follows directly from Eq. 2.5 under the assumption that the IGM is nearly completely ionized and the radiative recombination coefficients of H I and He II have the same temperature dependence.

The dependence of the column density ratio η on the ionizing background leads to different theoretical estimates of its value depending on the underlying radiation sources (see also Chapter 4). The intergalactic UV background as modelled by Haardt & Madau (1996) yields $\eta \sim 45$ at $z = 2-3$. For this background quasars are the primary sources. A similar model is computed by Fardal et al. (1998), who find $\eta \sim 50-100$ in the same redshift range. As claimed by the authors, the difference compared to Haardt & Madau (1996) is due to a different treatment of self-shielding and cloud re-emission. The updated version of Haardt & Madau

(2001) including also galaxies leads to $\eta \gtrsim 100$. Considering only the hard spectra of quasars would lead to small values $\eta \lesssim 10 - 20$. Contrarily, galaxies consisting of hot, massive PopII stars produce a rather soft spectrum, which results in high $\eta \sim 100 - 1000$. Whereas the high-energy radiation of metal-free PopIII objects leads to small values of $\eta \sim 10$ (Tumlinson et al. 2003).

Estimations of the column density ratio η from the first resolved He II Lyα forest data (Kriss et al. 2001; Shull et al. 2004; Zheng et al. 2004b; Reimers et al. 2004) revealed that η is fluctuating over several orders of magnitude ($\eta \lesssim 1$ up to $\gtrsim 1000$) on small scales ($\Delta z \approx 0.001$ corresponding to ~ 1 Mpc comoving). Assuming that these variations are real, several explanations have been proposed. The variations must be caused by spatial fluctuations of the ionizing radiation at the He II photoionization edge, since the typical mean free path of H I ionizing photons should be much larger than the distances between the sources. Therefore, a large number of sources is supposed to contribute to the H I photoionization rate and the hydrogen ionizing radiation can be considered as uniform. Possible reasons for the fluctuating He II photoionization rate are the spread of the spectral indices of quasars (Shull et al. 2004), their finite lifetimes (e.g. Croft 2004), as well as density variations in the IGM or filtering of radiation by radiative transfer effects.

As shown by Bolton et al. (2005) part of the scatter can be explained by local variations of the He II ionizing photons due to the relatively small number of QSOs contributing to the ionizing radiation. According to the authors, a small fraction of space must be exposed to harder radiation, since their models failed to reproduce very low column density ratios ($\lesssim 1$), which have been found by Zheng et al. (2004b, see also Chapters 5 and 6). Croft (2004) argued that fluctuation in the UV background on small scales (~ 1 Mpc) might be expected if quasars emit their ionizing radiation in short bursts of $\sim 10^6$ yr in length and there is a wide range of quasar spectral indices. In this case the scale of the variations would be given by the thickness of the light echos of the QSO radiation.

2.3. Probing the IGM by quasar absorption lines

Absorption lines in the spectra of quasars arise from the intergalactic gas intersected by the line of sight. The different strength of the observed features are due to density fluctuations of the gas (e.g. Davé et al. 1999; Schaye 2001). According to the scenario of structure formation in a Λ cold dark matter (ΛCDM) universe, the gas is trapped by dark matter halos tracing the spatial distribution of the dark matter (e.g. Cen et al. 1994; Zhang et al. 1995; Hernquist et al. 1996; Davé et al. 1999; Springel et al. 2005). Hydrodynamical simulations of structure formation well reproduce the appearence of the observed Lyα forest interpreting it as a fluctuating Gunn Peterson effect (reviewed e.g. by Davé 2003). In this context, modelling an observed spectrum by a sample of discrete absorption lines is certainly an oversimplification. However, fitting line profiles is one of the standard procedures to analyze quasar absorption lines since it is the best method to treat line blends, particularly if two different species are involved.

In the method of line profile fitting, the optical depth is usually given by a Voigt profile, the convolution of a Doppler and a Lorentz profile. While the Lorentz part dominates the wings of the line, the line core is given by the Doppler profile. Damping wings get only important at high densities ($N \gtrsim 10^{20}\,\mathrm{cm}^{-2}$). Absorbers showing damping wings in their H I Lyα line profile are classified as so-called damped Lyα (DLA) systems. Since the number of absorbers decreases with column density (e.g. Hu et al. 1995; Kirkman & Tytler 1997; Kim et al. 2001), DLAs are relatively rare. Therefore, analyzing observed spectra is mostly concerned with absorbers that can be well modelled neglecting the Lorentz part, which would make the fitting procedure more expensive. Since this work deals only with absorbers well beyond the regime of damping, we concentrate on Doppler profiles here.

Generally, the optical depth is given by

$$\tau_\lambda = \int \kappa_0\, n(s)\, \phi_\lambda\, ds\,, \tag{2.8}$$

with the opacity κ_0, density n, and the profile function ϕ_λ. The integral means the spatial extension of the absorber along the line of sight. The opacity

$$\kappa_0 = \frac{\pi e^2}{m_e c^2}\, f \cdot \lambda_0^2$$

depends of the oscillator strength f and the rest wavelength λ_0 of the specific transition. A Gaussian (or a Voigt function if necessary) is considered as profile function. The optical depth is then

$$\tau_\lambda = \frac{\sqrt{\pi} e^2}{m_\mathrm{e} c}\, \frac{f\lambda_0}{b} \int n(s) \cdot \exp\left(-\left(c\frac{\lambda - \lambda_\mathrm{c}}{b\lambda_\mathrm{c}}\right)^2\right) ds\,. \tag{2.9}$$

Here, $\lambda_\mathrm{c} = (1 + z) \cdot \lambda_0$ is the observed, i.e. redshifted, central wavelength of the line and the Doppler parameter $b = \mathrm{FWHM}/(2\sqrt{\ln 2})$ measures the line width. Thus, only the density n depends on the spatial coordinate s. Since the size of the absorber and also its density distribution is usually unknown, the integral cannot be solved. Therefore, the column density

$$N = \int n\, ds \tag{2.10}$$

is defined, which is the number of absorbing atoms per cm^2. Hence, the optical depth can be written as

$$\tau_\lambda = \frac{\sqrt{\pi} e^2}{m_\mathrm{e} c}\, \frac{f\lambda_0 N}{b} \cdot \exp\left(-\frac{\Delta v^2}{b^2}\right), \tag{2.11}$$

with $\Delta v = c \cdot ((\lambda - \lambda_\mathrm{c})/\lambda_\mathrm{c})$. If a Gaussian provides an insufficient approximation of the profile function and a Voigt

profile has to be considered, the last term in Eq. 2.11 has to be replaced by the Voigt function.

The observed flux

$$F(\lambda) = F_0 \cdot e^{-\tau_\lambda} \otimes P(\lambda)$$

is the given profile $F_0\, e^{-\tau_\lambda}$ convolved with the line spread function $P(\lambda)$ of the instrument. The instrumental profile $P(\lambda)$ is usually assumed to be a Gaussian, where the resolution of the data, $R = \lambda/\Delta\lambda$, is related to the width of the Gaussian by $\sigma = \lambda/(2\sqrt{2\ln 2}R)$.

The continuum $F_0 = F_0(\lambda)$ is wavelength dependent as well and represents the emission spectrum of the observed QSO. Usually, a QSO emits a power law spectrum $\propto \nu^\alpha$ overlayed by broad emission lines originating from H I and metal ions. For studies investigating the absorption features, a spectrum usually is normalized. The continuum normalization can be performed by different strategies. One possibility is to fit a polynomial to spectral regions apparently free from line absorption. In this work, the continuum normalization of the optical data is realized in course of the line fitting procedure. The employed fitting procedure CANDALF (developed by R. Baade) performs the line parameter and continuum optimization simultaneously. A Levenberg-Marquardt algorithm (e.g. Press et al. 1994, p. 683) is used for parameter optimization and the continuum is modelled by Legendre polynomials.

The line width is usually described in the microturbulent sense defining the Doppler parameter b (km s^{-1}). Due to the lack of knowledge of effective broadening mechanisms it is common practice to consider a combination of thermal $b_{\rm therm}$ and turbulent broadening $b_{\rm turb}$,

$$b = \sqrt{b_{\rm therm}^2 + b_{\rm turb}^2}\,. \tag{2.12}$$

The term of turbulent broadening subsumes stochastic line broadening due all kinds of velocities except thermal. While

$$b_{\rm therm} = \sqrt{\frac{2kT}{m}} \tag{2.13}$$

affects the line width according to the mass m of the absorbing atom (T denotes the temperature of the absorbing gas and k Boltzmann's constant), turbulent broadening has the same effect on all species. Another particular mechanism affecting the line width is broadening due to the Hubble expansion. Spatially expanded absorbers are broadened by the differential Hubble flow.

The strength of an absorption feature generally depends on the particle density. One class of absorbers are so-called Lyman limit systems (LLS) with column densities $\sim 10^{17}$ cm^{-2}. They are characterized by a break at the Lyman limit, whose rest wavelength is at $\lambda_{\rm LL} = 912$ Å. The spectrum of HS 1700+6416 shows seven optically thin LLS. Some of the Lyman breaks can be seen in the low resolution UV spectrum taken with HST/STIS, which is presented in Fig. 2.3. The strength of the break is proportional to the absorber's column density

$$N_{\rm LLS}({\rm H\,I}) = \frac{\tau_{\rm LL}}{\sigma_0}\left(\frac{\lambda_{\rm LL}}{\lambda_0}\right)^3 (1+z_{\rm LLS})^3 \tag{2.14}$$

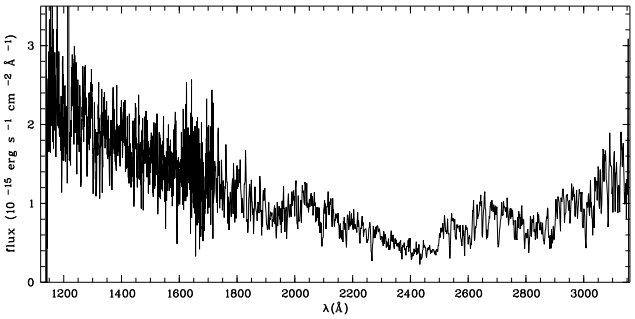

Fig. 2.3: Low resolution UV spectrum of the quasars HS 1700+6416 observed with HST/STIS. More details of the data are given in Chapter 5.2.

(Møller & Jakobsen 1990), where $\sigma_0 = 6.3 \cdot 10^{-18}$ cm^2 is the photoionization cross section of H I, λ_0 the observed position of the break, $\tau_{\rm LL}$ its optical depth, and $z_{\rm LLS}$ denotes the redshift of the system. Bluewards of the Lyman limit break, the observed flux recovers due to the ν^{-3} dependence of the Lyman continuum opacity on the frequency ν.

3. Effects of unrecognized metal lines in the HeII Lyα forest

A modified version of this Chapter will be published with the title "The He II Lyα forest: evaluation of simulated spectra" by Fechner, C. & Reimers, D. in the conference proceedings "Astrophysics in the Far Ultraviolet – Five Years of Discovery with FUSE" (ASP Conf. series) edited by G. Sonneborn, W. Moos, and B.-G. Anderson (astro-ph/0410622).

The observation of the He II Lyα forest in comparison to H I absorption is a useful tool to explore the physical conditions in the intergalactic medium (IGM) at high redshift. Due to its atomic parameters He II absorption is expected to be stronger than H I by the factor η. This column density ratio $\eta = N(\mathrm{He\,II})/N(\mathrm{H\,I})$ is predicted theoretically to be in the range of $\sim 50-100$ (Haardt & Madau 1996; Fardal et al. 1998) assuming the diffuse background radiation of quasars. Variations in η can be used to examine the sources and fluctuations of the intergalactic ionizing continuum.

Recent analyses of the resolved He II Lyα forest towards the QSO HE 2347-4342 reveal values of the column density ratio η ranging from 1 to $>$ 1000 (Kriss et al. 2001; Shull et al. 2004; Zheng et al. 2004b). Therefore, the authors suggest that the intergalactic UV background radiation is strongly variable on very small scales ($\Delta z = 0.001$) requiring the dominance of local sources. However, the scatter can only be explained partly by the different spectral indices of QSOs ranging from $\alpha = 0$ to 3 (Telfer et al. 2002), since the observed scales are much smaller than the typical distances between AGN. Another finding is that absorbers in H I voids show higher η values, a phenomenon that is not understood till now.

On the basis of simulated spectra we investigate, whether the typical quality of the present data is sufficient to recover a constant η, and which effects are produced artificially by the analysis technique. Furthermore, we examine the impact of additional metal line absorption on the results.

3.1. Creating artificial datasets

We generate an artificial Lyα forest in the redshift range $2.292 \le z \le 2.555$, which corresponds to the wavelength coverage of the lower FUSE detector segment. The assumed statistical properties of the H I Lyα forest are based on the observations towards the QSO HS 1700+6414, where we identified 339 Lyα lines in the redshift range $2.274 < z < 2.744$. The column density distribution function with $\beta = 1.5$ is adopted from Kirkman & Tytler (1997). Our observed line sample leads to $\beta = 1.63 \pm 0.08$ for absorbers with $13.0 \le \log N \le 15.0$. Fitting a truncated Gaussian to the Doppler parameter distribution we find $b_0 = 27\,\mathrm{km\,s^{-1}}$, $\sigma_b = 8.75\,\mathrm{km\,s^{-1}}$, and $b_{\min} = 10\,\mathrm{km\,s^{-1}}$ in good agreement with Hu et al. (1995). In addition, the parameters of the simulated line sample are correlated by $b_{\min} = 10.5 + 1.3 \cdot (\log N - 12.5)$ following Misawa (2002). The resolution of $R \approx 40\,000$ and the signal-to-noise ratio of $S/N \sim 100$ were chosen to match the characteristic of high-resultion spectra taken with VLT/UVES or Keck/HIRES.

The same artificial H I spectrum will be used in Chapter 5 to test the validity of the analysis procedures and to investigate possible effects of thermal broadening. Here, the He II Lyα forest is computed from the artificial H I data using $\eta = 80$, the mean value as found by Kriss et al. (2001), and a temperature of 10^4 K, which is consistent with $b_{\min,\mathrm{H\,I}} = 10\,\mathrm{km\,s^{-1}}$. Metal absorption lines were added with strength and distribution as expected in the spectrum of HS 1700+6416. Line parameters were taken from the observed FUSE spectrum of HS 1700+6416 from the spectral range 1140 – 1180 Å redwards of the He II emission. The resolution of $R \approx 15\,000$ and the signal-to-noise ratio of $S/N \sim 5$ were chosen to match the typical values of real FUSE data. The resulting spectra are shown in Fig. 3.1.

3.2. Analysis of the simulated spectra

The artificial H I Lyα forest is analyzed by fitting Doppler profiles. As can be seen from Fig. 3.2, the statistical properties of the sample are recovered. Under the simulated conditions our sample is complete down to $\log N \sim 12.0$. Due to blending effects, the deduced Doppler parameter distribution is broadened by 28 %.

The He II Lyα forest lines are treated the same way, using the derived H I parameters. We fix the line redshift and the b-parameter assuming pure turbulent broadening, where Doppler parameters with $b < 10.0\,\mathrm{km\,s^{-1}}$ are not considered. The resulting η values are shown in Fig. 3.3. The numbers of the following statistical analysis are summarized in Table 3.1.

From the spectrum without any metal line absorption we find a mean value of $\langle \log \eta \rangle = 1.77 \pm 0.43$, which is less than the expected 1.903. The median, which gives less weight to outliers, is 1.86. From the spectrum with additional metal lines we get $\langle \log \eta \rangle = 1.90 \pm 0.49$ (median 1.95). These values suggest that a scatter of about 0.5 dex in η is due to the method. To analyze in detail what causes the extreme deviations we refer to η values outside the range $\log \eta = 1.903 \pm 0.500$. Without metals 2.6 % of the absorbers have high and about 14 % low values. The reasons for the extreme η values are

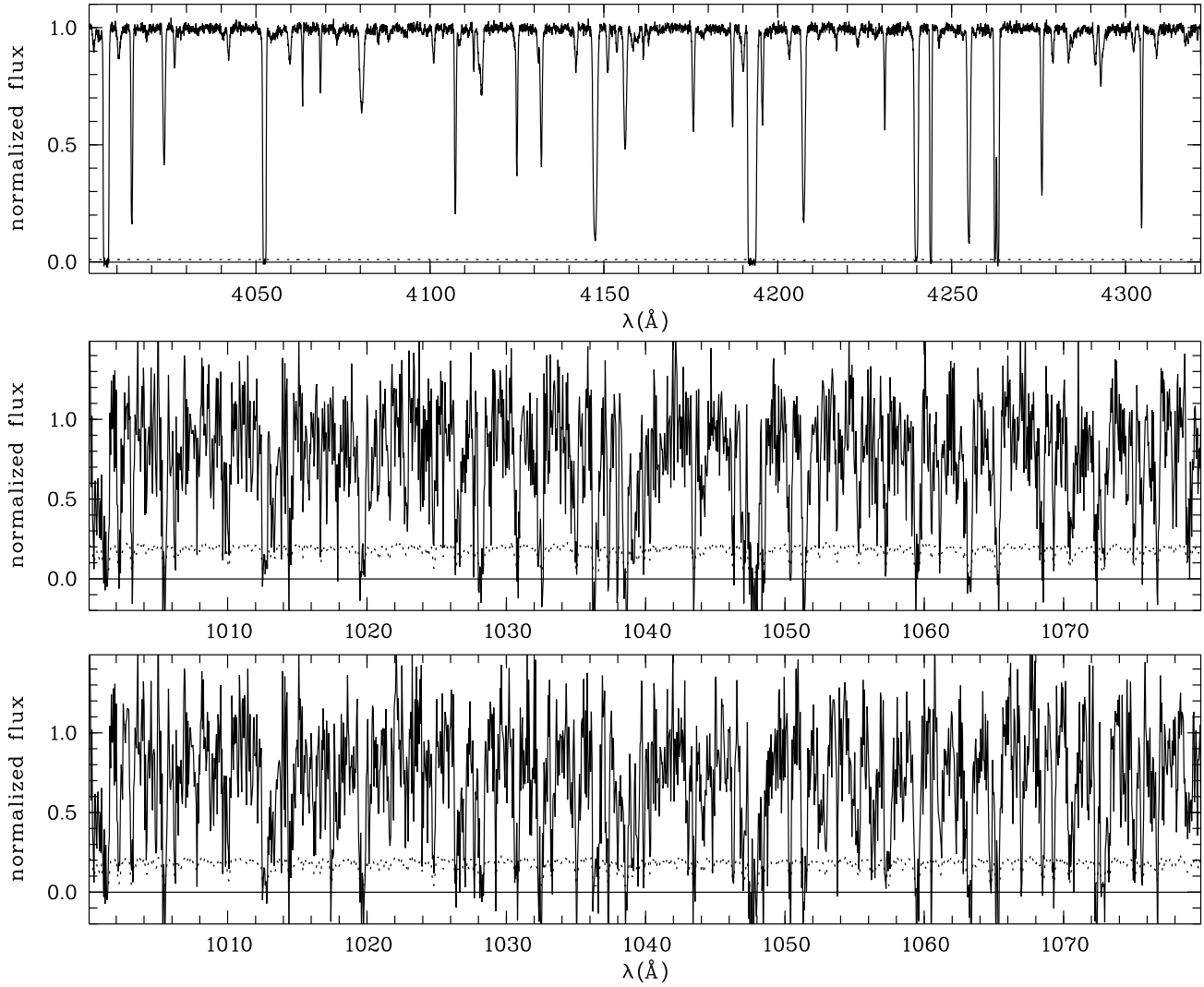

Fig. 3.1: Simulated data. The upper panel shows the artificial H I Lyα forest. The He II spectra are computed from the simulated H I data using $\eta = 80$ and $T_{\rm IGM} = 10^4$K. The spectrum in the lower panel shows the result of the sprinkled metal lines.

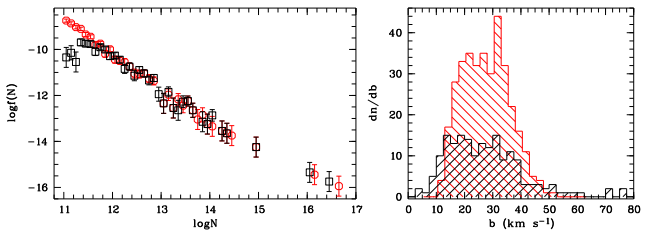

Fig. 3.2: Statistical properties of the simulated and recovered H I line sample. The left panel shows the column density distribution function. The recovered line sample (open squares) is complete down to $\log N = 12.0$. The Doppler parameter distribution (right panel) is simulated as a truncated Gaussian, which is recovered slightly shifted and smeared out. Although there are recovered lines with Doppler parameters below $b_{\rm min}$ they are not considered in the He II analysis.

- the He II line is narrower than the adopted pure turbulent H I Doppler parameter
- weak H I lines, whose parameters are estimated incorrectly or which are misidentified
- blending with other He II lines
- line saturation leading to erroneous column densities

The last three points can lead, in principle, to high as well as low η values, while the first one produces only low η values. In contrast to Shull et al. (2004) who found a correlation between low density H I absorbers and high column density ratios using an apparent optical depth method, we find weak H I lines often leading to small η. This can be explained by the large uncertainties of weak lines, concerning the line position. Thus, the column densities of the He II lines with fixed redshifts are underestimated. However, also strong H I lines lead to low column density ratios. Considering line samples with $\log N_{\rm H\,I} > 13.5$, the column density ratio is on average $\log \eta = 1.33 \pm 0.75$ and 1.57 ± 0.80 for the spectrum without and with additional metal line absorption,

Table 3.1: Summary of the analysis of the $\log\eta$-distribution.

	without metals	with metals
$\langle\log\eta\rangle$	1.77 ± 0.43	1.90 ± 0.47
$\log\eta_{\rm median}$	1.86	1.95
lines with $\log\eta < 1.4$	22 (14.2 %)	16 (10.2 %)
lines with $\log\eta > 2.4$	4 (2.6 %)	9 (5.8 %)
reasons for small η:		
H I misidentification	9 (40.9 %)	5 (31.3 %)
saturation	4 (18.2 %)	4 (25.0 %)
$b = b_{\rm turb}$ assumption	5 (22.7 %)	3 (18.8 %)
line blending	2 (9.1 %)	2 (12.5 %)
unknown	2 (9.1 %)	2 (12.5 %)
reasons for high η:		
metal	0	7 (77.8 %)
saturation	1 (25.0 %)	1 (11.1 %)
weak HI	3 (75.0 %)	0
unknown	0	1 (11.1 %)

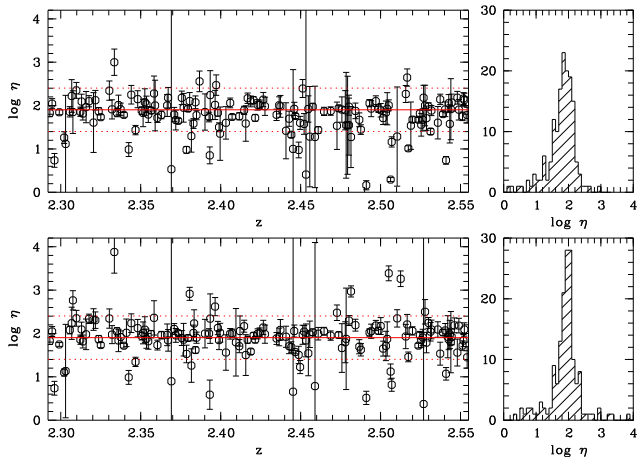

Fig. 3.3: Values of the column density ratio η for the He II spectrum without (upper panel) and with (lower panel) additional metal line absorption. The horizontal line indicates the expected value $\log\eta = 1.90309$ corresponding to $\eta = 80$. The dotted lines represent the range $\log\eta = 1.903 \pm 0.005$.

respectively. These values are significantly below the mean column density ratio of the total samples. In Chapter 5 we will present a more detailed investigation of this point. We will come to the conclusion that part of the η values of high density H I absorbers are underestimated due to inadequate treating of thermal line broadening.

Generally, the presence of metal lines leads to higher η values as can be seen from the lower panel of Fig. 3.3, where 80 % of the extremely high η values are due to metals. Furthermore, there are fewer low η absorbers, since blending with metal lines counteracts the other effects. About 15 % of the superimposed metal lines cause higher η values. All of them affect mainly weak absorbers with $\log N \lesssim 12.0$. This is plausible since metal lines are expected to be narrow and weak in comparison to the Lyα features. If blended with a strong, possibly saturated Lyα line, the metal absorption would hardly be detectable.

3.3. Conclusions

Using an artificial H I Lyα forest spectrum we simulate the corresponding He II forest with a fixed value of η and a Doppler parameter consisting of a thermal ($T_{\rm IGM} = 10^4$ K) and a turbulent part. In a second step, metal lines with line strengths and line density as expected in case of HS 1700+6416 are superimposed.

The standard analysis of the spectra by fitting Doppler profiles yields a scatter in η by a factor of ~ 10 due to imperfect line recovery especially of weak H I lines due to limited resolution and S/N. Since we choose the resolution and signal-to-noise of the simulated data comparable to typical values of observations, we conclude that part of the variations in η found by previous analyses of the He II Lyα forest towards HE 2347-4342 is an artifact. Outliers can be produced by various reasons like saturation or blending effects as well as misidentification of weak H I lines. Additionally, He II features may be narrower than the assumed purely turbulent Doppler parameter. Extremely high η values (up to $\gtrsim 1000$) arise predominantly in the connection with metal line absorption. According to our simulations 80 % of the extreme η values above the mean are caused by metal lines. Considering the total sample 5 % of the η values are contminated by metals.

Finally, we find no correlation between small column densities (in voids) and high η values as claimed by Shull et al. (2004). However, there are indications that strong H I lines result in small column density ratios. This question will be addressed again in Chapters 5 and 6.

4. Metal line systems in the spectrum of HS 1700+6416

Observations with the Far UV Spectroscopic Explorer (FUSE) for the first time resolved the He II Lyα forest (λ_0 = 303.7822 Å) towards two lines of sight, HE 2347-4342 (Kriss et al. 2001; Shull et al. 2004; Zheng et al. 2004b) and HS 1700+6416 (Reimers et al. 2004). Comparison to the H I Lyα forest revealed strong variations of the He II/H I ratio. Since He II/H I depends on the shape of the ionizing radiation, a strongly fluctuating metagalactic UV background is implied. The radiation background is believed to be generated by the light of quasars and stellar sources such as star-forming galaxies reprocessed in the clumpy matter of the intergalactic medium (IGM; e.g. Haardt & Madau 1996, 2001; Fardal et al. 1998). Due to the evolution of the sources, cosmic expansion, and the process of structure formation, even the UV background evolves with redshift. Deviations from the mean metagalactic background may also be due to the spatial vicinity of local sources. Observational hints for such effects are found by Boksenberg et al. (2003) and Levshakov et al. (2003), supported by recent theoretical work of Schaye (2004) and Miralda-Escudé (2005).

Possible sources affecting the ionization conditions of intergalactic absorbers are quasars along the line of sight of the background QSOs as well as star-forming galaxies. Searches for galaxies close to the sight lines of background quasars find a correlation between the Lyα forest and the galaxy density in the low redshift universe (e.g. Bowen et al. 2002) as well as at high redshifts (Adelberger et al. 2003). The authors conclude that both classes of objects trace the same large scale structure. The vicinity of an absorber to a galaxy is supposed to make the galaxy's radiation dominate over the general UV background, at least if there are enough photons escaping from the galaxy (Bianchi et al. 2001; Steidel et al. 2001).

QSOs close to the line of sight are expected to produce a transverse proximity effect resulting in a reduction in the strength of the Lyα forest absorption due to the hard radiation of the QSO (Bajtlik et al. 1988). This effect has been measured in the spectra of QSOs close to the emission redshift (e.g. Scott et al. 2000), but except in the quasar Q0302-003 (Dobrzycki & Bechtold 1991; Jakobsen et al. 2003) no transverse proximity effect could be detected so far (Schirber et al. 2004; Croft 2004). The authors argue about an increase of the gas density in the vicinity of QSOs , anisotropy of the QSO emission, and time variability in order to explain the absence of the proximity effect.

In this Chapter, we present a study of the rich metal line spectrum of the QSO HS 1700+6416 (z = 2.72, α(2000.0) = $17^{\rm h}01^{\rm m}00\overset{\rm s}{.}6$, δ(2000.0) = +61°12′09″). This object is exceptionally bright in the optical (V = 16.1). Although it provides seven optical thin Lyman limit systems (LLS) along the line of sight and is variable in the UV (Reimers et al. 2005b), HS 1700+6416 is one of the few quasars, where He II is observable (Davidsen et al. 1996; Reimers et al. 2004). Due to its brightness, HS 1700+6416 has been addressed in several analyses dealing with metal line systems (e.g. Reimers et al. 1992; Vogel & Reimers 1993, 1995; Köhler et al. 1996; Petitjean et al. 1996; Tripp et al. 1997; Simcoe et al. 2002, 2005), and due to its rich metal line spectrum, it has been target of deep direct observations in several spectral ranges aiming to identify objects which give rise to the Lyman limit absorption (Reimers et al. 1995, 1997b; Teplitz et al. 1998; Erb et al. 2003; Shapley et al. 2005). Our main objective is to predict the metal line content of the FUSE spectral range in the spectrum of this quasar, which will be considered in the analysis of the He II Lyα forest towards this quasar. Since the available He II data is rather noisy ($S/N \sim 5$), the identification of narrow absorption features due to transitions of metal ions is nearly impossible. Nevertheless, simple tests with simulated data indicate that the presence of unrecognized metal line absorption may bias the derived He II/H I ratio (Chapter 3). Thus, an investigation of the metal line content in the corresponding spectral region (1000 – 1180 Å) will improve the analysis of the He II forest.

In order to model metal absorption line systems, photoionization calculations are performed. One basic assumption concerns the shape of the ionizing energy distribution. We use the modelling procedure to study the potential and restrictions of observed metal absorption systems with the aim to constrain the shape of the UV ionizing background. Because of the numerous metal line systems in the spectrum and the many observations already made, HS 1700+6416 is highly eligible for this task. As a first step, we compute photoionization models based on different ionizing radiation backgrounds for each system. The resulting models are compared to the observed features and checked for the plausibility of the model parameters, deciding which one of the presumed energy distributions leads to the best description of the system.

This Chapter is organized as follows: Having presented the observations in Section 4.1 we describe the modelling procedure and its limitations in Section 4.2 and 4.3. The observed systems are outlined individually in Section 4.4 also presenting the models. The results from the analysis of the whole sample and their implications are discussed in Section 4.5. Finally, the prediction for the metal lines in the FUSE spectral range is presented.

4.1. Observations

The optical data have been taken with the HIRES spectrograph at the Keck telescope. We have got two datasets already published by Songaila (1998) and Simcoe et al. (2002). These two datasets are co-added resulting in a spectrum with a total exposure time of 84 200 s and a signal-to-noise of $S/N \sim 100$ at 4000 Å. The co-added spectrum covers the wavelength range 3680 – 5880Å with a resolution of $R \sim 38\,000$. The wavelength coverage of the Simcoe et al. (2002) data goes down to $\sim$ 3220 Å with decreasing S/N and reaches upto $\sim$ 6140 Å. To identify and model the metal line systems, we use the whole wavelength range.

The UV data are taken from the Hubble archive. HS 1700+6416 was observed with STIS using the Echelle E140M grating ($R \sim 45\,800$) in 1998 July 23 – 25. The data cover the wavelength range 1142 – 1710 Å. The exposure time of $\sim$ 76 500 s leads to a poor signal-to-noise of $\sim$ 3. Therefore, we only use the best portion of the spectrum (1230 – 1550 Å). Due to its rather limited quality, the STIS spectrum is used predominately for consistency checks. Nevertheless, in case of the low redshift systems ($z \lesssim 1$), the vast majority of the absorption lines is located in the UV, and a more quantitative way to consider the corresponding transitions is necessary. Therefore, the data are smoothed applying a Savitzky-Golay filter (see e.g. Press et al. 1994, p. 650) and fitted as described below. However, we avoid to use the derived numbers, if possible.

The wavelength scales of the optical and the UV data have been checked to be well aligned. Interstellar absorption of Na I is detected in the optical at $v = (-35.0 \pm 0.1)\,\mathrm{km\,s^{-1}}$, in good agreement with interstellar absorption of S II, O I, Si II, and Fe II measured in the UV.

The HST archive contains further UV data taken with the instruments FOS and GHRS, respectively, presented by Vogel & Reimers (1995) and Köhler et al. (1996). These datasets are in general less noisy ($S/N \gtrsim 10$) but since they have only medium resolution ($R \approx 1300$ and slightly higher), we reject them for this analysis, except for using the optical depths of the LLS.

All metal line systems have been identified by looking for features like the doublets of C IV and/or Mg II in the optical and then searching for further transitions expected to arise in the optical and UV from the list of Verner et al. (1994). The results have been compared with the identifications made in former work (Vogel & Reimers 1995; Köhler et al. 1996; Petitjean et al. 1996; Tripp et al. 1997; Simcoe et al. 2002, 2005). The line parameters of the absorption features are estimated using the line fitting program CANDALF developed by R. Baade, which performs simultaneously a Doppler profile line fit and the continuum normalization. The derived column densities are given in the Appendix (Tables A.1, A.2, A.3, and A.4).

4.2. Modelling procedure

In analyzing the observed systems we use the photoionization code CLOUDY version 94.00 (Ferland 1997). In order to investigate the shape of the ionizing radiation, eight different energy distributions are considered, among them the Haardt & Madau (2001) background (HM) at the appropriate redshift. Compared to the classical Haardt & Madau (1996) radiation field the new version includes contributions of galaxies. We use a model where the escape fraction of Lyman limit photons from a galaxy is $f_{\mathrm{esc}} = 0.1$. In addition, we use three different types of modified HM continua. One possible modification is a shift of the break at 4 Ryd to lower energies. The filtered radiation might change this way, if absorption by the He II Lyman series becomes important in addition to the He II continuum at redshifts below 3. We create modified Haardt-Madau energy distributions, shifting the 4 Ryd break to 3.0 (HM3) and 2.0 Ryd (HM2), respectively. In a third modification, the plateau at energies < 1 Ryd is scaled with the factor 0.1 (HMs0.1). Since at these low energies the background is dominated by the radiation of galaxies, a lower flux level mimics roughly a reduction of the fraction of the galaxy radiation. All Haardt-Madau type spectra are shown in the upper panel of Fig. 4.1 at a redshift $z \sim 2$.

Furthermore, typical spectral energy distributions of galaxies and quasars are used in order to examine the possible presence of local sources dominating the ionizing radiation. Actually, the energy distribution of a local source and the general background should be merged to present a more realistic model (Boksenberg et al. 2003; Simcoe et al. 2005). Here, we start with the extreme assumption that the absorber is solely illuminated by the local source. A model starburst galaxy with a constant star formation rate after 0.001 Gyr given by Bruzual A. & Charlot (1993, SB) is adopted as a pure galaxy spectrum. The energy distribution of an AGN is taken from Mathews & Ferland (1987, MF) as it is implemented in CLOUDY. For comparison pure power law models $f_\nu \propto \nu^\alpha$ with $\alpha = -1.5$ (PL15) and -0.5 (PL05), respectively, are adopted as well.

For each of the considered ionizing energy distributions and each system a grid of models is computed. The model parameters are the observed H I column density, the ionization parameter, which is chosen as $-4.0 \leq \log U \leq 0.5$, the metallicity in units of the solar value ($-3.0 \leq \log(Z/Z_\odot) \leq 0.0$), and the hydrogen density ($-5.0 \leq \log n_{\mathrm{H}} \leq 3.0$). The models depend only weakly on the hydrogen density but its importance increases for high ionization parameters. Solar metallicities are taken from Grevesse & Sauval (1998) with the updates from Holweger (2001). The helium abundance is assumed to be primordial.

On the computed grids, the best fitting models are chosen by considering the most reliable observed column densities. If possible we use the column density ratios of two ionizations stages of the same element, e.g. $N(\mathrm{C\,IV})/N(\mathrm{C\,III})$. The estimated grid parameters are the starting values for a detailed calculation, where the ionization parameter, the

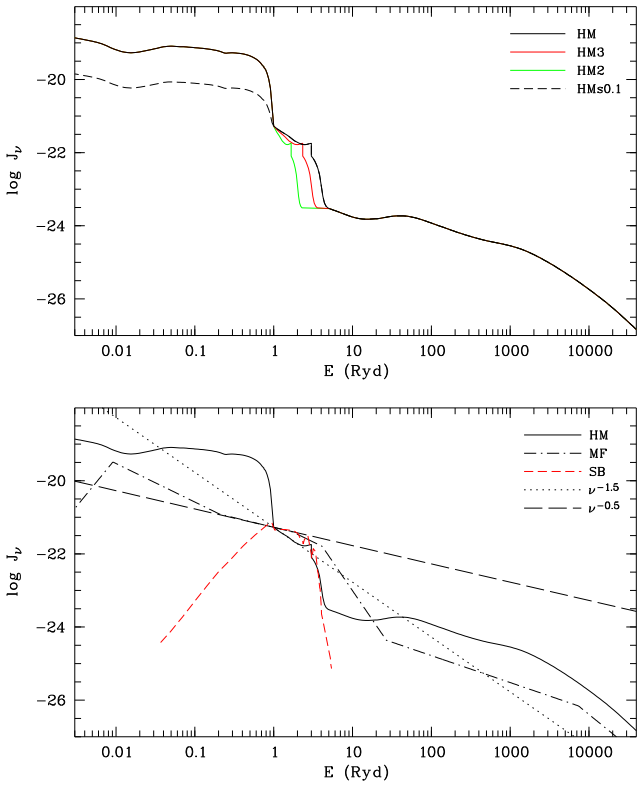

Fig. 4.1: The shapes of the ionizing radiation used for the presented investigation. The upper panel shows the UV background of Haardt & Madau (2001) at $z \sim 2$ and the considered modifications with the 4 Ryd break shifted to 3.0 and 2.0 Ryd, respectively (solid lines). The dashed line represents the modification, where the low energy part (< 1 Ryd) is scaled by a factor 0.1. The lower panel presents the energy distributions for a starburst galaxy (Bruzual A. & Charlot 1993, short dashed line), an AGN (Mathews & Ferland 1987, dot-dashed), and power laws with $\alpha = -1.5$ (dotted) and $\alpha = -0.5$ (long dashed), respectively. The Haardt & Madau (2001) background at $z \sim 2$ (solid line) is also given for a better orientation.

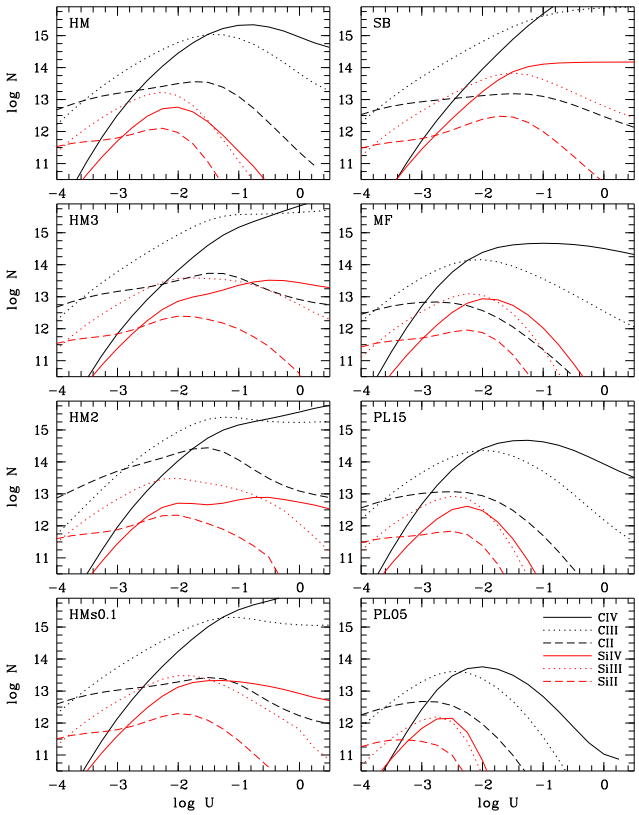

Fig. 4.2: Dependence of the column density on the ionization parameter $\log U$ of ions of carbon (C II, C III, C IV) and silicon (Si II, Si III, Si IV) for the ionizing spectra considered in the modelling procedure (see text). The legend is given in the lower right panel. The column density of neutral hydrogen in $\log N_{\rm H\,I} = 16.83$, the metallicity is [M/H] = −2.0 and density $\log n_{\rm H} = -2.0$ for all models.

hydrogen density, and the metallicity are optimized, using the related CLOUDY command. Deviations from the solar abundance pattern are also considered if suggested by the data with the purpose to recover the abundance pattern usually found for low metallicity gas. Throughout this Chapter abundances are given in the common notation $[{\rm M/H}] = \log({\rm M/H})_{\rm obs} - \log({\rm M/H})_{\odot}$.

For illustrating the importance of the UV background, Fig. 4.2 presents how the column density of ions of carbon (C II, C III, C IV) and silicon (Si II, Si III, Si IV) changes with the ionization parameter for the considered ionizing energy distributions. Particularly for $\log U \gtrsim -2.5$ significant differences are present, even if the UV background is only moderately changing as given in case of the HM-like spectra (left panels of Fig. 4.2).

A synthetic spectrum based on the resulting parameters is computed for comparing the model with the data and evaluate the quality of the fit. For each transition, Doppler profiles are calculated, adopting the column density directly from the model result. The Doppler parameter b is derived from the model temperature as follows: Using the Doppler parameter of one unblended well-measured line, the turbulent part of the b-parameter is computed using $b^2 = (2kT/m) + b^2_{\rm turb}$, where T is the temperature obtained for the model, m the mass of the considered element and k Boltzmann's constant. The estimated turbulent part $b_{\rm turb}$ is fixed for all lines, while the thermal contribution is re-computed for each element. The exact redshift of the lines is also adopted from one unblended, well-measured transition. The resulting spectrum is then broadened to the resolution of the observed data. Thus, a quantitative comparison with the Keck data can be performed. Furthermore, the models are checked for consistency with the STIS data.

The evaluation of the goodness of fit is performed by estimating a χ^2 as a quantitative criterion. We use

$$\chi^2 = \frac{1}{n}\sum_{i=1}^{n}\left(\frac{f_{{\rm obs},i} - f_{{\rm mod},i}}{\sigma_i}\right)^2 , \qquad (4.1)$$

where $f_{{\rm obs},i}$ and $f_{{\rm mod},i}$ is the observed and modelled flux at pixel i, respectively, σ_i is the error of the observed flux, and n is the number of pixels considered for the χ^2 estimation. Since lines arising in the STIS part of the spectrum would

dominate the χ^2, only features observed in the Keck spectrum are regarded. The lines and intervals appropriate to be used have to be selected for each system individually.

4.3. Limitations

Many metal absorption line systems are multi-phase absorbers, which means low and high ionized absorption features are not formed in the same volume (examples of well studied low redshift absorption systems can be found e.g. in Ding et al. 2003; Zonak et al. 2004; Masiero et al. 2005). Especially O VI is believed to arise in a spatially more extended, low density gas (e.g. Lopez et al. 1999; Simcoe et al. 2002). Thus, it is clear that our models are only a first step. More realistical descriptions should take into account the probably multi-phase nature of the absorbers. In the simple models presented here, the modelled ionization levels partly depend on the strategy of the analysis. Depending on the available observed line ratios either the low or the high ionization phase is reproduced. The choice of the constraining ions depends on the observed spectrum. In most of the cases C III/C IV or Si III/Si IV can be used, since mostly C IV and Si IV are unambiguously detected and the column density can be estimated reliably even if the features are rather weak. Contrarily, the features of the low ionization phase are more often located in the Lyα forest, where blending limits the measurability of column densities. Nevertheless, in a few cases ratios like C II/C III or Si II/Si III are more prominent than the highly ionized species and therefore the low ionization component is modelled. There are also systems, where C III and/or Si III cannot be detected because they are blended with strong or saturated Lyα forest lines. In this case ratios like C II/C IV or Si II/Si IV have to constrain the model, which is extremely problematic, since the ions may originate in distinct volumes. We will discuss the implications of approaches like this in more detail when the respective systems are presented.

Another problem is the considered amount of neutral hydrogen. Usually, the Lyα line is saturated and only in a few cases substructures in the H I features become visible in higher order Lyman series. For systems at $z < 1.5$, Lyα is located beyond the observed spectral range (except the $z = 0.2140$ system), thus we adopt the column densities measured by Vogel & Reimers (1995) using the Lyman limit break. Anyhow, following the described modelling procedure it is necessary to distribute the total H I column density over the subcomponents observed in the metal lines. This is done by following the distribution of appropriate metals. If possible all ionization stage are considered, e.g. $N(\mathrm{C_{tot}}) = N(\mathrm{C\,II}) + N(\mathrm{C\,III}) + N(\mathrm{C\,IV})$ or $N(\mathrm{Mg_{tot}}) = N(\mathrm{Mg\,I}) + N(\mathrm{Mg\,II})$. Due to incomplete coverage of the ionization stages, the distribution of neutral hydrogen according to this method is a considerable source of systematic error. If only part of the measured H I absorption is associated to the metal absorption, the absolute elemental abundances are underestimated. However, the relative abundances are probably not affected.

But also handling relative abundances may cause problems, since they depend on the shape of the ionizing background. The value of [Si/C] derived from observations is typically [Si/C] $\lesssim 0.5$, consistent with the predictions in theoretical supernova yields from various progenitor properties (Woosley & Weaver 1995; Heger & Woosley 2002; Chieffi & Limongi 2004; Umeda & Nomoto 2002, 2005). However, since ionization corrections are needed, the [Si/C] derived from observations depends on the adopted UV background. Aguirre et al. (2004) pointed out that [Si/C] gets higher for harder ionizing radiation. They found [Si/C] ~ 1.5 for an unrealistic hard UV background. However, Qian & Wasserburg (2005) predict that [Si/C] can be as high as ~ 1.3, if the metals are produced by very massive stars ($> 100\,M_\odot$) adopting a model of Umeda & Nomoto (2002).

Furthermore, only eight discrete shapes of the UV background are considered. This means, we follow a very simple approach to constrain the shape of the ionizing background from observed data. A real fit would require some kind of algorithm (a possible method has recently been introduced by Agafonova et al. 2005). Thus, our results do not represent the ionizing radiation most probably illuminating the absorbing gas. But they provide models, which fit the observed data more accurately and reasonably than the models based on the other energy distributions considered here.

4.4. Observed systems

The spectrum of HS 1700+6416 is characterized by a huge amount of metal line absorption features. This rich metal line spectrum has been studied in detail with medium resolution in the UV (Reimers et al. 1992; Vogel & Reimers 1995; Köhler et al. 1996) and with high resolution in the optical (Petitjean et al. 1996; Tripp et al. 1997; Simcoe et al. 2002).

Including the seven LLS, we identify 25 metal line systems in the spectrum of HS 1700+6416. Three metal line systems located at $z = 2.7124, 2.7164$, and 2.7443 are apparently associated with the QSO. Each of them show a multicomponent velocity structure. In two of them, N v, a typical transition observed in associated systems, is detected and signs of partial coverage are seen. The intergalactic absorption systems cover a redshift range $0.2 \lesssim z \lesssim 2.6$. The seven Lyman limits systems are located at $z = 0.8643, 1.1573, 1.7241, 1.8450, 2.1680, 2.3155$, and 2.4331. Four of the intervening systems (at $z = 2.0211, 2.1278, 2.1989$, and 2.3079) show only metal absorption features of C IV. Thus, it is impossible to constrain models. However, the expected C IV $\lambda\lambda 312.5, 312.4$ lines can be computed directly from the estimated line parameters, and will be considered in the predicted metal line spectrum.

In the following, we present the observations of the identified metal line systems. The models are discussed and the most appropriate one is derived.

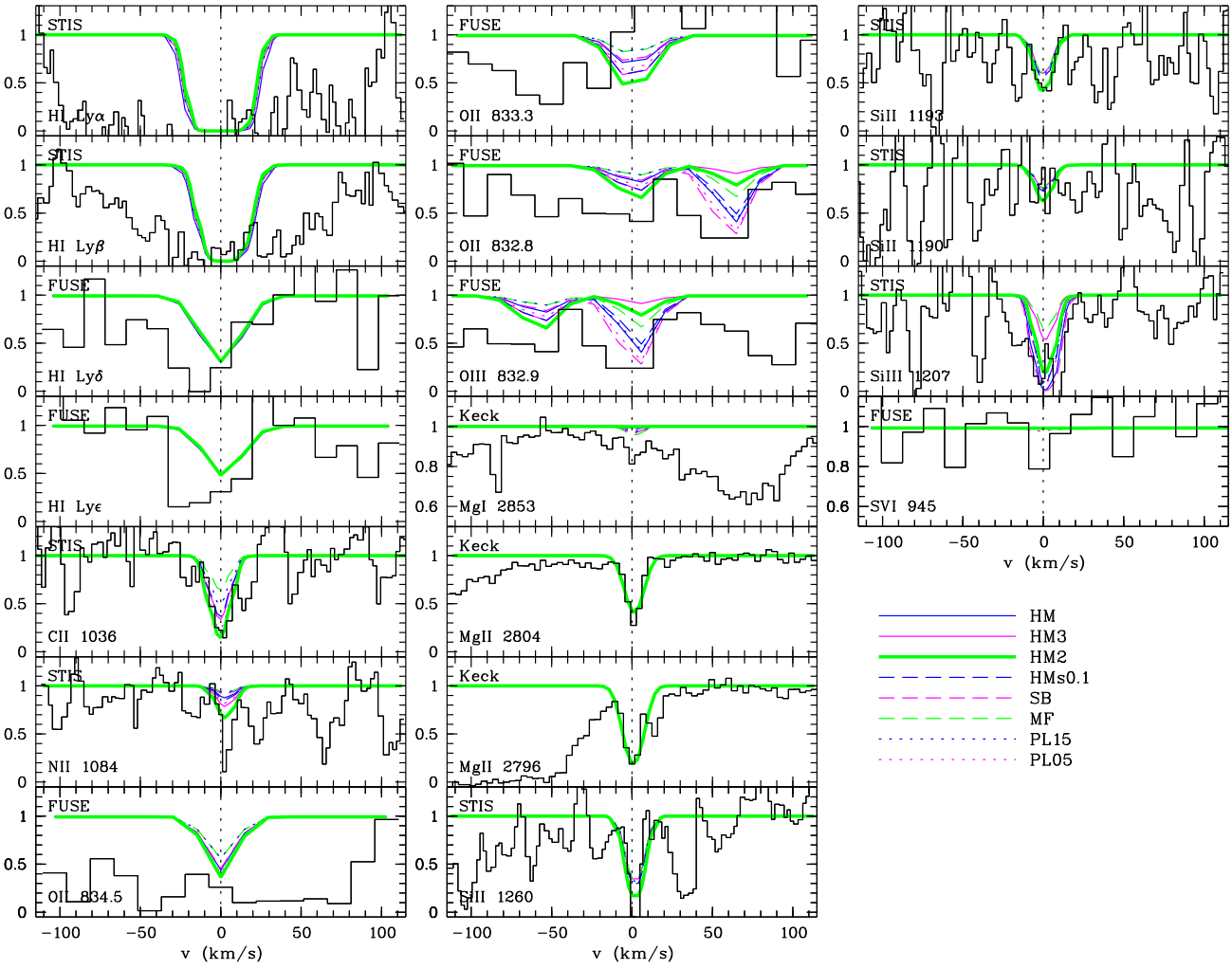

Fig. 4.3: Observed and modelled absorption lines of the system at $z = 0.2140$. The histogram-like lines give the observed flux at the expected position of the indicated transitions. The name of the observing spectrograph is indicated in the upper left corner of each panel. The plotted STIS data is unsmoothed, i.e., no Savitzky-Golay filter is applied. The preferred model HM2 is presented as the thick line. All other models are shown as thinner lines for a rough comparison.

4.4.1. System $z = 0.2140$

The lowest redshifted metal line absorber is located at $z = 0.2140$ (Fig. 4.3). According to Reimers et al. (1989, 1997b), the X-ray cluster Abell2246 ($z = 0.25$) gives rise to this system. Because of the low redshift, Mg II is visible in the optical. Mg I may be present as well, but its identification is questionable. The magnesium features shows no velocity substructure. In the UV besides H I Lyα, features of C II, Si II, and Si III are clearly detected. Probably N II is also present.

Since the models are based on the noisy STIS observations, a quantitative statement is difficult. Mg II is used to fix the b-parameter, therefore it is reproduced well with all models, even though super-solar abundances are needed in any case. But the absorption feature claimed for Mg I is underpredicted. Notable but still insignificant features are produced by the MF, SB, HMs0.1, and PL05 model. In the UV, the C II and silicon features are well reproduced using HM, HM2, SB, or PL05. All other models underestimate the strength of at least one ion. The strongest N II feature is predicted by the HM2 model.

Since only magnesium is observed in the optical part of the spectrum, it is impossible to quantify the goodness of the models by the χ^2-method introduced in Section 4.2. Therefore, the evaluation of the results is based on the discussion above. The favoured models are then HM, HM2, and PL05. Considering the model parameters, HM and PL05 require unphysically high or low densities ($\log n_{\rm H} = 2.5$ or -6.8), respectively, and very high abundances (the metallicity derived for the PL05 model exceeds the solar values by more than 1 dex). Whereas, using the HM2 background leads to a very dense ($\log n_{\rm H} = 0.29$) but cold ($T = 10^{3.63}$ K) absorber with somewhat super-solar abundances ([M/H] = 0.19) and [Si/C] = 0.17.

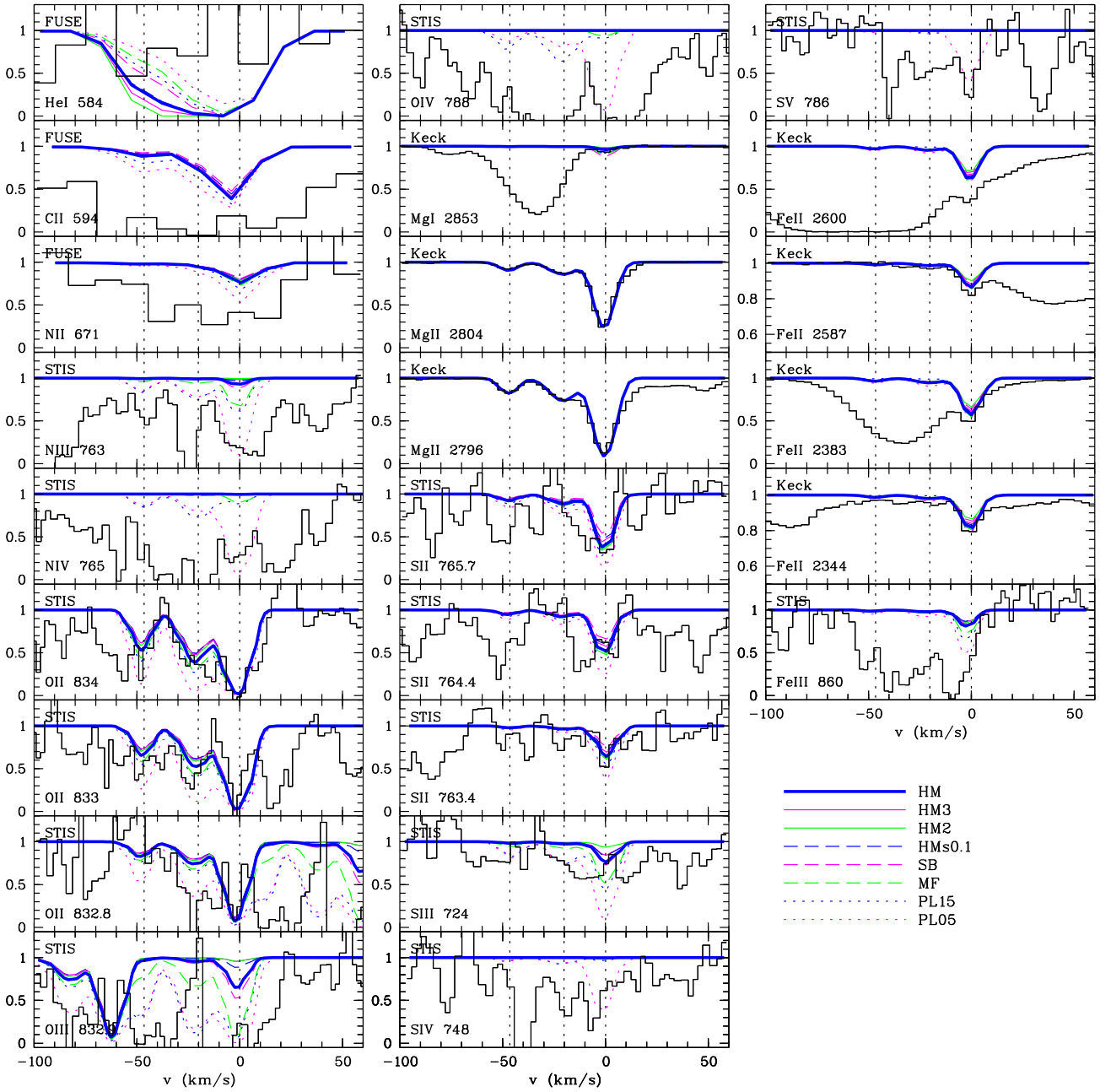

Fig. 4.4: Observed and modelled absorption lines of the system at $z = 0.7222$. The preferred model is HM.

4.4.2. System $z = 0.7222$

The absorber at $z = 0.7222$ might be an additional Lyman limit system. Even though the FOS data analyzed by Vogel & Reimers (1995) reveals no Lyman limit, the STIS data indicate a break at the corresponding position. Furthermore, Vogel & Reimers (1995) measure a H I column density of $\log N = 16.20$, which may give rise to an optically thin LLS. In the Keck data, we detect Mg II in three, probably four subcomponents spread over a velocity range of $\sim 50\,\mathrm{km\,s^{-1}}$. The λ2796.4 doublet component is blended with Si IV of the $z = 2.4331$ system. At the velocity of the strongest Mg II component, Mg I and Fe II are present as well. The STIS data indicates the presence of several additional ions of nitrogen, oxygen, and sulphur. The column densities are estimated assuming the Mg II velocity structure and fitting line profiles of the same ion simultaneously.

The models are based on the ions observed in the optical, i.e. on magnesium and iron. The ionization parameter and density as well as the metallicity are fixed considering Mg II and Fe II. Thus, all other lines are predicted by the models (shown in Fig. 4.4). For all ions of a single element, an offset in line strength may be given, if deviations from the solar abundance pattern are present.

Discussing the models, we concentrate on the strongest component. The ratio Mg I/Mg II is modelled well with HM,

HMs0.1, MF, PL15, and PL05. Mg I is overproduced by SB, while it is underestimated by HM3 and HM2. A significant amount of nitrogen (N III as well as N IV) is produced by the hard spectra of MF and both the power laws, and all models predict N II absorption consistent with the FUSE data. O II is overestimated for the PL05 model. Very little O III and no detectable O IV at all is predicted by the softer ionizing backgrounds (all the HM-like radiation fields and SB), while the models with harder spectra lead to O III absorption consistent with the STIS data (MF) or in case of the power laws even more. Little O IV absorption is predicted by the MF and PL15 models. The PL05 model leads to prominent O IV features absolutely consistent with the data. The higher ionization stages of sulphur (S IV and S V) are only present for the power law models. The prediction by PL05 fits the data well, but the lower ionization stages S II and S III are overestimated. The hard models tend to overpredict S III, while it is consistent with the data for all other models.

Since we observe three transitions in the optical, χ^2-values can be derived. We consider Mg I, Mg II λ2084, and Fe II λ2344 and find HM to lead to the best model ($\chi^2 = 10.7$). The models based on the hard ionizing spectra (MF, PL15, and PL05) fit slightly worse. Since the power law models overestimate some oxygen and sulphur ions, we look for the best model among HM and MF. All these models have high densities ($\log n_{\rm H} > 1.0$ or higher), which appear to be unrealistic. However, since the models barely depend on the density, especially at low ionization parameters, we can claim the density to be unknown. From the appearance of the modelled features, under the assumption that as much observed absorption as possible originates from the system, HM is preferred, which is also consistent with the estimated χ^2.

4.4.3. System $z = 0.8643$

The absorber at $z = 0.8643$ gives rise to an optically thin LLS. Mg II, located in the optical, shows a complex velocity structure with seven subcomponents spread over $\sim 150\,\mathrm{km\,s^{-1}}$ (Fig. 4.5). We use the Mg II velocity splitting to fit the ions arising in the STIS portion of the spectrum (N III, N IV, O III, O IV, S III, S IV, and S V), where the weakest component is neglected. Thus, we concentrate on the six main features. Continuum windows are present for Mg I, Al III and Fe II.

Because of only one ion observed in the optical, the models have to be constrained on the basis of the less confident UV lines. We adopt S III and S IV as suitable lines, which therefore are fitted well by all models. Thus, S II and S V can be used to constrain the model. While S II is predicted consistent with the data by all models, S V appears to be overpredicted in any case except the SB model. The nitrogen abundance is scaled to match the observed feature of N IV. The models HM3, HMs0.1, and SB predict slightly too much N III absorption, while N II is modelled consistently for all models. We left the carbon abundance unscaled obtaining a prediction of C II. Too much C II absorption is produced by the models HM3, HM2, and both the power laws.

Following this discussion, the best models are HM, HMs0.1, and SB. Evaluation of the derived model parameters exhibits that they are spread over a wide range, since six subcomponents are concerned. Because of the similarity of the ionizing spectra, the distribution of the elemental abundances over the subcomponents obtained is very similar regarding the HM and HMs0.1 model. [S/H] is roughly constant for all components with ~ -0.35 for HM and ~ -0.68 for HMs0.1. Unlike this, the sulphur abundances are spread over a range of roughly 0.34 dex for the SB model, while here [Mg/H] ~ -1.03 is nearly constant for all subcomponents. For lack of further arguments, we keep HM, HMs0.1, and SB as different but equivalent models for the $z = 0.8643$ absorber.

4.4.4. System $z = 1.1573$

The Lyman limit system at $z = 1.1573$ shows Mg II absorption in the optical. We assume only one component even though asymmetries in the Mg II profiles indicate the presence of at least two unresolved components (see Fig. 4.6). Furthermore, Fe II and Al II can be detected in the Keck part of the spectrum. Al III might be present, but cannot be identified because of blending with Lyα forest lines. Si II λ1526.7 may be identified as well, but a reasonable profile fit was impossible. C IV could in principle be observed in the optical part of the spectrum at this redshift, but the expected features would arise in the Lyγ absorption troughs of the $z \approx 2.433$ absorption complex. Thus, C IV might be present but its column density cannot be measured. The red wing of the absorption troughs at the expected position of C IV might suggest the presence of an high ionization phase shifted by $\sim 40\,\mathrm{km\,s^{-1}}$. This component may be also present in oxygen (O III, O IV, O V), even though due to saturation the identification is questionable. In the UV, we measure column densities of N II, N III, O III, O V, S III, and S IV. Additionally, He I is detected.

For constraining the model parameters, we use Mg II and Fe II. Furthermore, a solar abundance pattern is assumed. In this case, the low ionization stages like C II, Si II, N II, O II, and Al II are fitted well with the models based on soft ionizing radiation. The harder UV backgrounds (MF, PL15, and PL05) overestimate the low ionization stages but produce significant features of transitions from higher ionized elements, which appear only sparsely using the softer spectra. Of course, each model could be further optimized by scaling the elemental abundances. However, the best fitting model found this way is HMs0.1 leading to the best description of the low ionization stages.

Lines of high ionization stages of neon are expected in the FUSE spectral range. However, if present, the Ne IV $\lambda\lambda\lambda$541, 542, 543 triplet would by located above the He II emission redshift, and Ne V λ480 would be blended with complex C IV absorption of the $z = 2.3155$ LLS. The only feature, that might be underestimated, is Ne VII λ465, expected to arise at 1003.6 Å. If the analysis of the He II Lyα

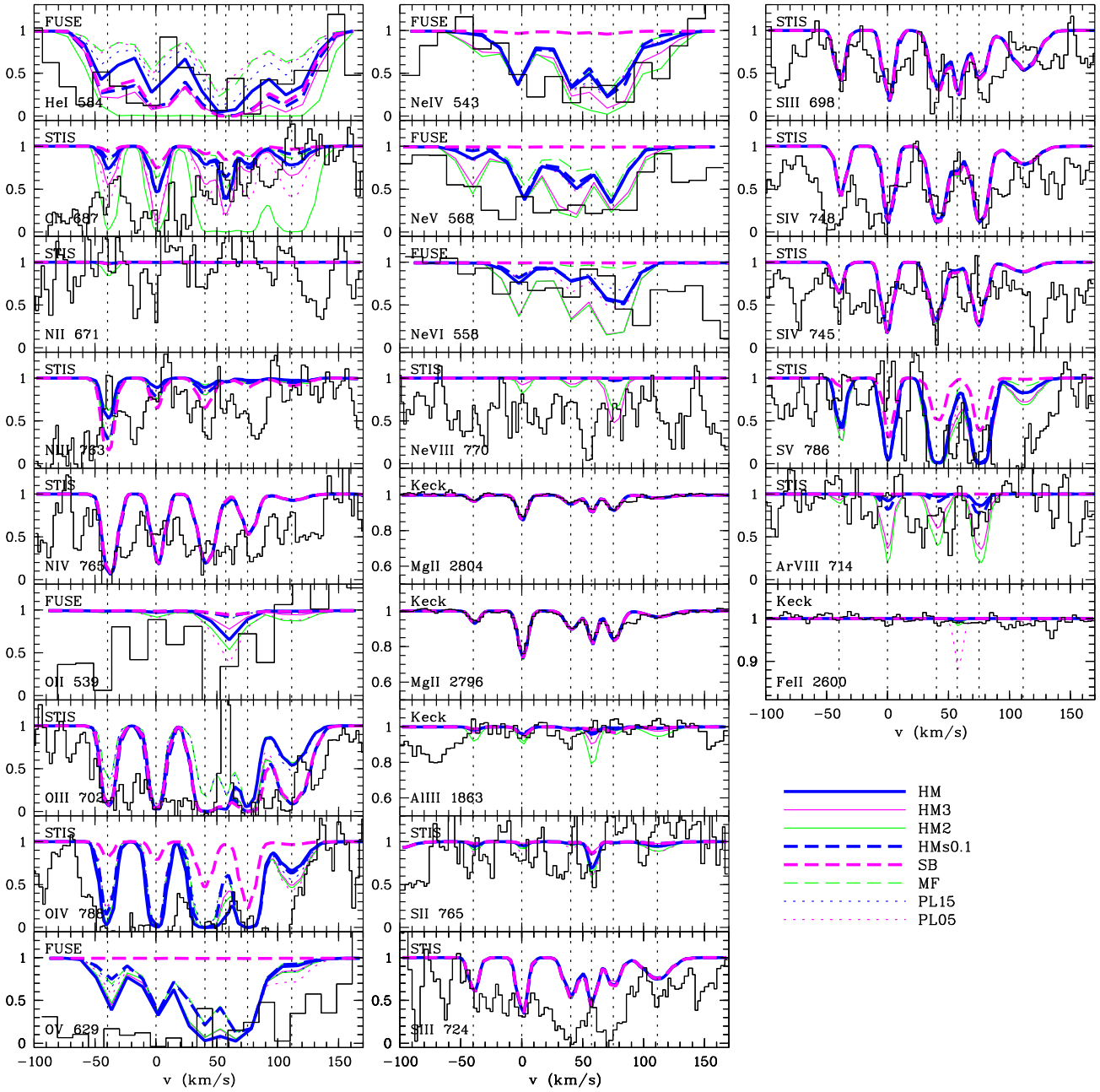

Fig. 4.5: Observed and modelled absorption lines of the system at $z = 0.8643$. The preferred models are HM, HMs0.1, and SB.

forest lead to a high value of η at this redshift, it might originate from unidentified additional absorption of Ne VII.

4.4.5. System $z = 1.4941$

The $z = 1.4941$ system shows two strong and one weak subcomponent of the C IV doublet in the optical (Fig. 4.7). Weak Si IV absorption may also be present, but only the λ1393.8 component is unblended. If this feature is misidentified, the derived column density serves as an upper limit. Additional upper limits can be derived for C II, Al II, Al III, and Fe II. In the UV, we clearly detect O IV, which is fitted using the velocity spread observed in C IV. Furthermore, this system may show He I absorption.

The ionization parameter for each model is fixed using C IV and Si IV and assuming a solar abundance pattern. Since the column density of Si IV suffers from significant uncertainties due to the weakness of the absorption features, the derived models are very preliminary. However, the model HM2 heavily overproduces He I, C II, and O III. Similar problems arise in case of HM3, HMs0.1, and SB, while the prediction of He I and O III absorption made with the hard radiation fields (MF, PL15, and PL05) is consistent with the data.

Even though only a few lines are observed in the optical, it is possible to derive a χ^2 considering C II λ1335, both com-

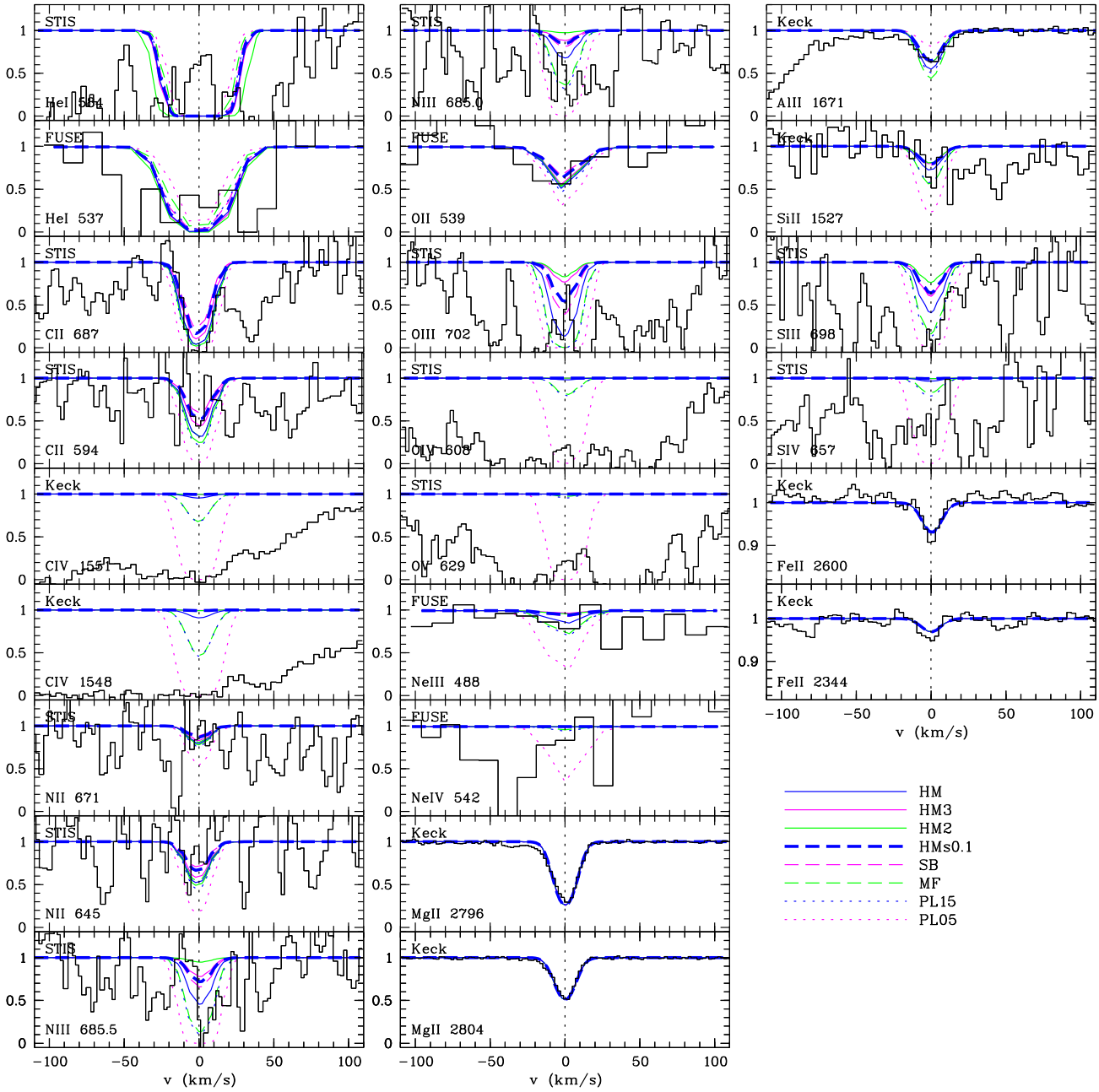

Fig. 4.6: Observed and modelled absorption lines of the system at $z = 1.1573$. The preferred model is HMs0.1.

ponents of C IV, Al II λ1671 and Si IV λ1394. The best value reveals the model PL15 ($\chi^2 = 0.99$), which is consistent with the discussion above as well.

Due to the few lines observed for this system, one should keep in mind that the model is rather ambiguous. Considering deviations from the solar abundance pattern, e.g. a modification of the oxygen abundance, may lead to different results and possibly to prefer another model background.

4.4.6. System $z = 1.7241$

Another Lyman limit system is located at $z = 1.7241$ (Fig. 4.8). The H I Lyα transition can be observed in the Keck spectrum. Features of C IV and Si IV are clearly detected, but since they are located in the Lyα forest, it is difficult to determine a velocity structure. Possible, there is a second component of C IV at $\sim 40\,\mathrm{km\,s^{-1}}$ visible also in C II. However, we assume a single component, which is visible in C IV as well as Si IV. The λ1393.8 component of Si IV is blended with the C II feature of the $z = 1.8450$ system. Only the λ1334.5 component of C II is located in the optical. Since the feature is weak, the derived column density is quite uncertain and may serve only as an upper limit. If Si III is present, it is heavily blended and an estimate of its column density is impossible. Upper limits can be derived for Si II and Al III. In the STIS portion of the spectrum, we identify ions of neon

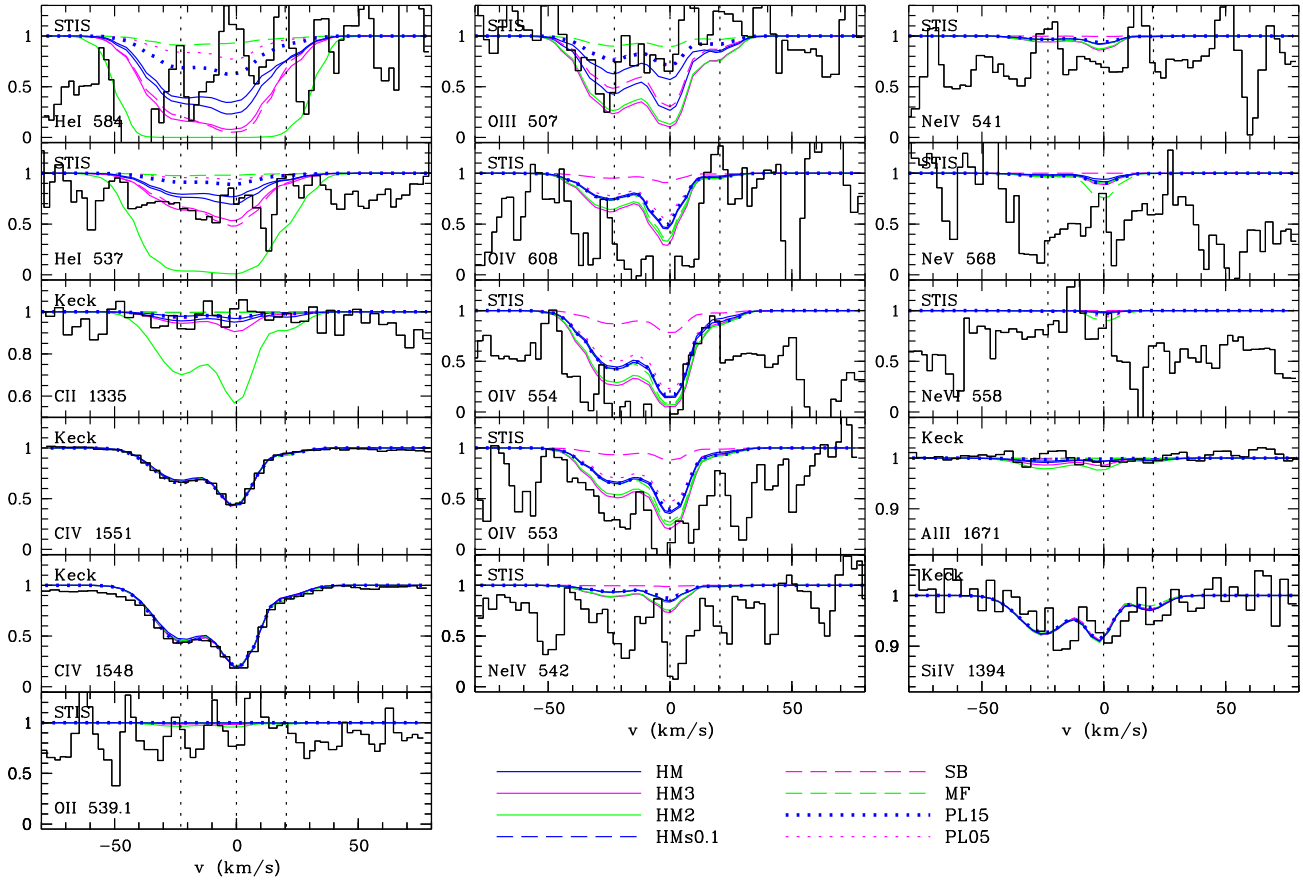

Fig. 4.7: Observed and modelled absorption lines of the system at $z = 1.4941$. The preferred model is PL15.

and oxygen as well as He I absorption.

The ionization parameter of each model is constrained using the ratio O III/O IV. Then, the abundances of carbon and silicon have been scaled to match the observed column densities of C IV and Si IV, respectively. Additionally, the marginally detected C II feature and the non-detection of Si II give requirements for the elemental abundances. To evaluate the goodness of the models, the main characteristics are the strength of Si IV, the width of the H I Lyα feature, i.e. the temperature of the absorber, the amount of He I absorption, and the strength of the C II feature. C II is overestimated by HM2 and both the power law models. The hard backgrounds (MF, PL15, and PL05) fit best the He I absorption, while the soft spectra tend to overproduce it. Concerning the width of the H I absorption, the modified HM backgrounds (HM3, HMs0.1, and HM2) lead to the highest temperatures ($\sim 10^{4.6}$ K), and thus give the best fits. All models except SB underestimate Si IV. Since both components are at least partly blended, this might suggest that the detected features do not originate mainly from silicon.

Enough transitions are detected in the optical spectral range to derive χ^2-values. Reasonable velocity intervals are chosen covering the features of H I Lyα, C II, C IV, Al III, Si II, and Si IV. As expected, the contributions of H I, C II, and Si IV dominate χ^2. If Si IV is considered in the estimate of χ^2, the best fitting model is SB ($\chi^2 = 3.00$). If it is neglected, HM3 fits the system best ($\chi^2 = 1.60$). Being aware of the uncertainty of the presence of Si IV, we prefer model HM3.

4.4.7. System $z = 1.8450$

The Lyman limit system at $z = 1.8450$ shows complex absorption with at least three subcomponents spread over $\sim 65\,\mathrm{km\,s^{-1}}$ (Fig. 4.9). The features are clearly detected in C IV, where the strongest component is saturated in both the doublet components, and C II, which is blended with the Si IV λ1394 component of the $z = 1.7241$ system, as well as in Si IV, Si III, and Si II. The red component of Si III appears to be blended with Lyα forest lines. Furthermore, we detect Al II and Al III. Even N V is present. The Mg II doublet was observed by Tripp et al. (1997). Since it is located outside the coverage of the Keck data, we adopt their colum density value. In the UV, we identify O III, Ar IV and several ions of neon. In this system He I appears also to be present.

The variety of transitions observed in the optical should give good constraints of the models. The ratios of the ions of carbon, silicon, and aluminium are supposed to restrict well-defined models. Nevertheless, none of the backgrounds produce a model fitting the low ionized lines and the lines of highly ionized elements simultaneously. For example, HM3 and HMs0.1 produce only very little C II absorption,

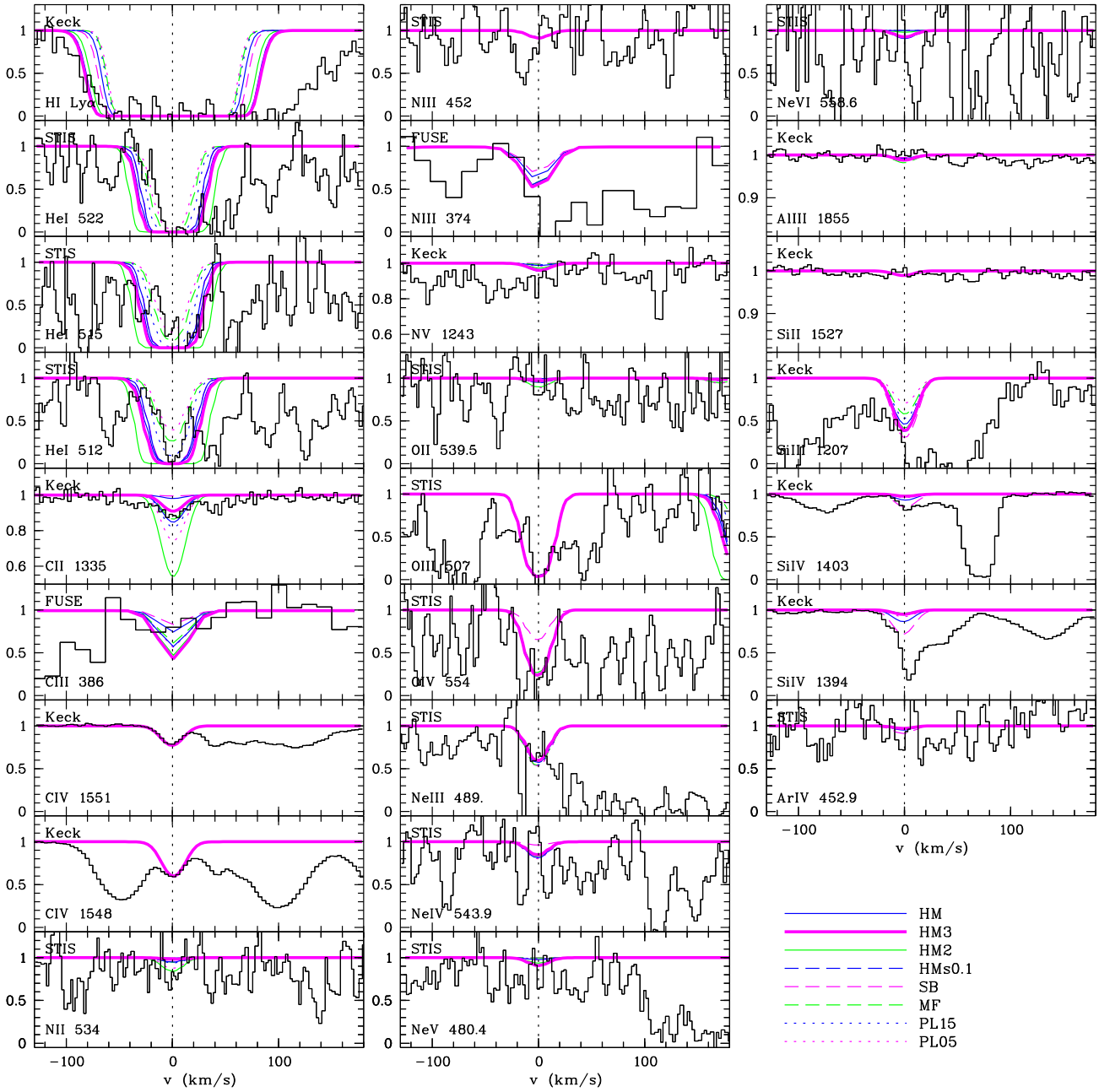

Fig. 4.8: Observed and modelled absorption lines of the system at $z = 1.7241$. The preferred model is HM3.

but match well the observed C IV column density. Model PL15 and MF have problems to not overproduce Si II without underestimating Si IV.

We compute χ^2 considering appropriate velocity intervals of H I Lyα, C II λ1335, C IV (both doublet components), Al II, Al III (both components), Si II λ1527, and Si IV (both components). The χ^2-value is then strongly dominated by the carbon lines, especially by the C IV doublet. The best fitting model is that one based on the MF energy distribution. Despite carbon, the next dominating lines for the χ^2 are H I Lyα, where we concentrate on the blue wing of the observed feature, and silicon (especially Si III and Si IV). Considering silicon, the best fits are produce by the models SB and HM2. While HM2 matches the blue wing of the H I Lyα feature, SB leads to a lower absorber temperature and thus a narrower line. A further indicator for the goodness of the fit may be the amount of He I absorption. HM2 severely overproduces He I. Also the models HM and SB predict stronger He I than consistent with the data.

Considering all arguments above, we come to the conclusion that the system at $z = 1.8450$ is probably a multi-phase absorber and should be analyzed applying a more sophisticated model. However, our simple approach indicates ionization by a hard UV background. This is in line with the detection of N V, which is never seen in the 'normal' IGM, but always requires a nearby AGN. We derive consistent models

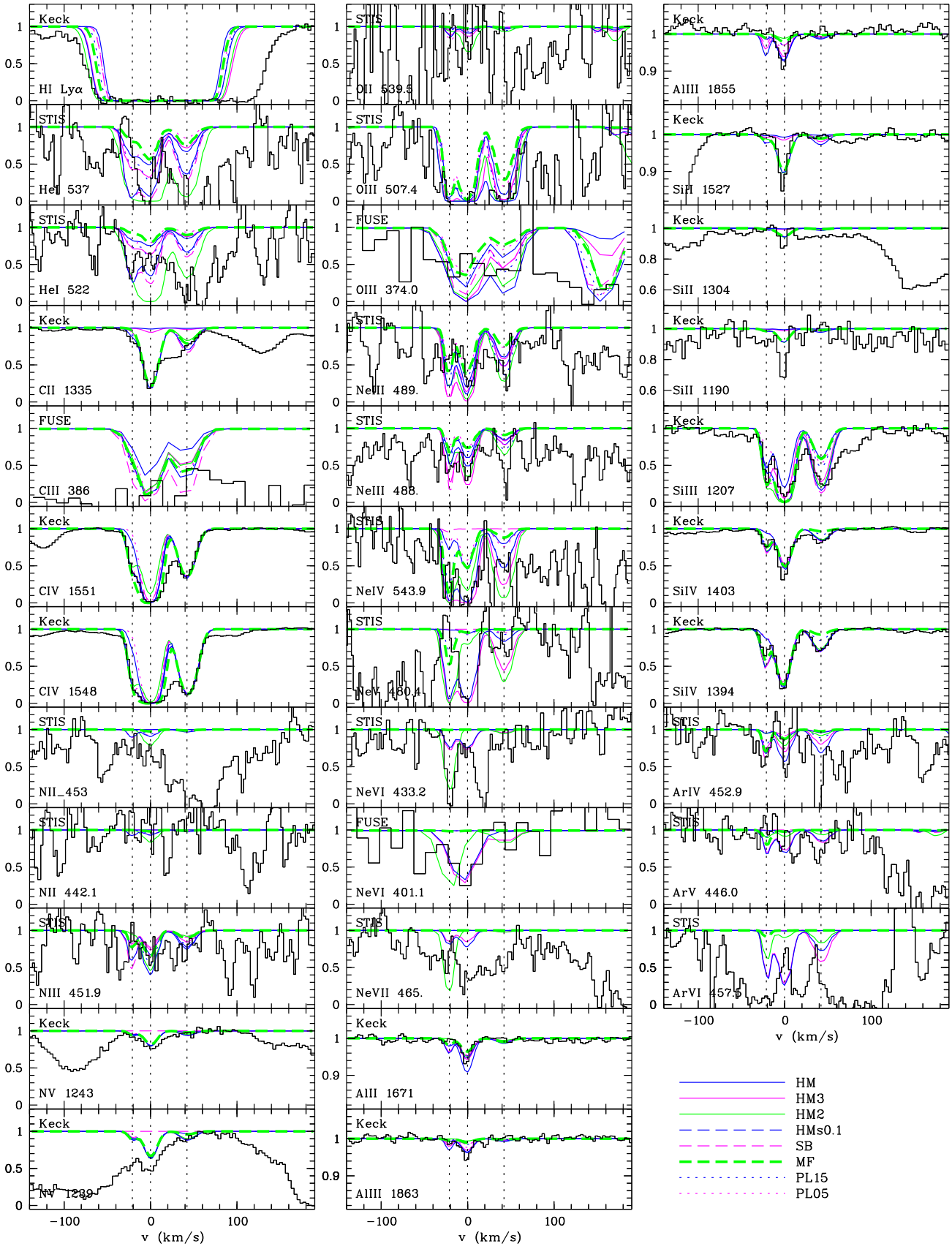

Fig. 4.9: Observed and modelled absorption lines of the system at $z = 1.8450$. The preferred model is MF.

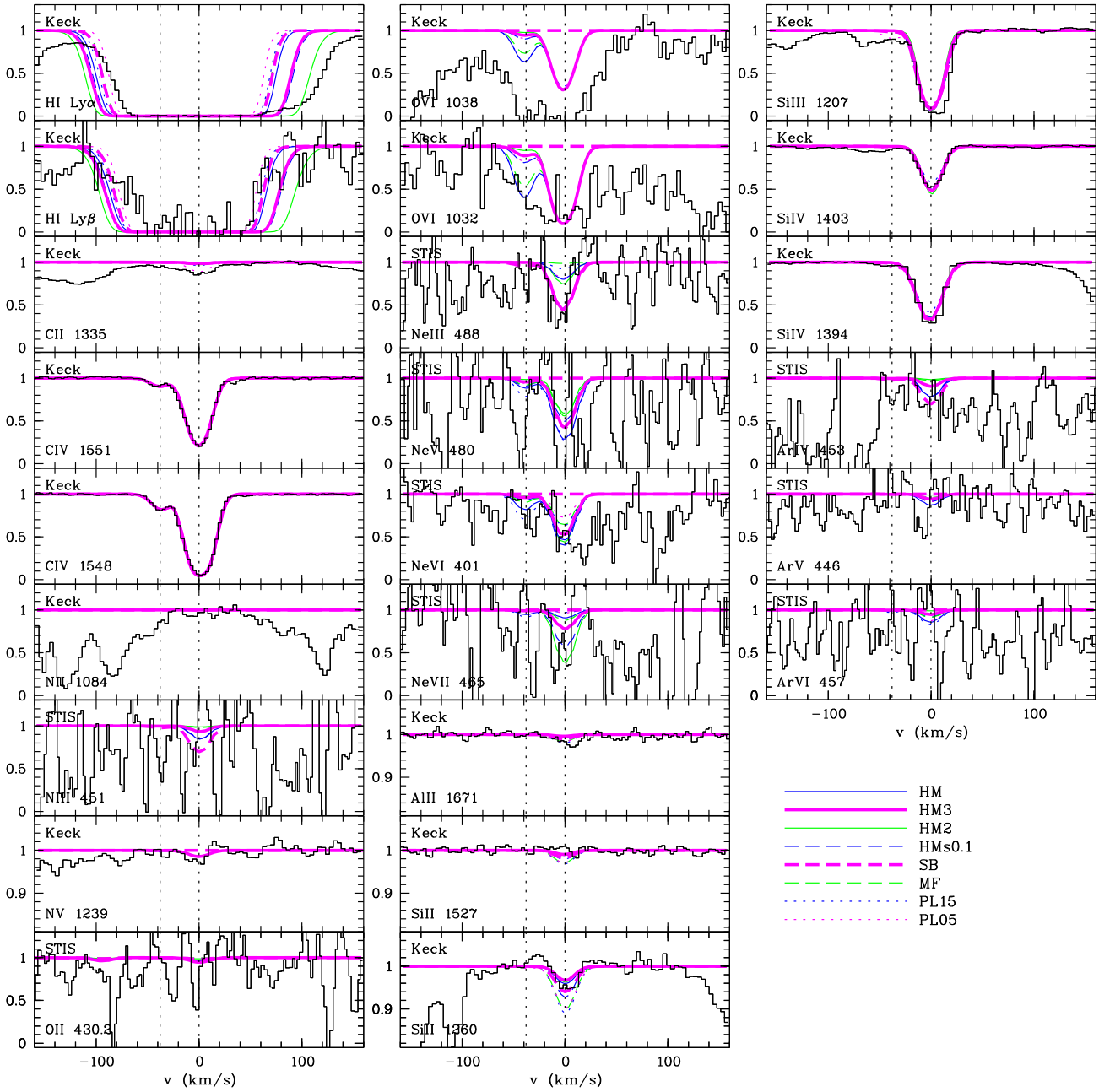

Fig. 4.10: Observed and modelled absorption lines of the system at $z = 2.1680$. The preferred models are HM3 and SB.

adopting the MF energy distribution or a power law (PL15 and PL05). The lowest χ^2 is produced for MF (155.6).

4.4.8. System $z = 2.1680$

At $z = 2.1680$ another Lyman limit system arises (Fig. 4.10). Lyα and Lyβ are detected in the Keck spectrum. We clearly identify C IV, Si III, and Si IV in two subcomponents, where the stronger one appears to be an unresolved blend of at least two components. O VI absorption might be present but is blended. Furthermore, the measured C II column density might be biased by unresolved blending with Lyα forest lines. In this case, the derived values serve as upper limits. The detection of Si II is very uncertain. Thus, the given value may represent an upper limit. Neon is identified in the UV, argon might be present as well.

All models lead to strong hydrogen lines, broader than the observed features, indicating a problem with the H I distribution. The best fitting models are then MF, PL05, PL15, and SB. Another crucial transition is Si II. Even if it is not present, there are upper limits that have to be considered. The models based on hard ionizing spectra (both the power laws, MF, but also HMs0.1), overproduce Si II. The feature claimed for as C II is reproduced only by PL05, the other models produce nearly no C II absorption at all.

Thus, we compute χ^2 on the basis of C IV (both compo-

nents), N v λ1239, Al ii, Si ii λ1527 and λ1260, and Si iv λ1403. The dominating transition is then Si iv, which is fitted best with PL05 and SB. According to the overall χ^2-value, the best fitting models are SB, HM3, and HM (3.67, 4.10, 4.38). Considering the width of the H i features, the SB model is preferred, but assuming a different amount of neutral hydrogen associated to the metal absorption, HM3 and HM provide consistent models as well. Comparing the HM3 and HM model, HM leads to very high [Si/C] abundances ($\sim$ 2.0), while HM3 reveals the more realistic value [Si/C] $\sim$ 0.9. The SB model leads to [Si/C] ~ -0.4 for the main component.

4.4.9. System $z = 2.2896$

For the system at $z = 2.2896$, we detect the Lyman series down to Lyδ, although Lyγ and δ are very noisy. Weak C iv is visible with three components spread over $\sim$ 30 km s^{-1} and weak Si iv features are detected in the λ1393.8 doublet component. The corresponding C iii absorption is identified in the optical, but the velocity structure cannot be resolved due to noise (see Fig. 4.11). Therefore, it is impossible to distribute the total column density of neutral hydrogen over the subcomponents reasonably. We therefore concentrate on the main component assuming that it gives rise to the bulk of the H i and C iii absorption.

All derived models are very similar to each other. We specify a χ^2 considering appropriate velocity intervals of C iii λ977, C iv λ1551, N ii λ1084, Al ii, Si ii λ1260, and Si iv λ1394. The features of H i as well as Si iii are neglected in lack of a reasonable choice of an velocity interval, although they are important indicators to estimate the best fitting model. Considering Si iii, absorption consistent with the observation is predicted by the models SB and PL15, while it is overestimated severely by the models HM2, MF, HM, and PL05. Regarding the actual numbers of χ^2, all models are of comparable quality. The smallest χ^2-values are provided by HM3, HMs0.1, SB, and PL05 (0.86 for all of them). PL05 is rejected, since it overproduces Si iii. Comparing HM3, HMs0.1, and SB, the HM3 model is preferred, since the derived [Si/C] abundance is more realistic (0.89 in comparison to $-0,17$ and -0.44) at a metallicity of [M/H] = -3.31.

4.4.10. System $z = 2.3155$

The Lyman limit system at $z = 2.3155$ gives rise to a very complex structure of metal line absorption. We find six components spread over $\sim$ 130 km s^{-1}, with four main components at -49 km s^{-1}, 0 km s^{-1}, 35.1 km s^{-1}, and 77 km s^{-1} (Fig. 4.12), which we consider individually in the following investigation. The two blue components are visible in almost all detectable ions, while the red components are less strong. Unfortunately, some important transitions are blended with Lyα forest lines, and an estimate of column densities is impossible for C iii and Si iii. Also the O vi profiles suffer from blending with forest lines and the derived values are biased with large systematic uncertainties. Al ii is blended with the λ1548.2 component of C iv arising from the system at $z = 2.5785$. This makes the fitting procedure complicated, but since the doublet component λ1550.8 of the $z = 2.5785$ system is unblended, the derived values are supposed to be reliable. Al iii is located outside the observed spectral range, thus we adopt the value measured by Tripp et al. (1997). Nearly all C iv absorption is saturated in both the doublet components, as well as the strongest subcomponent in Si iv. Possibly, we also detect N v, which usually is not detected in intervening systems.

Analyzing this system, it is evident that it is a multi-phase absorber. None of the models reaches a satisfactory description of both the low and highly ionized species (see Fig. 4.12). This is illustrated particularly by O vi. Only weak features for the blue components are predicted, while a stronger line consistent with the observation is produced for the red component. The reason is the way we fix the ionization parameter. For both the blue components we use the ratio of Si ii/Si iv, which is more reliable than C ii/C iv, since the column densities suffer less from saturation effects. Whereas, for the red components, no Si ii feature is observed and the ratio of the ions of carbon has to serve to fix the ionization parameter. If the bulk of the C iv absorption originates in a high ionization phase, but most of the Si iv arises from low ionized gas, we probe two different gas phases whether the model is based on silicon or carbon. Using two sucessive ionization stages should avoid this problem. However, since both C iii and Si iii are blended and unresolved in the present data, there is no possibility to do so. Tripp et al. (1997) made some efforts to model this system as well (with their data, they resolve three components, which correspond to three of the main components considered in this analysis). They failed to derive a single phase model and suggest a multi-phase gas, too.

Comparing the models with the observational data, the red wing of the H i features (Lyα and Lyβ) is poorly described by all models. The best are MF and SB, since they produce the lowest temperature ($T \sim 10^{4.0}$ K) of the red component. Concerning H i, we distributed the measured total column density to the subcomponents according to carbon. Since we only account for the four main components, the amount of H i may be overestimated. But the error is supposed to be small, since the contribution of the weaker components to the total carbon column density is negligible.

A reasonable χ^2-value is difficult to define since only parts of the absorption complexes are modelled. Therefore, we define velocity intervals for each subcomponent using lines we expect to have no systematic errors. The χ^2-value of the blue component considers C ii λ1036, N ii λ1084, Al ii, Si ii $\lambda\lambda\lambda$1527, 1304, 1193, and Si iv λ1403. Si iv dominates the value but is similar for all models. Best fitting models are both the power laws, HM, HMs0.1, and SB.

Considering the central blue component the situation gets even worse, since Al ii is blended and thus cannot be included in the χ^2-estimate. Si iv is unusable as well, since no reasonable velocity interval can be defined. With these exceptions we use the same transitions as before. Then χ^2

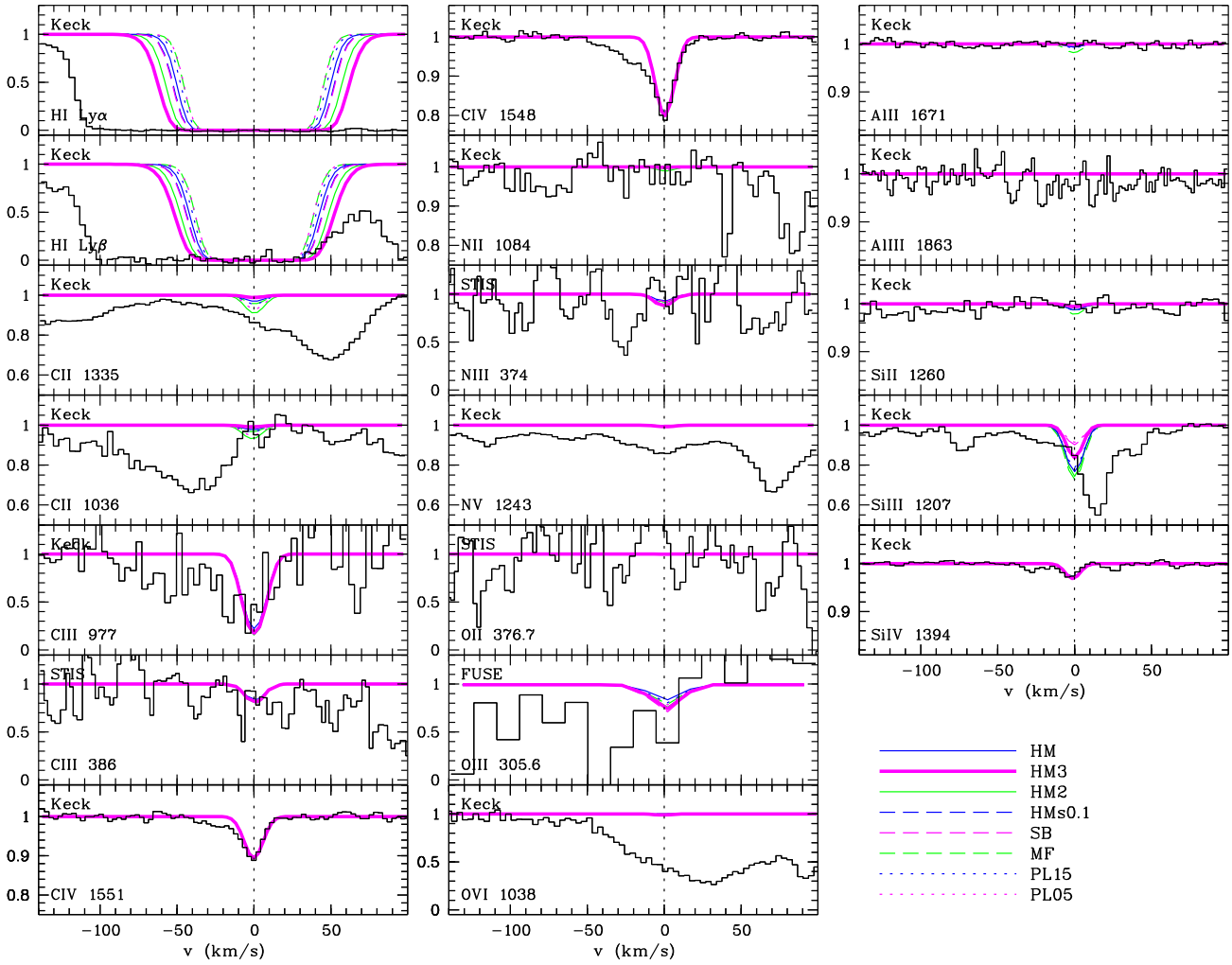

Fig. 4.11: Observed and modelled absorption lines of the system at $z = 2.2895$. The preferred model is HM3.

is dominated by the Si II lines, which differ only marginal in the appearance of the profiles. The MF model underestimates N II, but no further results can be conclude from the χ^2-values of the single lines, since they strongly resemble for each model. N V, which is not considered in the χ^2, is slightly overproduced by the HM3 model.

Regarding the component at 35.1 km s^{-1}, only very few lines are appropriate to estimate a χ^2-value. We chose N II λ1084, N V λ1243, and Si II λ1527 and find that all HM-like models are preferred. Additionally, both the power laws and the MF model overproduce C II. SB severely overestimates N III, which is also overpredicted by MF, HMs0.1, and HM. Thus, HM3 and HM2 are the best fitting models with respect to this component.

For the red component, the lines for the χ^2-estimate have to be chosen considering the high ionization gas phase. We use appropriate velocity intervals of C II λ1335, C IV λ1551, N V λ1243, Si II λ1527, and Si IV λ1403. The χ^2-value is dominated by C IV. The strongest deviations from the observed features are found for SB and HMs0.1, which also produce no N V.

In order to decide which ionizing radiation field is optimal for reproducing the whole system, we determine a total χ^2-value considering all the lines and velocity intervals contributing to the χ^2-values of the subcomponents. Following the resulting numbers, HM3 produces the best fitting model ($\chi^2 = 52.1$). Regarding ionization parameter, density, and temperature, the different gas phases can be recovered. The red subcomponents are modelled to be the hottest ($10^{4.45}$ K) and most dense (0.35 cm^{-3}) absorber with the highest ionization parameter ($\log U \gtrsim -1.38$), while both the blue absorbers are somewhat colder ($\sim 10^{4.23}$ K) and thinner ($\lesssim 0.06$ cm^{-3}) leading to a lower ionization parameter ($\log U \sim -2.2$). The metallicity is set to [M/H] ~ -0.55 corresponding to the silicon abundance of the bluest system. We derive [Si/C] ~ 0.25 in case of the blue components and ~ 0.78 for the red, highly ionized components.

The LLS at $z = 2.3155$ is a very complex system. The models, we have derived, are certainly oversimplifications and do not serve as a realistical description of the physical conditions in the absorbing gas. But since our main concern in the presented work is the derivation of the metal lines ex-

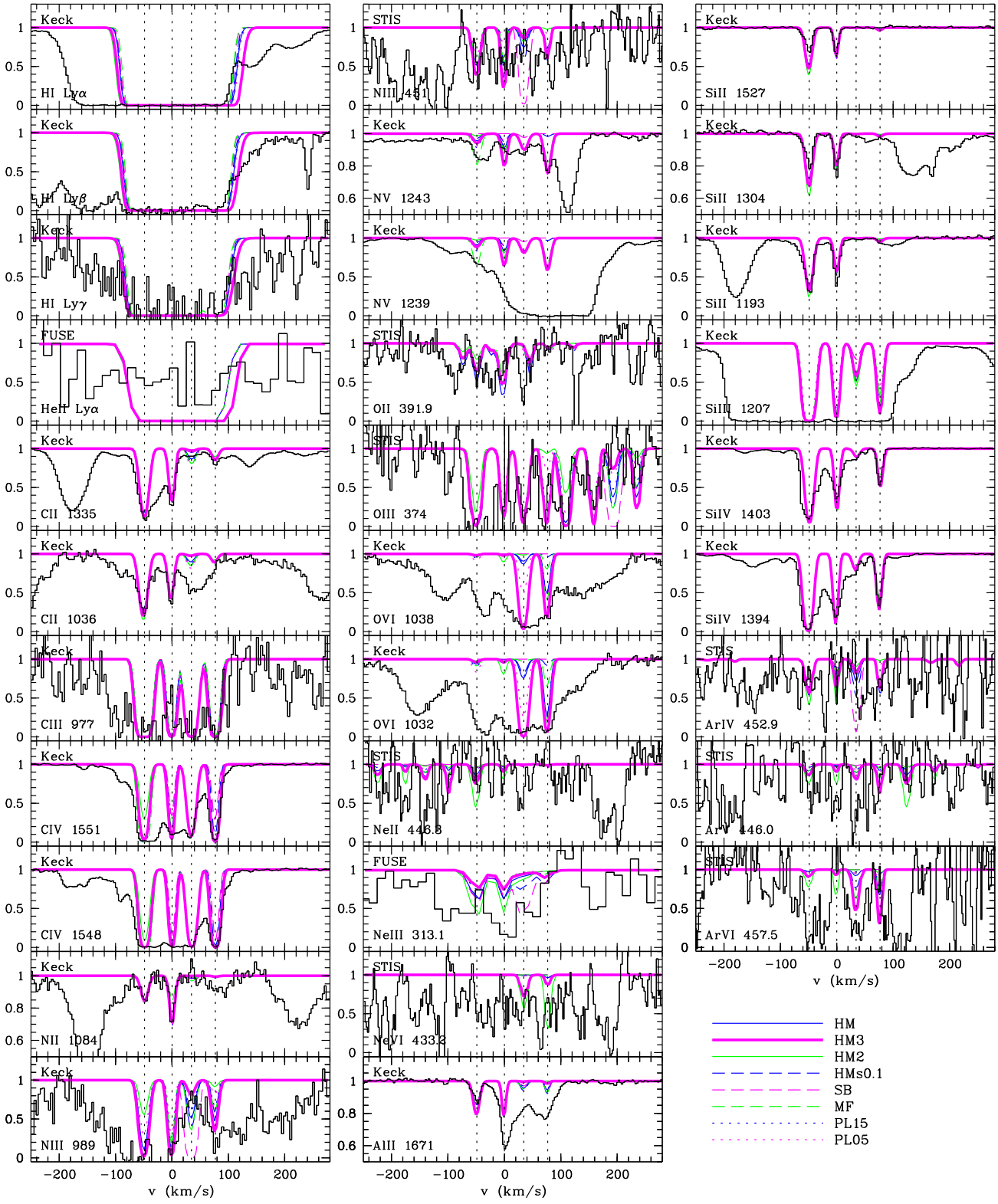

Fig. 4.12: Observed and modelled absorption lines of the system at $z = 2.3155$. The preferred model is HM3.

pected in the far-UV and the investigation of the ionizing UV background rather than exploring the physical state of Lyman limit systems, we quit the modelling of the system at this point and address a deeper analysis to future work.

Due to the multi-phase nature of this system, we likely underpredict the absorption of high or low ionization stages for the blue or red subcomponents, respectively, in the FUSE spectral range. Except the C IV λ312.4, 312.5 doublet, only

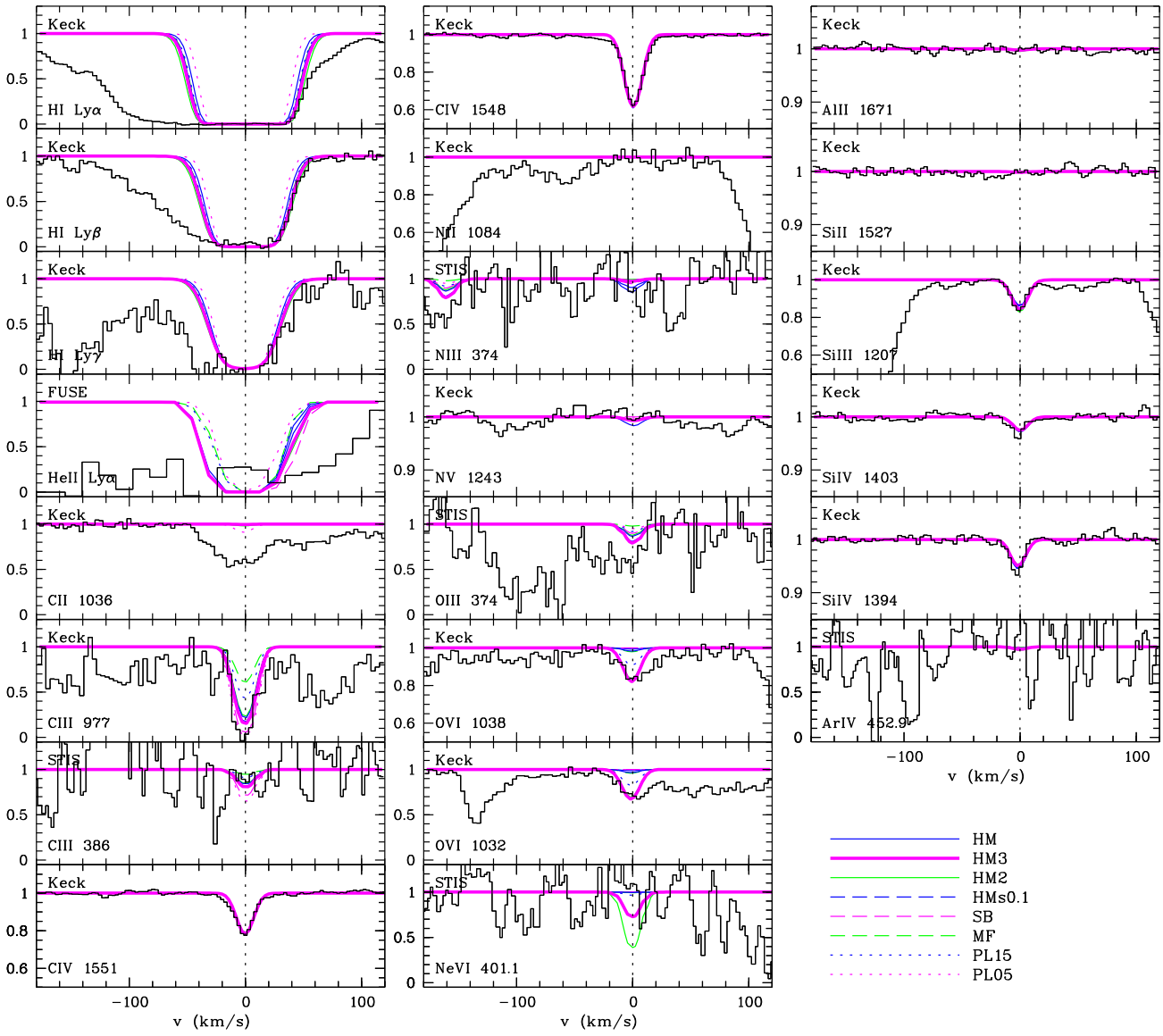

Fig. 4.13: Observed and modelled absorption lines of the system at $z = 2.3799$. The preferred model is HM3.

lines from low ionization stages are expected (C III, N III, O III, Ne III). According to Fig. 4.12 C III, N III, and O III are modelled confidently, while Ne III may by unterestimated. In case of a high η value at the corresponding wavelength (1037.9 Å), additional absorption due to Ne III should be considered. The UV doublet of C IV is certainly underpredicted, since the doublet observed in the optical is saturated and underestimated by the model at least for the blue components. However, the features are expected to arise close to the interstellar C II λ1036 line. Since saturated interstellar absorption of C II λ1334 is observed in the STIS data, the λ1036 component will be of comparable strength and therefore dominate the blend with C IV.

4.4.11. System $z = 2.3799$

The system at $z = 2.3799$ shows absorption features of C III, C IV, Si III, Si IV, and O VI in the optical data (Fig. 4.13). C II seems to be present, too, but is surely blended. Thus, the derived column density suffers from systematical uncertainties and may serve as an upper limit. Clear non-detections are Si II and N V. Furthermore, we could derive limits for N II, Al II, and Fe II. In the UV, we may detect several ionic transitions of argon. The triplett of Ar IV ($\lambda\lambda\lambda$451.2, 451.9, 452.9) is obviously present, but appears to be shifted ($\sim +10\,\mathrm{km\,s^{-1}}$) with respect to the optical transitions. Ar V and Ar VI appear to be present, too, but might be blended with sulpher and carbon features arising from the $z = 1.1573$ and $z = 1.8450$ LLS, respectively. The H I

Lyman series is detected down to Lyδ, which is strongly affected by noise, but Lyα, Lyβ, and Lyγ are used to estimate the column density.

The observed features show no substructure. There may be a small shift of $\sim 5\,\mathrm{km\,s^{-1}}$ between the centroids of O VI and those of carbon and silicon. Blending with Lyα forest lines, however, might mimic a shifted position. Furthermore, the O VI features are unusually broad ($b = (18.6 \pm 1.2)\,\mathrm{km\,s^{-1}}$).

Fortunately, all other optical metal lines are apparently unblended, so that we can compute a χ^2 with several ions. We use appropriate velocity intervals of H I Lyβ, C IV (both components), N II λ1084, N V λ1243, both components of O VI, Al II, Si II λ1527, Si III, and both components of Si IV. C III λ977 is rejected for the χ^2-estimation, since the comparison with the λ386 component in the STIS data suggests that it might be polluted by additional absorption. Regarding the H I feature, we concentrate on the red wing of the profile, which is mismatched by the models based on the hard ionizing spectra (both the power laws, MF, but also HMs0.1), while the softer spectra fit well. The dominating contribution comes from O VI. Here, the best fitting models are produced by HM3 and HM2. Si III is slightly underestimated by HM and PL05. Considering the overall fit and the actual numbers, HM3 is the preferred model ($\chi^2 = 2.14$), while HM2 fits only slightly worse ($\chi^2 = 2.28$). This suggests that a further optimized ionizing continuum might have a break slightly below 3 Ryd.

4.4.12. Systems $z = 2.4321$ and $z = 2.4331$

There is a strong absorption complex at $z \approx 2.433$, which we assume as two systems at $z = 2.4321$ and $z = 2.4331$, respectively. The latter appears to cause the observed Lyman limit. Considering the Lyman series up to Lyδ, we estimate the column densities $\log N_{\mathrm{H\,I}} = 15.53 \pm 0.03$ and $\log N_{\mathrm{H\,I}} = 16.84 \pm 0.35$ for the $z = 2.4321$ and $z = 2.4331$ system, consistent with the value measured from the Lyman limit by Vogel & Reimers (1995). Additionally, the red wing of the Lyα absorption trough contains a significant amount of hydrogen without any metal line absorption. The column density is hard to quantify because of blending with Lyα forest lines in Lyβ and γ and poor data quality for Lyδ. The H I absorption complex is presented in Fig. 4.14. Besides the systems discussed in this Subsection it shows as well the features of the systems at $z = 2.4386$ and $z = 2.4405$, presented in the next Subsection. The narrow feature in between the two saturated absorption troughs visible in the Lyα panel is Si III of the $z = 2.3155$ LLS. He II Lyα is shown as well. For a better orientation, one doublet component of C IV is also presented, since it illustrates the velocity structure visible in the associated metal lines.

Considering the $z = 2.4321$ system (Fig. 4.15), the model parameters are constrained by the carbon ions, although C IV λ1551 is blended with the first C IV doublet component of the $z = 2.4386$ system. For the resulting models, we compute χ^2-values based on the features of H I Lyβ and Lyγ,

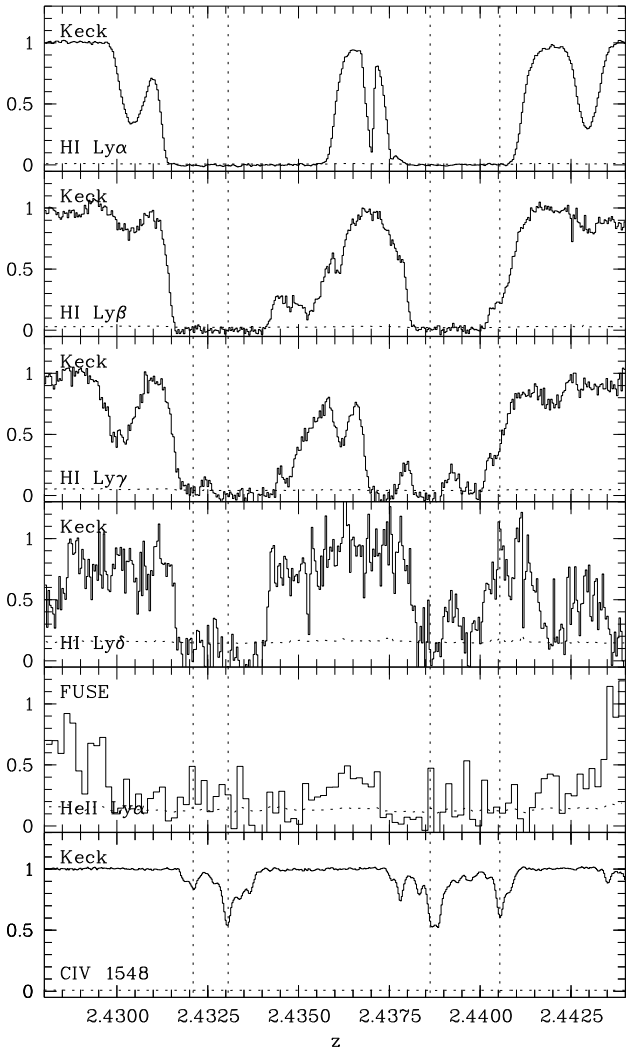

Fig. 4.14: Observed H I absorption complex at $z \sim 2.435$. Presented are the features of the Lyman series down to Lyδ and He II Lyα (the corresponding FUSE data is presented in Chapter 5 and Reimers et al. 2004). The lower panel shows the corresponding C IV λ1548 absorption complexes. The vertical dotted lines indicate the position of the main component of the systems at $z = 2.4321, 2.4331, 2.4386, 2.4405$.

C II λ1335, C III λ977, C IV λ1548, N V λ1243, Al II, and Si IV λ1394. None of the lines dominates the χ^2-value, even though the greatest differences are found for the H I features. While the HM3 and HM2 models fit well the blue wing of the features, both the power laws as well as MF produce lines too narrow to match the observations. Regarding the transitions not included into the χ^2-estimation, we have several models producing Si III and O VI absorption consistent with the data. Models predicting Si III are HM, SB, PL15, PL05, and MF, where the latter slightly overproduced the strength of the absorption features. Whereas only HM3 and HM2 predict perceivable absorption of O VI, which is still consistent with the data. According to the χ^2-estimation, the best fitting model is yielded with the HM3 background ($\chi^2 = 1.13$).

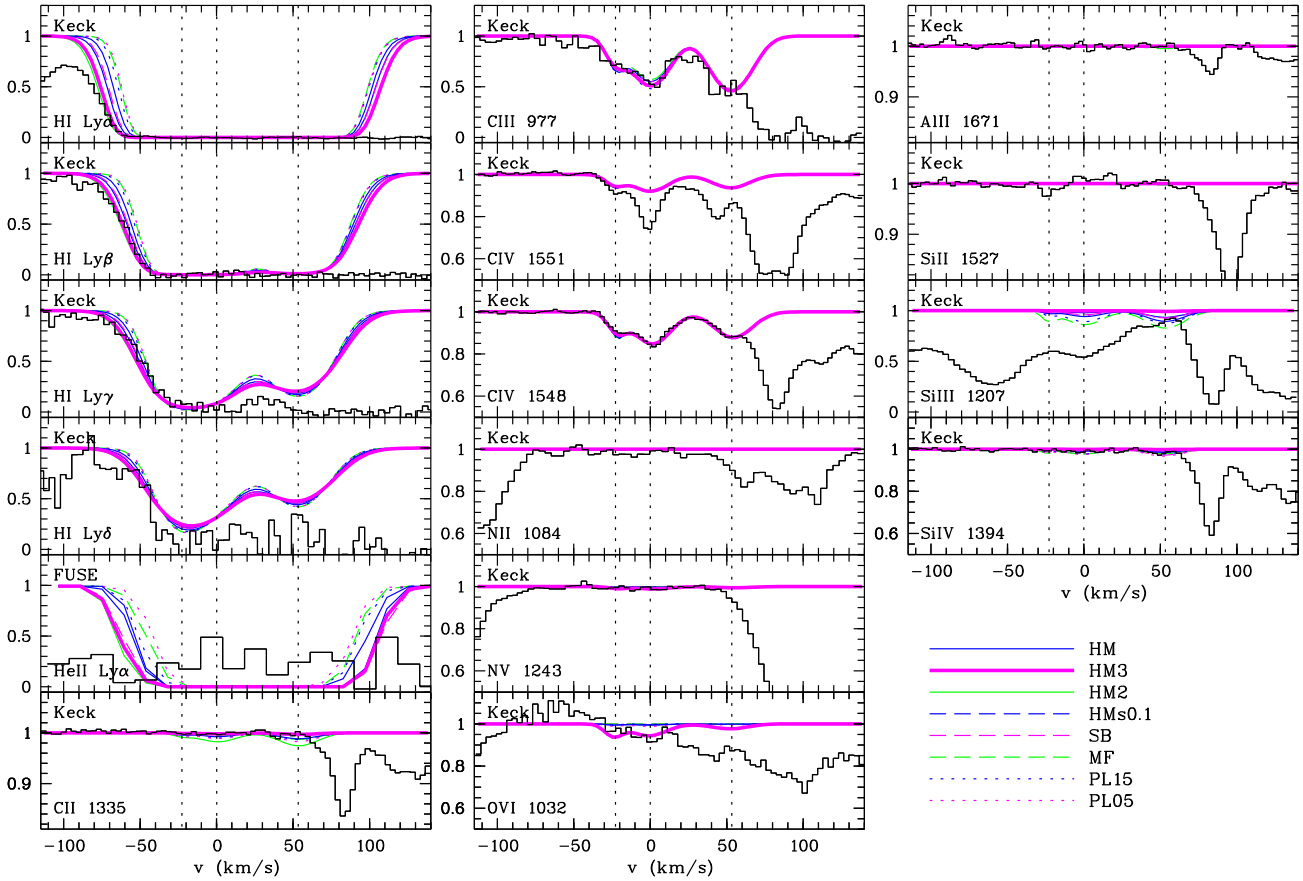

Fig. 4.15: Observed and modelled absorption lines of the system at $z = 2.4321$. The preferred model is HM3.

In case of the $z = 2.4331$ system (Fig. 4.16), we decide on a line sample to compute χ^2-values, which consists of appropriate velocity intervals of H I Lyδ, C IV λ1548, N V λ1239, Al II, Si II λ1193, Si III, Si IV λ1394, and S VI λ945. PL05 provides a poor description of the observations. C IV is significantly underestimated, while Si II is overproduced. Furthermore, the SB model predicts too much N III absorption and no S VI features at all. Differences in the predicted strength of O VI cannot serve as indicator for the quality of the models, since we can only place an upper limit on its column density due to the observational data. We detect a shift between the position of silicon and C IV of $(2.66 \pm 0.28)\,\mathrm{km\,s^{-1}}$ in the blue component. This might be interpreted as an indication of a multi-phase absorber with a more complicated structure than assumed here.

While the estimated χ^2-values are dominated by Si III as well as C IV, there are only little differences in the actual numbers for all models except PL05. The C IV is best fitted by the HM2 model, since it produces a slightly broader profile than the other models, while Si III is matched slightly better by the HM3 model. But at least, these are only marginal differences. Considering the total χ^2, HM3 (20.04) and HM2 (20.12) are the best fitting models. HM3 produces too much Al II absorption in the middle component, while HM2 underestimates Si II worse than HM3. The situation seems comparable to the $z = 2.3799$ absorber, where the optimal position of the break is apparently shifted to energies slightly below 3 Ryd. We prefer the HM3 model.

4.4.13. Systems $z = 2.4386$ and $z = 2.4405$

The absorption complex of the systems at $z = 2.4386$ and $z = 2.4405$ is shifted roughly $500\,\mathrm{km\,s^{-1}}$ from the LLS discussed in the previous section. Lyα shows a broad absorption trough, but considering higher Lyman series, distinct features are visible and the column densities can be measured (Fig. 4.14). We estimate $\log N_{\mathrm{H\,I}} = 15.78 \pm 0.07$ at $z = 2.4386$ and $\log N_{\mathrm{H\,I}} = 14.45 \pm 0.24$ at $z = 2.4405$. The large error bar for the latter value arises, since it is estimated using only Lyβ. In between at $z = 2.4397$, another strong H I system ($\log N_{\mathrm{H\,I}} = 15.49 \pm 0.04$) is detected. Maybe, the metal line absorption belongs to the stronger H I but is shifted by $\sim 75\,\mathrm{km\,s^{-1}}$. However, weak absorption features of carbon (C III, C IV) and O VI are apparently associated to this strong H I absorber (Fig. 4.17). According to C IV, four subcomponents can be identified for the $z = 2.4386$ system, clearly present in Si III and Si IV as well. The system at $z = 2.4405$ spread up in three subcomponents considering C IV. The corresponding silicon features are very weak and only measurable for the strongest component, which we

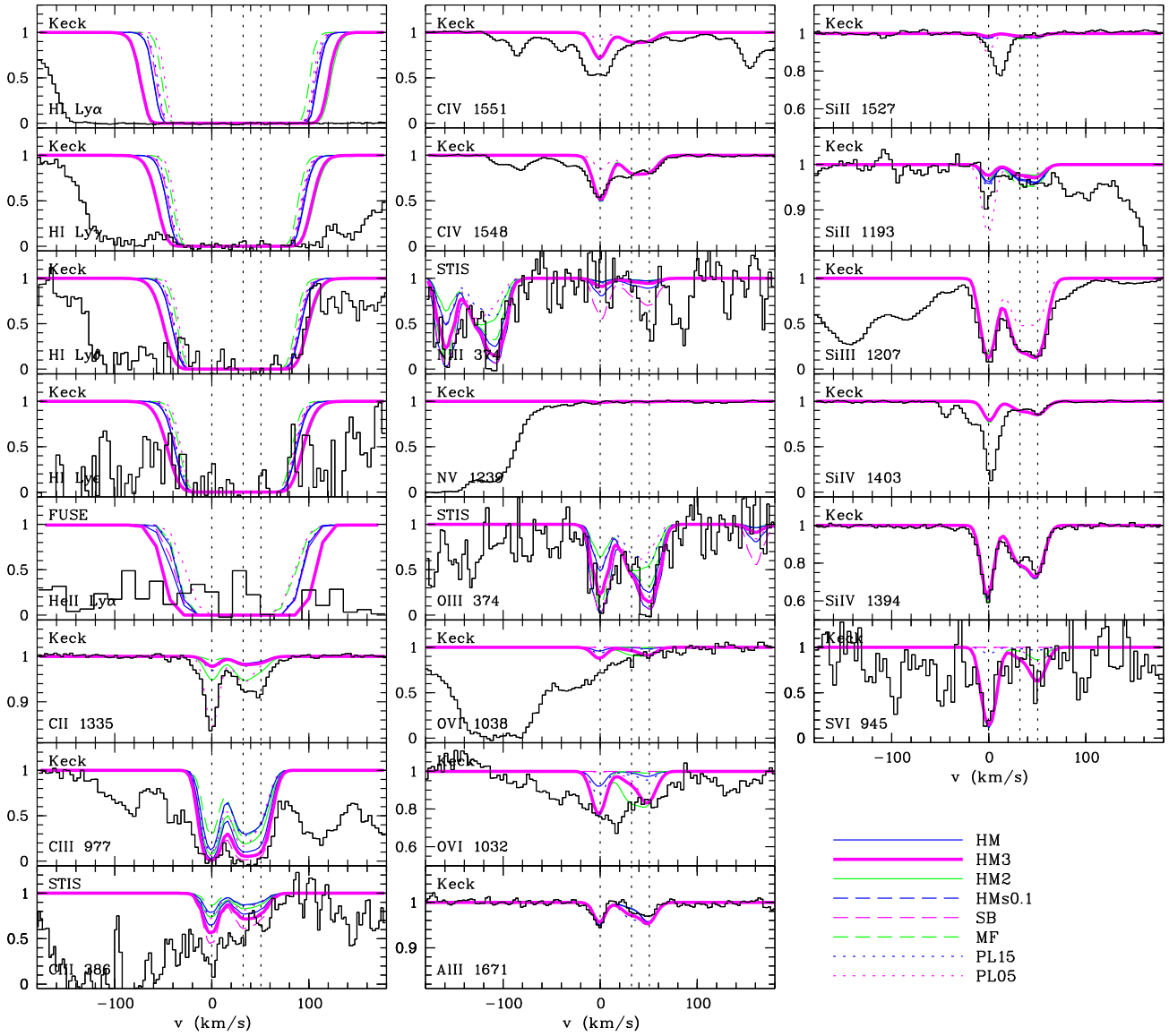

Fig. 4.16: Observed and modelled absorption lines of the system at $z = 2.4331$. The preferred model is HM3.

concentrate on in course of the modelling procedure (Fig. 4.18).

Considering the system at $z = 2.4386$, the amount of neutral hydrogen distributed to the bluest subcomponent is overestimated. Thus, the derived metallicities for this component are definitely too low, but the main conclusions remain unaffected. We define appropriate velocity intervals to compute χ^2-values based on H I Lyδ, C II λ1335, C III λ977, C IV λ1551, N V λ1243, Al II, Si II λ1527, Si III, and both the doublet components of Si IV. The interval including H I is concentrated on the red wing of the feature, and only the two blue components are considered regarding C III. O VI and S VI are not included, since we can only place upper limits on the presence of these transitions. The χ^2-values are dominated by Si III, since it is modelled to be narrower than observed in all models, but MF, HM2, PL05, and HMs0.1 match the observational profile best. The model PL05 fails because it predicts a significant Si II feature, which is not observed, and clearly underestimates the C IV absorption of the reddest component.

According to the derived numbers, the MF model fits the observations best ($\chi^2 = 4.46$). Both the red components in C III are rather weak, but since the λ977 feature is definitely affected by blending with a Lyα forest line, even weak absorption is consistent with the data. A further constraint on the C III column density of these two components could be provided by the λ386 line, but at the corresponding wavelength, the STIS data suffer from insufficient S/N. However, the ionization parameters of the components are based on the column density ratio of silicon. The estimated overall metallicity is [M/H] = −1.29. Relative abundances are [Si/C] = −0.77, −0.16, 0.86, 0.69.

Even though the system at $z = 2.4405$ shows three subsystems with respect to C IV, we concentrate the analysis on

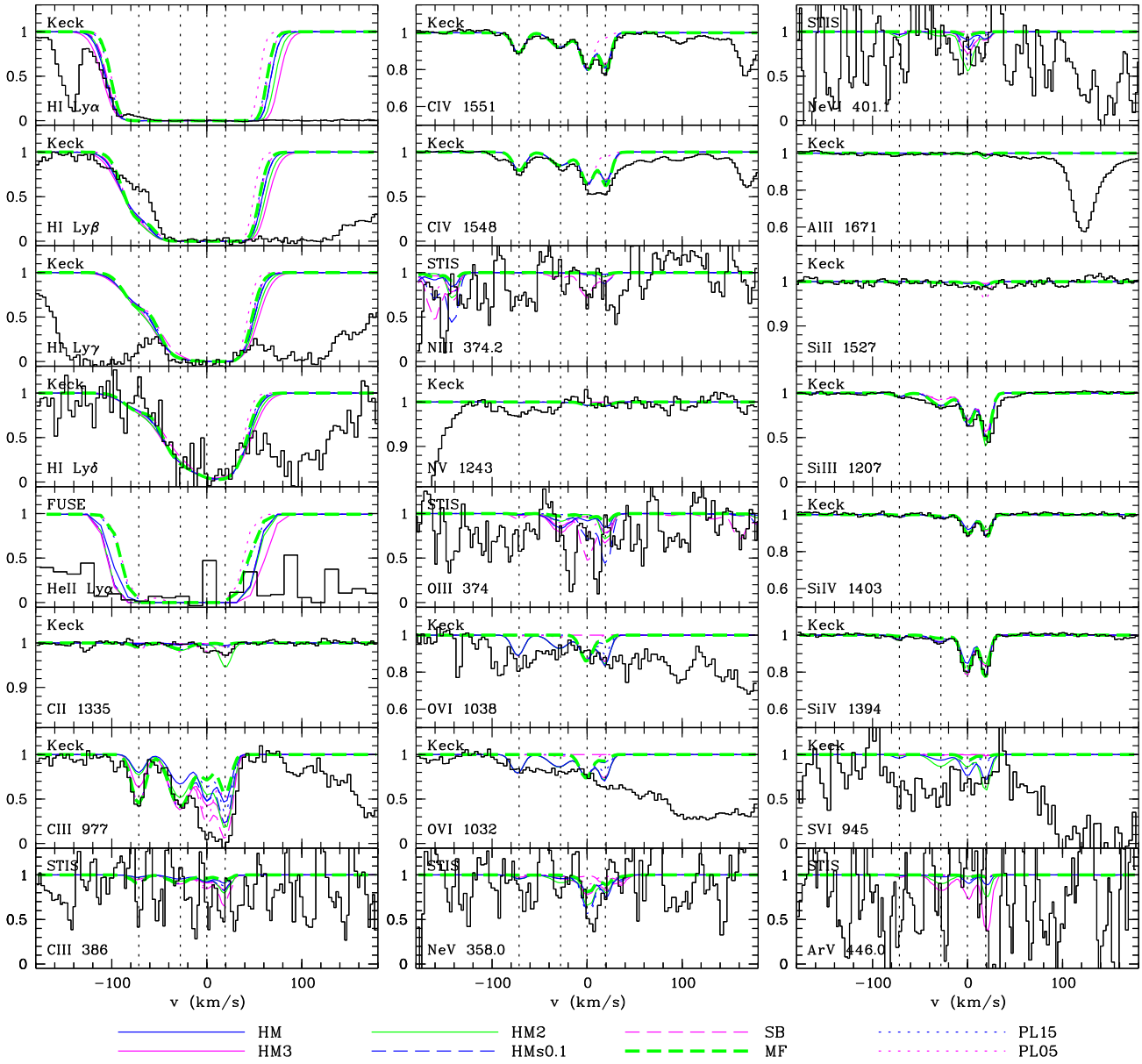

Fig. 4.17: Observed and modelled absorption lines of the system at $z = 2.4386$. The preferred model is MF.

the main component (at 0 km s^{-1} in Fig. 4.18). This means again that we probably overestimate the amount of neutral hydrogen associated with the absorber. For this reason, we neglect the H I profile in the computation of χ^2. The models HM and PL05 result in low temperatures, e.g. narrow H I profiles, which are too deep in the line core regarding Lyβ. But following the argumentation above, we cannot conclude on a shortcoming of these models.

We compute χ^2-values based on appropriate velocity intervals of C II λ1335, both doublet components of C IV, N III λ989, N V λ1243, Si II λ1527, Si III, and both the components of Si IV. The latter ions illustrate the goodness of the models. While the models HM3 and both the power laws overestimate the amount of silicon absorption, HM and HM2 fit well. Si III is well described by SB, but Si IV is overproduced. Considering also the contributions of the other lines to χ^2, we find the best fitting model to be HM ($\chi^2 = 1.64$). The SB model produces a good description of the observations as well ($\chi^2 = 1.83$). For further evaluation we keep both models as possible descriptions of the observed system.

The system at $z = 2.4397$ (or at $v = -71.1$ km s^{-1} with respect to $z = 2.4405$) is also modelled best using the HM ionizing radiation. The derived metallicity is [C/H] = −2.86, which is more than 1 dex lower than in case of the $z = 2.4405$ central component. Adopting the starburst radiation field, the −71.1 km s^{-1} absorber leads also to a lower metallicity ([C/H] = −3.86 in comparison to −2.14 for the central component), indicating that the enrichment history of the IGM is highly inhomogeneous.

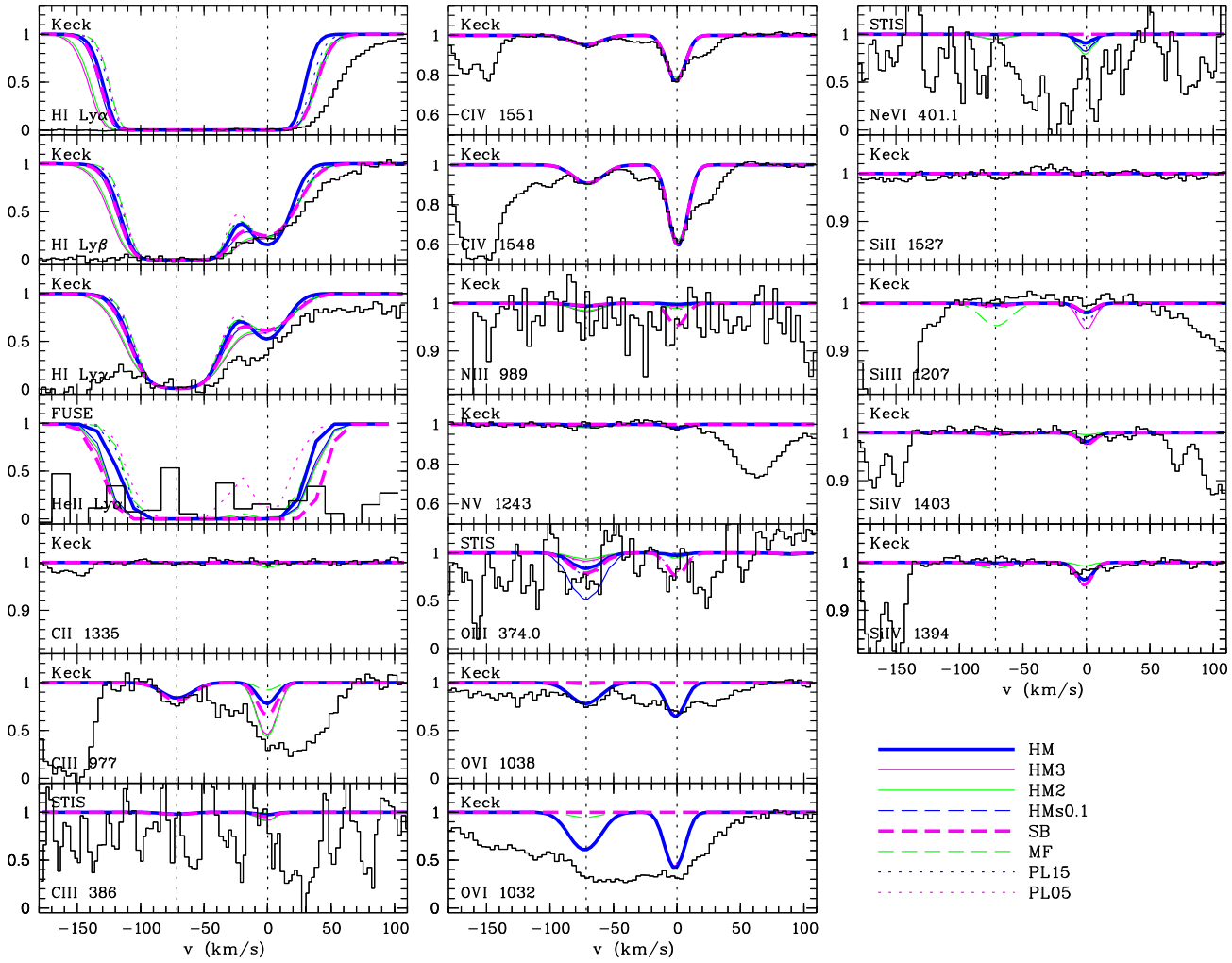

Fig. 4.18: Observed and modelled absorption lines of the system at $z = 2.4405$. The preferred models are HM and SB.

4.4.14. System $z = 2.4965$

The system at $z = 2.4965$ shows only weak C IV and probably O VI (see Fig. 4.19). If C III is present as well, its detection is very uncertain because of blending. For the few different ions observed the models are constrained using the C IV/O VI column density ratio. Since we cannot be sure, whether O VI is really detected, the model interpretation has to be considered carefully.

The main discrepancies of the models are found in the H I profile. The best fitting model with respect to neutral hydrogen is then HM3. This is confirmed by the computed χ^2-value based on the lines H I Lyα and Lyβ, C II λ1335, both components of C IV, N III λ989, N V λ1243, O VI λ1038, Si II λ1527, and Si IV λ1394. Of course, the dominating profiles are those of H I. The numbers concerning the continuum windows are comparable, and there are only little differences for C IV. Considering C IV, the HM3 model slightly underestimates the observed column density. Whereas the feature, we identified as O VI, is modelled best by HM3 and HM2. Both models also predict weak Ne V and Ne VI absorption consistent with the data. Therefore, HM3 is the preferred model ($\chi^2 = 3.86$).

4.4.15. System $z = 2.5683$

Rather weak metal line features arise from the system at $z = 2.5683$ as can be seen from Fig. 4.20. C IV shows two subcomponents close to another ($\Delta v = 17\,\mathrm{km\,s^{-1}}$), also present in C III. The observed, weak O VI features cannot be resolved into two subcomponents. Thus, the measured values can be considered as an upper limit for both components. For silicon the weaker, red component is below the detection limit. The higher order Lyman series lines of hydrogen are blended with forest lines. Therefore, the most confident column density results from the Lyα fit, which we performed simultaneously with Lyβ.

Comparing the photoionization models with the data, the blue wing of Lyβ and the red wing of Lyγ are supposed to be appropriate, even though all models overestimate H I. This may be due to a wrong distribution of the total amount of neutral hydrogen to the subcomponents, or only part of the

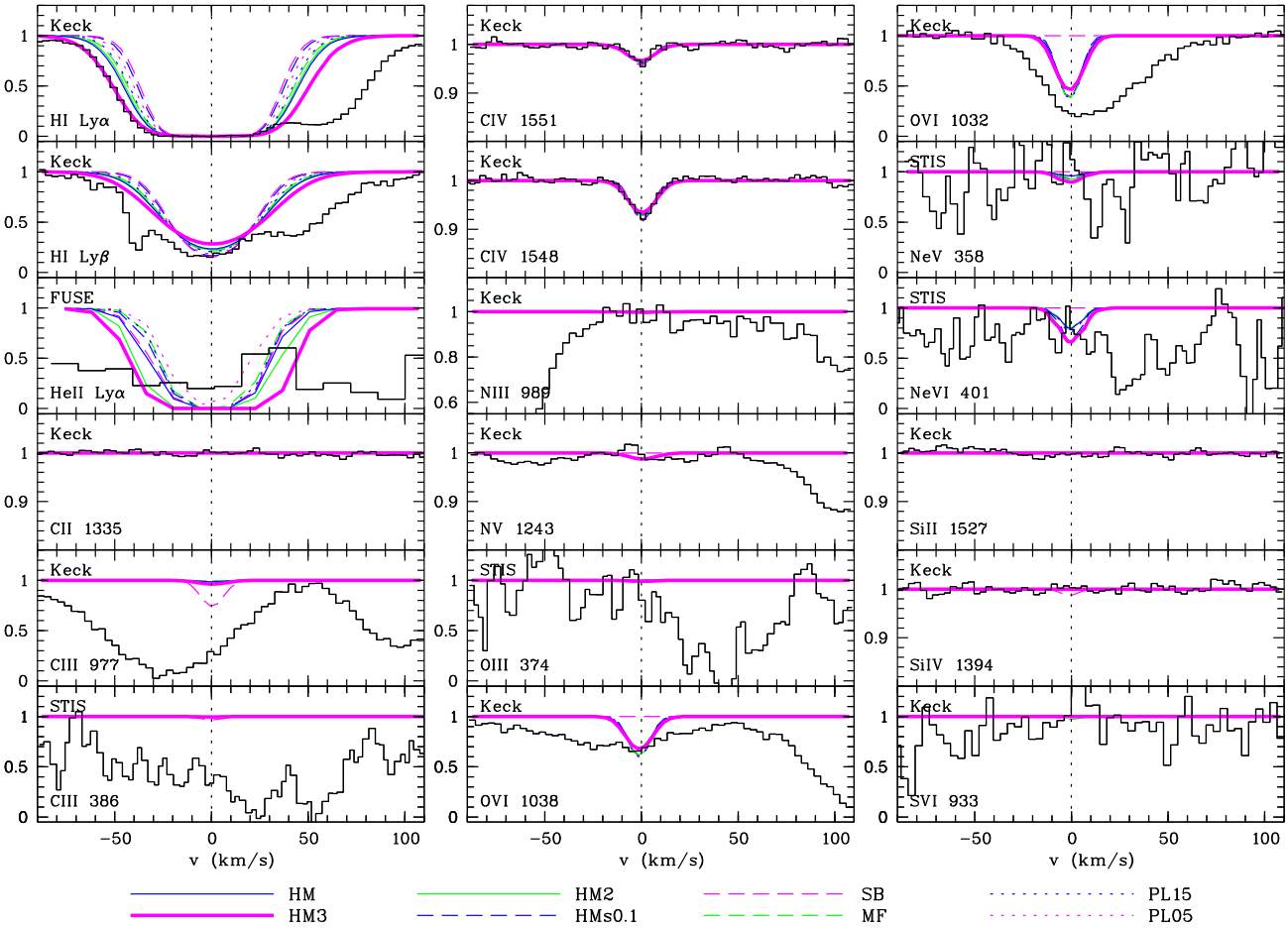

Fig. 4.19: Observed and modelled absorption lines of the system at $z = 2.4965$. The preferred model is HM3.

measured H I column density is associated to the metal line absorption. Another possibility is, that all models underestimate the temperature of the absorber, since the comparison of the artificial profile to the observed data shows that the observed profiles have much smoother and broader wings indicating a higher temperature. However, the broadest and thus best fitting profiles are produced by the models HM2 and HM3.

We compute the χ^2-values adopting appropriate velocity intervals of H I Lyβ, C II λ1135, C III λ977, both components of C IV, N V λ1239, Si III, and both doublet components of Si IV. As discussed above, the χ^2-values are dominated by H I, but also Si III contributes above average. Regarding Si III, the best fits are yielded using the PL15, MF, or HMs0.1 radiation backgrounds, which are the best fitting models if H I is ignored, while HM overestimated the observed column density significantly. The decision for the best fitting model depends on whether the H I profile is considered or not. If we include the profile of Lyβ, HM2 and HM3 are the best fitting models, whereas PL15 fits best if H I is neglected. However, only HM3 and HM2 provide enough O VI absorption to fit the observed features ([O/C] $\approx$ 0.5). We claim HM2 to be the best fitting model ($\chi^2 = 4.19$). Because the quality of the HM3 fit is only slightly inferior ($\chi^2 = 4.23$), we may conclude that the energy distribution of ionizing radiation could be optimized positioning a break at a low energy slightly above 2 Ryd.

4.4.16. System $z = 2.5785$

The broad Lyα absorption trough of the system at $z = 2.5785$ separates into two distinct features at $-50\,\mathrm{km\,s^{-1}}$ and $25\,\mathrm{km\,s^{-1}}$ visible in Lyγ and higher order Lyman series (Fig. 4.21). Each of the subsystems can be separated into two components, with respect to C IV. The complex of the C IV λ1548 component is blended with Al II of the system at $z = 2.3155$. The center of the blue H I features mismatches the center of the blue subcomponents observed in the metal line transitions. They appear to be shifted by roughly $20\,\mathrm{km\,s^{-1}}$. This leads to an overproduction of neutral hydrogen in the blue components for all models. Thus, the derived metallicities are supposed to be slightly underestimated.

We compute χ^2 considering H I Lyϵ, C II λ1335, C IV λ1551, Si II λ1527, both doublet components of Si IV, and S VI λ945. The dominating contributions are given by C IV

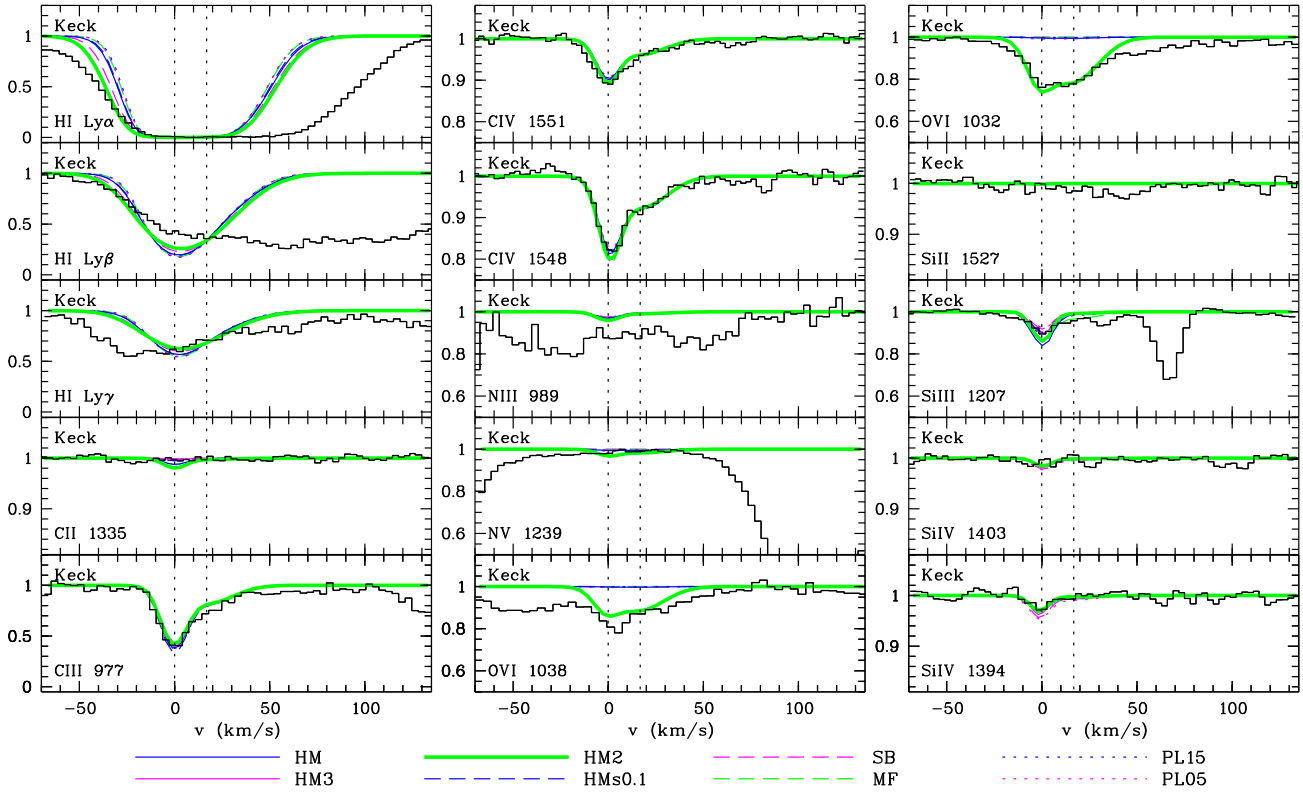

Fig. 4.20: Observed and modelled absorption lines of the system at $z = 2.5683$. The preferred model is HM2.

and Si III, which are observed to be broader than predicted by the models. Best fitting models with regard to C IV are HM2 and HM3, and HM and MF with respect to Si III. The feature of C II is overestimated by the models PL05 and HM2. PL05 also predicts too much absorption in Si IV. Considering the red component of neutral hydrogen in Lyϵ, the modified HM models are slightly too broad, while MF, PL15 and SB fit well the observed profile.

Regarding the transitions not included into the χ^2-computation, HM3 severely overestimates Ne V. The reddest feature of C III might be underpredicted by all models except PL05 and SB. But possibly it is blended with the low redshift Lyα forest. Thus, it is not clear, if the total feature is due to C III. Unfortunately, the λ386 transition is blended as well and therefore cannot answer the question. A significant amount of O VI is produced by the models HM, HM3, HM2, and PL15. But HM and PL15 are then severely overpredicting the blue features of O III.

Considering all arguments given above, the best fitting model is HM3 ($\chi^2 = 4.99$), even though it underestimates the Si III component at $-18.5\,\mathrm{km\,s^{-1}}$. According to the HM3 model, silicon is overabundant by more than 1 dex ([Si/C] = 2.98, 1.93, 0.63, 1.76) in nearly all subcomponents. Test calculation showed, slight changes in the position of the break of the ionizing radiation would cause significant variations for [Si/C]. A further refinement of the UV background might possibly decrease the silicon overabundance.

4.5. Discussion

From the 25 observed metal line systems we were able to derive models for 18 systems with the purpose to predict the metal line spectrum in the far-UV. Photoionization models were evaluated with the aim to determine the ionizing UV background which produces the best description of the observed lines and of the predicted far-UV spectrum. The investigation is based on the comparison of eight different background shapes. A summary of the results is given in Table 4.1, which is presented graphically in Fig. 4.22, where we exclude the systems associated to the QSO. Thus, the total number of systems considered here is 22. Note that systems at $z \leq 1.1573$ (except the $z = 0.7222$ system) show only very few lines in the optical. Realistic error estimates are therefore not possible and the models of the low redshift systems have been evaluated using more qualitative arguments.

Evaluating the sample reveals HM3 to be the model leading largely to the best description. HM3 denotes a UV background based on the Haardt & Madau (2001) energy distribution, where the break at 4 Ryd is shifted to 3 Ryd. Seven of 11 systems with $z > 2$ find HM3 to be the best radiation background, and one leads to HM2. As discussed in the previous Section there are hints that for several systems the break of a more optimized ionizing contiuum would be somewhere in between $2 - 3$ Ryd. This is consistent with recent results from Agafonova et al. (2005), who find a sig-

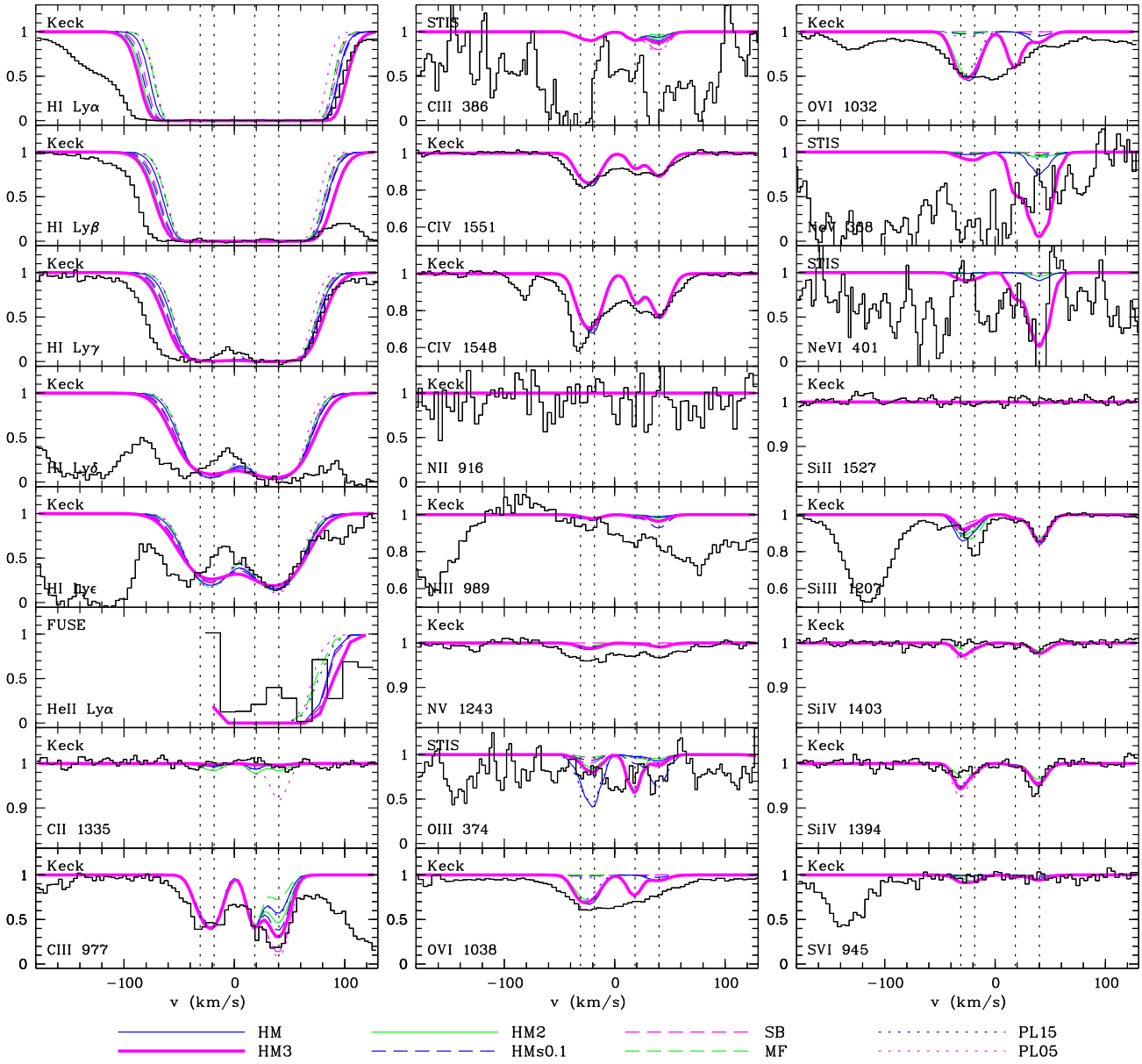

Fig. 4.21: Observed and modelled absorption lines of the system at $z = 2.5785$. The preferred model is HM3. The blue component of the He II profile is affected by the gap in the FUSE spectrum and therefore not observed.

nificant intensity decrease between 3 and 4 Ryd compare to the UV background of Haardt & Madau (1996) at $z \sim 3$ investigating four metal line systems with a more sophisticated method.

The classical HM background was only found in three cases ($z = 0.7772, 0.8643, 2.4405$), where the two more redshifted systems can be equivalently modelled with the SB ionizing radiation. The spectral energy distribution of a starburst galaxy, adopted from Bruzual A. & Charlot (1993), is found to be three times among the preferred models. The hard radiation of the quasar-like SED as derived by Mathews & Ferland (1987) is found in two cases. The HMs0.1 model, a HM background with reduced intensity for energies < 1.0 Ryd, is preferred twice for the systems at $z \sim 1$. Note that only the system at $z = 1.4941$ leads to the pure power law model with $\nu^{-1.5}$ (PL15). As discussed above, the model is extremely uncertain, due to few observed transitions.

The results suggest that a background similar to HM3 dominates at $z \gtrsim 2$, while at $z \lesssim 2$ no predominant shape of the ionizing radiation is found (see Table 4.1). This might indicate a major contribution of local sources at lower redshift because of less filtering of their radiation by the IGM due to advanced structure formation. Unfortunately, the systems at $z \lesssim 2$ are mainly observed in the UV spectral range where the data quality is insufficient to draw solid conclusions.

A possible modification of the ionizing background

Table 4.1: Summary of the radiation backgrounds that best model the metal line systems. The more objective procedure of computing χ^2-values to estimate the goodness of a fit could be applied to the systems at redshifts $z \geq 1.4941$ and $z = 0.7222$. Also given are the derived mean metallicity [M/H] and the abundance of [Si/C].

z	model	[M/H]	[Si/C]
0.2140	HM2	0.14	0.17
0.7222	HM	0.13	0.0[a]
0.8643	HM	−0.35	0.0[a]
	HMs0.1	−0.68	0.0[a]
	SB	−0.79	0.0[a]
1.1573	HMs0.1	−1.09	0.0[b]
1.4941	PL15	−0.97	0.0[b]
1.7241	HM3	−2.82	−0.09
1.8450	MF	−0.48	−0.68
2.0211	...	...	...
2.1287	...	...	...
2.1680	SB	−2.80	−0.43
	HM3	−3.23	0.90
2.1989	...	...	...
2.2896	HM3	−3.31	0.89
2.3079	...	...	...
2.3155	HM3	−0.55	0.25, 0.78[c]
2.3799	HM3	−1.40	1.07
2.4321	HM3	−2.33	0.0[d]
2.4331	HM3	−1.73	1.61
2.4386	MF	−1.29	−0.16, 0.69[c]
2.4405	HM	−0.37	1.01
	SB	−2.14	0.70
2.4965	HM3	−2.15	0.0[d]
2.5683	HM2	−1.71	1.49
2.5785	HM3	−2.78	2.45, 1.20[c]

[a] silicon outside observed spectral range
[b] uncertain detection of Si II or Si IV, respectively
[c] several subcomponents (see text)
[d] silicon not detected

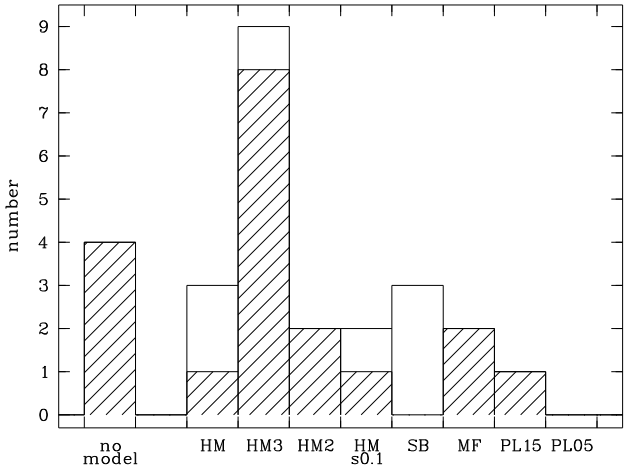

Fig. 4.22: Numbers of the best fitting models for all observed metal line systems except the associated systems. "no model" summerizes the systems for which no model can be derived because of the lack of observed ions. The hatched area contains systems with unique solutions, while the blank area includes ambiguous models as well (see Table 4.1). The total number of systems considered is 22.

would have implications for other quantities related to the shape of the background radiation like the measurement of the metallicity of the IGM. Exact estimates of the metallicty from observations are important e.g. to constrain the history of enrichment of the IGM (e.g. Qian & Wasserburg 2005). A rough comparison of the metallicity as traced by carbon derived for the preferred models of each system to the values found using the Haardt & Madau (2001) radiation field, indicates the trend that the models based on the softer radiation fields (HM3, HM2, HMs0.1, and SB) lead to increased ionization parameters and lower metallicity by roughly 0.5 dex in comparison to HM, while the harder MF radiation produces slightly lower ionization parameters and enhanced metallicity by about 0.4 dex. This means, a modification of the UV background would affect the determination of the metallicity of the IGM in the sense that abundances would descrease if the radiation softens in comparison to Haardt & Madau (2001), or increase with harder radiation. This is consistent when comparing the results from our best fit models to the metallicities estimated by Simcoe et al. (2005). They analyzed nine of the systems selected by O VI or N V absorption (Actually, they report on six systems but consider our systems at $z = 2.4321$, 2.4331, 2.4386, and 2.4405 as only one absorption system). Using a composite spectrum of Haardt & Madau (2001) and the energy distribution of a starburst, they find on average a mean metallicity roughly 0.4 dex higher than derived by our preferred HM3 models.

We find wide spread values for the silicon enhancement inferred from our models in the range $-0.7 \lesssim$ [Si/C] $\lesssim 1.6$ (summarized in Table 4.1). An unrealistically high value is found for the blue components of the system at $z = 2.5785$. Comparing to the results of Simcoe et al. (2005) we find at least the same tendencies, i.e. one silicon deficient system at $z = 1.8450$ and silicon enhancement for all other absorbers. This provides further arguments for HM3 being the preferred model in case of the $z = 2.1680$ system, since the SB model produces Si deficiency. As discussed in Section 4.3, [Si/C] depends on the enrichment history, but also on the adopted UV background (Aguirre et al. 2004). Since Simcoe et al. (2005) inferred a more smooth distribution of [Si/C], the differences are most likely caused by the adopted ionizing energy distribution. If we only consider the HM3/HM2 models, the silicon enhancement is on average [Si/C] $= 1.18 \pm 0.62$ (or 1.13 ± 0.32, if both the extreme outliers, which are single subcomponents of observed systems, are neglected). This is still about 1 dex higher than estimated by Simcoe et al. (2005) and illustrates the importance of the assumed UV background for the determination of the metallicity of intergalactic absorbers (see also Aguirre et al. 2004).

Summarizing all preferred models, we compute a final

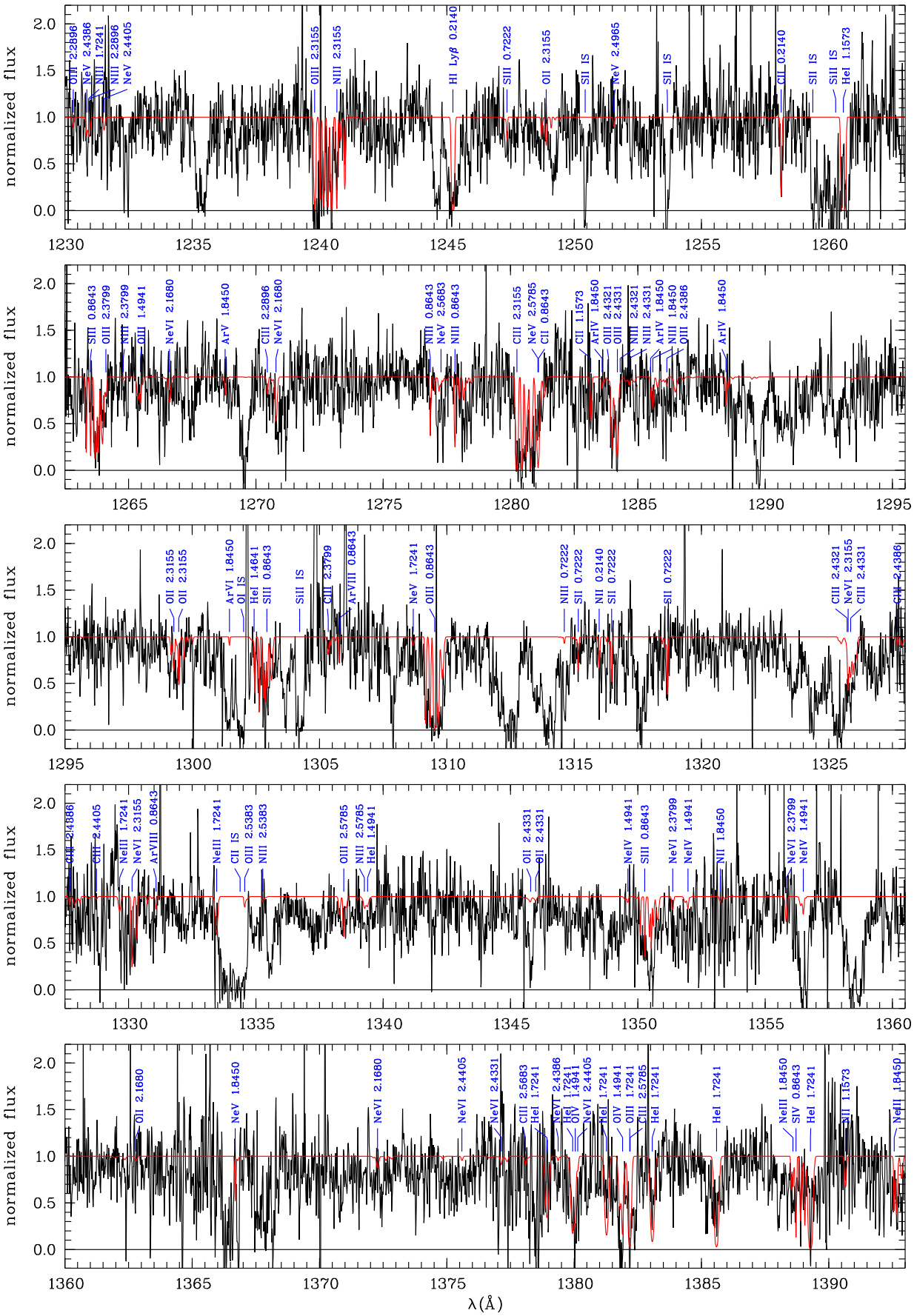

Fig. 4.23: Predicted metal line spectrum in the range 1230 – 1393 Å in comparison to the normalized STIS data (see text for details).

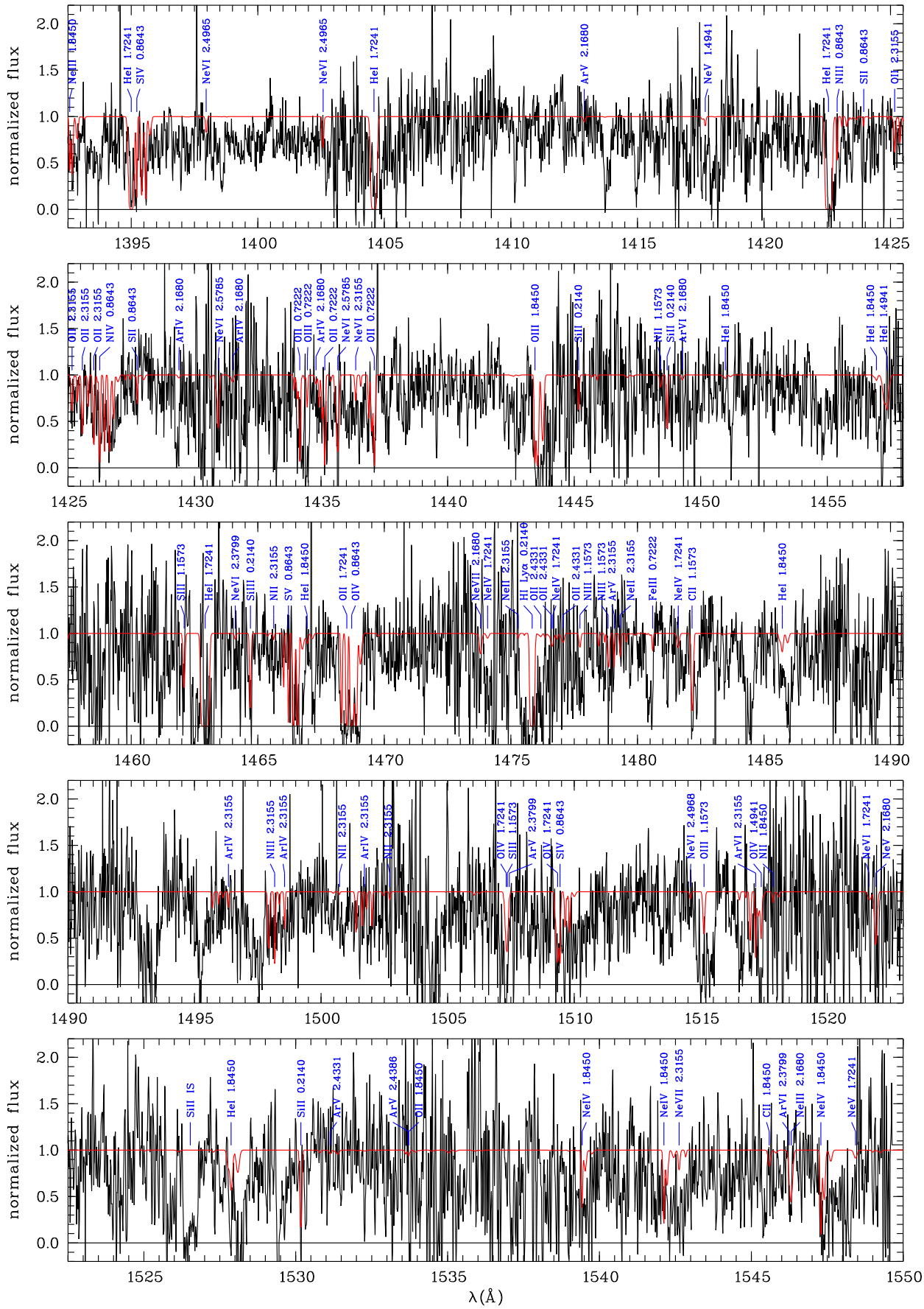

Fig. 4.24: Predicted metal line spectrum in the range 1393 – 1550 Å in comparison to the normalized STIS data (see text for details).

model for the STIS spectral range (1230 – 1550 Å). For the systems with several equivalent solutions the HM or HM3 model is adopted. The parameters of the modelled lines are summarized in the Appendix (Table A.6), and the resulting model is shown in Figures 4.23 and 4.24 in comparison to the observed data. The model includes H I and He I lines arising from the modelled metal line systems. Interstellar features are indicated as well. In the presented spectral range we detect galactic absorption of S II $\lambda\lambda\lambda$ 1250.6, 1253.8, 1259.5, Si II $\lambda\lambda\lambda$1260.4, 1304.4, 1526.7, O I λ1302.2, and C II λ1334.5. The feature at $\sim$ 1235.5 Å may be C III λ386.2 absorption from the system at z = 2.1989.

Comparing the resulting model to the observed spectrum, identification of all metal line features in the STIS data should be possible. Indeed, the model is consistent with the data in the whole spectral range. However, there are still narrow features remaining unidentified. Some of them may be metal line absorption as well, which has been ignored due to imperfect modelling. On the other hand, due to the limited quality of the data ($S/N \sim 3$) some narrow features are expected to be mimicked by noise peaks. In particular this is true at wavelengths $\gtrsim$ 1450 Å, where the noise level increases, but also at lower wavelengths noise might mimic narrow absorption features. Thus, Figures 4.23 and 4.24 give confindence that we have derived reasonable models. The remaining broader absorption lines are supposed to be Lyα lines arising from low redshift absorbers ($z \lesssim 0.28$) or higher order Lyman series transitions arising from absorbers at $z < 0.7$.

We roughly estimate how strongly the FUSE spectral range might be affected by lines of the higher Lyman series lines. Assuming all unidentified, strong features are low redshift Lyα lines, the expected positions of the higher order Lyman series lines are computed. Most of the systems are not expected to contribute to the absorption in the FUSE spectral range since higher order Lyman series lines located redwards of the He II forest are detected only very weakly. However, three systems at z = 0.1240, 0.0809, and 0.0237 possibly affect the He II Lyα forest. The Lyβ feature of the system at z = 0.1240 is blended with Lyδ of the metal line system at z = 0.2140 both located at $\sim$ 1153 Å. The corresponding Lyγ and δ features are expected at 1093.1 Å and 1067.5 Å, respectively. From the system at z = 0.0809 absorption is expected at 1108.7 Å (Lyβ) and 1051.2 Å (Lyγ), while the Lyβ features of the z = 0.0237 systems should be located at 1050.0 Å. Therefore, if the analysis of the FUSE data should lead to high η values at these positions, this may be due to higher order Lyman series lines of the low redshift H I forest.

4.5.1. Implications on the He II/H I ratio

FUSE observations of the He II Lyα forest towards HE 2347-4342 (Kriss et al. 2001; Shull et al. 2004; Zheng et al. 2004b) and HS 1700+6416 (Reimers et al. 2004, see also Chapter 5) found that the column density ratio $\eta = N(\mathrm{He\,II})/N(\mathrm{H\,I})$ is apparently fluctuating over roughly 2 dex on small scales ($\sim$ 1 Mpc). These results indicate the importance of local sources on the photoionization of the absorbing material.

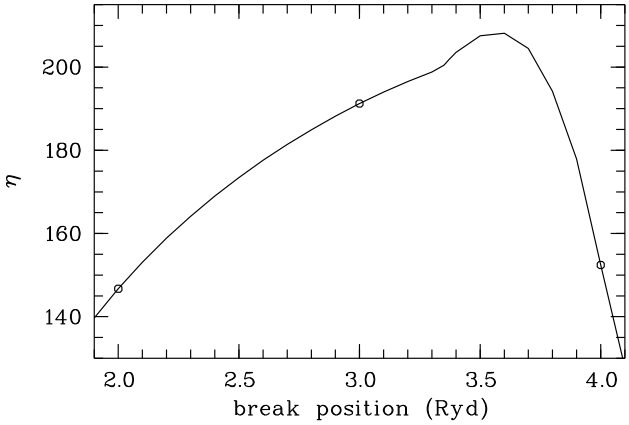

Fig. 4.25: Value of the column density ration η computed according to Eq. 4.4 versus the position of the break, which occurs in case of the classical Haardt & Madau (2001) background at 4 Ryd. The values corresponding to the models HM, HM3, and HM2 are marked with circles.

The column density ratio η depends on the radiation field and therefore can be used to diagnose its fluctuations. In photoionization equilibrium the density of hydrogen and helium is

$$n_{\mathrm{H\,I}} = \frac{n_e n_{\mathrm{H\,II}} \alpha^{(A)}_{\mathrm{H\,I}}}{\Gamma_{\mathrm{H\,I}}} \quad \text{and} \quad n_{\mathrm{He\,II}} = \frac{n_e n_{\mathrm{He\,III}} \alpha^{(A)}_{\mathrm{He\,II}}}{\Gamma_{\mathrm{He\,II}}}, \quad (4.2)$$

respectively, with the case A recombination rate coefficients $\alpha^{(A)}_{\mathrm{H\,I}} = 2.51 \cdot 10^{-13}\, T_{4.3}^{-0.755}\,\mathrm{cm^3\,s^{-1}}$ and $\alpha^{(A)}_{\mathrm{He\,II}} = 1.36 \cdot 10^{-12}\, T_{4.3}^{-0.70}\,\mathrm{cm^3\,s^{-1}}$. The photoionization rates Γ are

$$\Gamma_{\mathrm{H\,I}} = \int_{\nu_{\mathrm{LL,H\,I}}}^{\infty} 4\pi \frac{J_\nu}{h\nu}\, \sigma_{\mathrm{H\,I}}(\nu)\, d\nu\,, \quad (4.3)$$

in case of hydrogen and equivalent in case of He II. ν_{LL} denotes the ionizing threshold for H I (1 Ryd) or He II (4 Ryd), respectively. The cross section for photoionization decreases roughly with ν^{-3} above the ionizing threshold, thus it is $\sigma(\nu) = \sigma^0\,(\nu/\nu_{\mathrm{LL}})^{-3}$, with $\sigma^0_{\mathrm{H\,I}} = 6.30 \cdot 10^{-18}\,\mathrm{cm^2}$ and $\sigma^0_{\mathrm{He\,II}} = 1.58 \cdot 10^{-18}\,\mathrm{cm^2}$. Adopting primordial helium abundance ($Y = 0.244 \pm 0.002$; Burles et al. 2001) and assuming that the gas is almost fully ionized ($n_{\mathrm{H\,II}} \simeq n_{\mathrm{H}}$ and $n_{\mathrm{He\,III}} \simeq n_{\mathrm{He}}$), the ratio η can be written as

$$\eta = \frac{n_{\mathrm{He\,II}}}{n_{\mathrm{H\,I}}} \approx 0.437 \cdot T_{4.3}^{0.055} \cdot \frac{\Gamma_{\mathrm{H\,I}}}{\Gamma_{\mathrm{He\,II}}}\,. \quad (4.4)$$

The integrals given in Eq. 4.3, which are still contained in Eq. 4.4, can be further approximated, since the photoionization rates depend mainly on the specific intensity J_ν near the ionizing threshold ν_{LL} due to the ν^{-3}-dependence of the photoionization cross section. The result of this approximation can be found e.g. in Fardal et al. (1998) or Chapter 2.2.

However, we perform a numerical integration to estimate η according to Eq. 4.4 for each of the ionizing spectra used

in the analysis. Energy distributions depending on redshift (all HM-like spectra) are considered at $z \sim 2$. The HM background leads to $\eta \approx 150$, which is higher than the value usually referred to (~ 45, Haardt & Madau 1996). The reason is the inclusion of radiation of galaxies in the new version of the UV background radiation, which increases η (illustrated in Fig. 8 of Haardt & Madau 2001). In case of the HM spectrum used here, the escape fraction of Lyman limit photons from galaxies is 10 %. The spectrum with reduced flux at $E < 1$ Ryd produces the same η, since the energy range included by the integrals of the photoionization rates remain unaffected by the modification.

The dependence of η on the position of the break, which we shifted from its actual position at 4 Ryd to 3 (HM3) and 2 Ryd (HM2), respectively, is illustrated in Fig. 4.25. The shape of the curve is determined by the integrals of the photoionization rates $\Gamma_{\mathrm{H\,I}}$ and $\Gamma_{\mathrm{He\,II}}$ (Eq. 4.3). For break positions above 3.4 Ryd the ratio is dominated by $\Gamma_{\mathrm{He\,II}}$, which gets smaller with decreasing break position, i.e. η decreases with the maximum at ~ 3.6 Ryd. If the position of the break is at energies < 3.4 Ryd, the spectral energy distribution is flat at the He II ionization edge and the integral $\Gamma_{\mathrm{He\,II}}$ stays roughly constant. Whereas the photoionization rate of H I, and therefore η, decreases with decreasing position of the break.

The different ionizing spectra we used, lead to very different η values, as expected. The adopted energy distribution of a starburst galaxy (Bruzual A. & Charlot 1993, SB) produces a high value $\eta \approx 700$ due to the lack of helium ionizing photons. The AGN-like spectrum of Mathews & Ferland (1987, MF) as well as the power laws with $\alpha = -1.5$ (PL15) and -0.5 (PL05), respectively, are very hard, and thus lead to low η values. While PL15 reveals $\eta \approx 15$, MF ($\eta \approx 10$) and PL05 ($\eta \approx 5$) produce even lower values. Within our sample of metal line systems, the power laws are practically of no importance. But the MF and SB spectra lead in 11 % and 17 % of the investigated systems to a preferred model, even though there are equivalent descriptions based on a different energy distribution in case of SB. Thus, some of the extremely low and high η values found analyzing the He II observations towards HE 2347-4342 (Kriss et al. 2001; Shull et al. 2004; Zheng et al. 2004b) and HS 1700+6416 (Reimers et al. 2004), might be induced by ionizing radiation similar to the MF and SB energy distributions used in this analysis.

4.5.2. Correlation with galaxies

The field of HS 1700+6416 was target of deep observations aiming at the identification of star-forming galaxies (Teplitz et al. 1998; Erb et al. 2003; Steidel et al. 2005; Shapley et al. 2005). While Teplitz et al. (1998) report on two galaxies close to the line of sight, Shapley et al. (2005) identified 72 star-forming galaxies with $z \sim 2$ in the field of HS 1700+6416 (Fig. 4.26). Four of them are also reported in Erb et al. (2003), who give more accurate redshift measurements using the H α emission line and UV interstellar

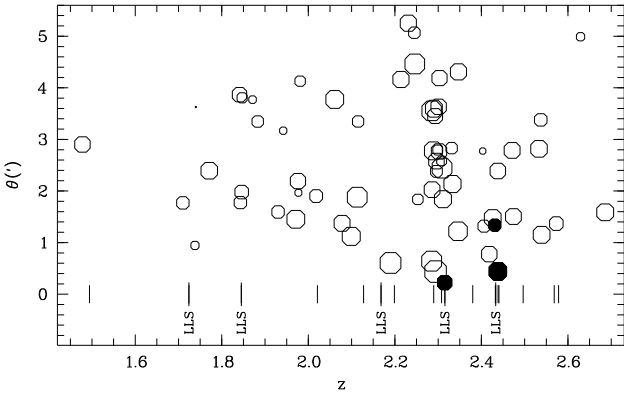

Fig. 4.26: The distribution of galaxies identified by Shapley et al. (2005) towards HS 1700+6416. The redshift of the galaxies versus their angular separation θ from the line of sight is presented. The size if the circles indicates the $\mathcal{R}$ magnitude of the galaxy. The vertical bars at the bottom represent the positions of the detected metal line systems. Lyman limit systems are labeled. Galaxies at least close as 1 Mpc (proper distance) to a metal line system are marked as filled circles.

absorption lines. Recently, Simcoe et al. (2005) studied the half of the absorbing systems investigated here in the context of their physical connection to the galaxies. In order to avoid any systematics due to unconsidered local sources Simcoe et al. (2005) used composite energy distributions of the HM background and the observed galaxies. Complementary, we investigate a possible correlation between the inferred best fit ionizing radiation and the vicinity of a galaxy. We use the formulas given by Liske (2000) assuming a cosmology with $\Omega_M = 0.3$, $\Omega_\Lambda = 0.7$, and $H_0 = 70\,\mathrm{km\,s^{-1}\,Mpc^{-1}}$ to compute the proper distance between the galaxies and the identified metal line systems. Coordinates and redshifts of the galaxies are taken from Shapley et al. (2005).

We investigate a possible correlation between the occurrence of galaxies and metal absorption systems counting the number of galaxy-system pairs within a certain distance interval. We concentrate on redshifts $1.70 \leq z \leq 2.60$, since in this range the coverage of both galaxies and metal line systems is good. The chosen interval contains 62 galaxies and 17 absorption systems. The majority of galaxy-system pairs, namely 38, are found for distances $D \leq 3.0$ Mpc with the maximum number of pairs for $D \sim 2$ Mpc. The main contribution to the determined number is provided by the metal line systems arising near several galaxies. Steidel et al. (2005) report on a proto-cluster at $z = 2.300 \pm 0.015$ containing 17 galaxies. We find three absorption systems in this region (among them one LLS), which are all closer than 12 Mpc to any of the cluster galaxies. Further groups of galaxies in the vicinity of absorbing systems are located at $z \sim 1.845$ (four galaxies, one LLS) and $z \sim 2.435$ (three galaxies, four metal line systems including one LLS). In total, 47 % of the metal line systems arise in regions with groups of galaxies with scales for the galaxy-system distance of $\sim 2 - 3$ Mpc. Performing a series of simple Monte Carlo simulations, where we arbitrarily distribute the appropriate

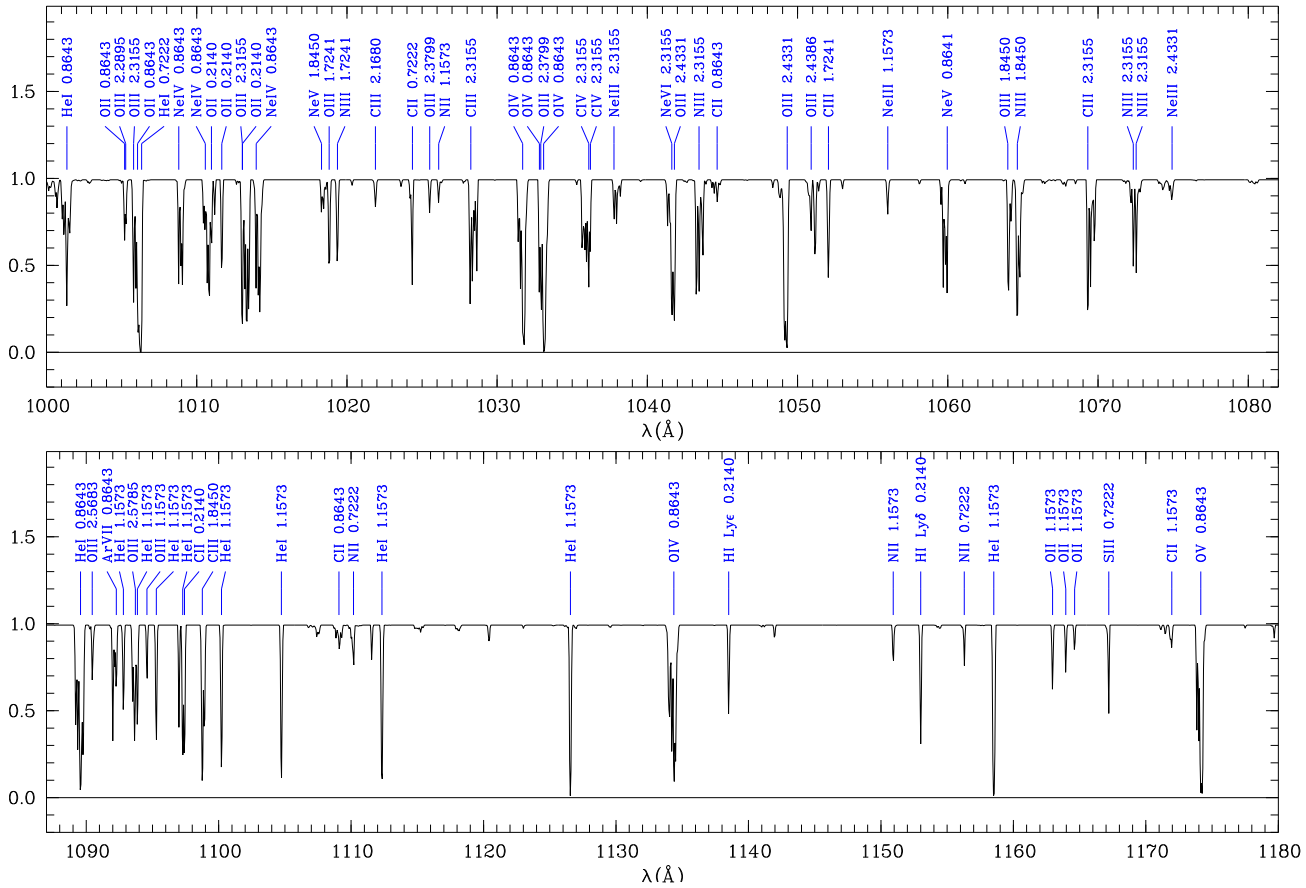

Fig. 4.27: Prediction of the metal line content in the FUSE spectral range based on the preferred ionizing energy distributions estimated in Section 4.4. In case of equivalent models, the result based on the HM model is adopted. Prominent features are labelled with ion and system redshift.

number of metal line systems in between the observed positions of the galaxies, we estimate the probability to find 33 pairs with $1.0 < D \leq 3.0\,\mathrm{Mpc}$ to be only $3.0 \cdot 10^{-10}$. This result is in agreement with the findings of other authors that galaxies and metal absorption systems both trace the same large scale structure (e.g. Bowen et al. 2002; Adelberger et al. 2003).

Following Schaye (2004), the influence of UV radiation of local sources such as galaxies should be important for metal line systems and high column density H I systems. With the present sample of absorption systems and the informations of the distribution of galaxies, an observational test of this prediction should be possible. But we find no obvious correlation between the distance to a galaxy and the radiation background leading to the best model of the absorber. The data show a correlation neither between the H I column density of the systems and the preferred background model, nor between $\log N_{\mathrm{H\,I}}$ and the distance to the next galaxy.

4.5.3. Prediction of metal lines in the FUSE spectral range

The primary aim of the presented investigation was to derive a prediction of the metal lines arising in the FUSE spectral range. The prediction of the metal line spectrum is important for the analysis of the He II features, since pollution by unrecognized metal lines may lead to biased results concerning the He II/H I ratio η (Reimers et al. 2004; Fechner & Reimers 2004). Thus, we summarize all line parameters produced by the preferred models discussed in Section 4.4 to compute a prediction for the appearance of the metal line spectrum in the FUSE spectral range (1000 – 1180 Å). In the three cases, where we found several equivalent solutions, we adopt the HM or HM3 model, respectively, which lead to a preferred description of the respective systems. The resulting expectation is presented in Fig. 4.27. Besides metal lines, the prediction also includes higher order Lyman series of H I ($z = 0.2140$) as well as He I features of the systems $z = 0.8643$ and 1.1573. A more conservative approach would be a prediction derived only using the Haardt & Madau (2001) UV background. The result would be qualitatively the same as shown in Fig. 4.27, since the prominent features are similar. A comparison between both models is shown in Fig. 4.28. In the FUSE spectral range 32 % of the pixels have different flux values if the preferred model or the HM model is considered. The average root mean square deviation is 0.056 considering only those pixels with different fluxes.

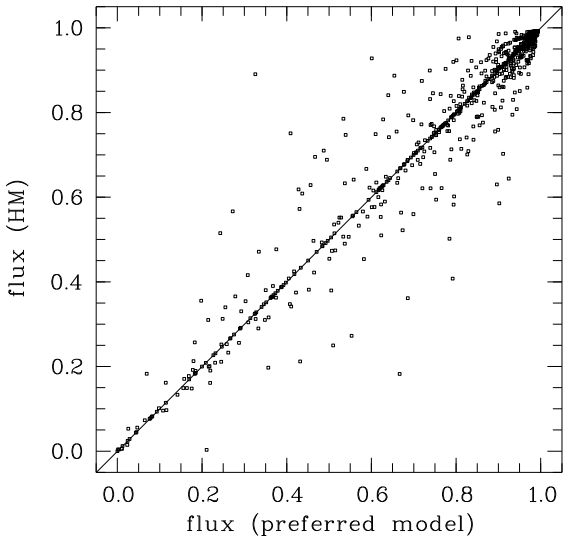

Fig. 4.28: Comparison of the fluxes predicted by the preferred models with those predicted by the HM models. The flux level differs in 32 % of the pixels. The root mean square deviation of these pixel is 0.056.

For the systems only seen in C IV, the λ312 features can be computed directly from the fitted line parameters. Only the system at $z = 2.3079$ contributes to the absorption in the FUSE spectral range and the expected features are weak ($\tau_0 \lesssim 0.2$). Furthermore, they are located at $\sim$ 1033.5 Å blended with the much stronger O IV λ554 feature ($\tau_0 \approx 151$) of the system at $z = 0.8643$.

Considering the multi-phase nature of several systems discussed in Section 4.4, we certainly have preferred low ionized species on average (outstanding examples are the systems at $z = 1.8450$ and 2.3155). The predicted line spectrum contains more features arising from low ionization stages (predominately O II, O III, C II, C III,N II, N III) than higher ionized ions like Ne IV – Ne VI, O V and Ar VII. Of course, this is also due to the rest wavelengths of the considered ions in combination with the redshifts of the absorbing systems, e.g. transitions with rest wavelengths < 400 Å enter the FUSE spectral range only for $z \gtrsim 1.5$. However, since the derived models often reveal problems to produce significant features of high ionization stages in the optical (like O VI), the far-UV prediction probably misses highly ionized lines rather than transitions of low ionized elements. As discussed in the corresponding Sections, there are only two cases, where possible underestimated absorption features may bias the He II column density. These are Ne VII λ465 of the $z = 1.1573$ system and Ne III of the system at $z = 2.3155$. The absorption lines are expected to arise at 1003.6 Å and 1037.9 Å, respectively. Thus, these wavelengths should be kept in mind to be possible biased when analyzing the He II Lyα forest.

A comparison to the observed FUSE data and the inclusion of the prediction into the analysis of the He II Lyα forest will be presented in Chapter 5.

4.6. Conclusions

In the spectrum of the QSO HS 1700+6416, we detect 25 metal line systems. 18 systems show absorption features in the present observational data taken with Keck/HIRES and HST/STIS, providing a sufficient number of ions in order to derive photoionization models. The adopted systems (seven of them are optical thin Lyman limit systems) are located at redshifts $0.2 < z < 2.6$. For each system we derive eight photoionization models based on different radiation backgrounds. As shape of the ionizing radiation we adopt the Haardt & Madau (2001) intergalactic background radiation and three different modifications of it, as well as the energy distribution of a starburst galaxy (Bruzual A. & Charlot 1993), an AGN (Mathews & Ferland 1987), and two power laws with $\alpha = -1.5$ and -0.5. Among these models, the best one is chosen by applying a χ^2-test. Since this procedure is only possible for systems with $z \geq 1.4941$ and for the $z = 0.7222$ system, the best fitting models for the remaining three low-redshift systems are selected by a more qualitative discussion. For nine systems (50 %) the preferred energy distribution is a modification of the UV background of Haardt & Madau (2001), where the break, usually located at 4 Ryd, is shifted to 3 Ryd. Additionally, the HM-like spectrum with the break shifted to 2 Ryd is found twice. Thus, roughly 60 % of the systems can be described with modified Haardt & Madau (2001) spectra, where the helium break is shifted to energies < 4 Ryd. For three absorbers the unchanged Haardt & Madau (2001) radiation is preferred, two of which can be equivalently modelled on the basis of other ionizing backgrounds. Furthermore, the energy distribution of starburst galaxies (Bruzual A. & Charlot 1993) or quasars (Mathews & Ferland 1987) lead to an appropriate description of the absorbers in three and two cases, respectively. All systems modeled with the ionizing radiation of starburst galaxies can be described alternatively with a different radiation background as well. There is a clear tendency for modified HM shapes prevailing at higher redshift ($z > 2$), while at lower redshifts individual sources like AGN and starburst galaxies appear to become more important.

These results imply that the assumption of a uniform intergalactic ionization background with a shape according to Haardt & Madau (2001) to investigate the metallicity of the IGM is at least problematic. A comparison between the derived carbon abundance using the preferred radiation field to that derived from the standard HM energy distribution reveals that assuming the HM background, the metallicity would be overestimated (underestimated), if the real ionizing radiation was softer (harder).

Considering that our sample probes the dense part of the IGM (only two systems reveal column densities of neutral hydrogen with $\log N_{\rm H\,I} < 15.0$), our results support the prediction of Schaye (2004) that radiation from local sources is likely to be important for systems with $N_{\rm H\,I} \gtrsim 10^{15}\,{\rm cm}^{-2}$, even though we find no systematic correlation between the preferred shape of the ionizing background, the H I column density, and the distance to the closest known galaxy.

Investigating the correlation between the metal line systems and galaxies along the line of sight at $z \sim 2$ discovered by Shapley et al. (2005), we find that about half of the considered systems arise in regions hosting groups of galaxies. This is consistent with the result from galaxy-Lyα forest surveys, which find that galaxies and absorption systems trace the same large scale structure (Bowen et al. 2002; Adelberger et al. 2003).

Different shapes of the ionizing radiation for different absorbers imply that the He II/H I ratio should vary when observed at distinct locations. Assuming a spectrum like that of Haardt & Madau (2001) and varying the position of the break, which is actually located at 4 Ryd, leads to values of He II/H I in the range of $140 - 210$. The maximum is reached when the position of the break is ~ 3.6 Ryd. The apparent correlation between the strength of the H I absorption and the column density ratio η in the sense that η is higher in H I voids (Shull et al. 2004; Reimers et al. 2004) cannot be addressed here, since we predominately probe dense gas in the vicinity of galaxies.

The presented analysis illustrates the potential of using metal line absorption systems to trace the shape of the intergalactic UV background using column density ratios. A more sophisticated method would require that the ionizing background can be derived self-consistently from the observed absorption features of a metal line system. A possible approach introduced by Agafonova et al. (2005) and applied by Reimers et al. (2005c, their appendix A), which parameterizes an initial shape of the background, e.g. that of Haardt & Madau (2001), and fits the parameters in the course of the analysis using a response function. Regarding the multitude of ions of elements like sulphur, oxygen, or neon with observable transitions in the spectral range covered by the STIS data, we emphasize the potential of high quality UV spectra, which would make it possible to obtain further constraints on the models. High resolution, high signal-to-noise UV data of quasars with numerous metal line systems in the optical would probably detect many intrinsic EUV transitions as well, as the example of HS 1700+6416 shows. Ratios of different ions from one element, for example S II – S VI, would make the investigation more independent of the metallicity and possible deviations from the solar abundance pattern, which would help to estimate the shape of the ionizing background at the location of the absorber.

The derived photoionization models are used to compute the expected appearance of the metal line spectrum (as well as contribution of low redshift H I absorption of higher order Lyman series and He I) in the spectral range covered by FUSE ($1000 - 1180$ Å). In Chapter 5, the predicted lines will be included in the analysis of the He II Lyα forest to avoid pollution of the He II/H I ratio by unrecognized metal line absorption.

5. The He II Lyα forest towards HS 1700+6416

The shape and the strength of the intergalactic UV background plays an important role in governing the evolution of the ionization state of the intergalactic medium (IGM). Since the IGM is observed to be highly ionized, ionization corrections have to be applied to measure properties of interest like its metallicity. The strength of the UV background, at least at the H I ionization edge, can be derived from the proximity effect (e.g. Scott et al. 2000), whereas more information is needed to constrain the shape of the ionizing radiation field. Agafonova et al. (2005) introduced a method to estimate the shape of the ionizing background from the observation of metal line absorbers.

Theoretical calculations model the shape of the UV background as the radiation of sources attenuated while propagating though the IGM. Quasars have been adopted as main sources (Haardt & Madau 1996; Fardal et al. 1998) whose radiation has been filtered by the IGM. Since hydrogen and helium are the most abundant elements in the IGM, the resulting shape of the mean UV background is characterized by a sharp break at 1 Ryd and another break at 4 Ryd.

Observational results, however, suggest that the intergalactic UV background is dominated not only by the filtered radiation of quasars but also by a significant contribution from the softer radiation of galaxies. This evidence comes from the study of the H I opacity (e.g. Kirkman et al. 2005) or the number density evolution of H I absorbers (e.g. Zhang et al. 1997; Bianchi et al. 2001), and also the derivation of reasonable metallicities from observed metal line absorption requires softer radiation (Aguirre et al. 2004). Recent computations of the UV background therefore consider the contribution of galaxy radiation (e.g. Haardt & Madau 2001). Furthermore, Schaye (2004) and Miralda-Escudé (2005) pointed out that local sources may dominate over the mean background.

Besides H I opacity measurements and the investigation of metal line systems, He II provides another observational probe of the UV background. Comparing the strength of the He II Lyα absorption to that of H I leads to the column density ratio $\eta = N_{\mathrm{He\,II}}/N_{\mathrm{H\,I}}$, which is directly related to the ionizing background at the H I and He II photoionization edge (e.g. Fardal et al. 1998). Low values are expected for hard radiation, while high values should be measured if the ionizing radiation is dominated by soft sources. However, the observation of the He II Lyα transition ($\lambda_{\mathrm{rest}} = 303.7822$ Å) is very difficult. An unabsorbed, UV-bright QSO is needed at redshift $z \gtrsim 2$ to be observable with HST/STIS or FUSE (Picard & Jakobsen 1993). Up to now six of such quasars have been found (Jakobsen et al. 1994; Davidsen et al. 1996; Reimers et al. 1997a; Anderson et al. 1999; Zheng et al. 2004a; Reimers et al. 2005a).

The He II Lyα forest has been resolved for the first time towards the quasar HE 2347-4342 with FUSE (Kriss et al. 2001; Shull et al. 2004; Zheng et al. 2004b). Different analysis methods have been applied to derive the column density ratio (line profile fitting was used by Kriss et al. (2001) and Zheng et al. (2004b), while Shull et al. (2004) applied an apparent optical depth method) and lead to the same results: The UV background is highly variable on small scales with a fluctuation of the column density ratio between $1 \lesssim \eta \lesssim 1000$ or even more. Additionally, Shull et al. (2004) find an apparent correlation between the η value and the strength of the H I absorption in the sense, that η appears to be larger in voids.

In this Chapter we present FUSE observations of the quasar HS 1700+6416, which provides the second line of sight with a resolved He II Lyα forest. Owing to the variability of the UV flux of this QSO (Reimers et al. 2005b), the data is of comparable quality to those of HE 2347-4342 ($S/N \sim 5$, $R \approx 20\,000$). The emission line redshift of HS 1700+6416 is $z_{\mathrm{em}} = 2.72$, i.e. this line of sight probes the post-reionization universe, while in the spectrum of HE 2347-4342 the end of the He II reionization phase has been detected (Reimers et al. 1997a). HS 1700+6416 has a rich metal line spectrum in the optical as well as in the UV comprising seven Lyman limit systems (LLS), which has been analyzed by several authors (e.g. Reimers et al. 1992; Vogel & Reimers 1993, 1995; Köhler et al. 1996; Petitjean et al. 1996; Tripp et al. 1997; Simcoe et al. 2002, 2005). Thus, metal line absorption features are also expected to arise in the far-UV polluting the Lyα forest absorption. Therefore, we will include a model of the metal line absorption in the analysis to obtain unbiased results. For this purpose, we derived a prediction of the metal line spectrum in the far-UV (Chapter 4), which we will consider in this work.

This Chapter is organized as follows: After presenting the observations in Section 5.1 and describing the extrapolation of the continuum for the FUSE spectral range in Section 5.2, we present the far-UV metal line prediction derived in Chapter 4 in Section 5.3 and give a comparison to the data. In Section 5.4 we discuss our artificial data and analyze them using the line profile-fitting procedure and the apparent optical depth method to investigate the applicability of these methods. The results derived from the observed data are presented and discussed in Section 5.5. We conclude in Section 5.6.

Table 5.1: Log of FUSE Observations of HS 1700+6416.

Observation ID	Date	$t_{\rm total}$ (s)	$t_{\rm night}$ (s)
P1100401	1999 Oct 14	57 038	23 275
C1230101	2002 May 15	54 710	17 702
C1230102	2002 May 16	53 821	15 663
C1230103	2003 Feb 27	156 963	93 828
C1230104	2003 Mar 03	130 605	51 584

5.1. Observations

The Far Ultraviolet Spectroscopic Explorer (FUSE) uses four independent optical channels to enable high-resolution spectroscopy in the far-ultraviolet wavelength range below 1200 Å. In each channel a primary mirror gathers light for a Rowland-circle spectrograph. Two-dimensional photon-counting detectors record the dispersed spectra. Two of the optical channels use LiF coatings on the optics to cover the 990 – 1187 Å wavelength range. The other two channels cover shorter wavelengths down to 912 Å using SiC-coated optics. Moos et al. (2000) give a full description of FUSE, and Sahnow et al. (2000) summarize its in-flight performance.

We observed HS 1700+6416 with FUSE through the 30″-square low-resolution apertures (LWRS) during three epochs – October 1999, May 2002, and February/March 2003. Table 5.1 gives details of the individual observations. Between the exposures in 2002 and 2003 the UV brightness of HS 1700+6416 increased by a factor ∼ 3 (see Reimers et al. 2005b). Therefore, the final data are of better quality than we originally expected. The total exposure time is roughly 453 137 s with 202 052 s during orbital night.

We use the FUSE calibration pipeline CALFUSE V2.2.1 to process the data. The earliest versions of the calibration pipeline are described by Sahnow et al. (2000). CALFUSE V2.2.1 is described in detail on the FUSE web site (http://fuse.pha.jhu.edu/analysis/pipeline_reference.html). The major improvements to the pipeline since the description of Sahnow et al. (2000) that are relevant for our work are that data screening for bursts has been automated, and that a two-dimensional, multicomponent model for the background has been implemented. The background model takes into account the uniform (but time-varying) particle background in the detector as well as the spatially varying and time-varying portions of the background due to scattered light within the instrument.

Since we are working at the very limits of instrument sensitivity, we take additional non-standard steps in our processing to reduce the background. We restrict the data to orbital night only (scattered light is ten times brighter during orbital day), and we select only detector events with pulse heights in the range 4 – 16. This reduces the background by an additional factor of two while still retaining photometric accuracy in the final result. Finally, since the instrument throughput is roughly a factor of three higher in the LiF channels compared to the SiC channels, we only use data from the LiF channels. The final spectrum therefore only covers the wavelength range 1000−1180 Å, with a gap at 1080−1086 Å due to the detector layout.

Each observation interval listed in Table 5.1 is processed separately. To assure the best spectral resolution and an accurate wavelength scale, we cross-correlate the overlapping wavelength regions of each extracted spectrum with each other. No wavelength shifts were identified that exceeded our final bin size of 0.05Å. The extracted spectra from each detector segment and exposure are then merged onto a uniform wavelength scale in 0.05Å bins. To maximize the resulting signal-to-noise ratio, each extracted spectrum is weighted by its exposure time, which is the optimal weighting for data with Poisson-distributed errors. The resulting spectrum shown in Fig. 5.1 has $S/N \sim 5$ and a spectral resolution of $R \sim 20\,000$.

In the final merged spectrum we notice some potential problems with the zero flux level, particularly in the data at wavelengths shortward of 1080 Å. Strong, saturated H I absorption is detected at $z \approx 2.315$ and $z \approx 2.433$ arising from LLS at these redshifts. At the corresponding positions in the FUSE spectrum (∼ 1007 Å and ∼ 1043 Å) strong but slightly unsaturated features are detected. Since the column density ratio η should be > 1 because of physical plausibility, these features actually have to be saturated. However, the troughs of these presumably saturated lines are consistent with zero flux within the errors of our $S/N \sim 5$ spectrum. We note the systematic errors that may result from this in our future discussion, but note that data at longer wavelengths ($\lambda > 1086$ Å) does not appear to have the same problem. Thus, we are confident we can obtain unbiased results in the range $2.58 < z < 2.72$. Problems with the interpretation of the results due to inaccuracies in the zero flux level in the range $2.29 < z < 2.56$ will be discussed later.

The H I Lyα forest was observed with Keck. We have access to two datasets already published by Songaila (1998) and Simcoe et al. (2002). These two datasets are co-added obtaining a resulting spectrum with a total exposure time of 84 200 s and a signal-to-noise of $S/N \sim 100$ at 4000 Å. The co-added spectrum covers the wavelength range 3680 – 5880 Å with a resolution of $R \sim 38\,500$. The Simcoe data covers wavelengths down to ∼ 3220 Å with less signal-to-noise. We also have used the absorption lines identified in this portion of the spectrum to constrain the metal line system models (see Chapter 4).

5.2. Continuum definition

In order to estimate the continuum in the FUSE portion of the spectrum we use low resolution data taken with HST/STIS in May 2003 simultaneously with the FUSE observations using the gratings G140L and G230L. The spectra cover the wavelength range 1150 – 3200 Å. The continuum is estimated considering galactic extinction, Lyman limit absorption, and the intrinsic spectral energy distribution of the

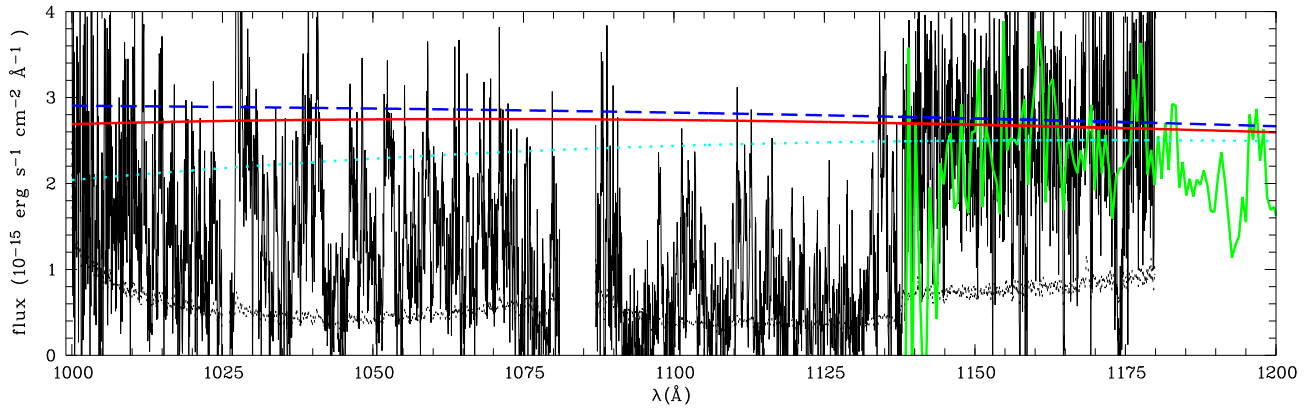

Fig. 5.1: The FUSE data and the extrapolated continuum. The solid line presents the continuum considering the Cardelli et al. (1989) extinction curve and $E(B-V) = 0.025$ (Schlegel et al. 1998). For comparison we show the extrapolated continuum using $E(B-V) = 0.060$ adopted from X-ray observations (Reimers et al. 1995) and the Cardelli et al. (1989, dotted line) or the Pei (1992, dashed line) extinction curve, respectively. Furthermore, we overlay the low resolution STIS data.

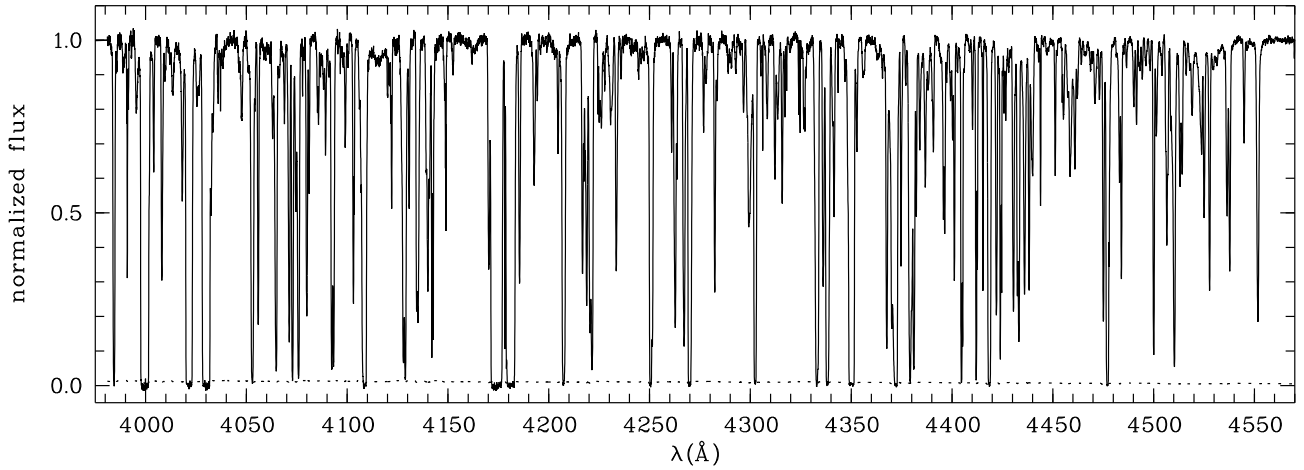

Fig. 5.2: The Keck data in the range $z > 2.27$. The data normalization is performed simultaneously with the estimation of the line parameters in course of the profile-fitting procedure.

QSO. Shortwards of the Lyman limit break the contribution of the optical depth of the LLS decreases due to the ν^{-3} dependence of the hydrogen photoionization cross section. The strength of the break is proportional to the H I column density of the systems (see Møller & Jakobsen 1990), which have been measured by Vogel & Reimers (1995).

The galactic extinction towards HS 1700+6416 is about $E(B-V) = 0.025$ following Schlegel et al. (1998), whose values are based on dust maps created from COBE and IRAS infrared data. X-ray observations of this quasar carried out by Reimers et al. (1995) yield a hydrogen column density of $N_{\rm H\,I} = (2.9 \pm 1.3) \cdot 10^{20}\,{\rm cm}^{-2}$. Following Diplas & Savage (1994), this corresponds to $E(B-V) = 0.06$. Though the latter value is derived from direct observations of this line of sight, it is based on the measurement of H I only, while Schlegel et al. (1998) use a combination of H I and the dust distribution. Therefore, we adopt the value $E(B-V) = 0.025$ from Schlegel et al. (1998).

The corrected flux is fitted with a power law $f_\nu \propto \nu^\alpha$ representing the intrinsic QSO continuum. The best fit succeeds using two power laws with a break at 2000 Å. The best fit yields $\alpha = -1.23$ at $\lambda < 2000$ Å and $\alpha = -1.54$ at $\lambda > 2000$ Å using the extinction curve of Cardelli et al. (1989). Comparing the STIS spectra to the FOS data analyzed by Vogel & Reimers (1995) taken in December 1991 the flux level is the same in the two datasets down to about 2000 Å. For this wavelength range the spectral index is in agreement with that derived from the older data. The continuum rises more steeply with decreasing wavelength in the FOS spectrum. At 1200 Å the flux level of the STIS data is depressed by a factor of about two in comparison to the FOS data. Between the two exposures in the course of the observations with FUSE separated about a year, the quasar flux increased about a factor ~ 3 in the far-UV. This means HS 1700+6416 is highly variable in the intrinsic EUV even on relatively short time scales (Reimers et al. 2005b). Thus, in order to extrapolate a reliable continuum it is very important to have simultaneous STIS and FUSE observations. Fig. 5.1 illustrates that the FUSE and STIS portion of the spectrum taken in 2003 are well matched.

A crucial point in the continuum extrapolation is the choice of the extinction curve especially because of its steep rise in the UV. Adopting the analytic formula of Cardelli et al. (1989) we find a flux level at 1000 Å of $\sim 2.69 \cdot 10^{-15}$ erg s^{-1} cm^{-2} Å^{-1}. Tests with the reddening value derived from the X-ray observations (Reimers et al. 1995) lead to a flux at 1000 Å depressed by $\sim 25\,\%$ (see Fig. 5.1). Adopting the analytical expression of Pei (1992) an the same reddening value leads to a flux level slightly above the original extrapolation. But since the FUSE spectrum is extremely noisy especially in the lower wavelength range, the dominating uncertainties result from the profile fitting. The choice of the flux level affects the results only marginally. The apparent optical depth method is more sensitive to the continuum level. Adopting the normalization according to the lower continuum level given in Fig. 5.1 would lower the η values of individual bins by roughly 0.2 dex near 1000 Å. However, we are confident, that the continuum extrapolation using the Cardelli et al. (1989) extinction curve and the $E(B-V)$ from Schlegel et al. (1998) represents a reasonable approximation of the real continuum.

The continuum in the Keck portion of the spectrum is estimated in the course of the line profile-fitting procedure. The line-fitting program CANDALF developed by R. Baade performs the Doppler profile fit and the continuum normalization simultaneously. Thus, the continuum determination in the Lyα forest is more reliable in comparison to an a priori continuum definition. The normalized Keck spectrum in the wavelength range corresponding to the He II data is shown in Fig. 5.2.

5.3. Metal line absorption

The spectrum of HS 1700+6416 is characterized by a large number of metal line absorption features in the optical spectral range (Petitjean et al. 1996; Tripp et al. 1997; Simcoe et al. 2002, 2005) as well as in the UV (Reimers et al. 1992; Vogel & Reimers 1993, 1995; Köhler et al. 1996). Since a significant contribution of absorption by metals is supposed to be present even in the far-UV, the expected metal lines in the FUSE portion have to be taken into account. Therefore, in Chapter 4 we construct photoionization models of the metal line systems with the main purpose to derive a prediction of the metal line features expected to arise in the FUSE spectral range. In the following the main results of Chapter 4 are summarized and we compare the predicted far-UV metal lines to the FUSE data. For details of the modelling procedure we refer to Chapter 4.

On the basis of the modelled column densities a metal line spectrum for the wavelength range 1000 – 1180 Å covered by FUSE is predicted. These lines (Fig. 4.27) are overlayed on the observed FUSE data in Fig. 5.3. It can be seen, that some rather strong features can be identified as metal lines. Obviously, the prediction is consistent with the data for most of the lines.

In case of the LLS at $z = 0.8643$, however, strong features of oxygen are predicted, but the observed spectrum shows less absorption. In particular, O IV is overestimated, as can be seen at $\sim$ 1032 Å and 1134 Å in Fig. 5.3. The model of this system is based on the Haardt & Madau (2001, HM) UV background. However, the spectral energy distribution of a starburst galaxy adopted from Bruzual A. & Charlot (1993, SB) leads to a reasonable model as well (Chapter 4). Therefore, another prediction is computed considering the results from the SB model for the $z = 0.8643$ system. The resulting metal line spectrum is also shown in Fig. 5.3. The main differences in the predicted lines are a decrease of the neon absorption (Ne III, Ne IV) in case of the SB model, but slightly stronger He I features. The predicted O IV features are consistent with the observed data. However, the strong feature at 1174 Å is mainly due to O V absorption from the $z = 0.8643$ system according to the HM model, while no O V absorption at all is predicted by the SB model. We find no alternative identification for this strong feature either proposed by the metal line system models or as part of the Lyman series of a strong, metal-free, low redshift system. Furthermore, no interstellar absorption line is expected at this wavelength. We conclude that the energy distribution of a starburst galaxy does not provide an optimum model of the $z = 0.8643$ system. Improvement of the photoionization model by adopting a different ionizing background is difficult since only a few transitions are observed in the optical. The vast majority of lines constraining the model are located in the UV, where the data suffers from low S/N. When we analyze the He II Lyα forest taking into account the metal line prediction, we will reconsider the lines of the $z = 0.8643$ systems with different strengths dependent on the adopted model (especially those of Ne IV and Ne V) and discuss possible effects on the results.

Absorption from galactic molecular hydrogen is expected

Table 5.2: Transitions of galactic H_2, that are observed unblended in the FUSE spectrum. The atomic data (rest wavelength λ_0 and oscillator strength f) are adopted from Abgrall et al. (1993a,b). The column density is estimated assuming $b = 5.0\,\mathrm{km\,s^{-1}}$ and $v = -45.7\,\mathrm{km\,s^{-1}}$.

transition	λ_0 (Å)	f	$\log N$
L (3 – 0) R (0)	1062.882	0.0178	16.00 ± 0.87
L (8 – 0) R (1)	1002.453	0.0183	17.83 ± 0.25
L (3 – 0) R (1)	1063.460	0.0119	
W (0 – 0) R (2)	1009.023	0.0156	14.72 ± 0.30
W (0 – 0) Q (2)	1010.938	0.0245	
W (0 – 0) P (2)	1012.170	0.0055	
L (7 – 0) R (2)	1014.977	0.0190	
L (7 – 0) P (2)	1016.458	0.0102	
L (6 – 0) P (2)	1028.106	0.0105	
L (5 – 0) R (2)	1038.686	0.0165	
L (4 – 0) P (2)	1053.283	0.0090	
L (8 – 0) R (3)	1006.413	0.0158	15.49 ± 0.30
W (0 – 0) R (3)	1010.129	0.0138	
L (6 – 0) R (3)	1028.983	0.0173	
L (5 – 0) R (3)	1041.157	0.0159	

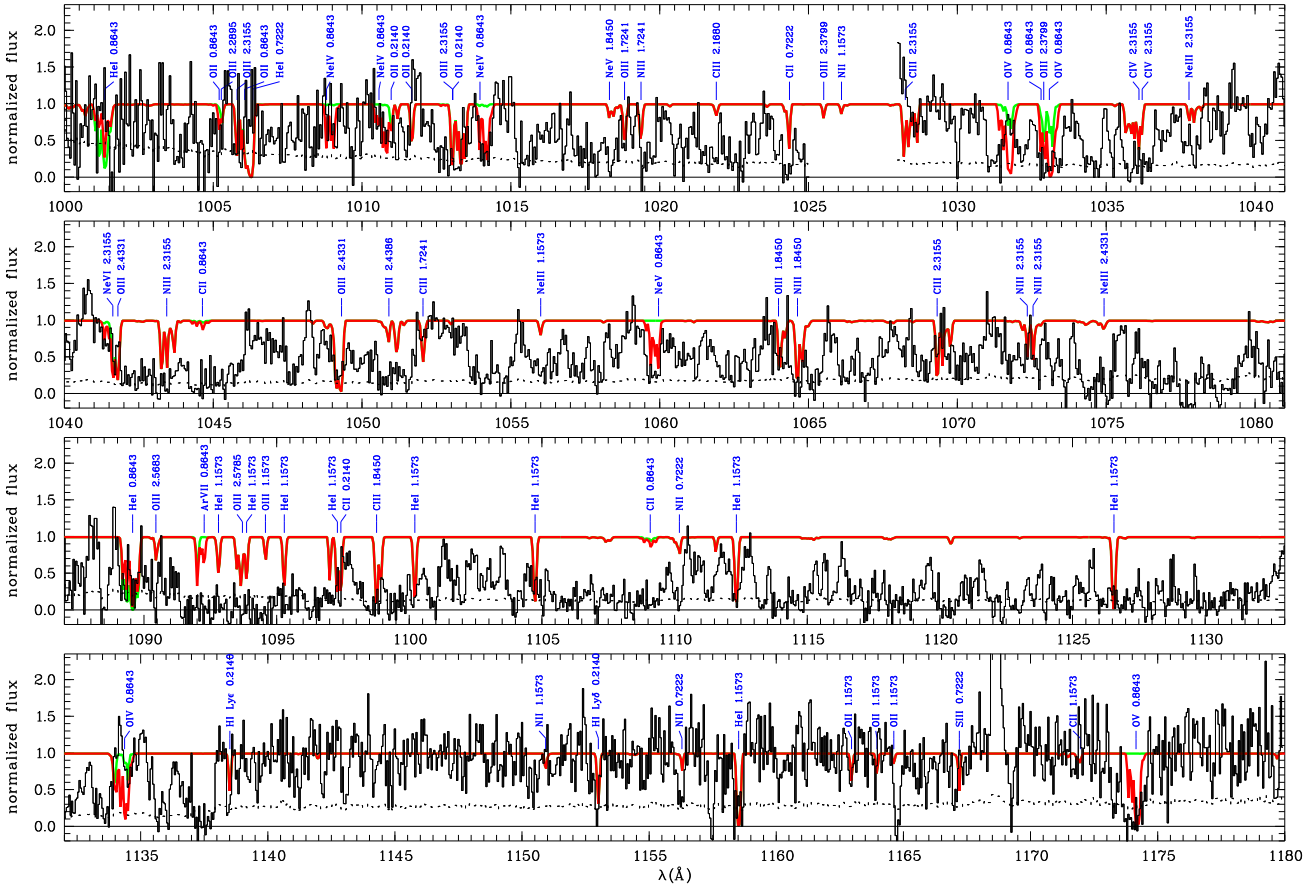

Fig. 5.3: Predicted metal line spectrum in comparison to the data. The predicted features are identified given the ion and the redshift of the system where they arise.

to arise additionally in the FUSE spectral range. Templates for the H_2 features with rest wavelengths in the far-UV including Lyman and Werner transitions and a detailed description of how to identify and eliminate them can be found in McCandliss (2003). Since the proposed procedure requires the detection of a sufficient number of undisturbed galactic H_2 features, it is inapplicable to our data. Instead, we proceed as follows: The templates from McCandliss (2003) are used to easily identify H_2 lines, considering that they may be slightly shifted in velocity space. Then, we select unblended features in the FUSE spectrum and fit them with Doppler profiles to estimate the line parameters. The selected transitions and the fitted line parameters are given in Table 5.2. All considered rotational transitions (ground state to $J'' = 0, 1, 2, 3$) can be modelled with a Doppler parameter $b = 5.0$ at a velocity $v = -45.7\,\mathrm{km\,s^{-1}}$. The derived column densities for every J'' are also listed in Table 5.2. Because of the few observed unblended lines and the poor data quality, the column densities, especially those of the lower rotational transitions, are very uncertain. Nevertheless, the derived values are roughly consistent with the column densities derived by Richter et al. (2001, 2003) for high- and intermediate-velocity clouds, respectively, towards extragalactic sources. In the final step, all transitions within the observed spectral range with $J'' = 0, 1, 2, 3$ are included into our model.

In the following we treat the H_2 model like the predicted metal absorption lines. Unless explicitly noted we refer to the predicted metal line absorption as well as galactic H_2 when talking about metal lines. Using either the profile-fitting procedure or the apparent optical depth method all additional lines are considered in the analysis of the He II Lyα forest. Besides the metal lines also the interstellar lines C II λ1036 and Ar I $\lambda\lambda$1048, 1067 are included.

The importance of metal line absorption in the FUSE spectral range is illustrated in Fig. 5.4. The upper panel shows the redshift distribution of η estimated by fitting Doppler profiles to the H I and He II Lyα forest ignoring metal line absorption (for details of the analysis procedure see Section 5.4.1), while metal line features have been considered in the lower panel. Lower limits indicate He II absorbers without detected H I counterpart. About 30 % of the apparent He II features have no H I counterpart when metal line absorption is ignored. The consideration of metal lines reduces the number of lower limits significantly, since several absorption features can be identified as metal lines. In this case only 23 % additional He II lines are needed. Data points that have been biased by metal line absorption, are marked in the lower panel of Fig. 5.4. In total roughly 25 % of the measured values are affected. For 16 % of the data points, η changes by more than $\Delta \log \eta = 0.01$ when extra

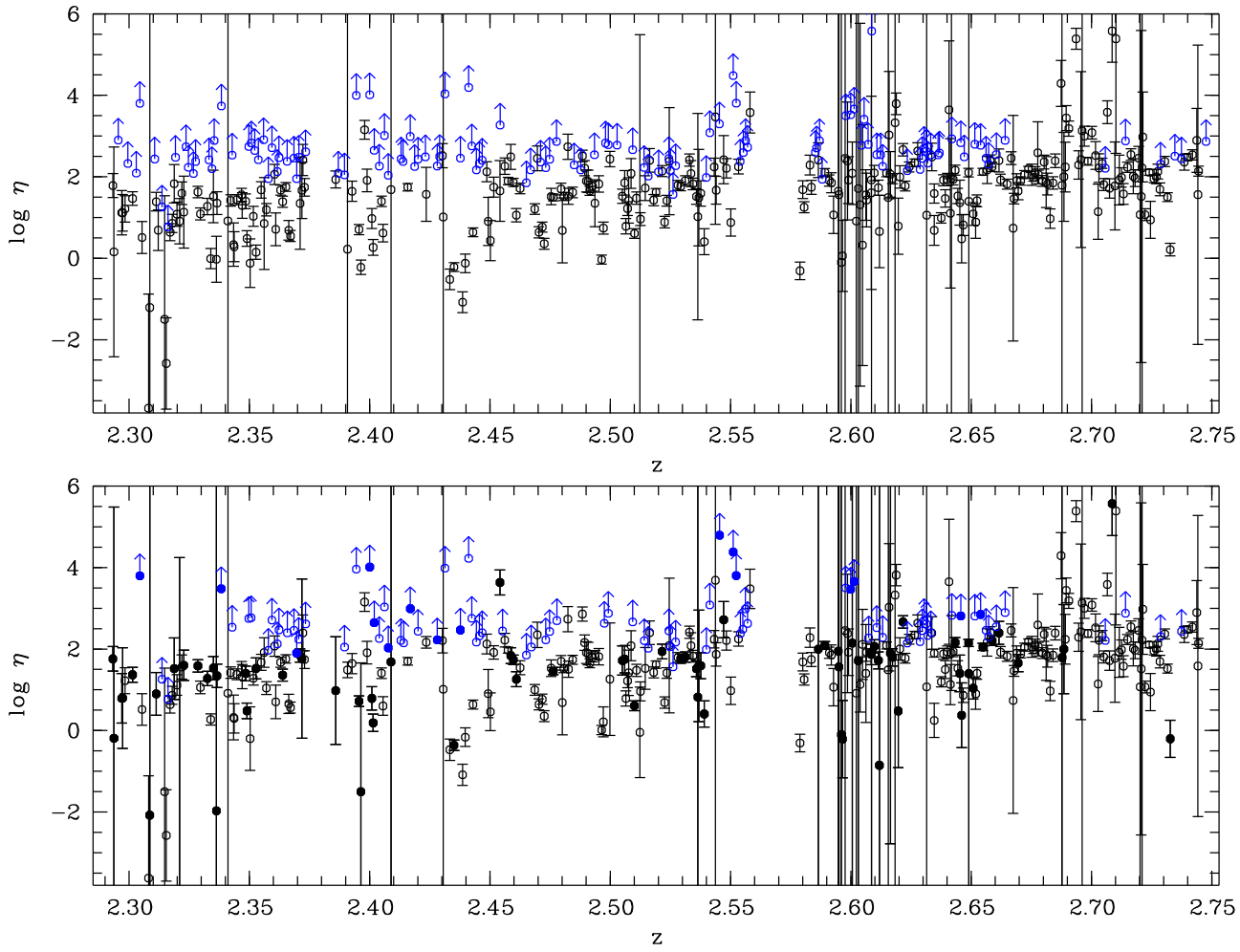

Fig. 5.4: Comparison of the $\eta(z)$ distribution ignoring metal line and galactic H_2 absorption (upper panel) and taking them into account (lower panel). Absorbers affected by extra absorption are marked as filled circles. Lower limits are based on He II features without detected H I counterparts. Their Doppler parameters are chosen to be $b = 27.0\,\mathrm{km\,s^{-1}}$.

absorption is taken into account. Considering only features of galactic H_2, about 6 % of the data points would have been biased, i.e. the major contribution comes from the predicted metal line absorption. There are no indications of unusually high column density ratios at the position of metal lines arising from the $z = 0.8643$ system.

The median column density ratio decreases from $\log \eta = 2.01$ if metal lines are neglected to 1.93 if they are taken into account. Consequently, the consideration of metal line absorption has no severe influence on the general statistical properties of the η distribution. The column density ratio of a single absorber, however, can be distorted up to an order of magnitude.

5.4. Simulations

Two different methods have been used so far to analyze the data of the He II Lyα forest towards HE 2347-4342. Kriss et al. (2001) and Zheng et al. (2004b) fit line profiles to the observed absorption features. The use of profile fits assumes the absorption features to arise from discrete clouds in the IGM, which is certainly an oversimplification. The alternative method measuring the apparent optical depth was also applied to the HE 2347-4342 data (Shull et al. 2004). In this case the column density ratio η is estimated by the ratio of the He II and H I optical depth per redshift or velocity bin. Since η is defined per bin, the assumption of discrete absorbers can be dropped in favour of a continuous medium, where the features are due to density fluctuations. A third approach fitting the optical H I Lyα forest directly to the UV spectrum in order to derive η is introduced in Chapter 6.

In order to study possible effects of the analysis method on the results we create artificial datasets. By evaluating the artificial spectra we investigate how the results are influenced by the applied method. For both methods we recognize problems which prevent the accurate reconstruction of the presumed η value. In the following we briefly summarize the methodical procedures, then describe the generation of the artificial data, and discuss the implications of the profile-fitting procedure and the difficulties using the apparent optical depth method.

5.4.1. Methods

In preparation of the profile fit of the He II spectrum, we first identify all H I Lyα features in the optical data and estimate their parameters by fitting Doppler profiles. In the case of strongly saturated Lyα lines higher orders of the Lyman series up to Lyϵ are considered as well to derive the parameters. Then, the He II Lyα forest is fitted fixing the redshift and the Doppler parameter derived from the corresponding hydrogen lines. The latter constraint implies, that we assume pure turbulent broadening. Zheng et al. (2004b) made the attempt to derive the dominant broadening mechanism from the HE 2347-4342 data fitting unblended He II features with a free b-parameter. They found a velocity ratio $\xi = b_{\rm He}/b_{\rm H}$ close to 1.0, suggesting turbulent broadening to be dominant. However, in Chapter 6 we demonstrate, that thermal broadening is important for part of the absorbers and can lead systematically to lower η values for high density H I absorbers.

The procedure of the apparent optical depth method applied to He II Lyα forest data as described by Shull et al. (2004) will be summarized briefly: The column density ratio is replaced by $\eta = 4 \cdot \tau_{\rm He\,II}/\tau_{\rm H\,I}$ (Miralda-Escudé 1993, more exactly the factor 4 represents the ratio of the rest wavelengths $\lambda_{0,\rm H\,I}/\lambda_{0,\rm He\,II} = 1215.6701/303.7822$), where the optical depths $\tau = -\ln F$ are measured per bin. In order to obtain physically reasonable values, bins with normalized fluxes F above unity are masked out as well as bins with flux values below zero. Additionally, bins with flux values within $1\,\sigma$ from unity or zero are not considered, since they cannot be distinguished statistically from the continuum or zero, respectively.

5.4.2. Creating artificial datasets

Based on the statistical properties of the H I Lyα forest as observed towards HS 1700+6416, a sample of lines is generated. The column density distribution function with $\beta = 1.5$ is adopted from Kirkman & Tytler (1997). Values in the range $11.0 \le \log N \le 18.0$ are simulated. Our observed line sample yields $\beta = 1.51 \pm 0.05$ for absorbers with $12.8 \le \log N \le 16.0$. The Doppler parameter distribution is described by a truncated Gaussian

$$\frac{{\rm d}\mathcal{N}(b)}{{\rm d}b} = \begin{cases} A \cdot \exp\left(-\dfrac{(b-b_0)^2}{2\,\sigma_b^2}\right) & b \ge b_{\rm min} \\ 0 & b < b_{\rm min} \end{cases}$$

with $b_0 = 27\,{\rm km\,s^{-1}}$, $\sigma_b = 8.75\,{\rm km\,s^{-1}}$, and $b_{\rm min} = 10\,{\rm km\,s^{-1}}$ as observed towards HS 1700+6416 in good agreement with Hu et al. (1995). In addition, the parameters of the simulated line sample are correlated by $b_{\rm min} = (1.3 \cdot (\log N - 12.5) + 10.5)\,{\rm km\,s^{-1}}$ following Misawa (2002). The artificial spectrum covers the redshift range $2.292 < z < 2.555$, which corresponds to wavelengths shorter than 1080 Å in the FUSE spectrum. No number density evolution is considered along this redshift interval. The minimal distance between two lines is ${\rm d}z = 0.0001$ as observed towards HS 1700+6416. In the given redshift range the separation corresponds to $\sim 20\,{\rm kpc}$. The resolution of $R = 40\,000$ and the signal-to-noise ratio of $S/N \sim 100$ are chosen to match the characteristics of high-resolution spectra taken with VLT/UVES or Keck/HIRES.

The He II Lyα forest is computed based on the artificial H I lines using $\eta = 80$, the mean value found by Kriss et al. (2001). Considering a temperature of 10^4 K the He II Doppler parameter is computed as

$$b_{\rm He\,II} = \sqrt{b_{\rm H\,I}^2 - 2kT\left(\frac{1}{m_{\rm H}} - \frac{1}{m_{\rm He}}\right)}. \qquad (5.1)$$

The assumed temperature is cooler than the average $2 \cdot 10^4$ K measured by Ricotti et al. (2000), but consistent with $b_{\rm min,\,H\,I} = 10\,{\rm km\,s^{-1}}$. Test calculations with higher temperatures indicate no difference in the results. Since the IGM is expected to have a distinctive temperature distribution, a constant temperature model is certainly an oversimplification, but serves to get an impression of the possible effects assuming pure turbulent broadening. For comparison we compute as well a He II dataset with $b_{\rm He\,II} = b_{\rm H\,I}$. The resolution of $R = 15\,000$ and the signal-to-noise ratio of $S/N \sim 5$ are chosen to match the typical values of real FUSE data.

Since the artificial spectra are generated from statistical assumptions alone, they provide only a simple approach to investigate the applicability of the methods. More realistic spectra based on hydrodynamical simulations are presented by Bolton et al. (2005). They find that the column density ratio can be estimated confidently by a line profile-fitting procedure (but see discussion below and in Chapter 6). Furthermore, their simulations permit the investigation of different UV backgrounds, whereas the simple statistical approach introduced here can provide only limited information about basic problems of the analysis procedures.

5.4.3. Profile fitting analysis

Having analyzed the artificial H I Lyα forest by fitting Doppler profiles, the statistical properties of the sample are recovered. Under the simulated conditions our sample is complete down to $\log N \sim 12.0$. Due to blending effects, the deduced Doppler parameter distribution is broadened by 28 %. The He II Lyα forest lines are treated the same way, using the derived H I parameters, with fixed line redshifts and b-parameters. Features with Doppler parameters $b < 10\,{\rm km\,s^{-1}}$ are not considered. The resulting η values are shown in Fig. 5.5. Both the combined thermal and turbulent as well as the pure turbulent broadened sample show a scatter in η of about 0.5 dex. Generally, the line sample that contains thermal broadening has more low η values. We find a statistical mean of $\log \eta_{\rm therm} = 1.77 \pm 0.43$ in comparison to $\log \eta_{\rm turb} = 1.86 \pm 0.37$ in the pure turbulent case, both still consistent with the presumed value of 1.90309. The median, which gives less weight to outliers, is $\log \eta_{\rm therm} = 1.86$ and $\log \eta_{\rm turb} = 1.90$, respectively.

There are various reasons for outliers lying outside the range $\log \eta = 1.903 \pm 0.500$. Both models show only about

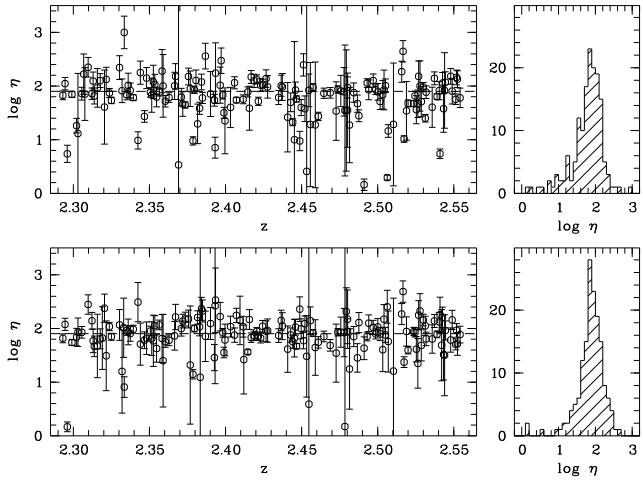

Fig. 5.5: Distributions of the column density ratio η derived from the artificial data with a Doppler parameter consisting of a thermal and a turbulent part (upper panel) or a pure turbulent b-parameter (lower panel) applying a profile-fitting procedure. The dashed line indicates the presumed value $\eta = 80$. In the course of the analysis pure turbulent broadening is assumed in both cases.

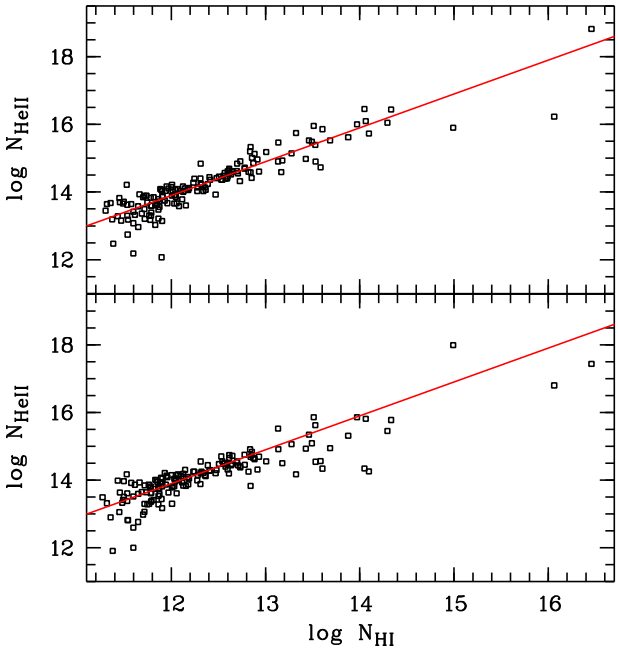

Fig. 5.6: Recovered He II column densities versus H I column densities in the pure turbulent case (upper panel) and for combined thermal and turbulent broadening (lower panel). The solid line represents the underlying correlation $\eta = 80$. For clarity, measurement errors are not plotted.

3 % high values caused by line saturation and blending effects, which can, in principle, produce low as well high η values. In the sample with pure turbulent broadening we find 8 % low η values while the thermal and turbulent broadened sample shows 14 % low values. Besides saturation and blending, the uncertainties of the parameters of weak H I lines resulting in large error bars are a primary reason. In the case of combined thermal and turbulent broadening some He II lines are narrower than the adopted pure turbulent b-parameter of H I. This effect produces about 25 % of the low values. Therefore, if the widths of intergalactic absorbers are not completely dominated by turbulent mechanisms, low η values can be caused by the assumption of pure turbulent broadening (see also Chapter 6).

In order to find a strategy for avoiding artificial scatter in the η distribution, we directly examine the correlation between H I and He II column density as presented in Fig. 5.6. The correlation fits well except for very low column densities ($\log N_{\rm H\,I} < 12.0$) where noise makes it difficult to derived accurate line parameters, and also for high column densities, where saturation of hydrogen lines plays a role (features are saturated when $\log N_{\rm H\,I} \gtrsim 14.5$ for $b \approx 27\,{\rm km\,s^{-1}}$). Since the redshift and Doppler parameter of the helium lines are fixed during the fitting procedure, the column densities are derived correctly if the underlying assumptions are correct. In the case of combined thermal and turbulent broadening the He II column densities are significantly underestimated for $\log N_{\rm H\,I} \gtrsim 13.0$, caused by the assumption of pure turbulent broadening. In Chapter 6 we argue that the incorrect assumption of pure turbulent broadening affects only lines above this H I column density. Thus, a stringent criterion to define a reasonable subsample would be $12.0 \leq \log N_{\rm H\,I} \leq 13.0$. Assuming pure turbulent broadening as a good approximation, $12.0 \leq \log N_{\rm H\,I} \leq 14.5$ provides a less stringent constraint.

Bolton et al. (2005) find a distribution similar to that shown in the lower panel of Fig. 5.6. Their lines samples contain only absorber with $\log N_{\rm H\,I} > 12.0$ and show enhanced scatter for $\log N_{\rm H\,I} > 13.0$ even in the case of a uniform UV background. Since they assumed turbulent broadening as well, the scatter most likely indicates the effect of thermal line widths. However, Bolton et al. (2005) neither discuss the origin of the scatter nor the possible implications of the assumption of pure turbulent broadened lines.

Applying the criteria derived above to the simulated datasets we find the statistical means $\log \eta_{\rm therm} = 1.85 \pm 0.21$ and $\log \eta_{\rm turb} = 1.92 \pm 0.21$ for the more stringent constraint ($12.0 \leq \log N_{\rm H\,I} \leq 13.0$). In the pure turbulent case, the underlying η value is recovered well, while it is still underestimated when thermal broadening plays a role. For both samples the statistical $1\,\sigma$ error has been reduced by a factor ~ 2 in comparison to the total sample. Considering the sample $12.0 \leq \log N_{\rm H\,I} \leq 14.5$ yields $\log \eta_{\rm therm} = 1.74 \pm 0.39$ and $\log \eta_{\rm turb} = 1.92 \pm 0.25$, respectively. Here, the underestimation of η for the data including thermal broadening gets worse and the scatter increases, while the mean value and $1\,\sigma$ error for the pure turbulent data do not change significantly.

5.4.4. Apparent optical depth method

The same artificial datasets are analyzed applying the apparent optical depth method. The resulting distribution for a

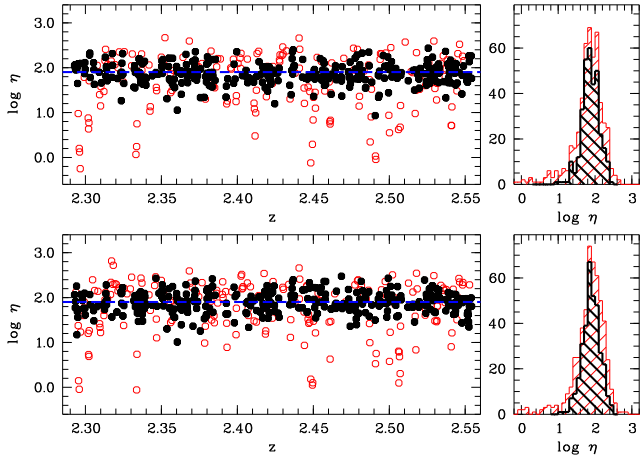

Fig. 5.7: Distributions of the column density ratio η derived from the artificial data with a Doppler parameter consisting of a thermal and a turbulent part (upper panel) or a pure turbulent b-parameter (lower panel) using the apparent optical depth method. The dashed line indicates the presumed value $\eta = 80$. The bin size is 20 km s^{-1}, corresponding to $\sim$ 0.05 Å in He II. Bins with $-2.0 \leq \log \tau_{\rm H\,I} \leq -1.0$ (see text) are denoted as filled circles, all others as open circles. The corresponding distributions are indicated as histograms in the right panels.

bin size of $\Delta v = 20\,\mathrm{km\,s^{-1}}$, corresponding to 0.05 Å in He II wavelengths, is shown in Fig. 5.7. This method leads to a scatter in η of about 0.5 dex for both models as well. The high values are statistically negligible, since they are only about 3 % for each sample. Again we find slightly more low η values when thermal broadening is present (roughly 13 % in comparison to 10 % in the case of pure turbulent broadening). This is plausible, since the He II optical depth in the wings of a thermally broadened, and therefore narrower feature is systematically lower than in the case of pure turbulence. In both models the underlying η is underestimated. We find the mean values $\log \eta_{\rm therm} = 1.80 \pm 0.44$ and $\log \eta_{\rm turb} = 1.84 \pm 0.41$. With increased bin size the mean values get even lower ($\log \eta_{\rm therm} = 1.75 \pm 0.39$ and $\log \eta_{\rm turb} = 1.77 \pm 0.38$ for $\Delta v = 60\,\mathrm{km\,s^{-1}}$, corresponding to a bin size of 0.20 Å in He II). Also the median underestimates the real η in the combined broadening case because of the excess of low values, even though this effect is smaller. We find $\log \eta_{\rm therm} = 1.88$ and $\log \eta_{\rm turb} = 1.90$ (bin size 20 km s^{-1}), in comparison to $\log \eta_{\rm therm} = 1.81$ and $\log \eta_{\rm turb} = 1.83$ with 60 km s^{-1} bin size.

The correlation between low H I optical depth, referred to as voids, and high η values as found by Shull et al. (2004) can also be seen in the simulated data even though it is not present in the underlying spectra. For further investigation of this point it is instructive to regard η as the correlation between $\tau_{\rm H\,I}$ and $\tau_{\rm He\,II}$. This is shown in Fig. 5.8 in the pure turbulent case for different signal-to-noise ratios of the He II data (100, 10, and 5, while $S/N = 100$ is constant for the H I spectra) and an example without any noise.

At the given S/N of the H I spectrum (= 100), optical depths down to $\log \tau_{\rm H\,I} > -2.0$ can be measured reliably, at

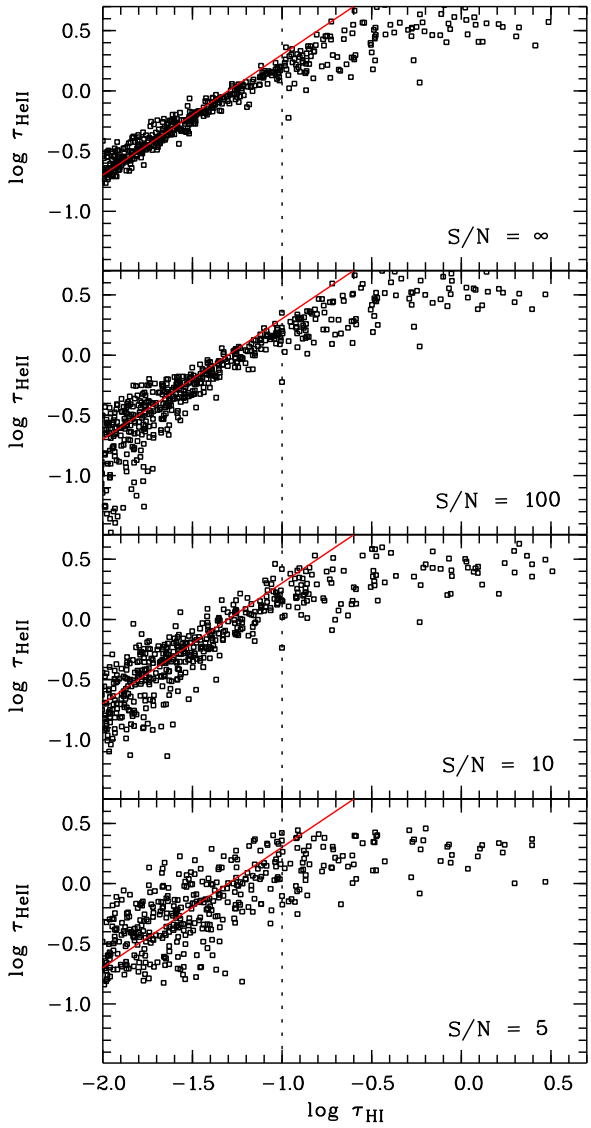

Fig. 5.8: The He II optical depth versus H I optical depth for simulated data with pure turbulent broadening. The specific signal-to-noise of the artificial helium dataset is given in each panel. The signal-to-noise ratio of the hydrogen spectrum is $S/N = 100$. The upper panel is based on artificial datasets with no noise at all. The resolution of the simulated spectra are $R_{\rm H\,I} = 40\,000$ and $R_{\rm He\,II} = 15\,000$, respectively. Each point represents a bin of 20 km s^{-1}. The solid lines indicate $\eta = 80$.

least in principle. If only bins detached by more than $2\,\sigma$ from unity are considered, the limit is $\log \tau_{\rm H\,I} > -1.7$. The scatter at low optical depths (e.g. for $\log \tau_{\rm H\,I} \lesssim -1.7$ in the case of $S/N = 100$ for H I as well as He II) is to due the noise. In order to avoid a contamination by noise-affected bins, the constraints defining the subsample should be chosen carefully. As can be seen from Fig. 5.8, the detection limit of the He II optical depth depends on the signal-to-noise, of course. In case of $S/N = 5$ the restriction is $\log \tau_{\rm He\,II} > -0.65$, or $\log \tau_{\rm He\,II} > -0.3$ for the $2\,\sigma$ constraint.

Even the analysis of the spectra without noise leads to

scatter around the underlying relation. Furthermore, bins with an optical depth above $\log \tau_{\rm H\,I} > -1.0$ (indicated by the vertical, dotted line in Fig. 5.8) yield He II optical depths clearly beneath the expected values. This flattening is due to line saturation, since saturated absorption features become broader and more smeared out at finite resolution. The difference in the profile does not only affect the saturated core but as well the wings of the line. Consequently, the flattening starts at relatively low hydrogen optical depths. Thus, a direct comparison of the apparent optical depths above a certain limit is not possible.

Savage & Sembach (1991) give a detailed description of the method and applicability using the apparent optical depth. They emphasize the possibility of finding line saturation in the analysis of line doublets. Hidden saturation can be seen if the apparent column density $N_a(v) \propto \tau_a(v)/f\,\lambda_0$ of a doublet pair differs with respect to the considered component. Since line saturation is important in the whole FUSE spectrum, the apparent optical depth method is not applicable to bins with $\tau_{\rm H\,I} > 0.1$ if the underlying η is roughly 80. Adopting a $1\,\sigma$ detection limit of $\tau_{\rm H\,I} > 0.01$ there is 1 dex of hydrogen optical depth left, allowing the apparent optical depth to be applied reasonably.

Fox et al. (2005) investigated the effect of noise on the apparent column density. They found that the apparent optical depth method will likely overestimate the true column density when applied to data with low S/N. Since the FUSE spectra are very noisy ($S/N \approx 5$), the results obtained by an apparent optical depth method have to be considered carefully.

The bins selected by $-2.0 \leq \log \tau_{\rm H\,I} \leq -1.0$ are marked in Fig. 5.7 and the overlay in the right panels shows their η distribution. Both the samples (pure turbulent and combined line widths) contain virtually no low η values and the fraction of high values is below 5 % in each case. As expected, the mean values approach the underlying η and the scatter decreases. We find $\log \eta_{\rm therm} = 1.88 \pm 0.24$ and $\log \eta_{\rm turb} = 1.90 \pm 0.24$, respectively, with a bin size of $20\,{\rm km\,s^{-1}}$. Fitting a Gaussian $A \cdot \exp(-(\log \eta - \log \eta_0)^2/2\,\sigma^2)$ to the $\log \eta$ distribution of the subsample leads to $\log \eta_0 = 1.90 \pm 0.01$ and $\sigma = 0.237 \pm 0.009$ in the case of pure turbulence. In the case of combined thermal and turbulent broadening we find $\log \eta_0 = 1.89 \pm 0.16$ and $\sigma = 0.213 \pm 0.012$. In comparison to the mean value of the sample without any noise, which is 1.89 ± 0.07 in the pure turbulent case, these values demonstrate that the scatter in the η distribution is mainly due to the noise level of the data. With the present FUSE data ($S/N \sim 5$) an η distribution with a scatter of roughly 13 % can be expected following the simulations.

5.4.5. Comparing profile fitting and apparent optical depth

The investigation of artificial spectra by fitting Doppler profiles or applying the apparent optical depth method exhibits differences of the robustness and applicability of the diagnostics. Concerning the apparent optical depth, line saturation in combination with the detection limit given by the noise leads to a relatively small interval of 1 dex in the hydrogen optical depth ($0.01 \leq \tau_{\rm H\,I} \leq 0.1$), where the method can be applied reliably. Besides limited resolution noise is the most crucial limitation, since measuring the apparent optical depth per velocity bin is directly sensitive to the noise level, while the impact of the assumption of pure turbulent line width is less significant (the deviation is roughly 1 %).

Since position and line width are fixed, noise has less influence using the standard profile-fitting method. Therefore, even saturation is less problematic. Hydrogen starts to be saturated at column densities $\log N_{\rm H\,I} \gtrsim 14.5$ and normally higher order Lyman series lines can be used to estimate the H I line parameters accurately in case of strong saturation. Thus, even saturated He II features may be evaluated reasonably. However, in the crowded Lyα forest the number of components may be ambiguous leading to larger uncertainties. Another point is, in analyzing the simulated data, we know that the correct profile function is applied since the datasets are created using it. When dealing with real data, the observed features can be described only approximately.

A sample restricted to lines that can be clearly identified and are insensitive to effects of thermal broadening is expected to yield the most reliable results. The selected lines have to be strong enough to be fitted unambiguously but are below the sensitivity limit for thermal line widths ($12.0 \leq \log N_{\rm H\,I} \leq 14.5$ or even less), since a line sample under the simplistic assumption of pure turbulent broadening will underestimate the true η values. According to the results of Chapter 6 features with $\log N_{\rm H\,I} \lesssim 13.0$ remain unaffected by effects of thermal broadening. Therefore a more stringent selection would be $12.0 \leq \log N_{\rm H\,I} \leq 13.0$.

Table 5.3 lists the recovered η values and their statistical $1\,\sigma$ errors using either the profile fitting or the apparent optical depth method. The median reproduces the underlying value of $\log \eta = 1.903$ within an accuracy of more than 93 % in all cases. The statistical mean underestimates the

Table 5.3: The η values recovered from the simulated data using the profile fitting or apparent optical depth method, respectively. The input value is 80, i.e. $\log \eta = 1.90309$. The first columns show the values for the profile-fitting analysis constraining the sample to $12.0 \leq \log N_{\rm H\,I} \leq 13.0$ (selected) and without any restriction (unselected). The columns at the right hand side give the results obtained with the apparent optical depth method (binning $20\,{\rm km\,s^{-1}}$) with $-2.0 \leq \log \tau_{\rm H\,I} \leq -1.0$ (selected) and for the total sample (unselected).

		profile fitting		apparent optical depth	
		$\langle \log \eta \rangle$	median	$\langle \log \eta \rangle$	median
turbulent	selected	1.92 ± 0.21	1.92	1.90 ± 0.24	1.89
	unselected	1.86 ± 0.37	1.90	1.84 ± 0.41	1.90
thermal	selected	1.85 ± 0.21	1.87	1.88 ± 0.24	1.88
	unselected	1.77 ± 0.43	1.89	1.80 ± 0.44	1.88

column density ratio fitting line profiles, particularly if thermal broadening is present. This is consistent with the results of Bolton et al. (2005), who come to the conclusion that the median gets closer to the underlying value, although they do not discuss possible reasons for this finding. Furthermore, the scatter is reduced by more than 40 % if only the selected subsamples are considered.

Following these results, we expect to find a scatter in $\log \eta$ of roughly 20 % by analyzing the observed spectra without any further selections. Applying the apparent optical depth method to a subsample with $0.01 \leq \tau_{\mathrm{H\,I}} \leq 0.1$ leads to a reduced scatter (13 %). For the profile-fitting procedure the scatter can be reduced as well down to about 11 % if only absorbers with $12.0 \leq \log N_{\mathrm{H\,I}} \leq 13.0$ are selected. This stringent constraint minimizes the effect of systematic underestimation of η if thermal line broadening is present.

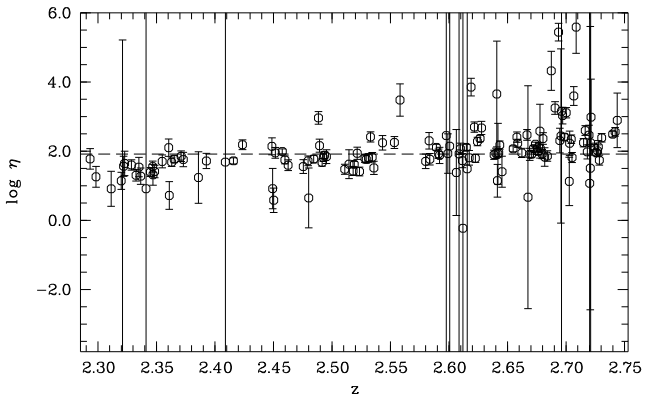

Fig. 5.9: Redshift distribution of the column density ratio η for absorbers with $12.0 \leq \log N_{\mathrm{H\,I}} \leq 13.0$. The dashed line indicates the median value $\log \eta = 1.92$.

5.5. Results and discussion

Having an idea of the advantages and limitations of the analysis methods, we present applications to the observed data and discuss their implications. In contrast to the simulated data, the observed spectra contain additional absorption features of metal lines and galactic molecular hydrogen absorption bands. The modelling of this additional absorption, as described in Section 5.3, is considered in the following analyses. In the course of the profile-fitting analysis, the metal line parameters are fixed during the fitting procedure. Using the apparent optical depth method, bins with a metal line or H_2 optical depth $\tau_{\mathrm{met}} > 0.05$ are omitted.

5.5.1. Profile fitting analysis

In the He II redshift range covered by FUSE ($z \gtrsim 2.29$) we find 326 H I Lyα lines in the Keck spectrum. Due to the FUSE detector gap and terrestrial airglow lines, the number of H I lines, that are supposed to be detectable in He II, reduces to about 300. In addition to the He II absorbers, which are identified in H I, we have to add several He II lines without any detected H I counterparts. These absorbers are about 23 % of all fitted He II lines. Furthermore, we include the metal absorption lines described in Section 5.3. The resulting distribution of the column density ratio η with redshift is shown in the lower panel of Fig. 5.4.

Because of the high fraction of lower limits, i.e. He II features without H I counterpart, the simple statistical mean of the absorbers with detected H I and He II ($\log \eta = 1.61 \pm 1.10$, median 1.75) is expected to be biased. Using the Kaplan-Meier estimator (e.g. Feigelson & Nelson 1985) to derive a mean value including the lower limits yields $\log \eta_{\mathrm{KM}} = 2.23 \pm 0.11$. The median of the total sample is $\log \eta = 1.93$ in good agreement with the results from the studies of the He II Lyα forest towards HE 2347-4342 (Kriss et al. 2001; Shull et al. 2004; Zheng et al. 2004b), revealing $\eta \approx 80$.

The values given above are estimated considering the total line sample. As we argue in Section 5.4, more confident results are expected to be found if the line sample is restricted. Therefore, we compute the mean column density ratio considering lines with $12.0 \leq \log N_{\mathrm{H\,I}} \leq 14.5$ and yield $\log \eta = 1.67 \pm 0.98$ (median 1.75). Since for all He II features without H I counterpart the lower limit of the hydrogen column density is less than 10^{12} cm^{-2}, no limits are included in the selected line sample.

Applying the more stringent selection criterion ($12.0 \leq \log N_{\mathrm{H\,I}} \leq 13.0$) results in $\log \eta = 1.96 \pm 0.95$ (median 1.92). The redshift distribution of η for this subsample is presented in Fig. 5.9. Even for the smallest sample the scatter of $\log \eta$ is roughly 50 %. This is significantly more than expected by the simulations. A possible explanation would be the redshift evolution of the column density ratio. Due to the evolution of the sources and absorbers that compose the properties of the UV background, η is expected to change with redshift (e.g. Fardal et al. 1998). Our artificial spectra are generated free from any evolution. Thus, the real data might mimic a higher overall scatter due to redshift evolution. We estimate the column density ratio in different redshift bins of the most stringently selected sample and find indeed an increase of the mean value with redshift. However, the scatter in each redshift bin is about 30 – 40 %, i.e. part of the scatter in the total redshift range might be due to evolution, but a significant fraction cannot be explained neither by statistical scatter nor by redshift evolution. This leads to the conclusion that the UV background is indeed fluctuating, even though the results from the profile-fit analysis are insensitive to the scales of the η variation (an attempt to derive these scales is made in Chapter 6).

For investigating the behaviour of η with the hydrogen column density, we concentrate on absorbers with $\log N_{\mathrm{H\,I}} < 15.0$. The H I features stronger than this threshold are associated with the LLS in the observed redshift range. Since LLS are believed to arise from material in the outer parts of galaxies, their column density ratio does not probe the ionizing conditions in the IGM but in a galaxy itself. These absorbers are excluded from the sample for the following investigation. Furthermore, we consider only absorbers de-

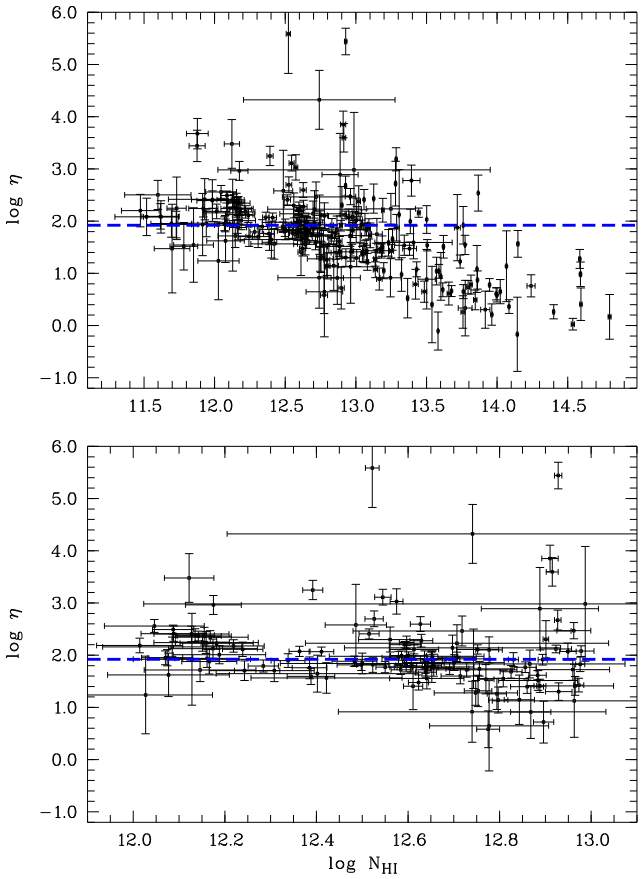

Fig. 5.10: Distribution of the column density ratio η with hydrogen column density $N_{\mathrm{H\,I}}$ (both logarithmic). Only absorbers detected in H I and He II with $\sigma(\log N_{\mathrm{H\,I,He\,II}}) < 1.0$ are shown. The upper panel presents the total sample with $\log N_{\mathrm{H\,I}} < 15.0$. The lower panel is a zoom-in to $12.0 \leq \log N_{\mathrm{H\,I}} \leq 13.0$. The dashed line represents the median value for the more constrained line sample $\log \eta = 1.92$.

tected in both H I and He II with reasonable column density uncertainties $\sigma(\log N_{\mathrm{H\,I,He\,II}}) < 1.0$. The distribution of $\log \eta$ with $\log N_{\mathrm{H\,I}}$ is shown in the upper panel of Fig. 5.10. A clear trend is seen, that $\log \eta$ decreases with increasing H I column density. We compute the Spearman rank-order correlation coefficient yielding $r_s = -0.58$. A linear fit to the data $\log \eta = a \cdot \log N_{\mathrm{H\,I}} + b$ leads to $a = -0.67 \pm 0.07$ and $b = 10.32 \pm 0.88$.

The analysis of the artificial data (Section 5.4) reveals that a correlation arises if a sample of lines broadened by thermal and turbulent processes is analyzed under the assumption of pure turbulent broadening. This effect is especially noticeable for the column density ratio of absorbers stronger than $\log N(\mathrm{H\,I}) \gtrsim 13$, as illustrated in Fig. 5.6 and discussed in the previous section (see also Chapter 6). In this case we find a Spearman rank coefficient of about −0.25. No correlation is found if the assumption of pure turbulent broadening is correct ($r_s \approx 0$). Indeed, the results of Zheng et al. (2004b) imply that the line width is dominated by turbulent broadening, but in Chapter 6 is shown that thermal broadening cannot be neglected completely.

The resulting numbers change only marginally if the subsample defined by $12.0 \leq \log N_{\mathrm{H\,I}} \leq 14.5$ is considered since 90 % of the absorbers with $\log N_{\mathrm{H\,I}} < 15.0$ are selected for the subsample as well. Applying the more stringent constraint ($12.0 \leq \log N_{\mathrm{H\,I}} \leq 13.0$) to the observed data yields a correlation coefficient $r_s = -0.28$ for the observed sample, which is only half of the value for the larger sample (presented in the lower panel of Fig. 5.10). The linear fit shows now a significantly flatter slope $a = -0.30 \pm 0.23$ and $b = 5.84 \pm 2.91$. Also in this case, the Spearman rank coefficients indicate a slight correlation for the artificial sample with fractional thermal broadening ($r_s \approx -0.2$) and no correlation for the pure turbulent broadened sample.

5.5.2. Apparent optical depth method

Considering the limitations discussed in Section 5.4, we apply the apparent optical depth method to the observed data. In addition, we use the metal line system models presented in Chapter 4 with the modifications discussed in Section 5.3 to omit bins which are affected by metal line absorption in the FUSE or the Keck data. Fig. 5.11 shows the resulting η distribution for both the whole data and the subsample selected by $-2.0 \leq \log \tau_{\mathrm{H\,I}} \leq -1.0$. The subsample consisting of 476 points (54 % of the total sample) only contains values in the range of $1.0 < \log \eta < 3.0$ with a mean value of $\langle \log \eta \rangle = 1.94 \pm 0.32$ (median 1.95). A consideration of the total sample yields $\log \eta = 1.70 \pm 0.60$ and a median of 1.78.

Fitting a Gaussian to the $\log \eta$ distribution of the subsample yields $\log \eta_0 = 1.950 \pm 0.020$ and $\sigma = 0.326 \pm 0.016$ corresponding to FWHM $= 0.767 \pm 0.037$. The width of the distribution is increased by more than 40 % in comparison to the artificial data. Thus, we may conclude, that in addition to a scatter in η due to noise and saturation effects a physically real variation of η is present.

Figures 5.11 and 5.12 show that η is decreasing with redshift. The presented η values are based on the effective optical depth of H I and He II, respectively, per $\Delta z = 0.05$ bin, where censored pixels have been neglected. In the resulting evolution η is rising from $\log \eta = 1.57 \pm 0.30$ at $z \approx 2.33$ up to 2.04 ± 0.32 at $z \approx 2.68$. This behaviour of the He II/H I ratio is expected, since it traces the evolution of the ionizing sources. According to Fardal et al. (1998), the observed evolution may be mainly based on a population of quasars with spectral indices $\alpha \sim -1.8$.

An important source of error regarding the redshift evolution of η are the uncertainties in the placement of the continuum in the FUSE spectrum, since the He II optical depth and thus the value of η directly depends on the position of the continuum level. As discussed in Section 5.2 the choice of the extinction curve, which is highly uncertain in the EUV, has a strong impact on the continuum level. Especially, if the continuum is extrapolated to a too low level at short wavelengths (e.g. the dotted curve in Fig. 5.1), the apparent optical depth and consequently the derived η gets too small. Since the extinction law is wavelength-dependent, the uncertainties increase with decreasing wavelength. Addition-

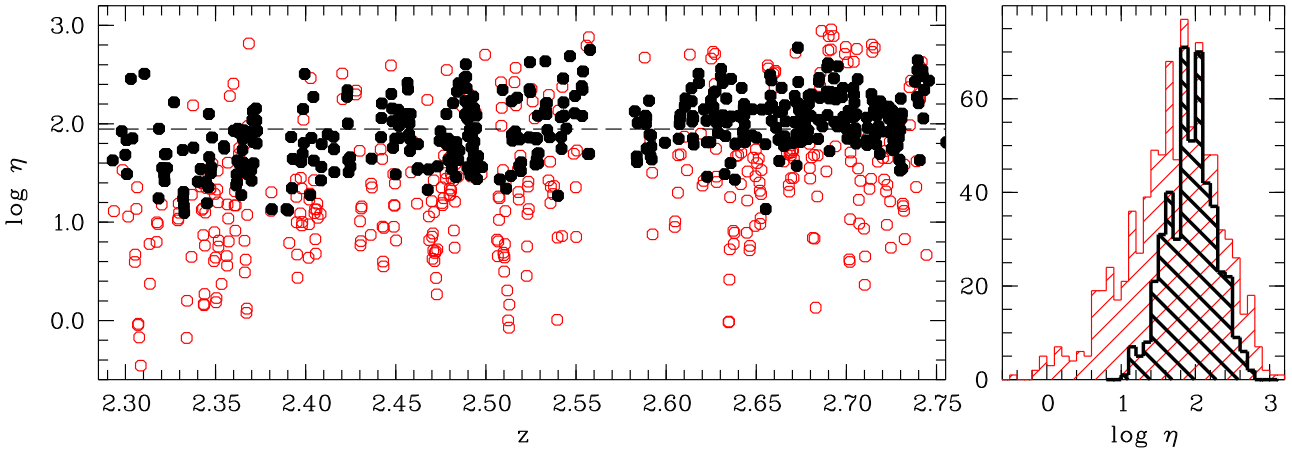

Fig. 5.11: Distribution of η derived form the observed data of HS 1700+6416 using the apparent optical depth method with a bin size of $\Delta v = 20\,\mathrm{km\,s^{-1}}$ omitting bins affected by metal line absorption. The selected subsample ($-2.0 \leq \log \tau_{\mathrm{H\,I}} \leq -1.0$) is indicated as circles and its η distribution is the narrower histogram in the right panel. The dashed line in the left panel represents the median value of the subsample $\log \eta = 1.95$.

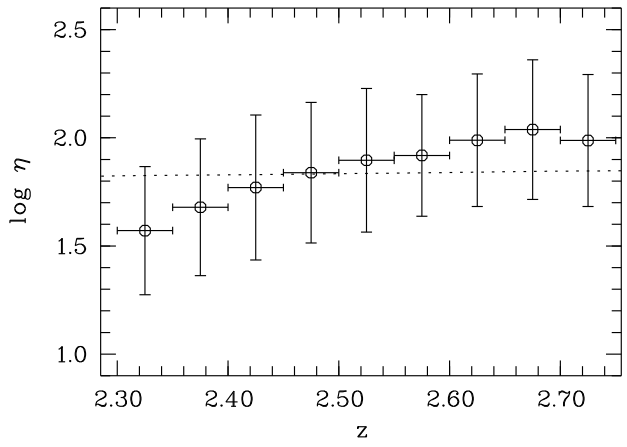

Fig. 5.12: Evolution of η with redshift. The dotted curve represents the expected values if the ionizing sources are quasars with a spectral index of $\alpha = -1.8$ as modelled by Fardal et al. (1998).

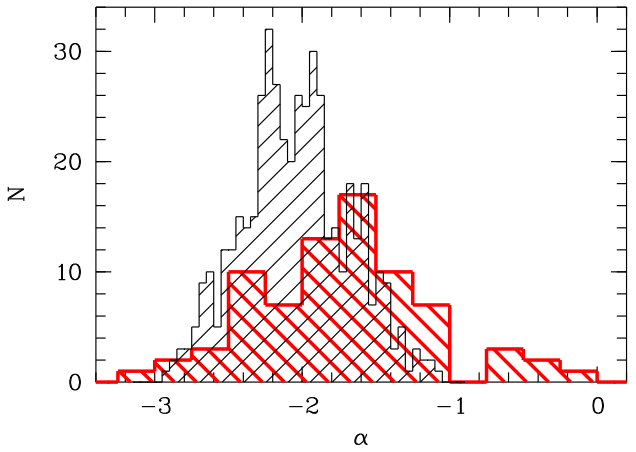

Fig. 5.13: Distribution of the spectral indices α (used as $f_\nu \propto \nu^\alpha$) for the observed sample (derived from the apparent optical depth result; thin line) and the whole sample from Telfer et al. (2002, larger bin size, thick line). The observed spectral indices are derived from the measured η values using the correlation illustrated as Model A2 in Fig. 10 of Fardal et al. (1998). Different bin sizes are used for a better presentation.

ally, the inaccurate definition of the zero flux level at short wavelengths results in systematically underestimated He II optical depths leading to low η values. Thus, it might be an artifact from the continuum definition and/or zero flux level estimation, that the observed evolution of $\log \eta$ appears to be steeper than predicted by the model of Fardal et al. (1998).

A correlation between the H I optical depth and the He II/H I ratio is still present in the subsample. The Spearman rank-order coefficient for this correlation is $r_s = -0.57$. However, also the subsamples of the artificial datasets show slight correlations leading to $r_s \approx -0.36$ for both broadening mechanisms. The slope describing the observed sample ($a = -0.71 \pm 0.05$) is twice as steep as those from the simulated datasets with uncertainties of the same order of magnitude. Therefore, it cannot be concluded with certainty whether the correlation between H I voids and high η values is real.

5.5.3. The ionizing background

Summarizing the results obtained by applying the apparent optical depth method and the profile-fitting procedure, we find a mean value of the column density ratio $\log \eta = 1.95$ (corresponding to $\eta \approx 89$). The observed scatter is larger than expected from the analysis of artificial data. Part of the enhanced scatter is possibly due to evolution of the column density ratio with redshift, which has not been incorporated in the artificial data. Measuring η and its scatter in smaller redshift bins suggests as well that part of the scatter must be attributed to physical effects beyond statistical noise.

The origin of the scatter must be related to fluctuations in the He II ionizing radiation since the photoionization rate of

H I can be assumed to be uniform (a more detailed argumentation is given by e.g. Bolton et al. 2005). Spatial variation at the He II ionization edge may be due to the wide range of spectral indices of the energy distribution of quasars (Zheng et al. 1997; Telfer et al. 2002; Scott et al. 2004). Shull et al. (2004) and Zheng et al. (2004b) compared the estimated column density ratios towards HE 2347-4342 to the distribution of the the spectral indices α of 79 quasars presented by Telfer et al. (2002). Both found an excess of softer radiation. Fig. 5.13 shows the distribution of α derived from the observed subsample applying the apparent optical depth method. The η values are converted into spectral indices using the relation between the He II/H I ratio and the source's spectral index presented by Fardal et al. (1998, their Fig. 10, Model A2). As a mean spectral index, we find $\langle\alpha\rangle = -2.04 \pm 0.36$. In comparison to the total sample of Telfer et al. (2002), we confirm the excess of softer spectral indices. One should keep in mind that the conversion from η into α is based on a phenomenological model, which certainly contains additional sources of error.

Following the arguments of Shull et al. (2004), it is possible to convert the η values directly into effective spectral indices. The effective spectral index $\alpha_{\rm eff}$ describes the radiation an absorber is directly exposed to rather than the radiation once emitted by the sources, i.e. it denotes the spectral index of the filtered radiation of the sources. Assuming a temperature of $T = 10^{4.3}$ K and the equality of the local spectral indices at 1 and 4 Ryd, respectively, leads to $\eta = 1.70 \cdot 4^{-\alpha_{\rm eff}}$ (for details see Shull et al. (2004) and references therein). Applying this relation the α distribution is broader and shifted to even softer indices: $\langle\alpha_{\rm eff}\rangle = -2.84 \pm 0.53$. The results from the profile-fitting method lead to similar numbers.

Bolton et al. (2005) have studied the observed spatial variation of the column density ratio arising from a fluctuating UV background. According to their model, the fluctuations are based on variations in the He II photoionization rate due to properties of the emitting quasars, such as the spatial distribution, luminosity function, and the spectral energy distribution (see also Fardal et al. 1998). Bolton et al. (2005) find η values scattered over 2 dex roughly consistent with the results from Zheng et al. (2004b), but failed to reproduce a significant number of points with $\eta < 10$. As discussed in the previous Sections, the results from the line profile-fitting procedure are likely to be biased due to thermal line broadening when considering high density absorbers (see also Chapter 6). Although Bolton et al. (2005) do not address this problem their Fig. 4 reveals an increased number of lines with a low column ratio for increasing H I column density. Considering only absorbers in a restricted column density range eliminates most of the points with very low η (see Figs. 5.9 and 5.11). We conclude that there are no absorbers exposed to radiation harder than those emitted by QSOs. Thus, the column density ratios inferred from the data of HS 1700+6416 support the model proposed by Bolton et al. (2005) to explain the spatial fluctuation of the column density ratio.

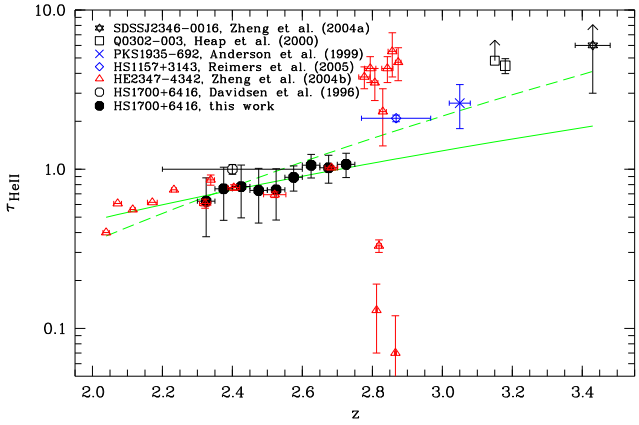

Fig. 5.14: Evolution of the He II opacity with redshift. In addition to the opacities measured in this work (filled circles), values measured towards five additional QSOs with detected He II absorption are shown. The solid curve represents the relation $\tau_{\rm He\,II} \propto (1+z)^{3.5}$ (Fardal et al. 1998) fitted to the data points $z < 2.75$. The dashed line indicates an overall fit to the data resulting in $\tau_{\rm He\,II} \propto (1+z)^{6.3\pm0.4}$.

Apart from scatter, the average value of the column density ratio can be roughly related to the dominating sources of ionizing radiation. The inferred value ($\eta \approx 89$) is in agreement with the results towards HE 2347-4342 (Kriss et al. 2001; Shull et al. 2004; Zheng et al. 2004b). It is consistent with the UV background of Haardt & Madau (2001) based on QSOs only. This is, however, in contradiction to the growing evidence that radiation from QSOs alone cannot reproduce current observational results (e.g. Heap et al. 2000; Smette et al. 2002; Aguirre et al. 2004; Bolton et al. 2005; Kirkman et al. 2005).

Our data reduction is still in need of improvement concerning the zero flux level (see Section 5.1). This is in particular true for shorter wavelengths. In order to exclude possible biases due to the reduction problems, we estimate the mean column density ratio for wavelengths longer than 1086 Å ($z > 2.58$), where the data reduction appears to be correct. We find $\log\eta = 2.26 \pm 0.84$ (median 2.11) adopting the profile-fitting results and a slightly lower value (≈ 2.04) using the apparent optical depth method. These values ($\eta \approx 110 \ldots 180$) are consistent with predictions for the UV background including also young star forming galaxies (Haardt & Madau 2001) and slightly higher than predicted by the models of Bolton et al. (2005) at the same redshift based on a modified version of the UV background of Madau et al. (1999).

5.5.4. Redshift evolution of the He II optical depth

Fig. 5.14 shows a compilation of the measured He II opacity $\tau_{\rm He\,II}$ from the literature (Davidsen et al. 1996; Anderson et al. 1999; Heap et al. 2000; Zheng et al. 2004a,b; Reimers et al. 2005a) together with our measurements from the FUSE spectrum of HS 1700+6416 (filled circles). Estimating the

mean normalized flux per redshift bin, pixels affected by metal line absorption are excluded. We find a mild evolution from $\tau_{\mathrm{He\,II}} = 0.65 \pm 0.24$ at $z = 2.30 - 2.35$ to 1.07 ± 0.19 at $z = 2.70 - 2.75$. These values are consistent with the opacity measurements towards HE 2347-4342 in the same redshift range (Zheng et al. 2004b).

Davidsen et al. (1996) estimated $\tau_{\mathrm{He\,II}} = 1.00 \pm 0.07$ at $\langle z \rangle = 2.4$ using a low resolution spectrum taken with the Hopkins Ultraviolet Telescope (HUT). As can be seen from Fig. 5.14 our values are systematically lower by about 25 %. Tests with the data uncorrected for metal line absorption suggest that this difference is partly due to the additional absorption by metal lines raising the opacity by roughly 10 %. Additionally, differences in the continuum level may account for the higher effective optical depth derived by Davidsen et al. (1996). However, the values are consistent on the $1\,\sigma$ level.

The solid line in Fig. 5.14 represents the relation $\tau_{\mathrm{He\,II}} \propto (z+1)^{3.5}$ (Fardal et al. 1998) providing a suitable fit to the data at $z < 2.75$. The value of the power law exponent $\gamma+1$ is chosen according to the results from H I Lyα forest statistics (e.g. Press et al. 1993; Kim et al. 2002a). Deviations from this relation at higher redshift are commonly interpreted as the evidence for the tail end of the epoch of He II reionization which completes at $z \sim 2.8$ (e.g. Reimers et al. 1997a; Kriss et al. 2001; Zheng et al. 2004b). At $z > 3$ very high values of the He II optical depth can be detected. A simple overall fit to all data points would lead to $\tau_{\mathrm{He\,II}} = 3.5 \cdot 10^{-4}\,(z+1)^{6.3\pm0.4}$ (dashed line in Fig. 5.14). This fit should not be interpreted as a reasonable model for the evolution of $\tau_{\mathrm{He\,II}}$.

5.6. Summary and conclusions

We have presented far-UV data of the quasar HS 1700+6416 taken with FUSE, which is the second line of sight permitting us to resolve the He II Lyα forest. The data are of comparable quality ($S/N \sim 5$, $R \approx 20\,000$) to those of HE 2347-4342 and cover the redshift range $2.29 \lesssim z \lesssim 2.75$. In this redshift range, no strong variations of the He II opacity are detected. The evolution of the effective optical depth is consistent with $(z+1)^{3.5}$, i.e. this line of sight probes the post-reionization phase of He II.

The column density ratio η has been derived using line profile fits and the apparent optical depth method, respectively. A preliminary study of simple artificial spectra created on the basis of the statistical properties of the Lyα forest including or neglecting thermal line broadening, respectively, reveals the shortcomings of the standard analysis methods. The reasons are noise, line saturation, and effects due to the assumption of pure turbulence if thermal broadening contributes to the line widths. We find that the profile-fitting procedure leads to reliable results only for absorbers with H I column densities in the range $12.0 \leq \log N_{\mathrm{H\,I}} \leq 13.0$. The apparent optical depth method is only valid in the range $0.01 \leq \tau_{\mathrm{H\,I}} \leq 0.1$. Otherwise, η would be underestimated in the case of strong H I absorption. Furthermore, a scatter in η of $10 - 15$ % is expected even if the underlying value is constant.

In order to avoid systematic biases due to additional absorption in the He II Lyα forest, a model of the metal line features expected to arise in the FUSE spectral range (Chapter 4) has been included in the analysis. We have also considered features of galactic H_2 absorption. 25 % of all fitted He II lines are affected by metal lines; for 16 % of the lines the derived η value changes significantly, i.e. by more than $\Delta \log \eta = 0.01$. Additionally, the required number of He II absorbers without detectable H I counterpart is reduced by 30 % if metal lines are taken into account, and the average η value slightly decreases. Although the consideration of metal line absorption does not distort strongly the statistical properties of the resulting η distribution, individual values could have been biased by up to an order of magnitude.

For the redshift range $2.58 \lesssim z \lesssim 2.75$, where the spectrum appears to be free of artifacts due to the reduction process, the data reveals $\log \eta \approx 2.1$ on average. This high value ($\eta \approx 126$) indicates a significant contribution of galaxies to the UV background at these redshifts, consistent with current results from studies of the H I opacity and the metallicity of the IGM.

The scatter of η is larger than expected compared to our analysis of artificial datasets. Therefore, we infer that the UV background really fluctuates, even though our present results are insensitive to the amplitude and scale of these variations. Converting the values of the column density ratio into spectral indices, we confirm the apparent excess of soft sources as found by Shull et al. (2004) and Zheng et al. (2004b). Our results suggest, that the apparent correlation between the η value and the strength of the H I absorption may be an artifact of the analysis method and does not reflect physical reality.

Since we have shown that the assumption of pure turbulent line broadening will lead to systematical errors, the next step in the analysis of the resolved He II Lyα forest should be to avoid this assumption. The apparent optical depth method applied to an appropriately restricted sample should lead to unbiased results independent of the dominant line broadening mechanism. A bin by bin comparison as performed by the apparent optical depth method provides little potential for taking into account a potentially dominant thermal broadening, while the profile-fitting procedure could drop the assumption of pure turbulence. However, obtaining reasonable fits would be more challenging due to the low S/N of the data. This would provide an independent strategy to estimate the IGM temperature.

6. Fluctuations of the UV background towards HS 1700+6416 and HE 2347-4342

The metagalactic ionizing radiation plays an important role for QSO absorption line studies probing the intergalactic medium (IGM). The IGM is highly photoionized and the UV background governs its ionization state. Estimates of the intergalactic metallicity are highly dependent on the presumed ionizing radiation (e.g. Aguirre et al. 2004). Nevertheless, the shape of the UV background is inaccessible to direct observation. Theoretical models based on the number, distribution, and spectral properties of underlying sources like AGN and starburst galaxies have been computed by e.g. Haardt & Madau (1996, 2001); Fardal et al. (1998); Bianchi et al. (2001). Efforts to derive the shape of the ionizing radiation from the observed column densities of different metal ions via photoionization calculations have been made recently by Agafonova et al. (2005). The observational studies suggest deviations from the shape predicted by "classical" theoretical models (see also Boksenberg et al. 2003, or Chapter 4). This is supported by recent theoretical work (Schaye 2004; Miralda-Escudé 2005) pointing out the importance of local radiation sources.

Apart from column density ratios of metal line absorption, the Lyα transition of He II ($\lambda_0 = 303.7822$ Å) provides a further possibility to probe the UV background observationally. The column density ratio $\eta = N_{\rm He\,II}/N_{\rm H\,I}$ depends on the photoionization rates of H I and He II and thus on the ionizing radiation at the H I (1 Ryd) and He II (4 Ryd) ionization threshold (e.g. Fardal et al. 1998). Furthermore, He II probes the low density phase of the IGM, since He II is more difficult to ionize than H I due to lower fluxes and cross sections at its ionizing threshold and the faster recombination of He III compared to H II.

Direct observations of He II Lyα absorption are very difficult due to the limited number of unabsorbed quasars (Picard & Jakobsen 1993). Up to now, six objects have been observed, showing He II absorption in their UV spectra. Only two of them (HE 2347-4243 at $z = 2.885$ and HS 1700+6416 at $z = 2.72$) are bright enough for high resolution spectroscopy with FUSE (Kriss et al. 2001; Shull et al. 2004; Zheng et al. 2004b; Reimers et al. 2004). The results from these data suggested that the UV background might fluctuate on small scales ($\Delta z \sim 0.001$) with an amplitude of several orders of magnitude ($\eta \lesssim 10$ up to $\gtrsim 1000$). Probable reasons for these fluctuations are the properties of the QSOs like the spread in the spectral indices (e.g. Telfer et al. 2002) and finite lifetimes, local density variations of the IGM (Miralda-Escudé et al. 2000) or filtering of radiation by radiative transfer effects.

Due to the limited quality of the FUSE data ($S/N \sim 5$) it is important to examine in detail the applicability of the adopted analysis methods. Shull et al. (2004) applied an apparent optical depth method, while all other studies are based on line profile fitting (Kriss et al. 2001; Zheng et al. 2004b; Reimers et al. 2004). Fox et al. (2005) showed that the apparent optical depth method overestimates the column density in case of low signal-to-noise. Furthermore, it is only valid for unsaturated lines (Savage & Sembach 1991). The applicability of line profile fitting was investigated by Bolton et al. (2005), who find that it leads to reliable results (but see discussion below), and the median provides more confident results than the mean. According to their study, the fluctuations in η are due to the small number of quasars that contribute to the He II ionization rate at any given point. They also conclude that a small fraction of space have to be exposed to a harder radiation, since they failed to reproduce column density ratios $\lesssim 1$, which are measured by Zheng et al. (2004b).

Here, we re-analyze the He II Lyα forest towards HE 2347-4342 and HS 1700+6416 applying a new method, which fits the optical data directly to the FUSE spectra. This approach minimizes effects of noise mimicking η variations when applying the apparent optical depth method, and it avoids the subjectivity of the line profile modelling, where the number of assumed components are due to arbitrary choice. In order to provide an alternative estimate of the scales on which η fluctuates, we follow several approaches. Furthermore, we investigate the effect of line broadening on the inferred η values.

This Chapter is organized as follows: New high quality, optical data of the H I Lyα forest towards HE 2347-4342 are presented in Section 6.1. In Section 6.2, we introduce the fit procedure (called spectrum fitting), which is applied to the data in Section 6.3. The results, possible effects due to thermal line broadening, and their implications are discussed in Section 6.4. We conclude in Section 6.5.

6.1. Data

HE 2347-4342 was observed with UVES at the second VLT unit telescope (Kueyen) during 13 nights at two epochs in 2000 and 2003. The details of the settings are presented in Table 6.1. In 2000, the observations were carried out as a part of the Large Program "The Cosmic Evolution of the Intergalactic Medium" (116.A-0106A) in the UVES dichroic modes resulting in a total wavelength coverage of $\sim 3000 - 10\,400$ Å. Additional observations were performed

Table 6.1: Observation diary of HE 2347-4342. All exposures use a 1″ slit and 2 × 2 binning. The seeing conditions were very good with 0.5″ – 1.0″.

date	mode	λ_{cen} (nm)	t_{exp} (s)
2000/10/07	DICHR#1	346/580	14 400
2000/10/08	DICHR#1	346/580	7 200
2000/10/08	DICHR#2	437/860	7 200
2000/10/09	DICHR#2	437/860	7 200
2000/11/19	DICHR#2	437/860	7 200
2003/06/05	BLUE	437	7 200
2003/06/06	BLUE	437	10 800
2003/06/07	BLUE	437	6 900
2003/06/08	BLUE	437	10 300
2003/06/12	BLUE	437	3 130
2003/06/17	BLUE	437	6 600
2003/06/24	BLUE	437	6 600
2003/07/06	BLUE	437	3 700
2003/08/05	BLUE	437	3 244

in 2003 in the blue with a central wavelength of 4370 Å. The slit width of 1″ and binning 2 × 2 were chosen to match the setting of the Large Program data. The resolution is $R \approx 45\,000$.

The data reduction was performed at Quality Control Garching using the UVES pipeline Data Reduction Software (Ballester et al. 2000). The vacuum-barycentric corrected spectra were co-added. Thus, for the wavelength range 3800 – 4950 Å the total exposure time is 28.24 hrs resulting in a signal-to-noise ratio of $S/N \approx 100$ in the Lyα forest.

The UV of HE 2347-4342 data have been taken with the FUSE satellite in 2000. The data were first presented by Kriss et al. (2001), and was newly reduced and re-analyzed twice (Shull et al. 2004; Zheng et al. 2004b). In this study we use the spectrum of Zheng et al. (2004b), and refer to their work for details of the data reduction. The resulting spectrum covers the spectral range 900 – 1188 Å. The signal-to-noise ratio is $S/N \approx 5$ in the best part (1088 – 1134 Å) and slightly less elsewhere. The resolution is $R \approx 20\,000$.

A low resolution STIS spectrum was taken simultaneously with the FUSE observations in August and October 2000 using the gratings G140L and G230L. The spectra cover the wavelength range 1120 – 3170 Å and are used to extrapolate the continuum to the FUSE spectral range. We estimate the continuum considering galactic extinction, Lyman limit absorption, and the intrinsic spectral energy distribution of the QSO. The extinction curve is adopted from Cardelli et al. (1989) assuming $E(B-V) = 0.014$ (Schlegel et al. 1998). In addition, there is a Lyman limit system (LLS) on the line of sight at $z \approx 2.735$. From the Lyman break we estimate the optical depth $\tau \sim 1.8$ leading to $\log N_{LLS} \approx 17.46$ following Møller & Jakobsen (1990), which is in good agreement with the results of Reimers et al. (1997a). However, the contributed optical depth of the LLS to the absorption in the FUSE spectral range is negligible ($\tau < 0.08$ at $\lambda < 1200$ Å) thanks to the ν^{-3} dependence of the Lyman continuum opacity. Considering the LLS optical depth and the extinction law, we estimate the intrinsic QSO power law to have a spectral slope of $\alpha \approx -0.46$.

The UV spectrum of HS1700+6416 taken with FUSE was first presented in Reimers et al. (2004). We use the reduced and normalized data set presented in Chapter 5, which has a resolution of $R \approx 20\,000$ and a signal-to-noise ratio of ~ 5. The corresponding H I Lyα forest was observed with Keck/HIRES. For a more detailed presentation of the optical data we refer to Chapters 4 and 5. The resolution is $R \approx 38\,000$ and $S/N \approx 100$.

6.2. Method

Previous studies of the He II Lyα forest are based on a profile-fitting procedure (Kriss et al. 2001; Zheng et al. 2004b; Reimers et al. 2004) or the apparent optical depth method (Shull et al. 2004). Both methods suffer from different shortcomings. The apparent optical depth method leads to reliable results only if lines are optically thin (Savage & Sembach 1991). In case of the He II forest many profiles are saturated. Thus, the validity of the apparent optical depth method is limited. Furthermore, the results strongly depend on the noise, which may mimic fluctuations of η.

In case of fitting line profiles to the data the H I spectrum is modelled by Doppler profiles. The derived line parameters are used to fit the He II data as well. In doing so, the line widths have been assumed to be dominated by turbulent broadening, i.e. $b_{\mathrm{He\,II}} = b_{\mathrm{H\,I}}$. This assumption is also made implicitly in the apparent optical depth method, and is inherent in our spectrum fitting method as well. However, fitting line profiles need the subjective decision how many components are used to model the observed features. Particularly, this problem gets significant for weak lines and complicated blends, where components may get lost or the decomposition is insufficient. Problems in the H I model may cause a poor description of the corresponding He II absorption, where the features are stronger but the data quality is worse. Therefore, apparent variations in η may be artifacts of an inadequate decomposition.

With the purpose to avoid a strong dependence on the noise as well as the subjectivity of a model, we develop a new method to estimate η. It is based on the idea to compare the He II and the H I Lyα forest directly without the need to provide a model of the data and without using a pixel by pixel (or bin by bin) technique which would be affected by the noise level of the data. Therefore, we fit the whole H I spectrum to the He II data by scaling it by $\eta = 4 \cdot \tau_{\mathrm{He\,II}}/\tau_{\mathrm{H\,I}}$ (Miralda-Escudé 1993), which is then the only free parameter.

Since an unbiased H I spectrum is needed, we identify the metal line systems in the optical data, fit Doppler profiles to the spectral range of interest and subtract them from the spectrum. Furthermore, we confine ourselves to the pure Lyα forest, and only the data between Lyα and Lyβ emission are suitable. In case of HE 2347-4342 these are wavelengths

$\gtrsim$ 4000 Å in the optical and $\gtrsim$ 1000 Å in the UV. Strong O VI absorption arising from a complex system associated with the QSO is present shortward of $\sim$ 4050 Å. Due to the complexity of the system and severe blending with forest lines (for a more detailed discussion see Fechner et al. 2004), we restrict the redshift range to $2.33 < z < 2.91$.

In preparation of a fit, the wavelength scales of the datasets are aligned scaling the optical data by a factor of 1215.6701 Å/303.7822 Å $\approx$ 4.00178. Furthermore, the resolution of the optical spectrum is changed to match the lower resolution of the FUSE data by a convolution with a Gaussian. The method assumes implicitly that line broadening is dominated by turbulent motion and the line widths are the same for H I and He II. Since the operation of convolution is commutative, the width of the Gaussian has to be $\sigma = (\sigma^2_{R=20\,000} - \sigma^2_{R=45\,000})^{1/2}$.

In order to perform the actual fit, a wavelength portion is chosen and $\log\eta$ is estimated to minimize

$$\chi^2 = \frac{1}{n}\sum_{i=1}^{n} \frac{\left(f_{\mathrm{He\,II},\,i} - \exp\left(-\frac{\eta}{4}\cdot\tau_{\mathrm{H\,I},\,i}\right)\right)^2}{\sigma^2_{\mathrm{He\,II},\,i} + \sigma^2_{\mathrm{H\,I},\,i}}\,, \tag{6.1}$$

where $f_{\mathrm{He\,II}}$ and $\tau_{\mathrm{H\,I}} = -\ln f_{\mathrm{H\,I}}$ are the normalized observed flux and the optical depth of He II and H I, respectively, with the uncertainties $\sigma_{\mathrm{He\,II}}$ and $\sigma_{\mathrm{H\,I}}$; n is the number of pixels in the chosen wavelength interval. The $1\,\sigma$ uncertainty of the fitted $\log\eta$ is estimated finding the values at which $\chi^2 = \chi^2_{\mathrm{min}} \pm \Delta\chi^2$ with $\Delta\chi^2 = 1.0$. We restrict the parameter space to values $0.0 \le \log\eta \le 4.5$.

The idea of fitting the spectra directly is illustrated in Fig. 6.1 for the spectral range 1088.0 – 1133.5 Å of HE 2347-4342, where the data quality of the UV spectrum is best. Each panel shows the normalized FUSE data in comparison to the aligned, metal line corrected H I spectrum scaled by $\log\eta = 0.0$ (i.e. unscaled), 1.0, 2.0, and 3.0, respectively. Obviously, some regions are consistent with $\log\eta \approx 1$ (e.g. 1112 – 1117 Å) or $\log\eta \approx 2$ (e.g. 1096 – 1103 Å). Whereas scaling the H I spectrum by $\log\eta \approx 3$ leads to almost complete absorption with few transmission windows, which is apparently not consistent with the He II observations in the presented wavelength range. The overall fit of this spectral range leads to $\log\eta = 1.81^{+0.48}_{-0.50}$ with $\chi^2 = 3.34$. However, the considered portion corresponds to $\Delta z \approx 0.15$, and obviously, η varies on smaller scales.

The definition of a scale in redshift, on which η is supposed to appear constant, is the most crucial point. The required length scale is given by the number of pixels n that are considered. If n is chosen too small, the result is severely affected by the noise level of the FUSE data. If n gets very small, the procedure approaches the apparent optical depth method. On the other hand, possible small-scale fluctuations will be smoothed and therefore remain undetected if the length scale is chosen too broad.

In order to investigate possible effects on the results, we follow four different approaches: (i) constant binning, (ii) binning "per eye", (iii) binning by χ^2-estimation, and (iv) averaging around each pixel. Most simply, bins of a fixed size are adopted. In this case, the bin size (we use 0.5 and 1.0 Å) and the positioning of the bins are free parameters. Therefore, fluctuations are investigated only on the given scale. In order to find a length scale, which is not fixed a priori, we define the fit intervals by eye. The advantage is that apparent changes of η as illustrated by Fig. 6.1 can be considered. On the other hand, the choice of the size of the intervals is made very subjectively. The more objective way is to start with a certain number of pixels and estimate the χ^2 of the fit. More pixels are added to the fit interval as long as the χ^2 of the fit decreases. If the χ^2 increases again, the interval is defined and the next evaluation starts. Test calculations show that in the case of HE 2347-4342 at least 15 pixels, corresponding to 0.375 Å have to be used for the first evaluation to avoid confusion due to the noise. Alternatively, we average over an interval of a certain size centered on every pixel. This procedure corresponds to a pixel by pixel estimation smoothed by averaging over a certain number of adjacent pixels. However, the results again depend on the number of pixels used, i.e. the degree of smoothing. A good choice appears to be 40 pixels corresponding to 1.0 Å.

6.3. Results

Applying the four scale-defining methods described above, the data are analyzed. For comparison, we also perform a Doppler profile analysis using the line fitting program CANDALF. The resulting distributions of η with redshift in case of HE 2347-4342 are presented in Fig. 6.2. The panels show the results for binning by eye, binning using the χ^2 method, and from the Doppler profile analysis. For a better orientation, the result for constant binning of 1.0 Å bin size are shown as overlay in each panel.

The low S/N of the FUSE data leads to large error bars, regardless of how the fit interval is defined. At longer wavelengths ($\gtrsim$ 1135 Å corresponding to $z \gtrsim 2.73$), instead of a forest structure, the He II absorption gets "patchy". This means that regions of high opacity and nearly complete absorption change with opacity gaps and continuum windows (Reimers et al. 1997a; Smette et al. 2002). Unlike the Lyα forest, the absorption in the patchy zone is thought to arise from a medium not yet fully reionized (Reimers et al. 1997a). Therefore, different results may be expected and we distinguish between the Lyα forest visible in He II and the patchy absorption towards HE 2347-4342. The slightly less redshifted QSO HS 1700+6416 probes only material that is already completely reionized. This means, solely Lyα forest absorption is detected. In the following, we first present the results from the Lyα forest and the patchy zone in the spectrum of HE 2347-4342 and thereafter HS 1700+6416.

6.3.1. The Lyα forest towards HE 2347-4342

As Lyα forest towards HE 2347-4342 we consider the wavelength range < 1134 Å or $z < 2.735$, respectively. As can be seen from Fig. 6.2, the η values in the redshift range

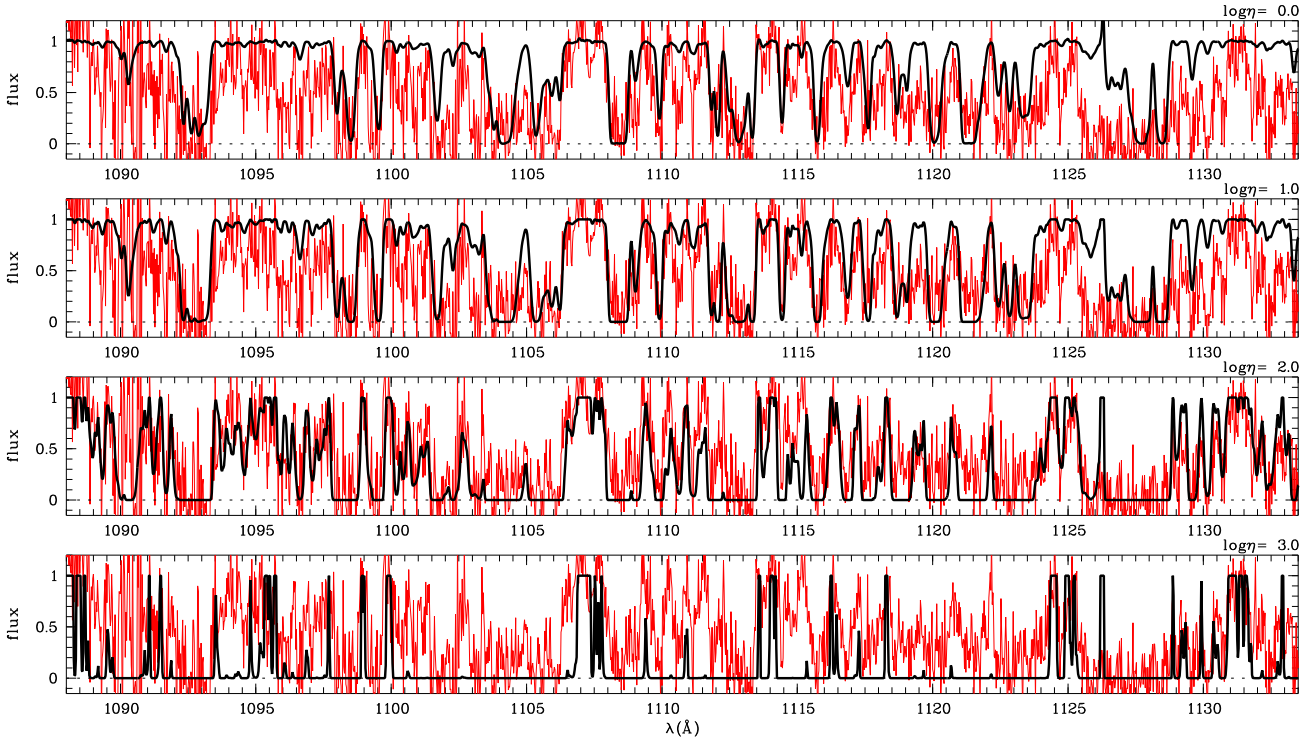

Fig. 6.1: Comparison of the observed He II data towards HE 2347-4342 to the metal subtracted, convolved H I spectrum scaled by $\log\eta$ = 0.0, 1.0, 2.0, and 3.0. Apparently, there are regions modelled well by $\log\eta \approx 1.0$ (e.g. 1112 – 1117 Å) or $\log\eta \approx 2.0$ (e.g. 1096 – 1103 Å and ∼ 1125 Å), respectively, while $\log\eta \approx 3.0$ would lead only to sparse regions with non-zero UV flux, which is inconsistent with the observations in this redshift range. Features that appear nearly overestimated by $\log\eta = 0.0$ (at ∼ 1104 Å, 1108.5 Å, and 1121.5 Å) correspond to weak metal line systems (see text).

$2.58 < z < 2.73$ are characterized by comparably small error bars. A close up to this range, where the data quality of the FUSE spectrum is best (1088 – 1134 Å), is shown in Fig. 6.3. In this figure the results from all different methods concerning the choice of the scale are presented. The fact that we find similar distributions of η with redshift for all scale definitions (panels a – d), gives confidence that the choice of the length scale has a minor influence on the results and can, in principle, be derived from the data. Even the column density ratios of the independent profile-fitting analysis are distributed similarly (Fig. 6.3e). This is noticeable in particular in the redshift regions 2.60 – 2.62, 2.645 – 2.66, and 2.68 – 2.70.

Extremely large error bars of the column density ratios obtained by profile fitting appear to be correlated to extreme η values or large uncertainties in the corresponding results of the spectrum fitting procedure. Obviously, there are problems with the data at ∼ 1093 Å, where several noise peaks in the FUSE data mimic an absorption structure different from that of H I (see also Fig. 6.1). Strong saturation, i.e. nearly complete absorption over roughly 4 Å, lead to large error bars at ∼ 1127 Å. A similar configuration produces the large uncertainties of the results from line profile fitting at ∼ 1105 Å, although the spectrum fitting results remain nearly unaffected.

The median value for this best region is $\log\eta \approx 1.75$ in case of the spectrum fitting method, similar for all adopted scales, and 1.80 in case of the profile fits considering also lower limits. This is slightly less than the mean value of $\eta = 80$ found by Kriss et al. (2001). The $1\,\sigma$ scatter related to the average is roughly 0.7 dex and slightly larger (∼ 0.8 dex) for the whole Lyα forest observed. Furthermore, almost all derived η values are below $\log\eta = 3.0$. Since very high η values are produced by soft radiation such as stellar sources, this might indicate that even though galaxies contribute to the ionizing radiation, they are not dominating the intergalactic UV background at the observed epoch.

Values of η significantly below the mean are visible at He II wavelengths around 1090 Å, 1104 Å, 1108 Å, and 1121 Å. In addition a local minimum is located at 1128 Å. Four of these minima coincide with metal line absorption systems at z = 2.6346, 2.6497, 2.6910, and 2.7121 (marked with arrows in Fig. 6.3a and summarized in Table 6.2) associated with saturated H I absorption features. The η minimum at 1090 Å is due to a H I line ($\log N \approx 13.0$), which seems to mismatch the absorption features in He II (see Fig. 6.1), probably an effect of the poor data quality at this spectral region. The metal line systems show weak C IV absorption ($\log N \lesssim 12.8$), prominent O VI features, and no low ionization species. Since the O VI features are located in the Lyα forest, their identification might be questionable due to blending with forest lines in at least one doublet component. Since the systemic redshift can be fixed by the unblended C IV, the existence of those systems is confirmed.

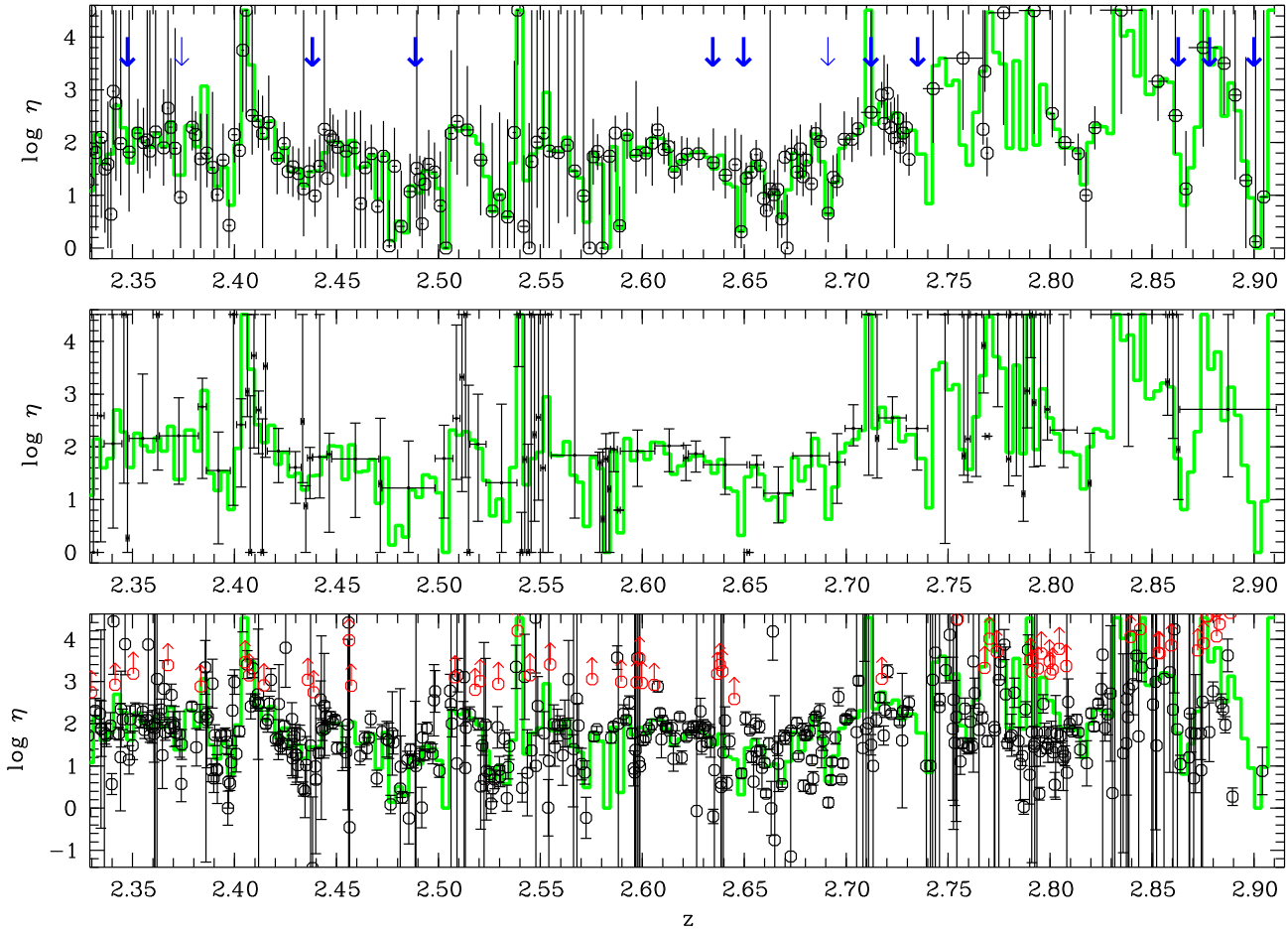

Fig. 6.2: Distribution of η with redshift towards HE 2347-4342 defining the fit interval by eye (upper panel) or using a χ^2 procedure (middle panel) as well as the result from profile fitting (lower panel). For a better orientation, the histogram-like line in each panel indicates η estimated with a constant 1.0 Å bin size. The redshifts of metal line absorption systems are marked as arrows in the upper panel.

However, the system at $z = 2.6910$ shows no C IV absorption and the λ1038 component of O VI is located in the Lyβ absorption trough of the LLS at $z \approx 2.735$. Thus the only evidence for metal line absorption is provided by the λ1032 component of O VI. Since the detected feature is narrow, $b = (11.06 \pm 0.81)\,\mathrm{km\,s^{-1}}$, it certainly originates from a metal ion, although an alternative identification cannot be ruled out completely.

Further apparent minima of η are found at lower redshift. The position of metal absorption systems are indicated as arrows in the upper panel of Fig. 6.2. The four metal line systems with $2.33 < z < 2.50$ showing only highly ionized species coincide again with minima of η. The system at $z = 2.4887$ appears to be located in between of two low η regions according to the upper panel of Fig. 6.2. However, referring to the lower panels, only the minimum at $z \sim 2.48$ may be real.

Additional low η regions are visible at $z \sim 2.39$ and 2.53. The latter might be affected by the extremely high noise in the corresponding He II wavelength range, while the first one is an apparent void in H I. Within $\Delta z \approx 0.063$ ($2.368 \lesssim z \lesssim 2.430$) we only detect lines with $\log N_{\mathrm{H\,I}} \lesssim 13.5$. At the central position of the void ($z \approx 2.398$), two stronger lines ($\log N_{\mathrm{H\,I}} \approx 13.5$) arise. We suspect that this void could be due to a quasar close to the line of sight, whose hard radiation field ionizes H I and He II resulting in the observed low η. Fitting the range $2.388 \lesssim z \lesssim 2.401$ yields $\log \eta = 1.72^{+1.19}_{-1.11}$. The appearance of the fit suggests fluctuations on scales smaller than $\Delta z \approx 0.013$ also reflected in the large $1\,\sigma$ errors.

Shull et al. (2004) found a correlation between the strength of the H I absorption and η, in the sense that higher η values are measured in H I voids. This finding was confirmed by Reimers et al. (2004) towards HS 1700+6416. We re-investigate this point estimating the mean H I opacity of the considered fit intervals. The distribution of η for constant bins of 1.0 Å size of high ($\tau_{\mathrm{H\,I}} > 0.05$) and low ($\tau_{\mathrm{H\,I}} < 0.05$) opacity is shown in the left panel of Fig. 6.4. Again, only the Lyα forest range is considered. The mean values are $\log \eta = 1.53 \pm 0.79$ and 1.98 ± 0.71 in the high and low opacity sample, respectively. For comparison, the corresponding distribution obtained from the profile-fitting

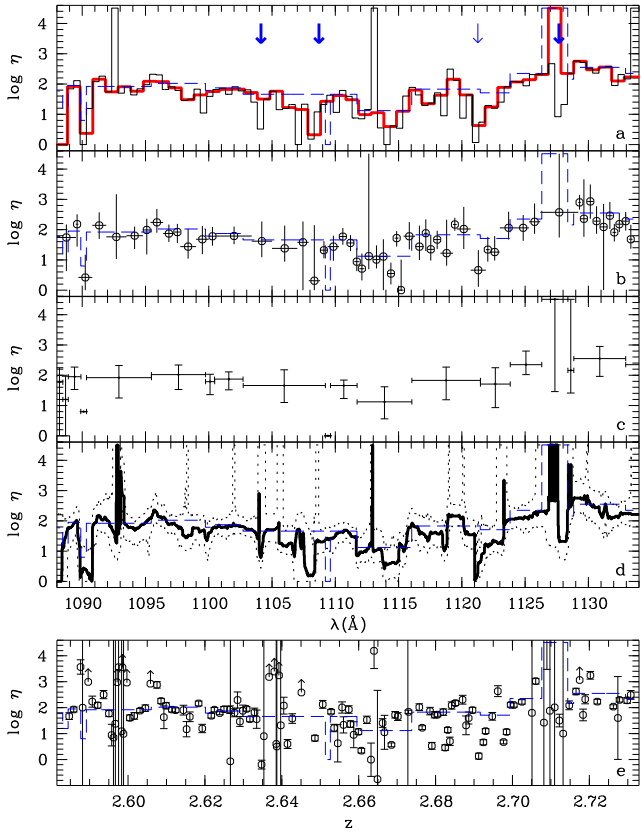

Fig. 6.3: Redshift distribution of η for the best part of the FUSE data (1088 – 1134 Å) of HE 2347-4342 using different fit interval definitions. (**a**): constant binning with bin sizes of 0.5 Å (thin line) and 1.0 Å (thick line). The uncertainties are omitted for a clearer presentation. (**b**): fit interval definition by eye. (**c**): bin size estimated by a χ^2 procedure. (**d**): estimation of η per pixel averaged over 1.0 Å, i.e. 40 pixels. The dotted line represents the $1\,\sigma$ uncertainties. (**e**): result from profile fitting. The dashed lines in each panel indicate the η distribution yielded with the χ^2 procedure (panel **c**) for better comparability. All presented errors specify $1\,\sigma$ uncertainties. The positions of metal absorption systems are indicated as arrows in panel **a**.

Table 6.2: Metal line systems with $z > 2.3$ in the spectrum of HE 2347-4342.

z	observed ions
2.3132[a]	C III, C IV, Si III, Si IV
2.3475	C III[c], C IV, O VI[b]
2.3741	O VI[b]
2.4382	C III[c], C IV, O VI[c]
2.4887	C IV, O VI[c]
2.6346	C IV, O VI
2.6497	C III[c], C IV, O VI
2.6910	O VI[a]
2.7121	C IV, O VI[a]
2.735[d]	C II, C III, O VI, Si III, Si IV
2.8628	C III, C IV, O VI
2.8781	C IV, N V
2.895[e]	C III, C IV, N V, O VI

[a] apparently related to a QSO close to the line of sight at $z = 2.31$ (Jakobsen, private communication)
[b] only one doublet component detected
[c] uncertain detection due to blends
[d] Lyman limit system
[e] complex associated system

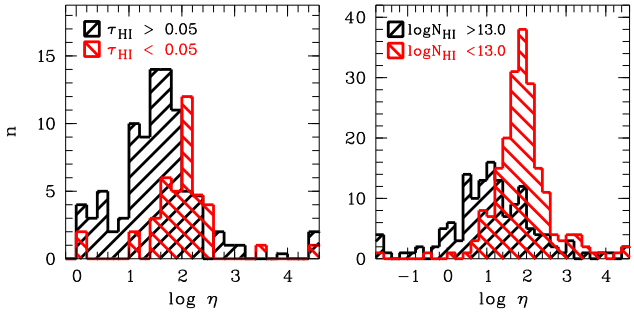

Fig. 6.4: Distribution of η in voids and filaments derived from binning with constant bin size (1 Å; left panel) and line profile analysis (right panel) in the Lyα forest region ($z \lesssim 2.73$) towards HE 2347-4342. Following Shull et al. (2004), voids are defined as bins with a mean opacity in hydrogen of $\tau_{\rm H\,I} < 0.05$. Concerning the results from the line profile-fitting procedure, we consider lines with $\log N_{\rm H\,I} > 13.0$ to arise from filaments.

procedure is presented in the right panel of Fig. 6.4. The optical depth of $\tau = 0.05$ at the central point of the Doppler profile for a H I Lyα line of the width $b = 27.0\,{\rm km\,s^{-1}}$ is reached at $\log N = 12.25$. In Lyα forest statistics, a void is defined as a region without any absorption features stronger than $\log N_{\rm H\,I} \sim 13.5$ over a certain comoving size (e.g. Kim et al. 2001). As a compromise and in order to maintain a sufficient number of high density absorbers, we consider lines with $\log N < 13.0$ as low density absorbers. Furthermore, lines with column densities $\lesssim 10^{13}\,{\rm cm^{-2}}$ seem to remain unaffected by effects of thermal line broadening (see Section 6.4 for more details). For the low density sample we find the mean value $\log \eta = 1.90 \pm 0.74$. Absorbers with $\log N > 13.0$ lead to $\log \eta = 1.21 \pm 1.50$. Considering different samples of strong H I absorbers, we find that the mean value of $\log \eta$ decreases with increasing line strength, either defined by optical depth or H I column density. This corresponds to the suggestion of Shull et al. (2004) that low density absorbers correlate with high η values. It is also consistent with the apparent correlation of metal line systems with strong H I absorption and low η values. We suspect that this correlation is, at least partly, due to thermal line broadening, which lead to an underestimation of the He II column density for absorption features with $\log N_{\rm H\,I} \gtrsim 13.0$ if turbulent line widths are assumed. We will return to this point for further discussion in Section 6.4.

6.3.2. The patchy zone towards HE 2347-4342

The He II absorption at $z > 2.73$ is characterized by broad absorption troughs with narrow regions of low opacity

(Reimers et al. 1997a; Kriss et al. 2001; Smette et al. 2002; Zheng et al. 2004b). Reimers et al. (1997a) argued that this patchy structure can be explained by the incomplete reionization of He II, where a component of smoothly distributed gas provides additional absorption. As can be seen from the lower panel Fig. 6.2, fitting line profiles to the high opacity regions leads to large error bars and more He II lines without H I counterparts have to be added. On average 0.53 additional lines per Å are needed in the patchy zone, while only 0.27 Å^{-1} are required in the Lyα forest.

Applying the spectrum fitting method, the resulting redshift distribution of η traces the position of complete absorption and opacity gaps. Due to the small number of bins, the distribution of η does not resemble a Gaussian. However, a fit of the H I spectrum to the He II data considering the total range of patchy absorption (1134 − 1188 Å) yields $\log \eta = 2.74^{+1.77}_{-0.76}$ in good agreement with the medians for the samples considering different bin sizes. The profile-fitting analysis leads to a median $\log \eta = 2.29$. In this case, the correlation between the strength of the H I absorption and the η value is recognized again, since we find $\log \eta = 2.54 \pm 1.07$ for the sample of weak absorbers with $\log N_{\text{H I}} < 13.0$ and $\log \eta = 1.70 \pm 0.80$ when $\log N_{\text{H I}} > 13.0$.

One of the opacity gaps coincides with a metal line system at $z = 2.8628$ (also noticed by Smette et al. 2002) showing transitions of high ionization stages (C IV, O VI). Furthermore, HE 2347-4342 has a complex associated system with strong absorption of C IV, N V, and O VI in more than 10 subcomponents spread over a wide velocity range of more than 1000 km s^{-1} (Fechner et al. 2004). The associated system also coincides with a low η region (see Fig. 6.2). However, no metal line absorption is detected for the low η region and opacity gap at $z \approx 2.82$.

6.3.3. HS 1700+6416

For the analysis of the He II data of the quasar HS 1700+6416, we follow the same method as described in Section 6.2. Additionally, the metal lines predicted to arise in the FUSE spectral range (Chapter 4) are considered during the optimization procedure modifying the χ^2-estimation (Eq. 6.1):

$$\chi^2 = \frac{1}{n} \sum_{i=1}^{n} \frac{\left(f_{\text{He II},i} - \exp\left(-\frac{\eta}{4} \cdot \tau_{\text{H I},i} - \tau_{\text{met},i}\right)\right)^2}{\sigma^2_{\text{He II},i} + \sigma^2_{\text{H I},i}} \,. \tag{6.2}$$

This strategy is used, since due to the noise the results are more stable if the UV metal lines are considered as part of the fit instead of removing their optical depth from the FUSE data.

Fig. 6.5 presents the redshift distribution of η towards HS 1700+6416 derived by spectrum fitting defining the fit interval by eye (upper panel), using a χ^2 procedure (middle panel), or adopting profile fits (lower panel). Metal lines and interstellar absorption have been considered when fitting Doppler profiles (for details see Chapter 5). In the redshift range $2.60 < z < 2.75$ there is apparently only little scatter in η. Indeed, the whole range ($2.5815 \leq z \leq 2.7527$, corresponding to $\Delta z = 0.1712$) can be fitted with $\log \eta = 2.11^{+0.45}_{-0.32}$, which is in good agreement with the mean and median values resulting from the applied methods. The low value of η at $z \approx 2.735$ is due to continuum in H I and He II. In this case, the applicability of the spectrum fitting method is limited and it tends to produce low η values.

Stronger fluctuations are visible in the lower redshift range, although the search for a redshift scale using χ^2-estimation leads to a broad range at $z = 2.462 \pm 0.080$ with $\log \eta = 1.67^{+0.50}_{-0.57}$. High η values are apparently found at $z \approx 2.41$. This peak is most likely due to strong interstellar C II λ1036 absorption, which is not considered in the spectrum fit procedure. Furthermore, strong C IV absorption from the Lyman limit system at $z = 2.3155$ is expected in the UV, which is probably underpredicted (see Chapter 4). Therefore, we overestimate the amount of absorption due to He II leading to unrealistically high values of η. Considering the interstellar C II absorption should reduce the derived values. Compared to the result from the Doppler profile fits, which includes the galactic C II line, no apparent high η peak is visible in agreement with the above arguments.

A second region with high η is found at $z \approx 2.55$ close to the gap in the FUSE spectrum. Some weak silicon lines from different metal line systems are removed in the corresponding H I wavelength range, which appear only slightly blended with Lyα lines. Thus, we do not expect any systematic uncertainties from the metal line removal. The corresponding He II spectral range shows saturated features, and no interstellar or metal line absorption is expected. However, the estimated η values have large error bars indicating that this high η region might not be real.

Close to the metal line system at $z = 2.4965$, a third region of increased η can be seen, where the redshift distribution yielded by profile fitting resembles that found with the spectrum fit. The most prominent H I Lyα feature is the central component in a region ($2.485 \lesssim z \lesssim 2.504$) of weak H I absorption, i.e. a void. In the corresponding He II spectral range strong absorption is detected. However, the two data points of very low η close to $z \approx 2.50$ derived from the profile fits reflect a major problem in the interpretation of the results concerning the zero flux level of the data. The H I features at this position appear stronger than the corresponding He II features. The same effect is also visible at $z \sim 2.31$, 2.435, and 2.46, where the H I absorption at the two first redshifts is particularly strong, since they are the Lyα features of Lyman limit systems. As can be seen from Fig. 6.6, the strong He II absorption features at $z \sim 2.435$ appear to be saturated, even though the line cores do not reach zero. Therefore, conclusions drawn from the low redshift portion of the FUSE data are very preliminary. However, in the longer wavelength part of the data (> 1087 Å), no indications for an incorrect zero flux level are found. Thus, results from the range $z > 2.58$ can be assumed to be more reliable.

In the spectrum of HS 1700+6416 25 metal line systems can be identified (e.g. Vogel & Reimers 1995; Köhler

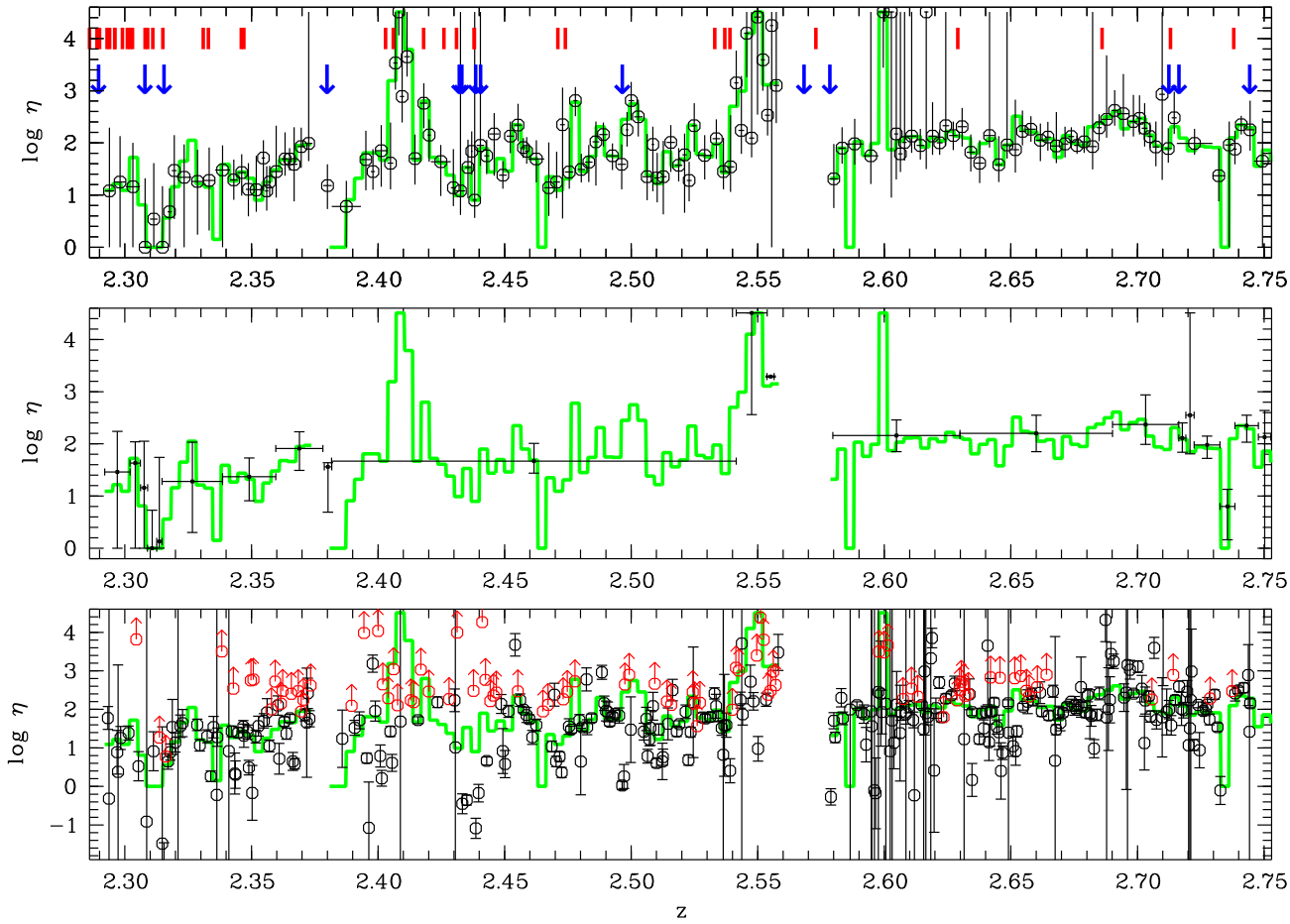

Fig. 6.5: Redshift distribution of η towards HS 1700+6416 according to the spectrum fitting method defining the fit interval by eye (upper panel) or using a χ^2 procedure (middle panel) as well as the result from profile fitting (lower panel). For a better orientation, the histogram-like line in each panel indicates η estimated with a constant 1.0 Å bin size. The redshifts of metal line absorption systems are marked as arrows in the upper panel, the position of galaxies close to the line of sight from the compilation of Shapley et al. (2005) are indicated by thickmarks as well.

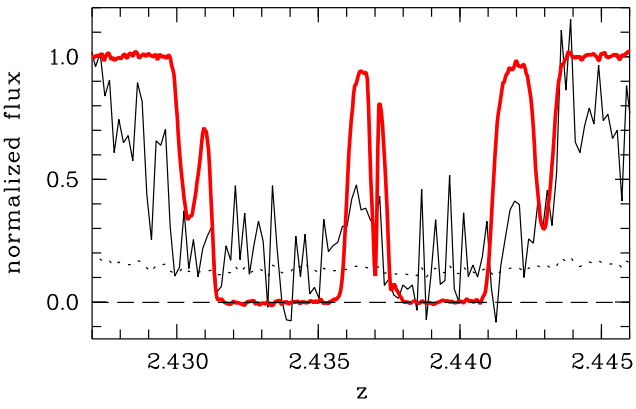

Fig. 6.6: Absorption features of H I Lyα (thick line) and He II Lyα (thin line) at $z \sim 2.435$. The profile of the He II features indicates saturation, even though the flux does not reach zero. The dotted line represents the error of the He II flux. The narrow line in between both the saturated H I troughs is Si II of the LLS at $z = 2.3155$.

et al. 1996, and Chapter 4). 13 of them are at redshifts $z > 2.29$, i.e. their He II absorption is located in the observed FUSE spectral range. However, three are affected by the H I Lyβ airglow emission or the gap in the spectrum. From the remaining systems, only three arise in the reliable upper wavelength range. All these are associated to the QSO showing absorption features of O VI and N V. The system at $z = 2.7443$ is blueshifted with respect to the quasars' emission redshift and shows multicomponent O VI absorption (Simcoe et al. 2002). Since these systems are certainly affected by the quasars' radiation, they are highly suitable to investigate the effect of hard ionizing radiation on η. Nevertheless, no indications for a proximity effect are noticeable in the distribution of η in Fig. 6.5. A slight dip might be present at $z \approx 2.71$ close to the metal line systems also visible in the profile-fitting result. Considering the blueshifted system, we do not find any hints for a depression of η.

The absence of a proximity effect in η seems to be in conflict with the presence of associated metal line absorption obviously exposed to hard quasar radiation. However, the observed redshifts of the metal line systems may not

be solely cosmological. This means, the absorbers may be located very close to the QSO ($\sim$ 10 kpc), ejected from the central region with high velocities. The system redshifted with respect to the QSO emission $z_{\rm em} \approx 2.72$ is supposed to trace infalling material, i.e. the distance to the central engine is unknown. Due to the short duty cycle of quasars ($\sim 10^6 - 10^7$ yr, e.g. Jakobsen et al. 2003; Schirber et al. 2004), the assumption of photoionization equilibrium might not be fulfilled for these systems. In addition, HS 1700+6416 is variable in the intrinsic EUV (Reimers et al. 2005b). However, short time variations are not supposed to cause deviations from ionization equilibrium.

However, there seems to be an apparent correlation of metal line systems and regions of low η at redshifts < 2.55 (see Fig. 6.5), which have to be interpreted carefully due to the discussed uncertainties in the zero flux level.

In Chapter 4 we found that the majority of the metal line systems with $z \gtrsim 2$ towards HS 1700+6416 can be modelled convincingly using a modified version of the Haardt & Madau (2001) UV background. The modification of the shape of the ionizing spectrum is a shift of the break usually located at 4 Ryd to lower energies (3 Ryd, HM3). The column density ratio η expected for this radiation field is $150 - 190$, depending on the exact position of the break. If this shape of the ionizing radiation is representative for the IGM in general, the expected column density ratio would be $\log \eta \sim 2.2$, consistent with the value found by fitting the H I spectrum to the upper FUSE spectral range. The metal line systems, however, probe the high density IGM. Therefore, according to the analysis of metal line systems, at least the high density absorbers are expected to show high η values, which contradicts the results obtained by measuring H I and He II directly. We suspect that this conflict can be solved if thermal line broadening is taken into account. The distribution of the Doppler parameters derived from line profile fitting has its maximum at $b_{\rm H\,I} \approx 23\,{\rm km\,s^{-1}}$. If this line width is interpreted to be completely thermal, the corresponding temperature is roughly $T \approx 3 \cdot 10^4\,{\rm K}$, which is close to the value $2 \cdot 10^4\,{\rm K}$ estimated by Ricotti et al. (2000). Lai et al. (2005) even predict temperature fluctuations due to inhomogeneous He II reionization with temperatures as high as $3 \cdot 10^4$ K. Thus, contributions from thermal broadening to the line width are expected to be important at least for part of the absorbers.

6.4. Discussion

The analysis of the He II data of HE 2347-4342 revealed an apparent correlation between regions of low η and the presence of metal line absorption systems. This finding is confirmed towards HS 1700+6416, albeit systematical uncertainties possibly affect the results of this line of sight. In order to investigate biases caused by the assumption made for the investigation, we analyze artifical data. Since turbulent line broadening is implicitly assumed in the spectrum fitting procedure, we consider two sets of profiles dominated by thermal and turbulent broadening, respectively.

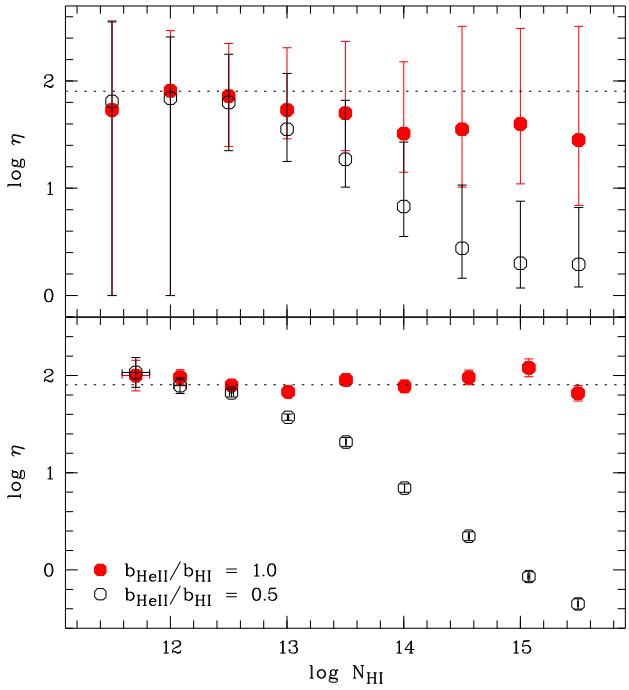

Fig. 6.7: Dependence of η on the strength of the H I absorption as derived from artificial absorption features in case of the spectrum fitting method (upper panel) and the profile-fitting procedure (lower panel). For several column densities of H I and $b_{\rm H\,I} = 27.0\,{\rm km\,s^{-1}}$, line profiles of H I and He II are calculated with $\eta = 80$ and $b_{\rm He\,II} = b_{\rm H\,I}$ (turbulent broadening, filled circles) or $b_{\rm He\,II} = 0.5 \cdot b_{\rm H\,I}$ (thermal broadening, open circles), respectively. The artificial data was analyzed assuming pure turbulent broadening. The dashed line indicates the presumed value of η.

The artificial lines are computed as Doppler profiles with $z = 2.6194$, $b_{\rm H\,I} = 27.0\,{\rm km\,s^{-1}}$ and different values of the H I column density with $11.5 \le \log N_{\rm H\,I} \le 15.5$. The He II column density is $\log N_{\rm He\,II} = \eta \cdot \log N_{\rm H\,I}$ with $\eta = 80$. Two He II features are computed for each column density representing both the extremes of line broadening, pure turbulence $b_{\rm He\,II} = b$ and thermal broadening $b_{\rm He\,II} = \frac{1}{2}\, b_{\rm H\,I}$. The generated line profiles are convolved to match the resolution of the observed optical ($R \approx 45\,000$) or UV spectra ($R \approx 20\,000$), respectively. Noise is added to have $S/N \sim 100$ in case of H I and ~ 5 in case of He II.

The simulated lines are analyzed twice, fitting the spectrum and Doppler profiles. Fig. 6.7 shows the inferred η as a function of the underlying H I column density. Both fitting procedures severely underestimate η for strong H I lines if the assumption of turbulent broadening is incorrect. Here we consider the extreme of pure thermal broadening, where the Doppler parameter of He II is half the value of H I. In reality, there will be a mixture of thermal and turbulent broadening. Zheng et al. (2004b) even find that turbulent broadening is dominant. Also Bolton et al. (2005) argue that thermal broadening is supposed to be negligible, since Hubble broadening is expected to be the dominant contribution to

the width of Lyα forest lines. However, the stronger the contribution of thermal broadening, the more the inferred η will underestimate the actual value.

If turbulent broadening is indeed dominating, line profile fitting recovers well the underlying η. In this case, the artificial lines are computed as Doppler profiles. Therefore, profile fits are supposed to recover the correct values, in particular since only a single line is considered. A more detailed exploration would require hydrodynamical simulations. Such an investigation is presented by Bolton et al. (2005) exploring the applicability of line profile fitting. They find that η is inferred accurately using this technique (but see discussion below).

According to our synthetic line profiles, the spectrum fitting method exhibits deviations from the underlying η value even in the case of turbulent broadening. The reason is that we use the relation $\tau_{\mathrm{He\,II}} = \eta/4 \cdot \tau_{\mathrm{H\,I}}$ to scale the H I spectrum, which is only valid for optically thin lines. Though the correct η is recovered within the $1\,\sigma$ error bars, the root-mean-square deviation is roughly 0.16 for column densities $\log N_{\mathrm{H\,I}} \geq 13.5$. Considering a sample of synthetic line profiles with $\log \eta = 1.0$, the spectrum fit method recovers the underlying column density ratio more accurately in the case of stronger H I features.

With this information about potential methodical problems, there are three possible interpretations of the apparent correlation between low η and strong H I absorption: (1) a methodical bias, (2) an effect of thermal line broadening, or (3) physical reality. In the following, we will discuss these interpretations and their implications.

6.4.1. Methodical uncertainties

Due to methodical effects η might be systematically underestimated for strong H I absorbers, since $\tau_{\mathrm{He\,II}} = \eta/4 \cdot \tau_{\mathrm{H\,I}}$ is only valid for optically thin lines. Since metal lines arise particularly in strong Lyα systems, this would lead to the apparent correlation. At first glance only the results from spectrum fitting should be affected in this way. In accordance with Fig. 6.7 and the investigation of Bolton et al. (2005) profile fits recover the underlying η values. However, the scatter plots of the column density ratio η presented by Bolton et al. (2005, their Fig. 4) show a slight tendency to smaller η values in the case of higher H I column densities, even for a uniform UV background. Due to the power law behaviour of the column density distribution function (e.g. Kirkman & Tytler 1997; Kim et al. 2001), high column density absorbers are less numerous than weaker lines. Thus, strong absorbers represent only a minor fraction of the investigated line sample with a negligible contribution to the overall statistics. Therefore, it is necessary to extend the analysis of simulated data with the purpose to obtain a sufficiently large statistical sample in order to investigate high column density absorbers ($\log N_{\mathrm{H\,I}} \gtrsim 14.0$) in more detail.

6.4.2. Thermal broadening

Assuming that the profile-fitting procedure recovers the column density ratio accurately, the apparent correlation between metal line absorption and low η should be no methodical artifact. The reason is that the correlation is also recognizable in the profile-fitting results (Fig. 6.2 and 6.5). Then, Fig. 6.7 suggests that the line widths of H I and He II features with associated metal line absorption might be dominated by thermal broadening. In general, lines with $N_{\mathrm{H\,I}} \gtrsim 10^{13}\,\mathrm{cm}^{-2}$, if dominated by thermal broadening, would produce extremely low η values due to the method for both procedures. As a consequence the majority of the lines showing low η values from profile fitting should be located close to the cut-off of the $b(N)$ distribution.

Fig. 6.8 shows the measured H I column density versus the b-parameter (both logarithmic) as well as $\log N_{\mathrm{H\,I}}$ versus the column density ratio η for the combined line sample of HE 2347-4342 and HS 1700+6416. The right panel illustrates the correlation of η with the strength of the H I absorption. Points with $\log \eta < 1.0$ are highlighted. Their average column density is 13.80 ± 0.92. Less than 18 % of the low η lines have H I column densities $< 10^{13}\,\mathrm{cm}^{-2}$, supporting the suspicion that only absorbers with column densities above this threshold are affected. In the N-b diagram points with $\log \eta < 1.0$ accumulate close to the lower envelope. This means, thermal broadening is expected to be relevant for these lines.

We roughly estimate the cut-off b-parameter by an iterative procedure (Schaye et al. 1999, 2000; Kim et al. 2002b) including only lines with $\sigma_b/b < 0.5$ and $\sigma_{\log N_{\mathrm{H\,I}}}/\log N_{\mathrm{H\,I}} < 0.5$. According to Hui & Gnedin (1997), the tight power law relation between the temperature and density is only valid in the low density IGM, which gives raise to the majority of the Lyα forest features. Using the relation between hydrogen column density and overdensity δ given by Schaye (2001), an overdensity of $\delta \approx 10$ roughly corresponds to $\log N_{\mathrm{H\,I}} \approx 15.0$. In order to avoid biases due to incompleteness (Kim et al. 2002b), only lines above the completeness limit are considered. We constrain the sample used for the fit to lines with $12.5 < \log N_{\mathrm{H\,I}} < 15.0$. The final sample contains about 66 % of the total lines and has a mean redshift of $\langle z \rangle = 2.58$.

For the model $\log b_{\mathrm{c}} = (\Gamma - 1) \cdot \log N_{\mathrm{H\,I}} + \log b_0$ we find $(\Gamma - 1) = 0.118 \pm 0.005$ and $\log b_0 = -0.27 \pm 0.07$ in agreement with the results of Kim et al. (2002b). Considering the low η lines ($\log \eta < 1.0$), about 66 % are within $5\,\sigma$ of the cut-off, where we adopt $\sigma = 0.026$ the standard error of the fit estimate. Furthermore, the mean column density ratio of all data points of the fit sample within $\log b_{\mathrm{c}} \pm 5\,\sigma$ is $\log \eta = 1.37 \pm 1.06$ (median 1.32), which is lower than the mean value of the total fit sample 1.58 ± 1.13 (median 1.56). The effect gets more pronounced for data points located closer to the cut-off. Considering the points within $2\,\sigma$ ($1\,\sigma$) the median value of $\log \eta$ is 1.23 (1.02). Extrapolating the estimated cut-off to lower and higher column densities, we find the same effect, i.e. the median column density

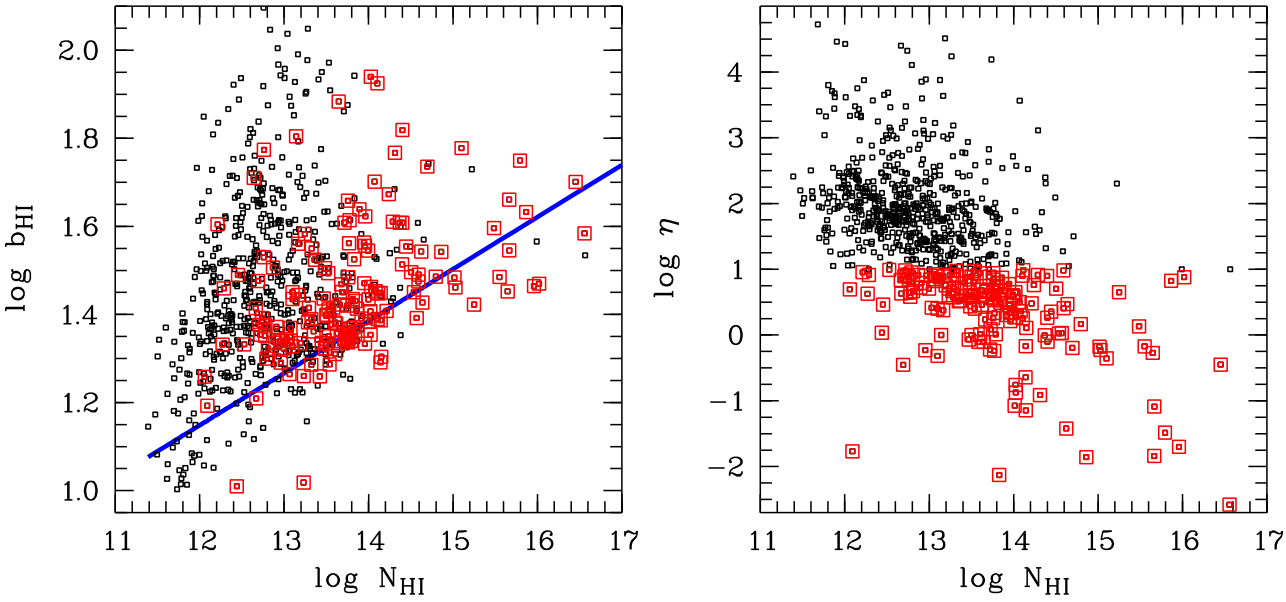

Fig. 6.8: Measured H I column density versus logarithmic Doppler parameter (left panel) for the combined line sample of HE 2347-4342 and HS 1700+6416. The solid line represents the iteratively estimated cut-off b-parameter $\log b_c = 0.118 \cdot \log N_{\rm H\,I} - 0.27$ (see text). Only lines with $12.5 < \log N_{\rm H\,I} < 15.0$ and $\sigma_b/b < 0.5$ and $\sigma_{\log N_{\rm H\,I}} / \log N_{\rm H\,I} < 0.5$ are considered. The right panel shows are the distribution of η with the H I column density. Lines with $\log \eta < 1.0$ are highlighted.

ratio decreases, the closer the considered lines are located to the cut-off. Within $5\,\sigma$ ($2\,\sigma$, $1\,\sigma$) the median value is $\log \eta = 1.51$ (1.29, 1.22).

Fig. 6.9 illustrates the dependence of the inferred column density ratio from the distance $d = |\log b_c - \log b_{\rm H\,I}|$ to the cut-off in the $b(N)$ distribution, i.e. from the contribution of thermal line broadening. The cumulative distribution of the median η values is given for the total ($\log N_{\rm H\,I} < 15.0$) sample as well as a low and high density subsample, which comprise the lines with $\log N_{\rm H\,I} < 13.0$ and $13.0 < \log N_{\rm H\,I} < 15.0$, respectively. It is clearly seen that the low density sample approaches a larger median η value ($\log \eta = 1.94$) than the high density sample (1.32). The low density sample reaches the plateau values close as 98 % at $d \approx 0.04$, where only 6 % of the data points are used to estimate the median. The same level, i.e. 98 % of the plateau value, is reached at $d \approx 0.62$ in the case of the high density sample, where 97 % of the absorbers are included. These numbers illustrate that high density absorption features are statistically more sensitive to the distance the the $b(N)$ cut-off than low density lines. The cumulative distribution of the total sample reaches a plateau value of 92 % of that of the low density sample, i.e. $\log \eta = 1.77$, but follows the smoother rise of the high density sample. 98 % of the plateau value is reached at $d \approx 0.34$.

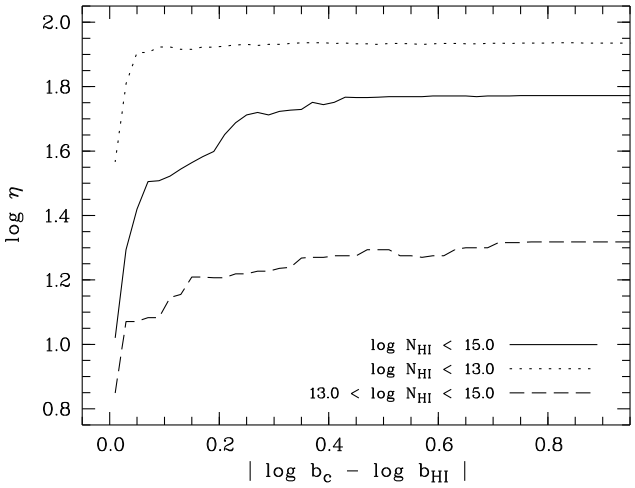

Fig. 6.9: Cumulative distribution of the median $\log \eta$ with the distance $d = |\log b_c - \log b_{\rm H\,I}|$ from the $b(N)$ cut-off. The median column density ratio is estimated considering all absorbers within the given distance from the cut-off $\log b_c$. The solid line represents all absorbers with $\sigma_b/b < 0.5$, $\sigma_{\log N_{\rm H}} / \log N_{\rm H\,I} < 0.5$, and $\log N_{\rm H\,I} < 15.0$. Additionally, the distributions of the low density sample containing absorbers with $\log N_{\rm H\,I} < 13.0$ (dotted) and the high density sample with lines $13.0 < \log N_{\rm H\,I} < 15.0$ (dashed) are indicated.

We conclude that absorption lines dominated by thermal broadening, i.e. located close the the thermal cut-off of the $b(N)$ distribution, reveal systematically low column density ratios η when applying standard analysis procedures. In consequence, the apparent correlation between the strength of the H I absorption and high η values should be reconsidered. As illustrated in Fig. 6.7, the column density ratio of weaker H I absorbers ($\log N \lesssim 13.0$) will be well recovered even if the assumption of turbulent broadening is incorrect. While weak H I lines supposedly represent an unbiased sample (represented by the low column density sample shown in Fig. 6.4), strong lines are expected to be biased towards lower η values. Hence, weak lines are expected to show on

average higher column density ratios than strong lines (see also Fig. 6.9). Thus, the correlation of the column density ratio with the strength of the H I absorption can be explained by inadequate handling of thermal broadened lines by the applied analysis procedures.

According to this result, only the low density Lyα forest should be used to estimate the column density ratio. Considering only absorbers with $\log N_{\rm H\,I} < 13.0$ the mean η value of the combined sample of HE 2347-4342 and HS 1700+6416 is $\log \eta = 2.03 \pm 0.89$ (median 1.94). If the patchy zone in the spectrum of HE 2347-4342 is neglected, we yield $\log \eta = 1.95 \pm 0.83$ (median 1.92). For the Lyα forest towards HE 2347-4342, we find 1.90 ± 0.74 (median 1.88), and towards HS 1700+6416 2.00 ± 0.92 (median 1.94). These values are roughly 0.3 dex higher than those obtained including the high density absorbers. The spectrum fitting method leads to values roughly 0.2 dex lower than those derived from the low density samples but are significantly higher than the average values for the total line samples, implying that it is less sensitive to the systematic errors due to thermal line widths. However, this is only valid on scales $\Delta z \gtrsim 0.1$. Variations of η on smaller scales are possibly affected by methodical uncertainties due to thermal line broadening.

Further support is provided by the photoionization models of the metal line systems in the spectrum of HS 1700+6416 derived in Chapter 4. The system at $z = 2.4965$, for example is modelled using a modified Haardt & Madau (2001) UV background (HM3). Doppler parameters are computed by comparing the model temperature with the observed b-parameter of a well-measured ion (for further details see Chapter 4). For this system, the velocity ratio $\xi = b_{\rm He\,II}/b_{\rm H\,I}$ is ~ 0.50, i.e. the line width is determined by pure thermal broadening. The modelled column density ratio is $\log \eta = 2.35$. Fitting line profiles, we assume pure turbulent broadening and find $\log \eta = 0.01 \pm 0.11$ (clearly seen in the lower panel of Fig. 6.5 at $z \approx 2.5$). This supports the above argumentation that the column density ratio is severely underestimated if absorbers with thermal line widths are analyzed assuming turbulent line broadening. Considering all metal line systems modelled in Chapter 4, the mean velocity ratio is $\xi = 0.59 \pm 0.08$, where the column density of the H I components is on average $\log N_{\rm H\,I} = 15.5 \pm 0.7$. Thus, according to the photoionization models the line widths of strong metal line systems towards HS 1700+6416 are basically due to thermal broadening and can therefore explain the apparent correlation between low η values.

6.4.3. Physical implications

Even if part of the low η values can be explained by systematical biases due to thermal broadening, part of them might be real. In such cases, the coincidence of low η values and metal line absorption systems, showing features of highly ionized material, suggest the vicinity of a hard radiation source like an AGN. Alternatively, the presence of O VI may also imply the presence of a hot, collisionally ionized gas phase. The suspected redshifts would be $z \sim 2.40$, 2.48, 2.63, 2.65, 2.69, as well as 2.82 and 2.86 towards HE 2347-4342. Further support for this assumption is provided by the detected metal lines of highly ionized species (see Table 6.2). Bolton et al. (2005) showed that fluctuations may be due to variations in the number, luminosity and spectral shape of the small number of QSOs. In our case, the redshift range $z \sim 2.40$ towards HE 2347-4342 is of particular interest. It is the center of an apparent void in H I, where we measure low η values. We find $\log \eta = 1.07^{+1.13}_{-1.07}$ for $2.39 < z < 2.40$. In the optical some weak absorption features with $\log N_{\rm H\,I} < 13.5$ are detected. The redshift ranges $2.376 < z < 2.384$ and $2.401 < z < 2.419$, where only H I lines with $\log N_{\rm H\,I} \lesssim 12.7$ are detected, exhibit high η values ($\log \eta = 2.14^{+0.49}_{-0.76}$ and $2.41^{+0.83}_{-0.67}$, respectively). Besides fluctuations due to statistical properties of the ionizing sources, this configuration may indicate the spatial vicinity of a QSO. However, since there are no published positions of QSOs close to this line of sight for the required redshift range, its presence cannot be confirmed to date.

Towards HS 1700+6416 the amplitude of the observed fluctuations is apparently smaller, in particular in the redshift range $2.58 < z < 2.75$ where the data quality is best. This may be partly due to the lower noise level of the FUSE data. HS 1700+6416 was target of deep direct observation campaigns with the aim to identify galaxies close to the line of sight (Teplitz et al. 1998; Erb et al. 2003; Shapley et al. 2005). Among the galaxies identified by Shapley et al. (2005) there are three objects showing indications of quasar activity. They are located at $z \approx 2.293$, 2.333, and 2.347, which is at the low edge of our FUSE data. We see indeed indications of relatively low η regions in this redshift range. However, due to the poor data quality in this part, this coincidence should be considered very preliminary.

6.5. Summary and conclusions

We have re-analyzed the He II data of the QSOs HE 2347-4342 and HS 1700+6416, both observed with FUSE. The new method we applied is based on the idea to fit the observed high-quality optical spectrum to the noisy far-UV data globally. This approach should minimize effects due to noise, which limits the applicability of the apparent optical depth method (Fox et al. 2005), and avoid the subjectivity of a profile-fitting procedure. Fitting the metal line cleaned H I Lyα forest to the He II data leads to $\log \eta = 1.79^{+0.71}_{-0.74}$ for $2.33 < z < 2.73$ towards HE 2347-4342 and $\log \eta = 1.95^{+0.48}_{-0.40}$ for $2.29 < z < 2.75$ towards HS 1700+6416. These results are in agreement with the median values from the Doppler profile analysis, however, lower than the median for lines with $\log N_{\rm H\,I} < 13.0$, which we interpret as due to the neglect of thermal broadening (see below). The mean value of the Lyα forest lines with $\log N_{\rm H\,I} < 13.0$ in both quasars is $\log \eta = 1.95 \pm 0.83$, i.e. $\eta \sim 90$.

Strong local deviations from the average suggest that the

column density ratio is fluctuating on smaller scales. In order to determine the redshift scale on which η fluctuates, we estimate the width of the spectral range, that can be fitted with a minimal χ^2. We find redshift intervals of the sizes $0.0013 \lesssim \Delta z \lesssim 0.0473$ in the case of HE 2347-4342. Due to the noisy FUSE data, the result is biased towards small scales. For the best part of the spectrum (1088 − 1134 Å), the average redshift interval is $\Delta z = 0.0082 \pm 0.0065$ (median 0.0072, i.e. $\sim 5.9\,h^{-1}$ Mpc comoving[1]). In case of HS 1700+6416, the typical length scale is $\Delta z = 0.0092$ (median) corresponding to $\sim 7.5\,h^{-1}$ Mpc comoving, but also scales up to $\Delta z = 0.1598$ are found. However, strong H I lines, whose line widths are dominated by thermal line broadening, may lead to an apparent decrease of η. Consequently, the derived scales are biased towards small values. Therefore, the resulting scales for fluctuations of the column density ratio are only preliminary until this influence of the line width on the results has been investigated in more detail. A rough estimate neglecting the small values leads to $\Delta z \sim 0.01 - 0.03$, corresponding to $8 - 24\,h^{-1}$ Mpc comoving.

Towards HE 2347-4342 we detect a H I void in the range $2.37 \lesssim z \lesssim 2.43$, also showing fluctuations of η on scales of $\Delta z \sim 0.01 - 0.02$ ($8.5 - 17.0\,h^{-1}$ Mpc comoving). The void's central region at $z \sim 2.40$ exhibits low η values suggesting the vicinity of a QSO close to the line of sight. On the other hand, no proximity effect can be seen towards HS 1700+6416, even though there are metal absorption systems showing material like N V and O VI supposed to be exposed to the quasar's radiation field.

The correlation between H I voids and small η values as claimed by Shull et al. (2004) and Reimers et al. (2004) has been re-investigated. We find that the distribution of the column density ratio η peaks at higher values for samples consisting of stronger H I absorption lines or higher H I optical depth, respectively. However, simple tests with artificial data reveal that both analysis procedures considered here would severely underestimate η in the case of strong H I absorption ($\log N \gtrsim 13.0$) if the line width would be dominated by thermal broadening. Investigating the $b(N)$ distribution of the line sample obtained from Doppler profile fitting, we find indeed that the majority (66 %) of lines with $\log \eta < 1.0$ is located within $5\,\sigma$ of the temperature cut-off. Inversely, the average column density ratio decreases if the considered line sample is located closer to the cut-off. The median value is $\log \eta = 1.23$ (1.02) for lines within $\pm 2\,\sigma$ ($1\,\sigma$) from the cut-off. Photoionization models of the metal line systems towards HS 1700+6416 (Chapter 4) support this finding, since there are indications that the line widths of most of the modelled systems are dominated by thermal broadening. Thus, at least part of the low η values are due to systematic biases caused by analyzing thermal broadened absorbers under the assumption of pure turbulent broadening. Since the sensitivity of the absorbers to this effect is correlated with the H I column density, thermal line broadening provides an explanation of the apparent correlation between η and the strength of the H I absorption. Consequently, only low density H I absorbers provide an unbiased sample, since their inferred results are insensitive to the assumed line broadening mechanism. As median column density ratios for absorbers with $\log N_{\mathrm{H\,I}} < 13.0$, we find $\log \eta = 1.90$ towards HE 2347-4342 and 1.94 towards HS 1700+6416. These values are about 10 % higher in comparison to those inferred from the total sample.

Metal line absorption usually arises from high density H I absorbers. Consequently, they lead systematically to low η values. This is particularly seen in the spectrum of HE 2347-4342. Towards this QSO the concerned systems show highly ionized species like C IV and O VI. The presence of high ionization lines suggests that the apparent correlation is not only a systematic effect due to the analysis method but the absorbers may be exposed to the hard radiation of local quasars. However, in order to verify this supposition, a search for QSOs in the field of HE 2347-4342 is required.

[1] $\{\Omega_{\mathrm{M}}, \Omega_{\Lambda}, h\} = \{0.3, 0.7, 0.7\}$

7. Conclusions

7.1. Summary

In this study the intergalactic UV background has been investigated using new observations of the He II Lyα forest towards the quasar HS 1700+6416 as well as He II data of the quasar HE 2347-4342. In addition, rough constraints on the shape of the UV background have been made analyzing the numerous metal line systems in the spectrum of HS 1700+6416. The analysis of the observed data has been combined with a simple study of artificial spectra. This combination allows to estimate the limitations of the applied methods, which turned out to be an important issue for the interpretation of the results.

In the following we summarize the main results of this study:

- Unrecognized metal line absorption in the He II Lyα forest can mimic high values of η. Thus, it is essential to consider expected metal line absorption in the analysis of the He II data.
- Applying the standard analysis methods (line profile fitting procedure and an apparent optical depth method) to the total dataset will lead to an underestimated average η value. This is due to effects of line saturation in the case of the apparent optical depth method and due to thermal line broadening in the case of the profile fitting procedure. Consequently, the applicability of the methods are restricted to subsamples of the data. Lines with $12.0 \leq \log N_{\mathrm{H\,I}} \leq 13.0$ or bins with $0.01 \leq \tau_{\mathrm{H\,I}} \leq 0.1$, respectively, are supposed to reveal unbiased results.
- Applying the methods to the restricted data, a scatter in the results of roughly $10 - 15\,\%$ is still expected, even if the underlying η value is constant. The accuracy of the apparent optical depth method is limited by the noise level of the spectra, and uncertainties due to the decomposition of blends affect the results fitting line profiles.
- A prediction of the metal lines expected to arise in the far-UV spectrum (1000 – 1180 Å) of HS 1700+6416 has been derived considering the observed metal line features in the optical and the UV. Among eight models based on different shapes of the ionizing radiation the best fitting one has been selected for each system. The majority of the systems at $z \gtrsim 2$ can be modelled best with a UV background similar to that of Haardt & Madau (2001), where the break usually located at 4 Ryd is shifted to lower energies ($\sim$ 3 Ryd). At lower redshifts ($z \lesssim 2$) individual sources seem to become more important for the ionization of the metal line systems, since we find no preferred radiation field.
- Comparing the results of the different photoionization models suggests that analyzing a metal line system adopting a Haardt & Madau (2001) UV background would overestimate the metallicity, if the true radiation field is softer.
- The He II Lyα forest towards HS 1700+6416 has been analyzed taking into account the expected metal line absorption as well as absorption arising from galactic molecular H_2. In comparison to the results from neglecting metal lines and galactic H_2, 25 % of the fitted He II features are affected by additional absorption. For 16 % of the lines the η value changes by more than $\Delta \log \eta = 0.01$. Furthermore, 30 % less He II components without detected H I counterpart are required, since some of the features can be identified as metal lines.
- The average η value towards HS 1700+6416 is $\eta \approx 130$ in the redshift range $2.58 < z < 2.75$ supporting the idea of a contribution of soft sources like galaxies to the UV background.
- The He II/H I ratio increases with redshift, consistent with theoretical predictions. Thus, the IGM is exposed to a softer radiation field at higher redshift. This finding can be explained by the higher fraction of diffuse gas at high redshift attenuating the radiation by reprocessing.
- The scatter in the redshift distribution of η is larger than expected from the artificial data assuming a constant value. This is still true even if a redshift evolution of η is taken into account. Thus, part of the scatter is supposed to be real.
- A new method of η estimation has been developed, where the observed H I spectrum is fitted directly to the He II data. This spectrum fitting method permits the estimate of the scales on which η varies. We find smooth variations on scales of $\Delta z \sim 0.01 - 0.03$, corresponding to $\sim 8 - 24\,h^{-1}$ Mpc comoving, or even larger.
- The smooth evolution of the He II opacity in the post-reionization universe ($z \lesssim 2.8$) is consistent with $\tau_{\mathrm{He\,II}} \propto (z+1)^{3.5}$.
- A crucial point of the analysis is the assumption of $b_{\mathrm{He\,II}} = b_{\mathrm{H\,I}}$, i.e. pure turbulent broadening. Tests with artificial data show that η is significantly underestimated for features with $N_{\mathrm{H\,I}} \gtrsim 10^{13}\,\mathrm{cm}^{-2}$, if the line width is dominated by thermal broadening. Estimating the cut-off of the $b(N)$ distribution, the average η values indeed decreased for line samples located close to the temperature cut-off by more than 0.5 dex.

- Since high density H I absorbers underestimate η more strongly than low density absorbers, if thermal broadening is present, a correlation between η and the strength of the H I absorption is implied. However, this correlation only reflects the problems assuming pure turbulent broadening.

7.2. Outlook

One of the main results from this study is that the assumption of pure turbulent line broadening is in general not fulfilled and limits the conclusions that can be made from the data. All analysis methods applied so far (line profile fits, apparent optical depth, and spectrum fitting) include this assumption and, therefore, suffer from the same limitations. The approach of the apparent optical depth and the spectrum fitting method are a priori not qualified to consider different line widths for H I and He II features. However, line profile fitting can easily abandon the assumption of pure turbulent broadening. In principle, the Doppler parameter of He II can be fitted independently, though physically reasonable results require values in the range $\frac{1}{2} b_{\mathrm{H\,I}} \leq b_{\mathrm{He\,II}} \leq b_{\mathrm{H\,I}}$. Due to the high noise level of the He II data the estimation of several free parameters per line is difficult and might give rise to additional uncertainties. However, future studies of the He II Lyα forest have to overcome these problems to make any progress.

In order to develop and test strategies to consider thermal line broadening, studies of simulated data are needed. They provide the possibility to control the basic physical and methodical aspects. The artificial data used in this work are generated on the basis of the observed statistical properties of the Lyα forest and, thus, present the simplest approach. A more sophisticated investigation requires hydrodynamical simulations. A first study of simulated data from the hydrodynamical point of view has been presented by Bolton et al. (2005). The authors show that line profile fitting reasonably recovers the underlying η values. However, they also make the assumption of purely turbulent line broadening and do not examine possible consequences. A detailed study addressing the question of thermal broadening on the basis of simulated data is needed. Since the discovered problems are more pronounced for strong H I absorption features, they need to be considered in particular. Due to the power law decline of the column density distribution function high density absorbers are less numerous than weak lines. Therefore, large line samples are required to investigate the behaviour of high density absorbers statistically.

Another open question is the scale of the η fluctuations. Since η is found to be recovered with a scatter over roughly 1 dex even if the underlying value is constant (the same result is obtained by Bolton et al. 2005), the estimate of the real underlying scales and amplitudes of the variation is not straight forward to define. Exploring these scales would give insight into the variations of the UV background and how the fluctuations are generated. In combination with searches for QSOs and galaxies close to the line of sight, the influence of local sources could be investigated observationally.

Observational campaigns to identify galaxies close to the line of sight of HS 1700+6416 have already been performed (Teplitz et al. 1998; Erb et al. 2003; Steidel et al. 2005; Shapley et al. 2005). Recent studies have related part of the metal line systems to the galaxies observed (Adelberger et al. 2005; Simcoe et al. 2005; Songaila 2005). A detailed investigation of a possible relation between the position of galaxies and the η value will be implemented in future work. Since it is still unknown whether ionizing photons can escape from galaxies at all, a relation between η and the large scale structure could be expected rather than a direct relation to the radiation. However, there are indications that some observed metal line systems are physically related to nearby galaxies and arise from outflowing material.

AGN close to the line of sight are expected to cause a transversal proximity effect in He II and therefore low η values, as detected towards the quasar Q 0302-003 by Jakobsen et al. (2003). Since there are no other examples of the transverse proximity effect in H I (e.g. Croft 2004; Schirber et al. 2004), the investigation of a possible correlation between η and the vicinity to QSOs could help to solve this discrepancy. However, as a first step observational campaigns searching for QSOs close to the lines of sight towards HS 1700+6416 and HE 2347-4342 have to be carried out.

Concerning the estimation of the shape of the UV background from observed metal line systems, pioneering work has been done by Agafonova et al. (2005). They parameterize the shape of the ionizing spectrum and then the parameters are optimized by a fitting algorithm. A physical explanation of the derived shape of the ionizing background has to be found a posteriori. Alternatively, a fit could be achieved by varying physical parameters. Since the theoretical predictions of the UV background depend on properties of the sources and absorbers like the spectral energy distribution of the contributing QSOs and the distribution of the intergalactic absorbers, different physical models of the UV background can be constructed by varying these properties. The plausibility of the models could then be constrained by the observed metal lines. This approach is complementary to that of Agafonova et al. (2005) and could help to bring together observational constraints and theoretical predictions of the shape of the UV background.

The discovery of additional He II absorbing quasars suitable for high resolution spectroscopy in the near future is rather unlikely. QSOs being UV bright and providing a transparent line of sight are rare (Picard & Jakobsen 1993). Improving the signal-to-noise ratio of the present data by a factor of 2 would require exposure times longer by a factor of 4. In case of the brightened HS 1700+6416, this would require additional night only data of roughly 600 ks. Thus, progress have to be made by more detailed studies of the present data starting with a deeper understanding of the methods used for the analysis.

A. Line parameters

A.1. Observed metal line systems towards HS 1700+6416

Table A.1: Measured column densities for the metal absorption systems at $z > 2.5$. Value marked with a colon (:) are derived from the STIS data and suffer from large uncertainties. If no value is given, the corresponding feature is not present or severely blended, and no upper limit can be estimated.

$\log N_{\rm ion}$	2.5683[a] 0.0 km s^{-1}	2.5683 16.9 km s^{-1}	2.5785[b] −30.7 km s^{-1}	2.5785 −18.5 km s^{-1}	2.5785 18.5 km s^{-1}	2.5785 40.2 km s^{-1}
H I	14.28	14.09	15.04	15.39	14.93	15.58
C II	< 11.63	< 11.63	< 11.68	< 11.68	< 11.67	< 11.68
C III	12.82 ± 0.11	12.45 ± 0.26	12.54 ± 0.10	12.18 ± 0.17	12.77 ± 9.59	13.30 ± 0.02
C IV	12.54 ± 0.13	12.53 ± 0.15	12.68 ± 0.06	13.23 ± 0.01	12.06 ± 0.16	13.05 ± 0.02
N II	< 12.10	< 12.08	...	...	...	...
N III	...	...	13.35 :	...	12.97 :	...
N V	< 11.59	< 11.59	< 11.86	< 11.86	< 11.86	< 11.86
O III	...	...	13.76 :	14.43 :	...	13.94 :
O VI	13.27 ± 0.14	...	...	14.18 ± 0.01	...	12.88 ± 0.08
Al II	< 10.67	< 10.67	< 10.96	< 10.96	< 10.94	< 10.94
Si II	< 11.51	< 11.51	< 11.57	< 11.57	< 11.57	< 11.57
Si III	11.654 ± 0.033	...	11.63 ± 0.05	11.90 ± 0.02	< 10.65	11.76 ± 0.02
Si IV	11.28 ± 0.11	< 11.11	11.63 ± 0.13	< 11.20	< 11.20	11.69 ± 0.05
Fe II	< 11.80	< 11.80	< 11.78	< 11.78	< 11.78	...

$\log N_{\rm ion}$	2.7124[c] −36.5 km s^{-1}	2.7124 0.0 km s^{-1}	2.7124 77.5 km s^{-1}	2.7164[c] −87.0 km s^{-1}	2.7164 0.0 km s^{-1}	2.7164 90.8 km s^{-1}
H I	11.915 ± 0.034	13.385 ± 0.003	13.231 ± 0.004	12.597 ± 0.016	12.627 ± 0.022	13.002 ± 0.045
C II	< 11.99	< 11.99	< 11.99	< 11.73	< 11.75	< 11.75
C III	< 11.57	...	...	...	< 11.60	...
C IV	12.513 ± 0.100	13.256 ± 0.017	12.414 ± 0.082	< 11.32	12.069 ± 0.148	< 11.31
N II	< 12.00	< 12.00	< 12.00	...	< 12.50	< 12.48
N III	< 12.30	< 12.28	< 12.26	...	< 12.27	< 12.27
N V	12.927 ± 0.218	13.584 ± 0.053	12.379 ± 0.044	12.289 ± 0.035	13.178 ± 0.007	< 11.49
O VI	...	...	...	13.659 ± 0.009	14.227 ± 0.007	13.517 ± 0.013
Ne VI	13.95 :	14.35 :	14.51 :	...	...	...
Si II	< 10.74	< 10.73	< 10.72	< 11.70	< 11.72	< 11.78
Si III	< 10.50	< 10.46	< 10.47	...	...	...
Si IV	< 11.00	< 11.00	< 11.00	< 11.00	< 11.01	< 11.01
S VI	< 12.14	12.211 ± 0.088	< 12.18	< 12.10	< 12.41	< 12.43
Fe II	< 12.19	< 12.18	< 12.20	< 12.41	< 12.41	< 12.43

[a] The total hydrogen column density estimated by fitting simultaneously Lyα and Lyβ is $\log N$(H I) = 14.50 ± 0.01. The values for the subcomponents are distributed according to carbon (C III and C IV).

[b] The total hydrogen column density estimated by fitting the Lyman series is $\log N$(H I) = 15.549 ± 0.022 at $v \approx -50$ km s^{-1} and $\log N$(H I) = 15.663 ± 0.037 at $v \approx 25$ km s^{-1}. The values for the subcomponents are distributed according to carbon (C III and C IV).

[c] System appears to be associated to the QSO and is not modelled.

Table A.2: The same as Table A.1 but for the metal absorption systems at $2.4 < z < 2.5$.

$\log N_{\rm ion}$	2.4321[a] $-23.2\,{\rm km\,s^{-1}}$	2.4321 $0.0\,{\rm km\,s^{-1}}$	2.4321 $52.8\,{\rm km\,s^{-1}}$	2.4331[b] $0.0\,{\rm km\,s^{-1}}$	2.4331 $32.4\,{\rm km\,s^{-1}}$	2.4331 $50.6\,{\rm km\,s^{-1}}$
H I	15.16	14.96	15.02	16.41	16.31	16.37
C II	< 11.45	< 11.45	< 11.45	12.808 ± 0.011	12.489 ± 0.019	11.71 :
C III	12.98 ± 0.07	12.01 ± 0.20	...	13.780 ± 0.098	...	14.242 ± 0.165
C IV	12.25 ± 0.05	12.78 ± 0.02	12.70 ± 0.04	13.192 ± 0.024	13.069 ± 0.039	12.667 ± 0.045
N II	< 12.23	< 12.20	< 12.23	< 12.25	< 12.29	< 12.21
N V	< 11.98	< 11.98	< 12.00	< 11.68	< 11.68	< 11.68
O III	...	...	...	15.61 :	...	14.83 :
O VI	< 12.38	< 12.30	< 12.38	< 13.10	< 13.10	< 13.00
Ne VI	14.09 :	13.94 :	14.61 :	14.91 :	...	14.19 :
Al II	< 10.33	< 11.39	< 11.29	10.977 ± 0.037	< 11.50	11.003 ± 0.047
Si II	< 11.33	< 11.39	< 11.39	12.357 ± 0.039	...	12.138 ± 0.076
Si III	...	12.69 ± 0.26	12.30 ± 1.11	12.824 ± 0.027	12.820 ± 0.088	12.799 ± 0.047
Si IV	< 11.14	< 11.10	< 11.15	12.609 ± 0.008	12.429 ± 0.011	12.476 ± 0.012
S VI	...	...	...	13.85 ± 1.34	< 12.00	13.21 ± 0.21
Ar IV	13.00 :	...	12.33 :	12.93 :	12.82 :	...
Ar V	...	...	12.44 :	12.14 :	12.64 :	...
Fe II	< 12.13	< 12.13	< 12.13	< 12.04	< 12.11	< 12.08

$\log N_{\rm ion}$	2.4386[c] $-72.3\,{\rm km\,s^{-1}}$	2.4386 $-28.6\,{\rm km\,s^{-1}}$	2.4386 $0.0\,{\rm km\,s^{-1}}$	2.4386 $19.1\,{\rm km\,s^{-1}}$	2.4405[d] $-71.1\,{\rm km\,s^{-1}}$	2.4405 $0.0\,{\rm km\,s^{-1}}$	2.4965 $0.0\,{\rm km\,s^{-1}}$
H I	14.32	15.13	15.30	15.40	15.490 ± 0.037	14.45 ± 0.24	14.536 ± 0.011
C II	< 11.47	< 11.48	11.89 ± 0.13	11.98 ± 0.10	< 11.42	< 11.48	< 11.63
C III	12.84 ± 0.03	13.06 ± 0.04	14.50 ± 0.37	...	12.45 ± 0.06	13.64 :	13.27 :
C IV	12.67 ± 0.01	12.71 ± 0.02	12.96 ± 0.18	12.85 ± 0.10	12.589 ± 0.018	13.065 ± 0.017	12.177 ± 0.028
N III	< 12.56	< 12.57	< 12.36	< 12.56	< 12.55	< 12.55	< 12.51
N V	< 11.69	< 11.69	< 11.69	< 11.69	< 12.07	< 12.07	< 11.94
O III	...	14.36 :	14.29 :	...	13.90 :	...	13.27 :
O VI	...	...	...	...	13.484 ± 0.065	13.20 ± 0.11	13.739 ± 0.007
Al II	< 10.31	< 10.30	< 10.30	< 10.30	< 10.32	< 10.31	< 10.34
Si II	< 11.29	< 11.29	< 11.29	< 11.29	< 11.30	< 11.30	< 11.41
Si III	...	12.69 ± 0.26	12.30 ± 1.11	...	< 10.68	< 10.70	...
Si IV	...	...	...	...	< 11.12	11.59 ± 0.09	< 11.10
S VI	...	...	...	...	...	...	< 12.60
Fe II	< 12.10	< 12.11	< 12.11	< 12.03	< 12.04	< 12.05	< 12.01

[a] The total hydrogen column density measured for the Lyman series is $\log N({\rm H\,I}) = 15.530 \pm 0.029$. The values for the subsystems are distributed according to carbon (C III and C IV).

[b] The total hydrogen column density measured for the Lyman series is $\log N({\rm H\,I}) = 16.84 \pm 0.35$. The values for the subsystems are distributed according to silicon (Si II, Si III, and Si IV).

[c] The total hydrogen column density measured for the Lyman series is $\log N({\rm H\,I}) = 15.783 \pm 0.066$. The values for the subsystems are distributed according to silicon (Si III and Si IV).

[d] The component at $-71.1\,{\rm km\,s^{-1}}$ may also be considered as a distinct system at $z = 2.4397$.

Table A.3: The same as Table A.1 but for the metal absorption systems at $2.0 < z < 2.4$.

$\log N_{\rm ion}$	2.1680[a] $-37.9\,{\rm km\,s^{-1}}$	2.1680 $0.0\,{\rm km\,s^{-1}}$	2.3155[b] $-48.8\,{\rm km\,s^{-1}}$	2.3155 $-33.3\,{\rm km\,s^{-1}}$	2.3155 $0.0\,{\rm km\,s^{-1}}$	2.3155 $35.1\,{\rm km\,s^{-1}}$	2.3155 $50.6\,{\rm km\,s^{-1}}$	2.3155 $76.9\,{\rm km\,s^{-1}}$
H I	15.58	16.83	16.38	...	15.91	15.53	...	15.61
C II	12.94 ± 0.43	12.83 ± 0.48	13.77 ± 0.01	...	13.56 ± 0.01	...	...	12.69 ± 0.10
C III	...	...	14.56 :	14.28 :	14.49 :	14.14 :	14.01 :	13.63 ± 0.12
C IV	12.766 ± 0.014	14.007 ± 0.003	15.07 ± 0.06	...	14.28 ± 0.05	14.04 ± 0.05	13.65 ± 0.12	14.35 ± 0.03
N II	< 12.55	< 12.54	12.93 ± 0.06	< 12.42	13.14 ± 0.04	< 12.41	< 12.41	< 11.49
N III	...	...	14.76 :	...	13.77 :	...	...	...
N V	< 11.84	< 11.8	13.05 ± 0.07	12.69 ± 0.09	13.09 ± 0.06	12.82 ± 0.14	12.57 ± 0.20	13.17 ± 0.03
O VI	...	...	14.35 ± 0.03	...	14.45 ± 0.18	...	...	13.84 ± 0.08
Ne III	14.10 :	14.45 :	...	...	...	...	...	...
Ne V	14.80 :	14.53 :	...	...	...	...	...	...
Ne VI	...	...	14.75 :	...	14.48 :	...	...	...
Ne VII	...	...	13.87 :	...	13.45 :	...	...	...
Al II	< 10.49	10.90 ± 0.09	11.43 ± 0.02	< 10.51	11.44 ± 0.04	...	...	...
Al III	< 10.89	< 10.93	12.20 ± 0.18	...	11.95 ± 0.18	...	...	...
Si II	< 11.02	11.73 ± 0.07	13.00 ± 0.01	< 11.51	12.73 ± 0.03	< 11.51	< 11.49	< 11.48
Si III	< 10.93	13.056 ± 0.046	...	...	...	...	...	...
Si IV	< 11.02	13.241 ± 0.002	13.748 ± 0.004	12.965 ± 0.09	13.435 ± 0.013	12.251 ± 0.019	11.918 ± 0.018	12.930 ± 0.005
Fe II	< 11.90	< 11.90	...	...	...	...	...	...

$\log N_{\rm ion}$	2.0211[c] $-63.5\,{\rm km\,s^{-1}}$	2.0211 $-35.3\,{\rm km\,s^{-1}}$	2.0211 $0.0\,{\rm km\,s^{-1}}$	2.0211 $17.2\,{\rm km\,s^{-1}}$	2.1278[c] $0.0\,{\rm km\,s^{-1}}$	2.1989[c] $-73.5\,{\rm km\,s^{-1}}$	2.1989 $-41.6\,{\rm km\,s^{-1}}$	2.1989 $0.0\,{\rm km\,s^{-1}}$
H I	...	...	15.29 ± 0.04	...	14.073 ± 0.004	...	...	15.437 ± 0.024
C IV	12.17 ± 0.03	11.45 ± 0.19	12.71 ± 0.02	12.05 ± 0.08	12.692 ± 0.012	11.72 ± 0.11	12.05 ± 0.05	12.87 ± 0.01
Al II	< 10.48	< 10.48	< 10.48	< 10.57	...	< 11.45	< 11.44	< 11.44
Si II	< 11.23	< 11.23	< 11.23	< 11.23	< 11.36	< 11.37	< 11.37	< 11.37
Si III	< 11.05	< 11.26	< 11.05	< 11.08	< 10.88	...	...	...
Si IV	< 11.14	< 11.13	< 11.13	< 11.13	< 11.05	< 11.28	< 11.30	< 11.27
Fe II	< 12.02	< 12.02	< 12.02	< 12.04	< 11.92	< 11.95	< 11.95	< 11.94

$\log N_{\rm ion}$	2.2895 $-22.4\,{\rm km\,s^{-1}}$	2.2895 $0.0\,{\rm km\,s^{-1}}$	2.2895 $4.3\,{\rm km\,s^{-1}}$	2.3079[e] $-38.0\,{\rm km\,s^{-1}}$	2.3079 $0.0\,{\rm km\,s^{-1}}$	2.3079 $15.9\,{\rm km\,s^{-1}}$	2.3799 $0.0\,{\rm km\,s^{-1}}$
H I	...	16.00 ± 0.07	...	...	16.43 ± 0.02	...	15.41 ± 0.17
C II	< 12.58	< 12.45	< 12.48	< 11.64	< 11.63	< 11.64	13.36 ± 0.65
C III	...	13.19 ± 0.09	...	...	...	...	13.50 ± 0.19
C IV	12.19 ± 0.83	12.51 ± 0.34	12.37 ± 0.15	12.54 ± 0.05	12.73 ± 0.08	13.23 ± 0.03	13.059 ± 0.005
N II	< 12.40	< 12.40	< 12.40	< 12.40	< 12.38	< 12.40	< 12.38
N V	...	...	...	< 12.06	< 12.07	< 12.07	< 11.71
O VI	...	...	...	...	...	...	14.497 ± 0.025
Al II	< 10.40	< 10.40	< 10.40	< 10.60	< 10.59	< 10.60	< 10.38
Si II	< 11.36	< 11.36	< 11.36	< 11.49	< 11.49	< 11.49	...
Si III	...	...	...	...	...	...	11.689 ± 0.035
Si IV	11.13 ± 0.16	11.30 ± 0.09	...	< 11.17	< 11.17	< 11.17	11.689 ± 0.037
Fe II	< 12.01	< 12.01	< 12.01	< 11.89	< 11.89	< 11.89	< 12.01

[a] The total column density of hydrogen $\log N_{\rm LLS} = 16.85$ is adopted from Vogel & Reimers (1995) and distributed to the subsystems according to C IV.

[b] The total H I fitted to the Lyman series is $\log N_{\rm LLS} = 16.56 \pm 1.06$. The given distribution follows the portions of carbon (C II, C III, and C IV). Al III arises outside the observed spectral portion, the corresponding values are taken from Tripp et al. (1997).

[c] For these systems no models are derived due to the lack of detected transitions.

Table A.4: The same as Table A.1 but for metal absorption systems at $z < 2.0$.

$\log N_{\rm ion}$	0.7222[a] $-46.5\,{\rm km\,s^{-1}}$	0.7222 $-20.2\,{\rm km\,s^{-1}}$	0.7222 $0.0\,{\rm km\,s^{-1}}$	0.8643[b] $-39.7\,{\rm km\,s^{-1}}$	0.8643 $0.0\,{\rm km\,s^{-1}}$	0.8643 $40.3\,{\rm km\,s^{-1}}$	0.8643 $57.2\,{\rm km\,s^{-1}}$	0.8643 $75.2\,{\rm km\,s^{-1}}$	0.8643 $111.3\,{\rm km\,s^{-1}}$
H I	14.92	15.24	16.12	15.19	15.82	15.51	15.61	15.71	15.26
N III	13.91 :	15.16 :	14.49 :	14.13 :	...	14.11 :	13.49 :	13.93 :	...
N IV	13.80 :	13.97 :	12.72 :	13.59 :	13.20 :	13.31 :	13.47 :	12.85 :	13.17 :
O I	13.37 :	13.51 :	14.11 :	...	...	...	...	...	...
O II	13.70 :	13.60 :	13.90 :	...	...	...	...	...	...
O III	14.70 :	15.77 :	14.39 :	14.50 :	14.57 :	14.95 :	...	15.69 :	14.43 :
O IV	13.68 :	16.41 :	14.83 :	15.40 :	15.01 :	15.52 :	...	15.12 :	...
Mg I	< 10.40	< 10.34	< 10.32	< 10.18	< 10.18	< 10.17	< 10.17	< 10.17	< 10.17
Mg II	11.70 ± 0.01	12.03 ± 0.01	12.91 ± 0.01	11.19 ± 0.04	11.82 ± 0.01	11.51 ± 0.03	11.61 ± 0.02	11.71 ± 0.02	11.26 ± 0.06
Al III	...	...	...	< 11.76	< 11.76	< 11.84	< 11.76	< 11.76	< 11.76
S II	12.87 :	12.81 :	12.60 :	...	...	...	...	...	...
S III	12.90 :	13.22 :	13.16 :	12.89 :	13.30 :	13.09 :	13.99 :	12.92 :	13.02 :
S IV	13.43 :	13.29 :	13.75 :	12.95 :	13.69 :	13.56 :	13.20 :	13.52 :	12.75 :
S V	12.63 :	12.61 :	12.65 :	12.19 :	12.71 :	13.75 :	12.53 :	14.73 :	12.68 :
Fe II	< 12.00	< 12.00	12.60 ± 0.02	< 11.22	< 11.22	< 11.22	< 11.23	< 11.23	< 11.30
Fe III	13.29 :	14.29 :	14.21 :	...	...	...	...	...	...

$\log N_{\rm ion}$	0.2140 $0.0\,{\rm km\,s^{-1}}$	1.1573[c] $0.0\,{\rm km\,s^{-1}}$	1.4941[d] $-22.9\,{\rm km\,s^{-1}}$	1.4941 $0.0\,{\rm km\,s^{-1}}$	1.4941 $20.5\,{\rm km\,s^{-1}}$	1.7241[e] $0.0\,{\rm km\,s^{-1}}$	1.8450[f] $-20.8\,{\rm km\,s^{-1}}$	1.8450 $0.0\,{\rm km\,s^{-1}}$	1.8450 $42.7\,{\rm km\,s^{-1}}$
H I	15.05 :	16.85	15.22	15.34	14.14	17.05	15.71	15.89	15.51
He I	...	15.03 :	...	14.22 :	...	15.61 :	14.94 :	15.12 :	14.73 :
C II	13.91 :	...	< 12.48	< 12.45	< 12.50	< 13.00	< 12.03	13.864 ± 0.014	13.400 ± 0.020
C IV	...	...	13.42 ± 0.02	13.54 ± 0.01	12.34 ± 0.11	13.23 ± 0.01	13.45 :	14.446 ± 0.003	13.769 ± 0.003
N II	...	13.13 :	...	...	...	...	...	...	...
N III	...	13.77 :	...	...	...	...	...	...	...
N V	...	...	...	...	...	...	< 12.47	13.20 ± 0.05	< 12.70
O III	...	14.63 :	...	...	...	14.52 :	14.20 :	16.36 :	15.95 :
O IV	...	...	14.38 :	15.06 :	13.95 :	14.04 :	...	...	...
O V	...	14.44 :	...	...	...	...	...	...	...
Ne III	...	...	...	...	...	13.70 :	...	...	...
Ne IV	...	...	...	...	...	...	14.12 :	14.53 :	14.80 :
Ne V	...	...	...	...	...	...	...	...	13.47 :
Ne VI	...	...	...	...	...	...	14.89 :	...	14.99 :
Ne VII	...	...	...	...	...	...	13.57 :	...	13.86 :
Mg I	11.32 ± 0.05	...	...	...	...	...	...	...	...
Mg II	12.76 ± 0.02	12.680 ± 0.004	...	...	...	...	...	12.65 ± 0.10	...
Al II	...	12.11 ± 0.03	< 10.50	< 10.50	< 10.50	...	< 10.40	11.02 ± 0.04	< 10.39
Al III	...	...	10.70	< 10.69	< 10.69	< 11.02	< 10.98	11.65 ± 0.03	< 11.01
Si II	12.89 :	...	...	...	...	< 11.45	< 11.39	12.293 ± 0.021	< 11.39
Si III	12.98 :	...	...	...	...	...	12.57 :	12.983 ± 0.019	12.841 ± 0.018
Si IV	...	...	12.00 ± 0.11	11.79 ± 0.15	11.37 :	12.77 ± 0.05	12.50 :	13.169 ± 0.006	12.600 ± 0.012
S III	...	13.96 :	...	...	...	...	...	...	...
S IV	...	12.96 :	...	...	...	...	...	...	...
Fe II	...	11.88 ± 0.04	< 12.30	< 12.25	< 12.30	...	< 11.67	< 11.67	< 11.68

[a] The total H I measured from the Lyman break by Vogel & Reimers (1995) is $\log N_{\rm LLS} = 16.20$. The given distribution follows magnesium (Mg I and Mg II).

[b] The total H I measured from the Lyman break by Vogel & Reimers (1995) is $\log N_{\rm LLS} = 16.35$. The given distribution follows Mg II.

[c] The H I feature is located outside the considered spectral portion. The column density is therefore adopted from Vogel & Reimers (1995).

[d] The H I feature is located outside the used spectral portion. Therefore, the column density is adopted from Vogel & Reimers (1995), who find $\log N({\rm H\,I}) = 15.60$. It is distributed to the subsystems according to C IV.

[e] The H I column density is adopted from Vogel & Reimers (1995).

[f] The total H I fitted to the Lyman series is $\log N_{\rm LLS} = 16.21 \pm 0.11$. The given distributions follows silicon (Si II, Si III, and Si IV). The column density of Mg II is adopted from Tripp et al. (1997).

A.2. Predicted metal lines

Table A.5: Predicted metal lines in the FUSE spectral range (1000 – 1180 Å). For each component is given the identification, the predicted wavelength λ_{obs}, the rest wavelength λ_{rest} and the oszillator strentgh f of the considered transition, the redshift of the component z, the predicted column density $\log N$, the computed Doppler parameter b, as well as the adopted model and the redshift of the system z_{sys} (for the nomenclature see Chapter 4).

ion	λ_{obs} (Å)	λ_{rest} (Å)	z	$\log N$	b (km/s)	f	model	z_{system}
O III	1000.0119	280.2340	2.568489	13.134	18.3	0.0111	HM2	2.5683
C III	1000.0372	291.3261	2.432707	13.087	16.7	0.0451	HM3	2.4321
C III	1000.1394	291.3261	2.433058	13.705	9.6	0.0451	HM3	2.4331
C III	1000.2475	291.3261	2.433429	13.527	13.3	0.0451	HM3	2.4331
C III	1000.3083	291.3261	2.433638	13.335	11.3	0.0451	HM3	2.4331
Ne VI	1000.3941	401.1400	1.493878	11.741	12.9	0.1700	PL15	1.4941
Ne VI	1000.4704	401.1400	1.494068	12.300	6.6	0.1700	PL15	1.4941
Ne VI	1000.5387	401.1400	1.494238	10.073	7.2	0.1700	PL15	1.4941
O IV	1000.5891	279.6310	2.578248	14.141	9.3	0.0278	HM3	2.5785
O IV	1000.7126	279.6310	2.578690	14.344	6.6	0.0278	HM3	2.5785
O IV	1000.7850	279.6310	2.578949	13.818	10.5	0.0278	HM3	2.5785
He I	1001.0383	537.0296	0.864028	14.115	7.9	0.0734	SB	0.8643
He I	1001.1709	537.0296	0.864275	14.765	9.0	0.0734	SB	0.8643
He I	1001.3053	537.0296	0.864525	14.407	10.1	0.0734	SB	0.8643
He I	1001.3620	537.0296	0.864631	14.572	7.9	0.0734	SB	0.8643
He I	1001.4219	537.0296	0.864742	14.624	9.8	0.0734	SB	0.8643
C III	1001.5196	291.3261	2.437796	12.837	8.0	0.0451	MF	2.4386
He I	1001.5426	537.0296	0.864967	14.205	14.8	0.0734	SB	0.8643
C III	1001.6657	291.3261	2.438297	13.050	13.2	0.0451	MF	2.4386
C III	1001.7611	291.3261	2.438625	12.431	8.0	0.0451	MF	2.4386
C III	1001.8249	291.3261	2.438844	12.630	6.2	0.0451	MF	2.4386
C III	1002.0633	280.0430	2.578248	12.908	10.2	0.0164	HM3	2.5785
C III	1002.0811	291.3261	2.439723	12.418	16.0	0.0451	HM	2.4405
C III	1002.1870	280.0430	2.578690	12.827	7.5	0.0164	HM3	2.5785
C III	1002.2595	280.0430	2.578949	13.120	11.2	0.0164	HM3	2.5785
C III	1002.3179	291.3261	2.440536	12.363	9.2	0.0451	HM	2.4405
O III	1002.7468	280.2340	2.578248	13.694	9.3	0.0111	HM3	2.5785
O III	1002.8706	280.2340	2.578690	13.997	6.6	0.0111	HM3	2.5785
O III	1002.9431	280.2340	2.578949	13.526	10.5	0.0111	HM3	2.5785
N III	1003.6305	292.4470	2.431837	11.959	7.1	0.0484	HM3	2.4321
N III	1003.7081	292.4470	2.432102	12.542	15.7	0.0484	HM3	2.4321
N III	1003.8850	292.4470	2.432707	12.550	16.5	0.0484	HM3	2.4321
N III	1003.9875	292.4470	2.433058	12.601	9.2	0.0484	HM3	2.4331
N III	1004.0961	292.4470	2.433429	12.285	13.0	0.0484	HM3	2.4331
N III	1004.1570	292.4470	2.433638	12.406	11.0	0.0484	HM3	2.4331
O II	1004.8706	539.0855	0.864028	12.500	4.2	0.0560	SB	0.8643
O II	1005.0036	539.0855	0.864275	12.168	4.6	0.0560	SB	0.8643
O II	1005.1386	539.0855	0.864525	12.511	7.0	0.0560	SB	0.8643
O II	1005.1955	539.0855	0.864631	12.794	4.0	0.0560	SB	0.8643
O II	1005.2556	539.0855	0.864742	12.709	6.4	0.0560	SB	0.8643
O III	1005.2878	305.5960	2.289598	13.363	6.6	0.4200	HM3	2.2896
N III	1005.3730	292.4470	2.437796	10.056	7.8	0.0484	MF	2.4386
O II	1005.3768	539.0855	0.864967	12.739	13.3	0.0560	SB	0.8643
N III	1005.5196	292.4470	2.438297	10.832	13.1	0.0484	MF	2.4386
N III	1005.6154	292.4470	2.438625	11.150	7.7	0.0484	MF	2.4386
N III	1005.6795	292.4470	2.438844	11.717	5.8	0.0484	MF	2.4386
O II	1005.7344	539.5489	0.864028	12.500	4.2	0.0370	SB	0.8643
O III	1005.7976	303.4110	2.314967	15.189	7.4	0.1410	HM3	2.3155
O II	1005.8675	539.5489	0.864275	12.168	4.6	0.0370	SB	0.8643
N III	1005.9367	292.4470	2.439723	11.804	15.8	0.0484	HM	2.4405
O III	1005.9613	303.4110	2.315507	14.770	4.3	0.1410	HM3	2.3155
O II	1006.0026	539.5489	0.864525	12.511	7.0	0.0370	SB	0.8643
O II	1006.0596	539.5489	0.864631	12.794	4.0	0.0370	SB	0.8643
O III	1006.0790	303.4110	2.315895	14.829	7.2	0.1410	HM3	2.3155
O II	1006.1197	539.5489	0.864742	12.709	6.4	0.0370	SB	0.8643
N III	1006.1744	292.4470	2.440536	11.201	9.0	0.0484	HM	2.4405
He I	1006.1756	584.3340	0.721919	14.186	6.6	0.2760	HM	0.7222
O III	1006.2194	303.4110	2.316358	14.945	5.4	0.1410	HM3	2.3155
O II	1006.2410	539.5489	0.864967	12.739	13.3	0.0370	SB	0.8643
He I	1006.2642	584.3340	0.722070	14.515	9.1	0.2760	HM	0.7222
O II	1006.3038	539.8544	0.864028	12.500	4.2	0.0190	SB	0.8643
He I	1006.3319	584.3340	0.722186	15.401	6.4	0.2760	HM	0.7222
O II	1006.4371	539.8544	0.864275	12.168	4.6	0.0190	SB	0.8643

Table A.5: continued.

ion	λ_{obs} (Å)	λ_{rest} (Å)	z	log N	b (km/s)	f	model	z_{system}
O II	1006.5722	539.8544	0.864525	12.511	7.0	0.0190	SB	0.8643
O II	1006.6292	539.8544	0.864631	12.794	4.0	0.0190	SB	0.8643
O II	1006.6894	539.8544	0.864742	12.709	6.4	0.0190	SB	0.8643
O II	1006.8107	539.8544	0.864967	12.739	13.3	0.0190	SB	0.8643
Ne IV	1008.6760	541.1270	0.864028	11.241	3.8	0.0560	SB	0.8643
Ne IV	1008.8095	541.1270	0.864275	12.484	4.1	0.0560	SB	0.8643
Ne IV	1008.9450	541.1270	0.864525	12.308	6.7	0.0560	SB	0.8643
Ne IV	1009.0021	541.1270	0.864631	10.387	3.6	0.0560	SB	0.8643
Ne IV	1009.0625	541.1270	0.864742	12.675	6.1	0.0560	SB	0.8643
Ne IV	1009.1841	541.1270	0.864967	10.669	13.2	0.0560	SB	0.8643
Ne III	1010.4214	283.1670	2.568288	11.782	5.9	0.0470	HM2	2.5683
Ne IV	1010.4394	542.0730	0.864028	11.241	3.8	0.1100	SB	0.8643
Ne III	1010.4783	283.1670	2.568489	11.421	18.1	0.0470	HM2	2.5683
Ne IV	1010.5731	542.0730	0.864275	12.484	4.1	0.1100	SB	0.8643
Ne IV	1010.7089	542.0730	0.864525	12.308	6.7	0.1100	SB	0.8643
Ne IV	1010.7661	542.0730	0.864631	10.387	3.6	0.1100	SB	0.8643
Ne IV	1010.8265	542.0730	0.864742	12.675	6.1	0.1100	SB	0.8643
Ne IV	1010.9484	542.0730	0.864967	10.669	13.2	0.1100	SB	0.8643
O II	1010.9789	832.7572	0.214014	14.088	6.3	0.0700	HM2	0.2140
O III	1011.1850	832.9270	0.214014	13.489	6.3	0.0998	HM2	0.2140
O II	1011.6736	833.3294	0.214014	14.088	6.3	0.1500	HM2	0.2140
C II	1012.6464	543.2570	0.864028	12.158	4.7	0.0349	SB	0.8643
C II	1012.7804	543.2570	0.864275	12.851	5.2	0.0349	SB	0.8643
C II	1012.9165	543.2570	0.864525	12.449	7.4	0.0349	SB	0.8643
C II	1012.9738	543.2570	0.864631	12.631	4.6	0.0349	SB	0.8643
C II	1013.0344	543.2570	0.864742	12.609	6.9	0.0349	SB	0.8643
O III	1013.0408	305.5960	2.314967	15.189	7.4	0.4200	HM3	2.3155
O II	1013.0528	834.4655	0.214014	14.088	6.3	0.2100	HM2	0.2140
C II	1013.1565	543.2570	0.864967	12.250	13.5	0.0349	SB	0.8643
O III	1013.2056	305.5960	2.315507	14.770	4.3	0.4200	HM3	2.3155
Ne III	1013.2418	283.1670	2.578248	11.918	8.7	0.0470	HM3	2.5785
O III	1013.3242	305.5960	2.315895	14.829	7.2	0.4200	HM3	2.3155
Ne III	1013.3669	283.1670	2.578690	13.212	6.0	0.0470	HM3	2.5785
Ne III	1013.4402	283.1670	2.578949	13.921	10.1	0.0470	HM3	2.5785
O III	1013.4657	305.5960	2.316358	14.945	5.4	0.4200	HM3	2.3155
Ne IV	1013.8282	543.8910	0.864028	11.241	3.8	0.1700	SB	0.8643
Ne IV	1013.9624	543.8910	0.864275	12.484	4.1	0.1700	SB	0.8643
Ne IV	1014.0986	543.8910	0.864525	12.308	6.7	0.1700	SB	0.8643
Ne IV	1014.1560	543.8910	0.864631	10.387	3.6	0.1700	SB	0.8643
Ne IV	1014.2166	543.8910	0.864742	12.675	6.1	0.1700	SB	0.8643
Ne IV	1014.3389	543.8910	0.864967	10.669	13.2	0.1700	SB	0.8643
Ne V	1018.3140	357.9500	1.844850	13.714	4.1	0.1350	MF	1.8450
Ne V	1018.3846	357.9500	1.845047	12.797	8.7	0.1350	MF	1.8450
Ne V	1018.5297	357.9500	1.845452	11.865	10.8	0.1350	MF	1.8450
C III	1018.6156	291.3261	2.496479	11.572	9.5	0.0451	HM3	2.4965
O III	1018.8233	374.0050	1.724090	14.524	13.1	0.0810	HM3	1.7241
N III	1019.3654	374.2040	1.724090	13.748	13.3	0.4240	HM3	1.7241
C III	1020.3335	310.1697	2.289598	13.181	7.5	0.0779	HM3	2.2896
C III	1021.7718	322.5741	2.167557	12.750	12.2	0.0452	HM3	2.1680
C III	1021.9011	322.5741	2.167958	14.160	13.5	0.0452	HM3	2.1680
N III	1022.5348	292.4470	2.496479	11.071	8.8	0.0484	HM3	2.4965
N II	1023.6096	474.4909	1.157280	13.289	9.0	0.0436	HMs0.1	1.1573
C II	1024.1972	594.8000	0.721919	12.940	5.1	0.1170	HM	0.7222
C II	1024.2874	594.8000	0.722070	13.269	8.1	0.1170	HM	0.7222
C II	1024.3563	594.8000	0.722186	14.133	5.0	0.1170	HM	0.7222
N III	1024.5020	323.4360	2.167557	10.652	11.7	0.0173	HM3	2.1680
N III	1024.6316	323.4360	2.167958	12.311	13.1	0.0173	HM3	2.1680
N III	1024.6825	323.4930	2.167557	10.652	11.7	0.0348	HM3	2.1680
N III	1024.8122	323.4930	2.167958	12.311	13.1	0.0348	HM3	2.1680
O III	1025.5102	303.4110	2.379937	13.716	8.9	0.1410	HM3	2.3799
N II	1026.1060	475.6481	1.157280	13.289	9.0	0.1420	HMs0.1	1.1573
O II	1026.1456	376.6930	1.724090	13.147	13.1	0.0290	HM3	1.7241
O II	1026.2873	376.7450	1.724090	13.147	13.1	0.0436	HM3	1.7241
C IV	1027.7426	312.4220	2.289598	12.636	7.5	0.1310	HM3	2.2896
C IV	1027.8446	312.4530	2.289598	12.636	7.5	0.0657	HM3	2.2896
C III	1028.2024	310.1697	2.314967	15.294	7.8	0.0779	HM3	2.3155
C III	1028.3698	310.1697	2.315507	15.019	4.9	0.0779	HM3	2.3155
C III	1028.4901	310.1697	2.315895	14.166	7.9	0.0779	HM3	2.3155
C III	1028.6337	310.1697	2.316358	14.671	6.2	0.0779	HM3	2.3155

Table A.5: continued.

ion	λ_{obs} (Å)	λ_{rest} (Å)	z	log N	b (km/s)	f	model	z_{system}
Ne III	1029.8381	313.0590	2.289598	12.347	5.9	0.0410	HM3	2.2896
O IV	1031.4227	553.3300	0.864028	12.984	4.2	0.1100	SB	0.8643
O IV	1031.5593	553.3300	0.864275	13.081	4.6	0.1100	SB	0.8643
O IV	1031.6978	553.3300	0.864525	13.671	7.0	0.1100	SB	0.8643
O IV	1031.7562	553.3300	0.864631	11.861	4.0	0.1100	SB	0.8643
O IV	1031.8179	553.3300	0.864742	13.962	6.4	0.1100	SB	0.8643
O IV	1031.9423	553.3300	0.864967	12.557	13.3	0.1100	SB	0.8643
O IV	1032.8114	554.0750	0.864028	12.984	4.2	0.2180	SB	0.8643
O III	1032.8953	305.5960	2.379937	13.716	8.9	0.4200	HM3	2.3799
O IV	1032.9482	554.0750	0.864275	13.081	4.6	0.2180	SB	0.8643
O IV	1033.0869	554.0750	0.864525	13.671	7.0	0.2180	SB	0.8643
O IV	1033.1454	554.0750	0.864631	11.861	4.0	0.2180	SB	0.8643
O IV	1033.2071	554.0750	0.864742	13.962	6.4	0.2180	SB	0.8643
O IV	1033.3317	554.0750	0.864967	12.557	13.3	0.2180	SB	0.8643
C IV	1033.4639	312.4220	2.307913	12.732	5.8	0.1310	obs	2.3079
C IV	1033.5201	312.4220	2.308088	13.233	17.4	0.1310	obs	2.3079
C IV	1033.5664	312.4530	2.307913	12.732	5.8	0.0657	obs	2.3079
C IV	1033.6227	312.4530	2.308088	13.233	17.4	0.0657	obs	2.3079
N III	1035.2857	314.7150	2.289598	12.675	7.0	0.1940	HM3	2.2896
C IV	1035.6687	312.4220	2.314967	14.210	7.8	0.1310	HM3	2.3155
C IV	1035.7715	312.4530	2.314967	14.210	7.8	0.0657	HM3	2.3155
C IV	1035.8373	312.4220	2.315507	14.093	4.9	0.1310	HM3	2.3155
C IV	1035.9401	312.4530	2.315507	14.093	4.9	0.0657	HM3	2.3155
C IV	1035.9585	312.4220	2.315895	14.026	7.9	0.1310	HM3	2.3155
C IV	1036.0613	312.4530	2.315895	14.026	7.9	0.0657	HM3	2.3155
C IV	1036.1031	312.4220	2.316358	14.362	6.2	0.1310	HM3	2.3155
C IV	1036.2059	312.4530	2.316358	14.362	6.2	0.0657	HM3	2.3155
Ne III	1037.7804	313.0590	2.314967	14.428	7.1	0.0410	HM3	2.3155
Ne III	1037.9493	313.0590	2.315507	14.017	3.8	0.0410	HM3	2.3155
Ne III	1038.0707	313.0590	2.315895	13.804	6.7	0.0410	HM3	2.3155
Ne III	1038.2157	313.0590	2.316358	13.995	4.8	0.0410	HM3	2.3155
C III	1039.5354	291.3261	2.568288	12.793	7.3	0.0451	HM2	2.5683
C III	1039.5939	291.3261	2.568489	12.533	18.6	0.0451	HM2	2.5683
O III	1041.2572	303.4110	2.431837	12.504	6.7	0.1410	HM3	2.4321
O III	1041.3376	303.4110	2.432102	13.073	15.5	0.1410	HM3	2.4321
O III	1041.5212	303.4110	2.432707	13.118	16.4	0.1410	HM3	2.4321
O III	1041.6276	303.4110	2.433058	14.502	8.8	0.1410	HM3	2.4331
O III	1041.7402	303.4110	2.433429	14.304	12.8	0.1410	HM3	2.4331
O III	1041.8034	303.4110	2.433638	14.676	10.7	0.1410	HM3	2.4331
C III	1042.4370	291.3261	2.578248	12.908	10.2	0.0451	HM3	2.5785
C III	1042.5657	291.3261	2.578690	12.827	7.5	0.0451	HM3	2.5785
C III	1042.6412	291.3261	2.578949	13.120	11.2	0.0451	HM3	2.5785
O III	1043.0650	303.4110	2.437796	12.124	7.6	0.1410	MF	2.4386
O III	1043.2171	303.4110	2.438297	12.926	13.0	0.1410	MF	2.4386
N III	1043.2700	314.7150	2.314967	14.453	7.6	0.1940	HM3	2.3155
O III	1043.3165	303.4110	2.438625	13.012	7.4	0.1410	MF	2.4386
O III	1043.3830	303.4110	2.438844	13.216	5.5	0.1410	MF	2.4386
N III	1043.4398	314.7150	2.315507	14.741	4.6	0.1940	HM3	2.3155
N III	1043.5351	292.4470	2.568288	12.293	6.8	0.0484	HM2	2.5683
N III	1043.5619	314.7150	2.315895	13.074	7.5	0.1940	HM3	2.3155
N III	1043.5938	292.4470	2.568489	12.067	18.4	0.0484	HM2	2.5683
O III	1043.6498	303.4110	2.439723	13.804	15.6	0.1410	HM	2.4405
N III	1043.7075	314.7150	2.316358	13.755	5.8	0.1940	HM3	2.3155
O III	1043.8964	303.4110	2.440536	12.755	8.8	0.1410	HM	2.4405
C II	1044.3020	560.2394	0.864028	12.158	4.7	0.0571	SB	0.8643
C II	1044.4403	560.2394	0.864275	12.851	5.2	0.0571	SB	0.8643
C II	1044.5806	560.2394	0.864525	12.449	7.4	0.0571	SB	0.8643
C II	1044.6397	560.2394	0.864631	12.631	4.6	0.0571	SB	0.8643
C II	1044.7022	560.2394	0.864742	12.609	6.9	0.0571	SB	0.8643
C II	1044.8281	560.2394	0.864967	12.250	13.5	0.0571	SB	0.8643
N III	1046.4479	292.4470	2.578248	12.157	9.7	0.0484	HM3	2.5785
N III	1046.5771	292.4470	2.578690	11.664	7.0	0.0484	HM3	2.5785
N III	1046.6528	292.4470	2.578949	12.431	10.8	0.0484	HM3	2.5785
O IV	1047.7041	608.3980	0.722070	10.202	8.0	0.0694	HM	0.7222
O IV	1047.7746	608.3980	0.722186	10.951	4.7	0.0694	HM	0.7222
C III	1048.3542	310.1697	2.379937	13.272	9.4	0.0779	HM3	2.3799
O III	1048.7558	305.5960	2.431837	12.504	6.7	0.4200	HM3	2.4321
O III	1048.8368	305.5960	2.432102	13.073	15.5	0.4200	HM3	2.4321
O III	1049.0216	305.5960	2.432707	13.118	16.4	0.4200	HM3	2.4321

Table A.5: continued.

ion	λ_{obs} (Å)	λ_{rest} (Å)	z	log N	b (km/s)	f	model	z_{system}
O III	1049.1288	305.5960	2.433058	14.502	8.8	0.4200	HM3	2.4331
O III	1049.2422	305.5960	2.433429	14.304	12.8	0.4200	HM3	2.4331
O III	1049.3059	305.5960	2.433638	14.676	10.7	0.4200	HM3	2.4331
O III	1050.5766	305.5960	2.437796	12.124	7.6	0.4200	MF	2.4386
O III	1050.7298	305.5960	2.438297	12.926	13.0	0.4200	MF	2.4386
O III	1050.8299	305.5960	2.438625	13.012	7.4	0.4200	MF	2.4386
O III	1050.8969	305.5960	2.438844	13.216	5.5	0.4200	MF	2.4386
O III	1051.1656	305.5960	2.439723	13.804	15.6	0.4200	HM	2.4405
O III	1051.4140	305.5960	2.440536	12.755	8.8	0.4200	HM	2.4405
C III	1052.0512	386.2028	1.724090	14.123	13.6	0.2160	HM3	1.7241
Ne III	1052.9855	488.1080	1.157280	13.282	8.8	0.0630	HMs0.1	1.1573
C IV	1055.9668	312.4220	2.379937	13.049	9.4	0.1310	HM3	2.3799
Ne III	1055.9992	489.5050	1.157280	13.282	8.8	0.1900	HMs0.1	1.1573
C IV	1056.0716	312.4530	2.379937	13.049	9.4	0.0657	HM3	2.3799
Ne III	1058.1198	313.0590	2.379937	13.364	8.5	0.0410	HM3	2.3799
O III	1060.8702	303.4110	2.496479	12.256	8.3	0.1410	HM3	2.4965
C III	1061.1390	322.5741	2.289598	13.181	7.5	0.0452	HM3	2.2896
N III	1063.7170	314.7150	2.379937	12.078	9.1	0.1940	HM3	2.3799
N III	1063.9743	323.4360	2.289598	12.675	7.0	0.0173	HM3	2.2896
O III	1063.9880	374.0050	1.844850	14.334	4.6	0.0810	MF	1.8450
O III	1064.0619	374.0050	1.845047	14.459	8.8	0.0810	MF	1.8450
N III	1064.1618	323.4930	2.289598	12.675	7.0	0.0348	HM3	2.2896
O III	1064.2135	374.0050	1.845452	14.024	10.9	0.0810	MF	1.8450
C III	1064.4519	310.1697	2.431837	12.350	7.6	0.0779	HM3	2.4321
C III	1064.5342	310.1697	2.432102	13.007	15.9	0.0779	HM3	2.4321
N III	1064.5542	374.2040	1.844850	12.746	4.9	0.4240	MF	1.8450
N III	1064.6280	374.2040	1.845047	14.271	8.9	0.4240	MF	1.8450
C III	1064.7218	310.1697	2.432707	13.087	16.7	0.0779	HM3	2.4321
N III	1064.7797	374.2040	1.845452	13.808	11.0	0.4240	MF	1.8450
C III	1064.8306	310.1697	2.433058	13.705	9.6	0.0779	HM3	2.4331
C III	1064.9457	310.1697	2.433429	13.527	13.3	0.0779	HM3	2.4331
C III	1065.0103	310.1697	2.433638	13.335	11.3	0.0779	HM3	2.4331
C III	1066.3000	310.1697	2.437796	12.837	8.0	0.0779	MF	2.4386
C III	1066.4555	310.1697	2.438297	13.050	13.2	0.0779	MF	2.4386
C III	1066.5572	310.1697	2.438625	12.431	8.0	0.0779	MF	2.4386
C III	1066.6251	310.1697	2.438844	12.630	6.2	0.0779	MF	2.4386
C III	1066.8979	310.1697	2.439723	12.418	16.0	0.0779	HM	2.4405
C III	1067.1500	310.1697	2.440536	12.363	9.2	0.0779	HM	2.4405
O II	1067.6036	391.9120	1.724090	13.147	13.1	0.0273	HM3	1.7241
O II	1067.6880	391.9430	1.724090	13.147	13.1	0.0548	HM3	1.7241
O II	1067.8487	392.0020	1.724090	13.147	13.1	0.0821	HM3	1.7241
O III	1068.5100	305.5960	2.496479	12.256	8.3	0.4200	HM3	2.4965
C III	1069.3226	322.5741	2.314967	15.294	7.8	0.0452	HM3	2.3155
C III	1069.4967	322.5741	2.315507	15.019	4.9	0.0452	HM3	2.3155
C III	1069.6218	322.5741	2.315895	14.166	7.9	0.0452	HM3	2.3155
C III	1069.7711	322.5741	2.316358	14.671	6.2	0.0452	HM3	2.3155
O II	1071.6350	376.6930	1.844850	12.286	4.6	0.0290	MF	1.8450
O II	1071.7094	376.6930	1.845047	12.943	8.8	0.0290	MF	1.8450
O II	1071.7829	376.7450	1.844850	12.286	4.6	0.0436	MF	1.8450
O II	1071.8573	376.7450	1.845047	12.943	8.8	0.0436	MF	1.8450
O II	1071.8620	376.6930	1.845452	12.762	10.9	0.0290	MF	1.8450
O II	1072.0100	376.7450	1.845452	12.762	10.9	0.0436	MF	1.8450
O II	1072.1629	429.9180	1.493878	11.643	13.1	0.0540	PL15	1.4941
N III	1072.1798	323.4360	2.314967	14.453	7.6	0.0173	HM3	2.3155
C IV	1072.1815	312.4220	2.431837	12.256	7.6	0.1310	HM3	2.4321
O II	1072.2446	429.9180	1.494068	11.292	7.0	0.0540	PL15	1.4941
C IV	1072.2643	312.4220	2.432102	12.790	15.9	0.1310	HM3	2.4321
C IV	1072.2879	312.4530	2.431837	12.256	7.6	0.0657	HM3	2.4321
O II	1072.3179	429.9180	1.494238	11.286	7.5	0.0540	PL15	1.4941
N III	1072.3543	323.4360	2.315507	14.741	4.6	0.0173	HM3	2.3155
N III	1072.3687	323.4930	2.314967	14.453	7.6	0.0348	HM3	2.3155
C IV	1072.3707	312.4530	2.432102	12.790	15.9	0.0657	HM3	2.4321
C IV	1072.4533	312.4220	2.432707	12.704	16.7	0.1310	HM3	2.4321
O II	1072.4696	430.0410	1.493878	11.643	13.1	0.1080	PL15	1.4941
N III	1072.4798	323.4360	2.315895	13.074	7.5	0.0173	HM3	2.3155
N III	1072.5433	323.4930	2.315507	14.741	4.6	0.0348	HM3	2.3155
O II	1072.5514	430.0410	1.494068	11.292	7.0	0.1080	PL15	1.4941
C IV	1072.5597	312.4530	2.432707	12.704	16.7	0.0657	HM3	2.4321
C IV	1072.5628	312.4220	2.433058	13.193	9.6	0.1310	HM3	2.4331

Table A.5: continued.

ion	λ_{obs} (Å)	λ_{rest} (Å)	z	log N	b (km/s)	f	model	z_{system}
O II	1072.6246	430.0410	1.494238	11.286	7.5	0.1080	PL15	1.4941
N III	1072.6295	323.4360	2.316358	13.755	5.8	0.0173	HM3	2.3155
N III	1072.6688	323.4930	2.315895	13.074	7.5	0.0348	HM3	2.3155
C IV	1072.6693	312.4530	2.433058	13.193	9.6	0.0657	HM3	2.4331
C IV	1072.6788	312.4220	2.433429	12.821	13.3	0.1310	HM3	2.4331
C IV	1072.7439	312.4220	2.433638	12.664	11.3	0.1310	HM3	2.4331
C IV	1072.7853	312.4530	2.433429	12.821	13.3	0.0657	HM3	2.4331
O II	1072.8088	430.1770	1.493878	11.643	13.1	0.1620	PL15	1.4941
N III	1072.8185	323.4930	2.316358	13.755	5.8	0.0348	HM3	2.3155
C IV	1072.8504	312.4530	2.433638	12.664	11.3	0.0657	HM3	2.4331
O II	1072.8906	430.1770	1.494068	11.292	7.0	0.1620	PL15	1.4941
O II	1072.9639	430.1770	1.494238	11.286	7.5	0.1620	PL15	1.4941
C IV	1074.0430	312.4220	2.437796	12.669	8.0	0.1310	MF	2.4386
C IV	1074.1495	312.4530	2.437796	12.669	8.0	0.0657	MF	2.4386
C IV	1074.1996	312.4220	2.438297	12.716	13.2	0.1310	MF	2.4386
C IV	1074.3020	312.4220	2.438625	12.958	8.0	0.1310	MF	2.4386
C IV	1074.3062	312.4530	2.438297	12.716	13.2	0.0657	MF	2.4386
Ne III	1074.3676	313.0590	2.431837	11.255	6.0	0.0410	HM3	2.4321
C IV	1074.3704	312.4220	2.438844	12.899	6.2	0.1310	MF	2.4386
C IV	1074.4086	312.4530	2.438625	12.958	8.0	0.0657	MF	2.4386
Ne III	1074.4505	313.0590	2.432102	11.941	15.3	0.0410	HM3	2.4321
C IV	1074.4770	312.4530	2.438844	12.899	6.2	0.0657	MF	2.4386
Ne III	1074.6399	313.0590	2.432707	12.114	16.1	0.0410	HM3	2.4321
C IV	1074.6451	312.4220	2.439723	12.558	16.0	0.1310	HM	2.4405
Ne III	1074.7497	313.0590	2.433058	13.577	8.2	0.0410	HM3	2.4331
C IV	1074.7518	312.4530	2.439723	12.558	16.0	0.0657	HM	2.4405
Ne III	1074.8659	313.0590	2.433429	13.412	12.5	0.0410	HM3	2.4331
C IV	1074.8991	312.4220	2.440536	13.069	9.2	0.1310	HM	2.4405
Ne III	1074.9312	313.0590	2.433638	13.785	10.3	0.0410	HM3	2.4331
C IV	1075.0057	312.4530	2.440536	13.069	9.2	0.0657	HM	2.4405
Ne III	1076.2329	313.0590	2.437796	11.491	7.4	0.0410	MF	2.4386
Ne III	1076.3898	313.0590	2.438297	12.282	12.8	0.0410	MF	2.4386
Ne III	1076.4924	313.0590	2.438625	12.235	7.0	0.0410	MF	2.4386
Ne III	1076.5610	313.0590	2.438844	12.534	5.0	0.0410	MF	2.4386
Ne III	1076.8362	313.0590	2.439723	11.276	15.4	0.0410	HM	2.4405
Ne III	1077.0907	313.0590	2.440536	11.867	8.6	0.0410	HM	2.4405
N III	1080.0507	314.7150	2.431837	11.959	7.1	0.1940	HM3	2.4321
N III	1080.1341	314.7150	2.432102	12.542	15.7	0.1940	HM3	2.4321
Ne VI	1080.2879	433.1760	1.493878	11.741	12.9	0.0310	PL15	1.4941
N III	1080.3245	314.7150	2.432707	12.550	16.5	0.1940	HM3	2.4321
Ne VI	1080.3703	433.1760	1.494068	12.300	6.6	0.0310	PL15	1.4941
N III	1080.4348	314.7150	2.433058	12.601	9.2	0.1940	HM3	2.4331
Ne VI	1080.4441	433.1760	1.494238	10.073	7.2	0.0310	PL15	1.4941
N III	1080.5517	314.7150	2.433429	12.285	13.0	0.1940	HM3	2.4331
N III	1080.6173	314.7150	2.433638	12.406	11.0	0.1940	HM3	2.4331
N III	1081.9258	314.7150	2.437796	10.056	7.8	0.1940	MF	2.4386
N III	1082.0836	314.7150	2.438297	10.832	13.1	0.1940	MF	2.4386
N III	1082.1867	314.7150	2.438625	11.150	7.7	0.1940	MF	2.4386
N III	1082.2557	314.7150	2.438844	11.717	5.8	0.1940	MF	2.4386
N III	1082.5324	314.7150	2.439723	11.804	15.8	0.1940	HM	2.4405
O III	1082.6578	303.4110	2.568288	13.297	6.5	0.1410	HM2	2.5683
O III	1082.7188	303.4110	2.568489	13.134	18.3	0.1410	HM2	2.5683
N III	1082.7882	314.7150	2.440536	11.201	9.0	0.1940	HM	2.4405
C III	1084.5018	310.1697	2.496479	11.572	9.5	0.0779	HM3	2.4965
O III	1085.6798	303.4110	2.578248	13.694	9.3	0.1410	HM3	2.5785
O III	1085.8139	303.4110	2.578690	13.997	6.6	0.1410	HM3	2.5785
O III	1085.8924	303.4110	2.578949	13.526	10.5	0.1410	HM3	2.5785
N II	1087.5980	436.1072	1.493878	11.137	13.2	0.0381	PL15	1.4941
N II	1087.6809	436.1072	1.494068	10.888	7.2	0.0381	PL15	1.4941
N II	1087.7552	436.1072	1.494238	10.638	7.6	0.0381	PL15	1.4941
Ne VI	1089.1457	399.8200	1.724090	12.950	12.7	0.0840	HM3	1.7241
He I	1089.2151	584.3340	0.864028	14.115	7.9	0.2760	SB	0.8643
He I	1089.3593	584.3340	0.864275	14.765	9.0	0.2760	SB	0.8643
He I	1089.5056	584.3340	0.864525	14.407	10.1	0.2760	SB	0.8643
He I	1089.5672	584.3340	0.864631	14.572	7.9	0.2760	SB	0.8643
He I	1089.6324	584.3340	0.864742	14.624	9.8	0.2760	SB	0.8643
He I	1089.7637	584.3340	0.864967	14.205	14.8	0.2760	SB	0.8643
C III	1090.2803	322.5741	2.379937	13.272	9.4	0.0452	HM3	2.3799
O III	1090.4545	305.5960	2.568288	13.297	6.5	0.4200	HM2	2.5683

Table A.5: continued.

ion	λ_{obs} (Å)	λ_{rest} (Å)	z	log N	b (km/s)	f	model	z_{system}
O III	1090.5159	305.5960	2.568489	13.134	18.3	0.4200	HM2	2.5683
He I	1092.0150	506.2000	1.157280	16.022	10.9	0.0011	HMs0.1	1.1573
C IV	1092.3770	312.4220	2.496479	12.196	9.5	0.1310	HM3	2.4965
C IV	1092.4854	312.4530	2.496479	12.196	9.5	0.0657	HM3	2.4965
Ne VI	1092.7415	401.1400	1.724090	12.950	12.7	0.1700	HM3	1.7241
He I	1092.8145	506.5706	1.157280	16.022	10.9	0.0015	HMs0.1	1.1573
N III	1093.1934	323.4360	2.379937	12.078	9.1	0.0173	HM3	2.3799
N III	1093.3861	323.4930	2.379937	12.078	9.1	0.0348	HM3	2.3799
O III	1093.4983	305.5960	2.578248	13.694	9.3	0.4200	HM3	2.5785
O III	1093.6333	305.5960	2.578690	13.997	6.6	0.4200	HM3	2.5785
O III	1093.7124	305.5960	2.578949	13.526	10.5	0.4200	HM3	2.5785
He I	1093.8651	507.0576	1.157280	16.022	10.9	0.0020	HMs0.1	1.1573
O III	1094.5843	507.3910	1.157280	13.648	8.9	0.1850	HMs0.1	1.1573
Ne III	1094.6042	313.0590	2.496479	10.712	7.4	0.0410	HM3	2.4965
He I	1095.2893	507.7178	1.157280	16.022	10.9	0.0027	HMs0.1	1.1573
C II	1097.0116	903.6235	0.214014	13.917	6.4	0.1620	HM2	0.2140
He I	1097.2854	508.6431	1.157280	16.022	10.9	0.0039	HMs0.1	1.1573
C II	1097.4220	903.9616	0.214014	13.917	6.4	0.3220	HM2	0.2140
C III	1098.6890	386.2028	1.844850	13.195	5.2	0.2160	MF	1.8450
C III	1098.7652	386.2028	1.845047	15.096	9.1	0.2160	MF	1.8450
C III	1098.9217	386.2028	1.845452	14.171	11.1	0.2160	MF	1.8450
He I	1100.2081	509.9979	1.157280	16.022	10.9	0.0054	HMs0.1	1.1573
N III	1100.3944	314.7150	2.496479	11.071	8.8	0.1940	HM3	2.4965
N II	1102.4236	442.0520	1.493878	11.137	13.2	0.0461	PL15	1.4941
N II	1102.5077	442.0520	1.494068	10.888	7.2	0.0461	PL15	1.4941
N II	1102.5829	442.0520	1.494238	10.638	7.6	0.0461	PL15	1.4941
He I	1104.7391	512.0982	1.157280	16.022	10.9	0.0084	HMs0.1	1.1573
C III	1106.7748	310.1697	2.568288	12.793	7.3	0.0779	HM2	2.5683
C III	1106.8371	310.1697	2.568489	12.533	18.6	0.0779	HM2	2.5683
C III	1107.0218	322.5741	2.431837	12.350	7.6	0.0452	HM3	2.4321
C III	1107.1073	322.5741	2.432102	13.007	15.9	0.0452	HM3	2.4321
C III	1107.3025	322.5741	2.432707	13.087	16.7	0.0452	HM3	2.4321
C III	1107.4156	322.5741	2.433058	13.705	9.6	0.0452	HM3	2.4331
C III	1107.5353	322.5741	2.433429	13.527	13.3	0.0452	HM3	2.4331
C III	1107.6026	322.5741	2.433638	13.335	11.3	0.0452	HM3	2.4331
C II	1108.7240	594.8000	0.864028	12.158	4.7	0.1170	SB	0.8643
C II	1108.8708	594.8000	0.864275	12.851	5.2	0.1170	SB	0.8643
C III	1108.9438	322.5741	2.437796	12.837	8.0	0.0452	MF	2.4386
C II	1109.0197	594.8000	0.864525	12.449	7.4	0.1170	SB	0.8643
C II	1109.0825	594.8000	0.864631	12.631	4.6	0.1170	SB	0.8643
C III	1109.1056	322.5741	2.438297	13.050	13.2	0.0452	MF	2.4386
C II	1109.1488	594.8000	0.864742	12.609	6.9	0.1170	SB	0.8643
C III	1109.2112	322.5741	2.438625	12.431	8.0	0.0452	MF	2.4386
C III	1109.2819	322.5741	2.438844	12.630	6.2	0.0452	MF	2.4386
C II	1109.2825	594.8000	0.864967	12.250	13.5	0.1170	SB	0.8643
C III	1109.5656	322.5741	2.439723	12.418	16.0	0.0452	HM	2.4405
C III	1109.8277	322.5741	2.440536	12.363	9.2	0.0452	HM	2.4405
C III	1109.8641	310.1697	2.578248	12.908	10.2	0.0779	HM3	2.5785
Ne II	1109.8745	445.0397	1.493878	10.562	12.9	0.0203	PL15	1.4941
Ne II	1109.9592	445.0397	1.494068	10.149	6.6	0.0203	PL15	1.4941
N III	1109.9797	323.4360	2.431837	11.959	7.1	0.0173	HM3	2.4321
C III	1110.0011	310.1697	2.578690	12.827	7.5	0.0779	HM3	2.5785
N II	1110.0068	644.6337	0.721919	12.349	5.0	0.2240	HM	0.7222
Ne II	1110.0350	445.0397	1.494238	10.201	7.2	0.0203	PL15	1.4941
N III	1110.0655	323.4360	2.432102	12.542	15.7	0.0173	HM3	2.4321
C III	1110.0814	310.1697	2.578949	13.120	11.2	0.0779	HM3	2.5785
N II	1110.1045	644.6337	0.722070	12.678	8.0	0.2240	HM	0.7222
N III	1110.1753	323.4930	2.431837	11.959	7.1	0.0348	HM3	2.4321
N II	1110.1792	644.6337	0.722186	13.539	4.8	0.2240	HM	0.7222
N III	1110.2611	323.4360	2.432707	12.550	16.5	0.0173	HM3	2.4321
N III	1110.2611	323.4930	2.432102	12.542	15.7	0.0348	HM3	2.4321
N III	1110.3745	323.4360	2.433058	12.601	9.2	0.0173	HM3	2.4331
N III	1110.4568	323.4930	2.432707	12.550	16.5	0.0348	HM3	2.4321
N III	1110.4946	323.4360	2.433429	12.285	13.0	0.0173	HM3	2.4331
N III	1110.5620	323.4360	2.433638	12.406	11.0	0.0173	HM3	2.4331
N III	1110.5702	323.4930	2.433058	12.601	9.2	0.0348	HM3	2.4331
N III	1110.6903	323.4930	2.433429	12.285	13.0	0.0348	HM3	2.4331
N III	1110.7577	323.4930	2.433638	12.406	11.0	0.0348	HM3	2.4331
N II	1111.5671	915.6131	0.214014	13.278	6.3	0.1450	HM2	0.2140

Table A.5: continued.

ion	λ_{obs} (Å)	λ_{rest} (Å)	z	log N	b (km/s)	f	model	z_{system}
N III	1111.9069	323.4360	2.437796	10.056	7.8	0.0173	MF	2.4386
N III	1112.0690	323.4360	2.438297	10.832	13.1	0.0173	MF	2.4386
N III	1112.1028	323.4930	2.437796	10.056	7.8	0.0348	MF	2.4386
N III	1112.1750	323.4360	2.438625	11.150	7.7	0.0173	MF	2.4386
N III	1112.2459	323.4360	2.438844	11.717	5.8	0.0173	MF	2.4386
Ar V	1112.2619	445.9970	1.493878	10.943	12.6	1.4000	PL15	1.4941
N III	1112.2650	323.4930	2.438297	10.832	13.1	0.0348	MF	2.4386
He I	1112.3290	515.6165	1.157280	16.022	10.9	0.0155	HMs0.1	1.1573
Ar V	1112.3468	445.9970	1.494068	11.054	5.8	1.4000	PL15	1.4941
N III	1112.3710	323.4930	2.438625	11.150	7.7	0.0348	MF	2.4386
N III	1112.4419	323.4930	2.438844	11.717	5.8	0.0348	MF	2.4386
N III	1112.5302	323.4360	2.439723	11.804	15.8	0.0173	HM	2.4405
N III	1112.7263	323.4930	2.439723	11.804	15.8	0.0348	HM	2.4405
N III	1112.7931	323.4360	2.440536	11.201	9.0	0.0173	HM	2.4405
Ne II	1112.9068	446.2556	1.493878	10.562	12.9	0.1020	PL15	1.4941
N III	1112.9892	323.4930	2.440536	11.201	9.0	0.0348	HM	2.4405
Ne II	1112.9917	446.2556	1.494068	10.149	6.6	0.1020	PL15	1.4941
Ne II	1113.0677	446.2556	1.494238	10.201	7.2	0.1020	PL15	1.4941
C IV	1114.8116	312.4220	2.568288	12.545	7.3	0.1310	HM2	2.5683
C IV	1114.8744	312.4220	2.568489	12.524	18.6	0.1310	HM2	2.5683
C IV	1114.9222	312.4530	2.568288	12.545	7.3	0.0657	HM2	2.5683
O II	1114.9308	391.9120	1.844850	12.286	4.6	0.0273	MF	1.8450
C IV	1114.9850	312.4530	2.568489	12.524	18.6	0.0657	HM2	2.5683
O II	1115.0081	391.9120	1.845047	12.943	8.8	0.0273	MF	1.8450
O II	1115.0190	391.9430	1.844850	12.286	4.6	0.0548	MF	1.8450
O II	1115.0963	391.9430	1.845047	12.943	8.8	0.0548	MF	1.8450
O II	1115.1670	391.9120	1.845452	12.762	10.9	0.0273	MF	1.8450
O II	1115.1868	392.0020	1.844850	12.286	4.6	0.0821	MF	1.8450
O II	1115.2552	391.9430	1.845452	12.762	10.9	0.0548	MF	1.8450
O II	1115.2642	392.0020	1.845047	12.943	8.8	0.0821	MF	1.8450
O II	1115.4231	392.0020	1.845452	12.762	10.9	0.0821	MF	1.8450
Ne III	1117.0846	313.0590	2.568288	11.782	5.9	0.0410	HM2	2.5683
Ne III	1117.1475	313.0590	2.568489	11.421	18.1	0.0410	HM2	2.5683
C IV	1117.9234	312.4220	2.578248	12.825	10.2	0.1310	HM3	2.5785
C IV	1118.0343	312.4530	2.578248	12.825	10.2	0.0657	HM3	2.5785
C IV	1118.0614	312.4220	2.578690	12.503	7.5	0.1310	HM3	2.5785
C IV	1118.1423	312.4220	2.578949	12.852	11.2	0.1310	HM3	2.5785
C IV	1118.1724	312.4530	2.578690	12.503	7.5	0.0657	HM3	2.5785
C IV	1118.2533	312.4530	2.578949	12.852	11.2	0.0657	HM3	2.5785
Ne III	1120.2027	313.0590	2.578248	11.918	8.7	0.0410	HM3	2.5785
Ne III	1120.3411	313.0590	2.578690	13.212	6.0	0.0410	HM3	2.5785
Ne III	1120.4221	313.0590	2.578949	13.921	10.1	0.0410	HM3	2.5785
N III	1122.9937	314.7150	2.568288	12.293	6.8	0.1940	HM2	2.5683
N III	1123.0570	314.7150	2.568489	12.067	18.4	0.1940	HM2	2.5683
Ar IV	1125.2376	451.2000	1.493878	11.238	12.6	0.5210	PL15	1.4941
Ar IV	1125.3234	451.2000	1.494068	11.144	5.8	0.5210	PL15	1.4941
Ar IV	1125.4002	451.2000	1.494238	10.312	6.8	0.5210	PL15	1.4941
N III	1126.1283	314.7150	2.578248	12.157	9.7	0.1940	HM3	2.5785
N III	1126.2674	314.7150	2.578690	11.664	7.0	0.1940	HM3	2.5785
N III	1126.3488	314.7150	2.578949	12.431	10.8	0.1940	HM3	2.5785
He I	1126.5591	522.2128	1.157280	16.022	10.9	0.0302	HMs0.1	1.1573
N III	1126.9060	451.8690	1.493878	12.829	13.2	0.0272	PL15	1.4941
Ar IV	1126.9085	451.8700	1.493878	11.238	12.6	1.0400	PL15	1.4941
N III	1126.9919	451.8690	1.494068	12.779	7.2	0.0272	PL15	1.4941
Ar IV	1126.9944	451.8700	1.494068	11.144	5.8	1.0400	PL15	1.4941
N III	1127.0689	451.8690	1.494238	12.046	7.6	0.0272	PL15	1.4941
Ar IV	1127.0714	451.8700	1.494238	10.312	6.8	1.0400	PL15	1.4941
C III	1127.8736	322.5741	2.496479	11.572	9.5	0.0452	HM3	2.4965
N II	1128.8263	452.6390	1.493878	11.137	13.2	0.0222	PL15	1.4941
N II	1128.9124	452.6390	1.494068	10.888	7.2	0.0222	PL15	1.4941
N II	1128.9894	452.6390	1.494238	10.638	7.6	0.0222	PL15	1.4941
Ar IV	1129.5021	452.9100	1.493878	11.238	12.6	1.5600	PL15	1.4941
Ar IV	1129.5882	452.9100	1.494068	11.144	5.8	1.5600	PL15	1.4941
Ar IV	1129.6654	452.9100	1.494238	10.312	6.8	1.5600	PL15	1.4941
N II	1130.3176	453.2370	1.493878	11.137	13.2	0.0625	PL15	1.4941
N II	1130.4038	453.2370	1.494068	10.888	7.2	0.0625	PL15	1.4941
N II	1130.4810	453.2370	1.494238	10.638	7.6	0.0625	PL15	1.4941
N III	1130.8872	323.4360	2.496479	11.071	8.8	0.0173	HM3	2.4965
N III	1131.0865	323.4930	2.496479	11.071	8.8	0.0348	HM3	2.4965

Table A.5: continued.

ion	λ_{obs} (Å)	λ_{rest} (Å)	z	log N	b (km/s)	f	model	z_{system}
S IV	1132.0618	657.3400	0.722186	10.446	4.4	1.1800	HM	0.7222
Ne V	1133.8270	357.9500	2.167557	12.855	10.9	0.1350	HM3	2.1680
Ne V	1133.9705	357.9500	2.167958	14.159	12.2	0.1350	HM3	2.1680
O IV	1134.0710	608.3980	0.864028	12.984	4.2	0.0694	SB	0.8643
O IV	1134.2212	608.3980	0.864275	13.081	4.6	0.0694	SB	0.8643
O IV	1134.3735	608.3980	0.864525	13.671	7.0	0.0694	SB	0.8643
O IV	1134.4377	608.3980	0.864631	11.861	4.0	0.0694	SB	0.8643
O IV	1134.5055	608.3980	0.864742	13.962	6.4	0.0694	SB	0.8643
O IV	1134.6423	608.3980	0.864967	12.557	13.3	0.0694	SB	0.8643
Ne VI	1137.4278	399.8200	1.844850	12.324	4.1	0.0840	MF	1.8450
Ne VI	1137.5068	399.8200	1.845047	10.914	8.7	0.0840	MF	1.8450
H I	1138.5066	937.8035	0.214014	15.053	10.3	0.0078	HM2	0.2140
Ar VI	1140.8991	457.4800	1.493878	11.009	12.6	0.9420	PL15	1.4941
Ar VI	1140.9861	457.4800	1.494068	11.368	5.8	0.9420	PL15	1.4941
Ne VI	1141.1830	401.1400	1.844850	12.324	4.1	0.1700	MF	1.8450
Ne VI	1141.2622	401.1400	1.845047	10.914	8.7	0.1700	MF	1.8450
N II	1141.9715	529.3572	1.157280	13.289	9.0	0.0819	HMs0.1	1.1573
N II	1150.9301	533.5099	1.157280	13.289	9.0	0.2560	HMs0.1	1.1573
C III	1151.0372	322.5741	2.568288	12.793	7.3	0.0452	HM2	2.5683
C III	1151.1021	322.5741	2.568489	12.533	18.6	0.0452	HM2	2.5683
H I	1153.0014	949.7431	0.214014	15.053	10.3	0.0139	HM2	0.2140
N III	1154.1127	323.4360	2.568288	12.293	6.8	0.0173	HM2	2.5683
N III	1154.1777	323.4360	2.568489	12.067	18.4	0.0173	HM2	2.5683
C III	1154.2501	322.5741	2.578248	12.908	10.2	0.0452	HM3	2.5785
N III	1154.3161	323.4930	2.568288	12.293	6.8	0.0348	HM2	2.5683
N III	1154.3811	323.4930	2.568489	12.067	18.4	0.0348	HM2	2.5683
C III	1154.3926	322.5741	2.578690	12.827	7.5	0.0452	HM3	2.5785
C III	1154.4762	322.5741	2.578949	13.120	11.2	0.0452	HM3	2.5785
N II	1156.1138	671.4102	0.721919	12.349	5.0	0.0730	HM	0.7222
N II	1156.2156	671.4102	0.722070	12.678	8.0	0.0730	HM	0.7222
N II	1156.2933	671.4102	0.722186	13.539	4.8	0.0730	HM	0.7222
N III	1157.3342	323.4360	2.578248	12.157	9.7	0.0173	HM3	2.5785
N III	1157.4771	323.4360	2.578690	11.664	7.0	0.0173	HM3	2.5785
N III	1157.5382	323.4930	2.578248	12.157	9.7	0.0348	HM3	2.5785
N III	1157.5609	323.4360	2.578949	12.431	10.8	0.0173	HM3	2.5785
N III	1157.6811	323.4930	2.578690	11.664	7.0	0.0348	HM3	2.5785
N III	1157.7649	323.4930	2.578949	12.431	10.8	0.0348	HM3	2.5785
He I	1158.5231	537.0296	1.157280	16.022	10.9	0.0734	HMs0.1	1.1573
Ne VII	1160.2927	465.2210	1.494068	10.445	6.6	0.3890	PL15	1.4941
O II	1162.9582	539.0855	1.157280	14.196	8.9	0.0560	HMs0.1	1.1573
O II	1163.9579	539.5489	1.157280	14.196	8.9	0.0370	HMs0.1	1.1573
O II	1164.6169	539.8544	1.157280	14.196	8.9	0.0190	HMs0.1	1.1573
S III	1167.0235	677.7460	0.721919	11.486	4.5	1.6400	HM	0.7222
S III	1167.1263	677.7460	0.722070	11.815	7.8	1.6400	HM	0.7222
S III	1167.2047	677.7460	0.722186	12.652	4.4	1.6400	HM	0.7222
Ne IV	1167.3623	541.1270	1.157280	10.452	8.8	0.0560	HMs0.1	1.1573
Ne IV	1169.4031	542.0730	1.157280	10.452	8.8	0.1100	HMs0.1	1.1573
O II	1171.1353	429.9180	1.724090	13.147	13.1	0.0540	HM3	1.7241
O II	1171.4704	430.0410	1.724090	13.147	13.1	0.1080	HM3	1.7241
O II	1171.8409	430.1770	1.724090	13.147	13.1	0.1620	HM3	1.7241
C II	1171.9573	543.2570	1.157280	13.820	9.2	0.0349	HMs0.1	1.1573
Ne IV	1173.3250	543.8910	1.157280	10.452	8.8	0.1700	HMs0.1	1.1573
O V	1174.1476	629.7300	0.864525	10.576	7.0	0.4990	SB	0.8643
O V	1174.2842	629.7300	0.864742	10.989	6.4	0.4990	SB	0.8643
Ne V	1177.5114	357.9500	2.289598	12.470	5.9	0.1350	HM3	2.2896
N III	1179.5074	684.9960	0.721919	11.628	5.0	0.1310	HM	0.7222
N III	1179.6113	684.9960	0.722070	11.958	8.0	0.1310	HM	0.7222
N III	1179.6906	684.9960	0.722186	12.766	4.8	0.1310	HM	0.7222
Ne VI	1180.0104	433.1760	1.724090	12.950	12.7	0.0310	HM3	1.7241

Table A.6: Predicted metal lines in the STIS spectral range (1230 − 1550 Å). Column notation as in Table A.5

ion	λ_{obs} (Å)	λ_{rest} (Å)	z	log N	b (km/s)	f	model	z_{system}
O III	1230.3259	374.0050	2.289598	13.363	6.6	0.0810	HM3	2.2896
Ne V	1230.5589	357.9500	2.437796	10.665	7.4	0.1350	MF	2.4386
Ne V	1230.7384	357.9500	2.438297	11.104	12.8	0.1350	MF	2.4386
Ne V	1230.8557	357.9500	2.438625	13.421	7.0	0.1350	MF	2.4386
N III	1230.9318	451.8690	1.724090	13.748	13.3	0.0272	HM3	1.7241
Ne V	1230.9341	357.9500	2.438844	13.008	5.0	0.1350	MF	2.4386
Ar IV	1230.9345	451.8700	1.724090	11.576	12.0	1.0400	HM3	1.7241
N III	1230.9805	374.2040	2.289598	12.675	7.0	0.4240	HM3	2.2896
Ne V	1231.2488	357.9500	2.439723	12.311	15.4	0.1350	HM	2.4405
Ne V	1231.5398	357.9500	2.440536	13.341	8.6	0.1350	HM	2.4405
Ne VI	1232.3207	433.1760	1.844850	12.324	4.1	0.0310	MF	1.8450
Ne VI	1232.4062	433.1760	1.845047	10.914	8.7	0.0310	MF	1.8450
N II	1233.0294	452.6390	1.724090	12.099	13.3	0.0222	HM3	1.7241
Ar IV	1233.7676	452.9100	1.724090	11.576	12.0	1.5600	HM3	1.7241
N II	1234.6584	453.2370	1.724090	12.099	13.3	0.0625	HM3	1.7241
O II	1239.1684	376.6930	2.289598	11.708	6.6	0.0290	HM3	2.2896
O II	1239.3394	376.7450	2.289598	11.708	6.6	0.0436	HM3	2.2896
O III	1239.8144	374.0050	2.314967	15.189	7.4	0.0810	HM3	2.3155
O III	1240.0162	374.0050	2.315507	14.770	4.3	0.0810	HM3	2.3155
O III	1240.1613	374.0050	2.315895	14.829	7.2	0.0810	HM3	2.3155
O III	1240.3344	374.0050	2.316358	14.945	5.4	0.0810	HM3	2.3155
N III	1240.4741	374.2040	2.314967	14.453	7.6	0.4240	HM3	2.3155
N II	1240.6595	436.1072	1.844850	10.802	4.9	0.0381	MF	1.8450
N III	1240.6759	374.2040	2.315507	14.741	4.6	0.4240	HM3	2.3155
N II	1240.7456	436.1072	1.845047	12.770	8.9	0.0381	MF	1.8450
N III	1240.8211	374.2040	2.315895	13.074	7.5	0.4240	HM3	2.3155
N II	1240.9223	436.1072	1.845452	12.529	11.0	0.0381	MF	1.8450
N III	1240.9944	374.2040	2.316358	13.755	5.8	0.4240	HM3	2.3155
O II	1241.4036	391.9120	2.167557	11.100	11.4	0.0273	HM3	2.1680
O II	1241.5018	391.9430	2.167557	11.100	11.4	0.0548	HM3	2.1680
O II	1241.5607	391.9120	2.167958	12.861	12.7	0.0273	HM3	2.1680
O II	1241.6589	391.9430	2.167958	12.861	12.7	0.0548	HM3	2.1680
O II	1241.6887	392.0020	2.167557	11.100	11.4	0.0821	HM3	2.1680
O II	1241.8458	392.0020	2.167958	12.861	12.7	0.0821	HM3	2.1680
H I	1245.2412	1025.7223	0.214014	15.053	10.3	0.0790	HM2	0.2140
Ar VI	1246.2167	457.4800	1.724090	11.505	12.0	0.9420	HM3	1.7241
S III	1247.1668	724.2890	0.721919	11.486	4.5	0.3520	HM	0.7222
S III	1247.2766	724.2890	0.722070	11.815	7.8	0.3520	HM	0.7222
S III	1247.3604	724.2890	0.722186	12.652	4.4	0.3520	HM	0.7222
O II	1248.7250	376.6930	2.314967	14.077	7.4	0.0290	HM3	2.3155
O II	1248.8974	376.7450	2.314967	14.077	7.4	0.0436	HM3	2.3155
O II	1248.9282	376.6930	2.315507	13.541	4.3	0.0290	HM3	2.3155
O II	1249.0744	376.6930	2.315895	12.654	7.2	0.0290	HM3	2.3155
O II	1249.1006	376.7450	2.315507	13.541	4.3	0.0436	HM3	2.3155
O II	1249.2468	376.7450	2.315895	12.654	7.2	0.0436	HM3	2.3155
O II	1249.2488	376.6930	2.316358	12.890	5.4	0.0290	HM3	2.3155
O II	1249.4212	376.7450	2.316358	12.890	5.4	0.0436	HM3	2.3155
N II	1251.5275	671.4102	0.864028	12.210	4.4	0.0730	SB	0.8643
Ne V	1251.5647	357.9500	2.496479	13.127	7.4	0.1350	HM3	2.4965
N II	1251.6933	671.4102	0.864275	11.079	4.9	0.0730	SB	0.8643
N II	1251.8614	671.4102	0.864525	11.140	7.1	0.0730	SB	0.8643
N II	1251.9322	671.4102	0.864631	11.134	4.3	0.0730	SB	0.8643
N II	1252.0071	671.4102	0.864742	10.382	6.6	0.0730	SB	0.8643
N II	1252.1580	671.4102	0.864967	11.434	13.4	0.0730	SB	0.8643
N II	1257.5715	442.0520	1.844850	10.802	4.9	0.0461	MF	1.8450
N II	1257.6588	442.0520	1.845047	12.770	8.9	0.0461	MF	1.8450
N II	1257.8380	442.0520	1.845452	12.529	11.0	0.0461	MF	1.8450
C II	1258.1273	1036.3367	0.214014	13.917	6.4	0.1230	HM2	0.2140
He I	1260.5719	584.3340	1.157280	16.022	10.9	0.2760	HMs0.1	1.1573
He I	1262.4008	506.2000	1.493878	13.384	15.4	0.0011	PL15	1.4941
He I	1262.4971	506.2000	1.494068	13.314	11.0	0.0011	PL15	1.4941
He I	1262.5833	506.2000	1.494238	12.543	10.4	0.0011	PL15	1.4941
He I	1263.3251	506.5706	1.493878	13.384	15.4	0.0015	PL15	1.4941
S III	1263.3377	677.7460	0.864028	12.890	3.2	1.6400	SB	0.8643
He I	1263.4214	506.5706	1.494068	13.314	11.0	0.0015	PL15	1.4941
S III	1263.5049	677.7460	0.864275	13.298	3.3	1.6400	SB	0.8643
He I	1263.5077	506.5706	1.494238	12.543	10.4	0.0015	PL15	1.4941
S III	1263.6746	677.7460	0.864525	13.111	6.3	1.6400	SB	0.8643

Table A.6: continued.

ion	$\lambda_{\rm obs}$ (Å)	$\lambda_{\rm rest}$ (Å)	z	log N	b (km/s)	f	model	$z_{\rm system}$
S III	1263.7461	677.7460	0.864631	13.105	2.8	1.6400	SB	0.8643
S III	1263.8217	677.7460	0.864742	12.934	5.7	1.6400	SB	0.8643
S III	1263.9741	677.7460	0.864967	13.009	13.1	1.6400	SB	0.8643
O III	1264.1135	374.0050	2.379937	13.716	8.9	0.0810	HM3	2.3799
He I	1264.5396	507.0576	1.493878	13.384	15.4	0.0020	PL15	1.4941
He I	1264.6360	507.0576	1.494068	13.314	11.0	0.0020	PL15	1.4941
He I	1264.7224	507.0576	1.494238	12.543	10.4	0.0020	PL15	1.4941
N III	1264.7861	374.2040	2.379937	12.078	9.1	0.4240	HM3	2.3799
O III	1265.3710	507.3910	1.493878	13.430	13.1	0.1850	PL15	1.4941
O III	1265.4676	507.3910	1.494068	13.314	7.0	0.1850	PL15	1.4941
O III	1265.5540	507.3910	1.494238	12.726	7.5	0.1850	PL15	1.4941
Ne II	1266.0711	445.0397	1.844850	11.373	4.1	0.0203	MF	1.8450
Ne II	1266.1590	445.0397	1.845047	11.928	8.7	0.0203	MF	1.8450
He I	1266.1860	507.7178	1.493878	13.384	15.4	0.0027	PL15	1.4941
He I	1266.2826	507.7178	1.494068	13.314	11.0	0.0027	PL15	1.4941
Ne II	1266.3393	445.0397	1.845452	11.639	10.8	0.0203	MF	1.8450
He I	1266.3691	507.7178	1.494238	12.543	10.4	0.0027	PL15	1.4941
Ne VI	1266.4526	399.8200	2.167557	12.697	10.9	0.0840	HM3	2.1680
Ne VI	1266.6129	399.8200	2.167958	13.926	12.2	0.0840	HM3	2.1680
Ne VII	1267.3039	465.2210	1.724090	11.981	12.7	0.3890	HM3	1.7241
He I	1268.4936	508.6431	1.493878	13.384	15.4	0.0039	PL15	1.4941
He I	1268.5904	508.6431	1.494068	13.314	11.0	0.0039	PL15	1.4941
He I	1268.6770	508.6431	1.494238	12.543	10.4	0.0039	PL15	1.4941
Ar V	1268.7945	445.9970	1.844850	12.104	3.1	1.4000	MF	1.8450
Ar V	1268.8825	445.9970	1.845047	11.374	8.4	1.4000	MF	1.8450
Ar V	1269.0633	445.9970	1.845452	10.448	10.5	1.4000	MF	1.8450
Ne II	1269.5302	446.2556	1.844850	11.373	4.1	0.1020	MF	1.8450
Ne II	1269.6182	446.2556	1.845047	11.928	8.7	0.1020	MF	1.8450
Ne II	1269.7991	446.2556	1.845452	11.639	10.8	0.1020	MF	1.8450
C III	1270.4518	386.2028	2.289598	13.181	7.5	0.2160	HM3	2.2896
Ne VI	1270.6338	401.1400	2.167557	12.697	10.9	0.1700	HM3	2.1680
Ne VI	1270.7946	401.1400	2.167958	13.926	12.2	0.1700	HM3	2.1680
He I	1271.8723	509.9979	1.493878	13.384	15.4	0.0054	PL15	1.4941
He I	1271.9693	509.9979	1.494068	13.314	11.0	0.0054	PL15	1.4941
He I	1272.0562	509.9979	1.494238	12.543	10.4	0.0054	PL15	1.4941
O II	1273.1988	376.6930	2.379937	11.670	8.9	0.0290	HM3	2.3155
O II	1273.3745	376.7450	2.379937	11.670	8.9	0.0436	HM3	2.3799
N III	1276.8519	684.9960	0.864028	14.226	4.4	0.1310	SB	0.8643
N III	1277.0209	684.9960	0.864275	13.476	4.9	0.1310	SB	0.8643
He I	1277.1102	512.0982	1.493878	13.384	15.4	0.0084	PL15	1.4941
N III	1277.1924	684.9960	0.864525	13.558	7.1	0.1310	SB	0.8643
He I	1277.2076	512.0982	1.494068	13.314	11.0	0.0084	PL15	1.4941
N III	1277.2647	684.9960	0.864631	12.495	4.3	0.1310	SB	0.8643
Ne V	1277.2686	357.9500	2.568288	12.512	5.9	0.1350	HM2	2.5683
He I	1277.2948	512.0982	1.494238	12.543	10.4	0.0084	PL15	1.4941
Ne V	1277.3406	357.9500	2.568489	12.655	18.1	0.1350	HM2	2.5683
N III	1277.3411	684.9960	0.864742	12.959	6.6	0.1310	SB	0.8643
N III	1277.4951	684.9960	0.864967	13.135	13.4	0.1310	SB	0.8643
N III	1277.8156	685.5130	0.864028	14.226	4.4	0.2610	SB	0.8643
N III	1277.9847	685.5130	0.864275	13.476	4.9	0.2610	SB	0.8643
N III	1278.1564	685.5130	0.864525	13.558	7.1	0.2610	SB	0.8643
N III	1278.2287	685.5130	0.864631	12.495	4.3	0.2610	SB	0.8643
N III	1278.3052	685.5130	0.864742	12.959	6.6	0.2610	SB	0.8643
N III	1278.4593	685.5130	0.864967	13.135	13.4	0.2610	SB	0.8643
C III	1280.2497	386.2028	2.314967	15.294	7.8	0.2160	HM3	2.3155
C III	1280.4580	386.2028	2.315507	15.019	4.9	0.2160	HM3	2.3155
C III	1280.6079	386.2028	2.315895	14.166	7.9	0.2160	HM3	2.3155
C II	1280.6854	687.0526	0.864028	12.158	4.7	0.2700	SB	0.8643
C III	1280.7867	386.2028	2.316358	14.671	6.2	0.2160	HM3	2.3155
Ne V	1280.8339	357.9500	2.578248	13.052	8.7	0.1350	HM3	2.5785
C II	1280.8550	687.0526	0.864275	12.851	5.2	0.2700	SB	0.8643
Ne V	1280.9920	357.9500	2.578690	13.852	6.0	0.1350	HM3	2.5785
C II	1281.0270	687.0526	0.864525	12.449	7.4	0.2700	SB	0.8643
Ne V	1281.0847	357.9500	2.578949	14.674	10.1	0.1350	HM3	2.5785
C II	1281.0995	687.0526	0.864631	12.631	4.6	0.2700	SB	0.8643
C II	1281.1761	687.0526	0.864742	12.609	6.9	0.2700	SB	0.8643
C II	1281.3306	687.0526	0.864967	12.250	13.5	0.2700	SB	0.8643
S IV	1282.8685	744.9070	0.722186	10.446	4.4	0.2510	HM	0.7222
C II	1283.1500	594.8000	1.157280	13.820	9.2	0.1170	HMs0.1	1.1573

Table A.6: continued.

ion	λ_{obs} (Å)	λ_{rest} (Å)	z	log N	b (km/s)	f	model	z_{system}
O III	1283.5243	374.0050	2.431837	12.504	6.7	0.0810	HM3	2.4321
Ar IV	1283.5962	451.2000	1.844850	12.376	3.1	0.5210	MF	1.8450
O III	1283.6235	374.0050	2.432102	13.073	15.5	0.0810	HM3	2.4321
Ar IV	1283.6853	451.2000	1.845047	12.081	8.4	0.5210	MF	1.8450
O III	1283.8497	374.0050	2.432707	13.118	16.4	0.0810	HM3	2.4321
Ar IV	1283.8682	451.2000	1.845452	11.391	10.5	0.5210	MF	1.8450
O III	1283.9809	374.0050	2.433058	14.502	8.8	0.0810	HM3	2.4331
O III	1284.1197	374.0050	2.433429	14.304	12.8	0.0810	HM3	2.4331
O III	1284.1976	374.0050	2.433638	14.676	10.7	0.0810	HM3	2.4331
N III	1284.2072	374.2040	2.431837	11.959	7.1	0.4240	HM3	2.4321
N III	1284.3064	374.2040	2.432102	12.542	15.7	0.4240	HM3	2.4321
N III	1284.5328	374.2040	2.432707	12.550	16.5	0.4240	HM3	2.4321
N III	1284.6640	374.2040	2.433058	12.601	9.2	0.4240	HM3	2.4331
N III	1284.8029	374.2040	2.433429	12.285	13.0	0.4240	HM3	2.4331
N III	1284.8809	374.2040	2.433638	12.406	11.0	0.4240	HM3	2.4331
N III	1285.4994	451.8690	1.844850	12.746	4.9	0.0272	MF	1.8450
Ar IV	1285.5023	451.8700	1.844850	12.376	3.1	1.0400	MF	1.8450
N III	1285.5886	451.8690	1.845047	14.271	8.9	0.0272	MF	1.8450
Ar IV	1285.5915	451.8700	1.845047	12.081	8.4	1.0400	MF	1.8450
O III	1285.7527	374.0050	2.437796	12.124	7.6	0.0810	MF	2.4386
N III	1285.7718	451.8690	1.845452	13.808	11.0	0.0272	MF	1.8450
Ar IV	1285.7746	451.8700	1.845452	11.391	10.5	1.0400	MF	1.8450
He I	1285.8844	515.6165	1.493878	13.384	15.4	0.0155	PL15	1.4941
O III	1285.9403	374.0050	2.438297	12.926	13.0	0.0810	MF	2.4386
He I	1285.9825	515.6165	1.494068	13.314	11.0	0.0155	PL15	1.4941
O III	1286.0628	374.0050	2.438625	13.012	7.4	0.0810	MF	2.4386
He I	1286.0703	515.6165	1.494238	12.543	10.4	0.0155	PL15	1.4941
O III	1286.1447	374.0050	2.438844	13.216	5.5	0.0810	MF	2.4386
N III	1286.4369	374.2040	2.437796	10.056	7.8	0.4240	MF	2.4386
O III	1286.4736	374.0050	2.439723	13.804	15.6	0.0810	HM	2.4405
N III	1286.6245	374.2040	2.438297	10.832	13.1	0.4240	MF	2.4386
N III	1286.7471	374.2040	2.438625	11.150	7.7	0.4240	MF	2.4386
O III	1286.7776	374.0050	2.440536	12.755	8.8	0.0810	HM	2.4405
N III	1286.8291	374.2040	2.438844	11.717	5.8	0.4240	MF	2.4386
N III	1287.1581	374.2040	2.439723	11.804	15.8	0.4240	HM	2.4405
N III	1287.4623	374.2040	2.440536	11.201	9.0	0.4240	HM	2.4405
N II	1287.6900	452.6390	1.844850	10.802	4.9	0.0222	MF	1.8450
N II	1287.7793	452.6390	1.845047	12.770	8.9	0.0222	MF	1.8450
N II	1287.9628	452.6390	1.845452	12.529	11.0	0.0222	MF	1.8450
Ar IV	1288.4609	452.9100	1.844850	12.376	3.1	1.5600	MF	1.8450
Ar IV	1288.5503	452.9100	1.845047	12.081	8.4	1.5600	MF	1.8450
Ar IV	1288.7339	452.9100	1.845452	11.391	10.5	1.5600	MF	1.8450
S IV	1288.8841	748.4000	0.722186	10.446	4.4	0.5000	HM	0.7222
O II	1289.2327	391.9120	2.289598	11.708	6.6	0.0273	HM3	2.2896
O II	1289.3347	391.9430	2.289598	11.708	6.6	0.0548	HM3	2.2896
N II	1289.3912	453.2370	1.844850	10.802	4.9	0.0625	MF	1.8450
N II	1289.4807	453.2370	1.845047	12.770	8.9	0.0625	MF	1.8450
O II	1289.5288	392.0020	2.289598	11.708	6.6	0.0821	HM3	2.2896
N II	1289.6644	453.2370	1.845452	12.529	11.0	0.0625	MF	1.8450
N II	1292.5559	474.4909	1.724090	12.099	13.3	0.0436	HM3	1.7241
O II	1292.7491	376.6930	2.431837	10.468	6.7	0.0290	HM3	2.4321
O II	1292.8489	376.6930	2.432102	11.081	15.5	0.0290	HM3	2.4321
O II	1292.9275	376.7450	2.431837	10.468	6.7	0.0436	HM3	2.4321
O II	1293.0274	376.7450	2.432102	11.081	15.5	0.0436	HM3	2.4321
O II	1293.0768	376.6930	2.432707	11.231	16.4	0.0290	HM3	2.4321
O II	1293.2089	376.6930	2.433058	12.764	8.8	0.0290	HM3	2.4331
O II	1293.2553	376.7450	2.432707	11.231	16.4	0.0436	HM3	2.4321
O II	1293.3487	376.6930	2.433429	12.701	12.8	0.0290	HM3	2.4331
O II	1293.3874	376.7450	2.433058	12.764	8.8	0.0436	HM3	2.4331
O II	1293.4272	376.6930	2.433638	13.044	10.7	0.0290	HM3	2.4331
O II	1293.5273	376.7450	2.433429	12.701	12.8	0.0436	HM3	2.4331
O II	1293.6058	376.7450	2.433638	13.044	10.7	0.0436	HM3	2.4331
O II	1294.9935	376.6930	2.437796	10.511	7.6	0.0290	MF	2.4386
O II	1295.1723	376.7450	2.437796	10.511	7.6	0.0436	MF	2.4386
O II	1295.1824	376.6930	2.438297	11.492	13.0	0.0290	MF	2.4386
O II	1295.3058	376.6930	2.438625	10.485	7.4	0.0290	MF	2.4386
O II	1295.3612	376.7450	2.438297	11.492	13.0	0.0436	MF	2.4386
O II	1295.3883	376.6930	2.438844	10.984	5.5	0.0290	MF	2.4386
O II	1295.4846	376.7450	2.438625	10.485	7.4	0.0436	MF	2.4386

Table A.6: continued.

ion	λ_{obs} (Å)	λ_{rest} (Å)	z	log N	b (km/s)	f	model	z_{system}
O II	1295.5672	376.7450	2.438844	10.984	5.5	0.0436	MF	2.4386
N II	1295.7082	475.6481	1.724090	12.099	13.3	0.1420	HM3	1.7241
O II	1295.7196	376.6930	2.439723	11.656	15.6	0.0290	HM	2.4405
O II	1295.8984	376.7450	2.439723	11.656	15.6	0.0436	HM	2.4405
O II	1296.0258	376.6930	2.440536	10.172	8.8	0.0290	HM	2.4405
O II	1296.2047	376.7450	2.440536	10.172	8.8	0.0436	HM	2.4405
O II	1299.1755	391.9120	2.314967	14.077	7.4	0.0273	HM3	2.3155
O II	1299.2783	391.9430	2.314967	14.077	7.4	0.0548	HM3	2.3155
O II	1299.3869	391.9120	2.315507	13.541	4.3	0.0273	HM3	2.3155
O II	1299.4739	392.0020	2.314967	14.077	7.4	0.0821	HM3	2.3155
O II	1299.4897	391.9430	2.315507	13.541	4.3	0.0548	HM3	2.3155
O II	1299.5390	391.9120	2.315895	12.654	7.2	0.0273	HM3	2.3155
O II	1299.6418	391.9430	2.315895	12.654	7.2	0.0548	HM3	2.3155
O II	1299.6853	392.0020	2.315507	13.541	4.3	0.0821	HM3	2.3155
O II	1299.7204	391.9120	2.316358	12.890	5.4	0.0273	HM3	2.3155
O II	1299.8232	391.9430	2.316358	12.890	5.4	0.0548	HM3	2.3155
O II	1299.8374	392.0020	2.315895	12.654	7.2	0.0821	HM3	2.3155
O II	1300.0189	392.0020	2.316358	12.890	5.4	0.0821	HM3	2.3155
Ar VI	1301.4619	457.4800	1.844850	11.956	3.1	0.9420	MF	1.8450
Ar VI	1301.5522	457.4800	1.845047	10.615	8.4	0.9420	MF	1.8450
He I	1302.3348	522.2128	1.493878	13.384	15.4	0.0302	PL15	1.4941
He I	1302.4341	522.2128	1.494068	13.314	11.0	0.0302	PL15	1.4941
S III	1302.4543	698.7310	0.864028	12.890	3.2	0.7830	SB	0.8643
He I	1302.5231	522.2128	1.494238	12.543	10.4	0.0302	PL15	1.4941
S III	1302.6267	698.7310	0.864275	13.298	3.3	0.7830	SB	0.8643
S III	1302.8017	698.7310	0.864525	13.111	6.3	0.7830	SB	0.8643
S III	1302.8754	698.7310	0.864631	13.105	2.8	0.7830	SB	0.8643
S III	1302.9533	698.7310	0.864742	12.934	5.7	0.7830	SB	0.8643
S III	1303.1104	698.7310	0.864967	13.009	13.1	0.7830	SB	0.8643
C III	1305.3413	386.2028	2.379937	13.272	9.4	0.2160	HM3	2.3799
O III	1307.7006	374.0050	2.496479	12.256	8.3	0.0810	HM3	2.4965
N III	1308.3964	374.2040	2.496479	11.071	8.8	0.4240	HM3	2.4965
Ne V	1308.6801	480.4100	1.724090	13.240	12.7	0.1050	HM3	1.7241
O III	1309.1667	702.3320	0.864028	14.490	4.2	0.1260	SB	0.8643
O III	1309.3400	702.3320	0.864275	14.600	4.6	0.1260	SB	0.8643
O III	1309.5159	702.3320	0.864525	14.950	7.0	0.1260	SB	0.8643
O III	1309.5899	702.3320	0.864631	14.055	4.0	0.1260	SB	0.8643
O III	1309.6683	702.3320	0.864742	15.316	6.4	0.1260	SB	0.8643
O III	1309.8261	702.3320	0.864967	14.375	13.3	0.1260	SB	0.8643
O IV	1312.4847	608.3980	1.157280	10.947	8.9	0.0694	HMs0.1	1.1573
N III	1314.4094	763.3400	0.721919	11.628	5.0	0.0839	HM	0.7222
N III	1314.5251	763.3400	0.722070	11.958	8.0	0.0839	HM	0.7222
N III	1314.6135	763.3400	0.722186	12.766	4.8	0.0839	HM	0.7222
S II	1314.9553	763.6570	0.721919	11.569	4.5	0.3980	HM	0.7222
S II	1315.0710	763.6570	0.722070	11.898	7.8	0.3980	HM	0.7222
S II	1315.1595	763.6570	0.722186	12.765	4.4	0.3980	HM	0.7222
Ne VI	1315.2469	399.8200	2.289598	11.792	5.9	0.0840	HM3	2.2896
N II	1315.9835	1083.9937	0.214014	13.278	6.3	0.1030	HM2	0.2140
S II	1316.2691	764.4200	0.721919	11.569	4.5	0.7950	HM	0.7222
S II	1316.3850	764.4200	0.722070	11.898	7.8	0.7950	HM	0.7222
S II	1316.4735	764.4200	0.722186	12.765	4.4	0.7950	HM	0.7222
N IV	1317.7273	765.1480	0.722186	10.501	4.8	0.6320	HM	0.7222
S II	1318.4611	765.6930	0.721919	11.569	4.5	1.1900	HM	0.7222
S II	1318.5772	765.6930	0.722070	11.898	7.8	1.1900	HM	0.7222
S II	1318.6658	765.6930	0.722186	12.765	4.4	1.1900	HM	0.7222
Ne VI	1319.5891	401.1400	2.289598	11.792	5.9	0.1700	HM3	2.2896
N II	1320.1521	529.3572	1.493878	11.137	13.2	0.0819	PL15	1.4941
N II	1320.2527	529.3572	1.494068	10.888	7.2	0.0819	PL15	1.4941
N II	1320.3429	529.3572	1.494238	10.638	7.6	0.0819	PL15	1.4941
O II	1324.6380	391.9120	2.379937	11.670	8.9	0.0273	HM3	2.3799
O II	1324.7428	391.9430	2.379937	11.670	8.9	0.0548	HM3	2.3799
O II	1324.9422	392.0020	2.379937	11.670	8.9	0.0821	HM3	2.3799
C III	1325.3852	386.2028	2.431837	12.350	7.6	0.2160	HM3	2.4321
Ne VI	1325.3903	399.8200	2.314967	11.134	7.1	0.0840	HM3	2.3155
C III	1325.4876	386.2028	2.432102	13.007	15.9	0.2160	HM3	2.4321
Ne VI	1325.6060	399.8200	2.315507	11.094	3.8	0.0840	HM3	2.3155
C III	1325.7212	386.2028	2.432707	13.087	16.7	0.2160	HM3	2.4321
Ne VI	1325.7611	399.8200	2.315895	14.102	6.7	0.0840	HM3	2.3155
C III	1325.8566	386.2028	2.433058	13.705	9.6	0.2160	HM3	2.4331

Table A.6: continued.

ion	λ_{obs} (Å)	λ_{rest} (Å)	z	log N	b (km/s)	f	model	z_{system}
Ne VI	1325.9462	399.8200	2.316358	13.661	4.8	0.0840	HM3	2.3155
C III	1326.0000	386.2028	2.433429	13.527	13.3	0.2160	HM3	2.4331
C III	1326.0805	386.2028	2.433638	13.335	11.3	0.2160	HM3	2.4331
C III	1327.6863	386.2028	2.437796	12.837	8.0	0.2160	MF	2.4386
C III	1327.8799	386.2028	2.438297	13.050	13.2	0.2160	MF	2.4386
C III	1328.0064	386.2028	2.438625	12.431	8.0	0.2160	MF	2.4386
C III	1328.0911	386.2028	2.438844	12.630	6.2	0.2160	MF	2.4386
C III	1328.4307	386.2028	2.439723	12.418	16.0	0.2160	HM	2.4405
C III	1328.7446	386.2028	2.440536	12.363	9.2	0.2160	HM	2.4405
Ne III	1329.6501	488.1080	1.724090	13.708	12.7	0.0630	HM3	1.7241
Ne VI	1329.7660	401.1400	2.314967	11.134	7.1	0.1700	HM3	2.3155
Ne VI	1329.9824	401.1400	2.315507	11.094	3.8	0.1700	HM3	2.3155
Ne VI	1330.1381	401.1400	2.315895	14.102	6.7	0.1700	HM3	2.3155
Ne VI	1330.3238	401.1400	2.316358	13.661	4.8	0.1700	HM3	2.3155
N II	1330.5084	533.5099	1.493878	11.137	13.2	0.2560	PL15	1.4941
N II	1330.6099	533.5099	1.494068	10.888	7.2	0.2560	PL15	1.4941
N II	1330.7007	533.5099	1.494238	10.638	7.6	0.2560	PL15	1.4941
Ne III	1333.4557	489.5050	1.724090	13.708	12.7	0.1900	HM3	1.7241
O III	1334.5575	374.0050	2.568288	13.297	6.5	0.0810	HM2	2.5683
O III	1334.6327	374.0050	2.568489	13.134	18.3	0.0810	HM2	2.5683
N III	1335.2676	374.2040	2.568288	12.293	6.8	0.4240	HM2	2.5683
N III	1335.3428	374.2040	2.568489	12.067	18.4	0.4240	HM2	2.5683
O III	1338.2826	374.0050	2.578248	13.694	9.3	0.0810	HM3	2.5785
O III	1338.4479	374.0050	2.578690	13.997	6.6	0.0810	HM3	2.5785
O III	1338.5447	374.0050	2.578949	13.526	10.5	0.0810	HM3	2.5785
N III	1338.9947	374.2040	2.578248	12.157	9.7	0.4240	HM3	2.5785
N III	1339.1600	374.2040	2.578690	11.664	7.0	0.4240	HM3	2.5785
N III	1339.2569	374.2040	2.578949	12.431	10.8	0.4240	HM3	2.5785
He I	1339.2861	537.0296	1.493878	13.384	15.4	0.0734	PL15	1.4941
He I	1339.3882	537.0296	1.494068	13.314	11.0	0.0734	PL15	1.4941
He I	1339.4797	537.0296	1.494238	12.543	10.4	0.0734	PL15	1.4941
O II	1344.1490	376.6930	2.568288	11.912	6.5	0.0290	HM2	2.5683
O II	1344.2248	376.6930	2.568489	11.507	18.3	0.0290	HM2	2.5683
O II	1344.3346	376.7450	2.568288	11.912	6.5	0.0436	HM2	2.5683
O II	1344.4103	376.7450	2.568489	11.507	18.3	0.0436	HM2	2.5683
O II	1344.4133	539.0855	1.493878	11.643	13.1	0.0560	PL15	1.4941
O II	1344.5158	539.0855	1.494068	11.292	7.0	0.0560	PL15	1.4941
O II	1344.6076	539.0855	1.494238	11.286	7.5	0.0560	PL15	1.4941
O II	1344.9782	391.9120	2.431837	10.468	6.7	0.0273	HM3	2.4321
O II	1345.0821	391.9120	2.432102	11.081	15.5	0.0273	HM3	2.4321
O II	1345.0846	391.9430	2.431837	10.468	6.7	0.0548	HM3	2.4321
O II	1345.1885	391.9430	2.432102	11.081	15.5	0.0548	HM3	2.4321
O II	1345.2871	392.0020	2.431837	10.468	6.7	0.0821	HM3	2.4321
O II	1345.3192	391.9120	2.432707	11.231	16.4	0.0273	HM3	2.4321
O II	1345.3910	392.0020	2.432102	11.081	15.5	0.0821	HM3	2.4321
O II	1345.4256	391.9430	2.432707	11.231	16.4	0.0548	HM3	2.4321
O II	1345.4566	391.9120	2.433058	12.764	8.8	0.0273	HM3	2.4331
O II	1345.5631	391.9430	2.433058	12.764	8.8	0.0548	HM3	2.4331
O II	1345.5689	539.5489	1.493878	11.643	13.1	0.0370	PL15	1.4941
O II	1345.6021	391.9120	2.433429	12.701	12.8	0.0273	HM3	2.4331
O II	1345.6281	392.0020	2.432707	11.231	16.4	0.0821	HM3	2.4321
O II	1345.6715	539.5489	1.494068	11.292	7.0	0.0370	PL15	1.4941
O II	1345.6838	391.9120	2.433638	13.044	10.7	0.0273	HM3	2.4331
O II	1345.7085	391.9430	2.433429	12.701	12.8	0.0548	HM3	2.4331
O II	1345.7634	539.5489	1.494238	11.286	7.5	0.0370	PL15	1.4941
O II	1345.7656	392.0020	2.433058	12.764	8.8	0.0821	HM3	2.4331
O II	1345.7902	391.9430	2.433638	13.044	10.7	0.0548	HM3	2.4331
O II	1345.9111	392.0020	2.433429	12.701	12.8	0.0821	HM3	2.4331
O II	1345.9928	392.0020	2.433638	13.044	10.7	0.0821	HM3	2.4331
O II	1346.3308	539.8544	1.493878	11.643	13.1	0.0190	PL15	1.4941
O II	1346.4335	539.8544	1.494068	11.292	7.0	0.0190	PL15	1.4941
O II	1346.5254	539.8544	1.494238	11.286	7.5	0.0190	PL15	1.4941
O II	1347.3133	391.9120	2.437796	10.511	7.6	0.0273	MF	2.4386
O II	1347.4199	391.9430	2.437796	10.511	7.6	0.0548	MF	2.4386
O II	1347.5099	391.9120	2.438297	11.492	13.0	0.0273	MF	2.4386
O II	1347.6164	391.9430	2.438297	11.492	13.0	0.0548	MF	2.4386
O II	1347.6228	392.0020	2.437796	10.511	7.6	0.0821	MF	2.4386
O II	1347.6382	391.9120	2.438625	10.485	7.4	0.0273	MF	2.4386
O II	1347.7241	391.9120	2.438844	10.984	5.5	0.0273	MF	2.4386

Table A.6: continued.

ion	$\lambda_{\rm obs}$ (Å)	$\lambda_{\rm rest}$ (Å)	z	$\log N$	b (km/s)	f	model	$z_{\rm system}$
O II	1347.7448	391.9430	2.438625	10.485	7.4	0.0548	MF	2.4386
O II	1347.8193	392.0020	2.438297	11.492	13.0	0.0821	MF	2.4386
O II	1347.8307	391.9430	2.438844	10.984	5.5	0.0548	MF	2.4386
O II	1347.9010	376.6930	2.578248	11.766	9.3	0.0290	HM3	2.5785
O II	1347.9477	392.0020	2.438625	10.485	7.4	0.0821	MF	2.4386
O II	1348.0336	392.0020	2.438844	10.984	5.5	0.0821	MF	2.4386
O II	1348.0674	376.6930	2.578690	12.090	6.6	0.0290	HM3	2.5785
O II	1348.0687	391.9120	2.439723	11.656	15.6	0.0273	HM	2.4405
O II	1348.0870	376.7450	2.578248	11.766	9.3	0.0436	HM3	2.5785
O II	1348.1649	376.6930	2.578949	11.665	10.5	0.0290	HM3	2.5785
O II	1348.1754	391.9430	2.439723	11.656	15.6	0.0548	HM	2.4405
O II	1348.2535	376.7450	2.578690	12.090	6.6	0.0436	HM3	2.5785
O II	1348.3510	376.7450	2.578949	11.665	10.5	0.0436	HM3	2.5785
O II	1348.3783	392.0020	2.439723	11.656	15.6	0.0821	HM	2.4405
O II	1348.3873	391.9120	2.440536	10.172	8.8	0.0273	HM	2.4405
O II	1348.4939	391.9430	2.440536	10.172	8.8	0.0548	HM	2.4405
O II	1348.6969	392.0020	2.440536	10.172	8.8	0.0821	HM	2.4405
Ne IV	1349.5045	541.1270	1.493878	13.007	12.9	0.0560	PL15	1.4941
Ne IV	1349.6074	541.1270	1.494068	13.067	6.6	0.0560	PL15	1.4941
Ne IV	1349.6996	541.1270	1.494238	12.014	7.2	0.0560	PL15	1.4941
N II	1349.8553	474.4909	1.844850	10.802	4.9	0.0436	MF	1.8450
N II	1349.9490	474.4909	1.845047	12.770	8.9	0.0436	MF	1.8450
S III	1350.0951	724.2890	0.864028	12.890	3.2	0.3520	SB	0.8643
N II	1350.1413	474.4909	1.845452	12.529	11.0	0.0436	MF	1.8450
S III	1350.2739	724.2890	0.864275	13.298	3.3	0.3520	SB	0.8643
C III	1350.3500	386.2028	2.496479	11.572	9.5	0.2160	HM3	2.4965
S III	1350.4552	724.2890	0.864525	13.111	6.3	0.3520	SB	0.8643
S III	1350.5316	724.2890	0.864631	13.105	2.8	0.3520	SB	0.8643
S III	1350.6124	724.2890	0.864742	12.934	5.7	0.3520	SB	0.8643
S III	1350.7752	724.2890	0.864967	13.009	13.1	0.3520	SB	0.8643
Ne VI	1351.3666	399.8200	2.379937	13.489	8.5	0.0840	HM3	2.3799
Ne IV	1351.8637	542.0730	1.493878	13.007	12.9	0.1100	PL15	1.4941
Ne IV	1351.9668	542.0730	1.494068	13.067	6.6	0.1100	PL15	1.4941
Ne IV	1352.0591	542.0730	1.494238	12.014	7.2	0.1100	PL15	1.4941
N II	1353.1474	475.6481	1.844850	10.802	4.9	0.1420	MF	1.8450
N II	1353.2413	475.6481	1.845047	12.770	8.9	0.1420	MF	1.8450
N II	1353.4341	475.6481	1.845452	12.529	11.0	0.1420	MF	1.8450
C II	1354.8165	543.2570	1.493878	12.134	13.4	0.0349	PL15	1.4941
C II	1354.9198	543.2570	1.494068	11.951	7.5	0.0349	PL15	1.4941
C II	1355.0123	543.2570	1.494238	11.529	7.9	0.0349	PL15	1.4941
Ne VI	1355.8281	401.1400	2.379937	13.489	8.5	0.1700	HM3	2.3799
Ne IV	1356.3976	543.8910	1.493878	13.007	12.9	0.1700	PL15	1.4941
O IV	1356.4937	787.7110	0.722070	10.202	8.0	0.1100	HM	0.7222
Ne IV	1356.5010	543.8910	1.494068	13.067	6.6	0.1700	PL15	1.4941
O IV	1356.5849	787.7110	0.722186	10.951	4.7	0.1100	HM	0.7222
Ne IV	1356.5937	543.8910	1.494238	12.014	7.2	0.1700	PL15	1.4941
O II	1361.7898	429.9180	2.167557	11.100	11.4	0.0540	HM3	2.1680
O II	1361.9621	429.9180	2.167958	12.861	12.7	0.0540	HM3	2.1680
O II	1362.1794	430.0410	2.167557	11.100	11.4	0.1080	HM3	2.1680
O II	1362.3517	430.0410	2.167958	12.861	12.7	0.1080	HM3	2.1680
O II	1362.6102	430.1770	2.167557	11.100	11.4	0.1620	HM3	2.1680
O II	1362.7826	430.1770	2.167958	12.861	12.7	0.1620	HM3	2.1680
Ne V	1366.6943	480.4100	1.844850	13.714	4.1	0.1050	MF	1.8450
Ne V	1366.7891	480.4100	1.845047	12.797	8.7	0.1050	MF	1.8450
Ne V	1366.9838	480.4100	1.845452	11.865	10.8	0.1050	MF	1.8450
Ne VI	1372.1097	433.1760	2.167557	12.697	10.9	0.0310	HM3	2.1680
Ne VI	1372.1172	399.8200	2.431837	12.097	6.0	0.0840	HM3	2.4321
Ne VI	1372.2232	399.8200	2.432102	12.358	15.3	0.0840	HM3	2.4321
Ne VI	1372.2833	433.1760	2.167958	13.926	12.2	0.0310	HM3	2.1680
Ne VI	1372.4650	399.8200	2.432707	11.937	16.1	0.0840	HM3	2.4321
Ne VI	1372.6052	399.8200	2.433058	12.946	8.2	0.0840	HM3	2.4331
Ne VI	1372.7537	399.8200	2.433429	12.355	12.5	0.0840	HM3	2.4331
Ne VI	1372.8370	399.8200	2.433638	12.797	10.3	0.0840	HM3	2.4331
Ne VI	1374.8309	399.8200	2.438625	12.598	7.0	0.0840	MF	2.4386
Ne VI	1374.9185	399.8200	2.438844	11.848	5.0	0.0840	MF	2.4386
Ne VI	1375.2700	399.8200	2.439723	11.739	15.4	0.0840	HM	2.4405
Ne VI	1375.5950	399.8200	2.440536	12.954	8.6	0.0840	HM	2.4405
Ne VI	1376.6472	401.1400	2.431837	12.097	6.0	0.1700	HM3	2.4321
Ne VI	1376.7536	401.1400	2.432102	12.358	15.3	0.1700	HM3	2.4321

Table A.6: continued.

ion	λ_{obs} (Å)	λ_{rest} (Å)	z	log N	b (km/s)	f	model	z_{system}
Ne VI	1376.9962	401.1400	2.432707	11.937	16.1	0.1700	HM3	2.4321
Ne VI	1377.1369	401.1400	2.433058	12.946	8.2	0.1700	HM3	2.4331
Ne VI	1377.2858	401.1400	2.433429	12.355	12.5	0.1700	HM3	2.4331
Ne VI	1377.3694	401.1400	2.433638	12.797	10.3	0.1700	HM3	2.4331
C III	1378.0827	386.2028	2.568288	12.793	7.3	0.2160	HM2	2.5683
C III	1378.1604	386.2028	2.568489	12.533	18.6	0.2160	HM2	2.5683
He I	1378.9344	506.2000	1.724090	16.330	17.4	0.0011	HM3	1.7241
Ne VI	1379.3699	401.1400	2.438625	12.598	7.0	0.1700	MF	2.4386
Ne VI	1379.4578	401.1400	2.438844	11.848	5.0	0.1700	MF	2.4386
Ne VI	1379.8105	401.1400	2.439723	11.739	15.4	0.1700	HM	2.4405
O IV	1379.9373	553.3300	1.493878	13.819	13.1	0.1100	PL15	1.4941
He I	1379.9439	506.5706	1.724090	16.330	17.4	0.0015	HM3	1.7241
O IV	1380.0425	553.3300	1.494068	13.940	7.0	0.1100	PL15	1.4941
Ne VI	1380.1365	401.1400	2.440536	12.954	8.6	0.1700	HM	2.4405
O IV	1380.1368	553.3300	1.494238	12.796	7.5	0.1100	PL15	1.4941
He I	1381.2705	507.0576	1.724090	16.330	17.4	0.0020	HM3	1.7241
O IV	1381.7952	554.0750	1.493878	13.819	13.1	0.2180	PL15	1.4941
O IV	1381.9006	554.0750	1.494068	13.940	7.0	0.2180	PL15	1.4941
C III	1381.9294	386.2028	2.578248	12.908	10.2	0.2160	HM3	2.5785
O IV	1381.9950	554.0750	1.494238	12.796	7.5	0.2180	PL15	1.4941
C III	1382.1000	386.2028	2.578690	12.827	7.5	0.2160	HM3	2.5785
O III	1382.1787	507.3910	1.724090	14.524	13.1	0.1850	HM3	1.7241
C III	1382.2000	386.2028	2.578949	13.120	11.2	0.2160	HM3	2.5785
He I	1383.0690	507.7178	1.724090	16.330	17.4	0.0027	HM3	1.7241
He I	1385.5896	508.6431	1.724090	16.330	17.4	0.0039	HM3	1.7241
S IV	1388.5277	744.9070	0.864028	12.934	3.2	0.2510	SB	0.8643
Ne III	1388.5939	488.1080	1.844850	13.700	4.1	0.0630	MF	1.8450
Ne III	1388.6903	488.1080	1.845047	13.830	8.7	0.0630	MF	1.8450
S IV	1388.7115	744.9070	0.864275	13.683	3.3	0.2510	SB	0.8643
Ne III	1388.8881	488.1080	1.845452	13.373	10.8	0.0630	MF	1.8450
S IV	1388.8980	744.9070	0.864525	13.535	6.3	0.2510	SB	0.8643
S IV	1388.9766	744.9070	0.864631	12.497	2.8	0.2510	SB	0.8643
S IV	1389.0597	744.9070	0.864742	13.514	5.7	0.2510	SB	0.8643
S IV	1389.2271	744.9070	0.864967	12.748	13.1	0.2510	SB	0.8643
He I	1389.2802	509.9979	1.724090	16.330	17.4	0.0054	HM3	1.7241
N II	1390.6552	644.6337	1.157280	13.289	9.0	0.2240	HMs0.1	1.1573
Ne III	1392.5682	489.5050	1.844850	13.700	4.1	0.1900	MF	1.8450
Ne III	1392.6648	489.5050	1.845047	13.830	8.7	0.1900	MF	1.8450
Ne III	1392.8632	489.5050	1.845452	13.373	10.8	0.1900	MF	1.8450
Ne VI	1393.0551	558.5900	1.493878	11.741	12.9	0.1400	PL15	1.4941
Ne VI	1393.1613	558.5900	1.494068	12.300	6.6	0.1400	PL15	1.4941
Ne VI	1393.2565	558.5900	1.494238	10.073	7.2	0.1400	PL15	1.4941
S IV	1394.3990	809.6680	0.722186	10.446	4.4	0.1040	HM	0.7222
He I	1395.0016	512.0982	1.724090	16.330	17.4	0.0084	HM3	1.7241
S IV	1395.0387	748.4000	0.864028	12.934	3.2	0.5000	SB	0.8643
S IV	1395.2234	748.4000	0.864275	13.683	3.3	0.5000	SB	0.8643
S IV	1395.4108	748.4000	0.864525	13.535	6.3	0.5000	SB	0.8643
S IV	1395.4898	748.4000	0.864631	12.497	2.8	0.5000	SB	0.8643
S IV	1395.5732	748.4000	0.864742	13.514	5.7	0.5000	SB	0.8643
S IV	1395.7415	748.4000	0.864967	12.748	13.1	0.5000	SB	0.8643
C II	1397.1685	560.2394	1.493878	12.134	13.4	0.0571	PL15	1.4941
C II	1397.2750	560.2394	1.494068	11.951	7.5	0.0571	PL15	1.4941
C II	1397.3705	560.2394	1.494238	11.529	7.9	0.0571	PL15	1.4941
Ne VI	1397.9622	399.8200	2.496479	13.535	7.4	0.0840	HM3	2.4965
O II	1398.4548	391.9120	2.568288	11.912	6.5	0.0273	HM2	2.5683
O II	1398.5336	391.9120	2.568489	11.507	18.3	0.0273	HM2	2.5683
O II	1398.5654	391.9430	2.568288	11.912	6.5	0.0548	HM2	2.5683
O II	1398.6442	391.9430	2.568489	11.507	18.3	0.0548	HM2	2.5683
O II	1398.7760	392.0020	2.568288	11.912	6.5	0.0821	HM2	2.5683
O II	1398.8547	392.0020	2.568489	11.507	18.3	0.0821	HM2	2.5683
O II	1402.3583	391.9120	2.578248	11.766	9.3	0.0273	HM3	2.5785
O II	1402.4693	391.9430	2.578248	11.766	9.3	0.0548	HM3	2.5785
O II	1402.5315	391.9120	2.578690	12.090	6.6	0.0273	HM3	2.5785
Ne VI	1402.5776	401.1400	2.496479	13.535	7.4	0.1700	HM3	2.4965
O II	1402.6329	391.9120	2.578949	11.665	10.5	0.0273	HM3	2.5785
O II	1402.6424	391.9430	2.578690	12.090	6.6	0.0548	HM3	2.5785
O II	1402.6804	392.0020	2.578248	11.766	9.3	0.0821	HM3	2.5785
O II	1402.7439	391.9430	2.578949	11.665	10.5	0.0548	HM3	2.5785
O II	1402.8536	392.0020	2.578690	12.090	6.6	0.0821	HM3	2.5785

Table A.6: continued.

ion	$\lambda_{\rm obs}$ (Å)	$\lambda_{\rm rest}$ (Å)	z	log N	b (km/s)	f	model	$z_{\rm system}$
O II	1402.9550	392.0020	2.578949	11.665	10.5	0.0821	HM3	2.5785
He I	1404.5858	515.6165	1.724090	16.330	17.4	0.0155	HM3	1.7241
Ne II	1409.8670	445.0397	2.167958	12.134	12.2	0.0203	HM3	2.1680
Ar V	1412.7209	445.9970	2.167557	10.595	10.0	1.4000	HM3	2.1680
Ar V	1412.8997	445.9970	2.167958	11.896	11.3	1.4000	HM3	2.1680
Ne II	1413.7189	446.2556	2.167958	12.134	12.2	0.1020	HM3	2.1680
O II	1414.2572	429.9180	2.289598	11.708	6.6	0.0540	HM3	2.2896
O II	1414.6618	430.0410	2.289598	11.708	6.6	0.1080	HM3	2.2896
O II	1415.1092	430.1770	2.289598	11.708	6.6	0.1620	HM3	2.2896
Ne V	1417.5699	568.4200	1.493878	12.774	12.9	0.0815	PL15	1.4941
Ne V	1417.6780	568.4200	1.494068	13.092	6.6	0.0815	PL15	1.4941
Ne V	1417.7748	568.4200	1.494238	11.436	7.2	0.0815	PL15	1.4941
S IV	1418.0662	657.3400	1.157280	10.696	8.5	1.1800	HMs0.1	1.1573
He I	1422.5547	522.2128	1.724090	16.330	17.4	0.0302	HM3	1.7241
N III	1422.8873	763.3400	0.864028	14.226	4.4	0.0839	SB	0.8643
N III	1423.0757	763.3400	0.864275	13.476	4.9	0.0839	SB	0.8643
N III	1423.2668	763.3400	0.864525	13.558	7.1	0.0839	SB	0.8643
N III	1423.3474	763.3400	0.864631	12.495	4.3	0.0839	SB	0.8643
N III	1423.4325	763.3400	0.864742	12.959	6.6	0.0839	SB	0.8643
S II	1423.4782	763.6570	0.864028	10.948	3.2	0.3980	SB	0.8643
N III	1423.6041	763.3400	0.864967	13.135	13.4	0.0839	SB	0.8643
S II	1423.6667	763.6570	0.864275	11.015	3.3	0.3980	SB	0.8643
S II	1423.8579	763.6570	0.864525	10.796	6.3	0.3980	SB	0.8643
S II	1423.9384	763.6570	0.864631	11.747	2.8	0.3980	SB	0.8643
S II	1424.0236	763.6570	0.864742	10.464	5.7	0.3980	SB	0.8643
S II	1424.1953	763.6570	0.864967	11.353	13.1	0.3980	SB	0.8643
S II	1424.9004	764.4200	0.864028	10.948	3.2	0.7950	SB	0.8643
Ne VI	1424.9747	433.1760	2.289598	11.792	5.9	0.0310	HM3	2.2896
S II	1425.0891	764.4200	0.864275	11.015	3.3	0.7950	SB	0.8643
O II	1425.1642	429.9180	2.314967	14.077	7.4	0.0540	HM3	2.3155
S II	1425.2805	764.4200	0.864525	10.796	6.3	0.7950	SB	0.8643
S II	1425.3612	764.4200	0.864631	11.747	2.8	0.7950	SB	0.8643
O II	1425.3961	429.9180	2.315507	13.541	4.3	0.0540	HM3	2.3155
S II	1425.4464	764.4200	0.864742	10.464	5.7	0.7950	SB	0.8643
O II	1425.5629	429.9180	2.315895	12.654	7.2	0.0540	HM3	2.3155
O II	1425.5719	430.0410	2.314967	14.077	7.4	0.1080	HM3	2.3155
S II	1425.6182	764.4200	0.864967	11.353	13.1	0.7950	SB	0.8643
O II	1425.7619	429.9180	2.316358	12.890	5.4	0.0540	HM3	2.3155
O II	1425.8039	430.0410	2.315507	13.541	4.3	0.1080	HM3	2.3155
O II	1425.9708	430.0410	2.315895	12.654	7.2	0.1080	HM3	2.3155
O II	1426.0227	430.1770	2.314967	14.077	7.4	0.1620	HM3	2.3155
O II	1426.1698	430.0410	2.316358	12.890	5.4	0.1080	HM3	2.3155
O II	1426.2548	430.1770	2.315507	13.541	4.3	0.1620	HM3	2.3155
N IV	1426.2574	765.1480	0.864028	13.566	4.4	0.6320	SB	0.8643
O II	1426.4217	430.1770	2.315895	12.654	7.2	0.1620	HM3	2.3155
N IV	1426.4463	765.1480	0.864275	13.193	4.9	0.6320	SB	0.8643
O II	1426.6208	430.1770	2.316358	12.890	5.4	0.1620	HM3	2.3155
N IV	1426.6379	765.1480	0.864525	13.300	7.1	0.6320	SB	0.8643
Ne VI	1426.6728	399.8200	2.568288	12.028	5.9	0.0840	HM2	2.5683
N IV	1426.7186	765.1480	0.864631	11.165	4.3	0.6320	SB	0.8643
Ne VI	1426.7532	399.8200	2.568489	12.406	18.1	0.0840	HM2	2.5683
N IV	1426.8039	765.1480	0.864742	12.856	6.6	0.6320	SB	0.8643
N IV	1426.9759	765.1480	0.864967	12.159	13.4	0.6320	SB	0.8643
S II	1427.2733	765.6930	0.864028	10.948	3.2	1.1900	SB	0.8643
S II	1427.4623	765.6930	0.864275	11.015	3.3	1.1900	SB	0.8643
S II	1427.6540	765.6930	0.864525	10.796	6.3	1.1900	SB	0.8643
S II	1427.7348	765.6930	0.864631	11.747	2.8	1.1900	SB	0.8643
S II	1427.8202	765.6930	0.864742	10.464	5.7	1.1900	SB	0.8643
S II	1427.9923	765.6930	0.864967	11.353	13.1	1.1900	SB	0.8643
Ar IV	1429.2017	451.2000	2.167557	10.533	10.0	0.5210	HM3	2.1680
Ar IV	1429.3826	451.2000	2.167958	12.056	11.3	0.5210	HM3	2.1680
Ne VI	1430.6551	399.8200	2.578248	12.841	8.7	0.0840	HM3	2.5785
Ne VI	1430.8318	399.8200	2.578690	13.344	6.0	0.0840	HM3	2.5785
Ne VI	1430.9353	399.8200	2.578949	14.276	10.1	0.0840	HM3	2.5785
N III	1431.3208	451.8690	2.167557	10.652	11.7	0.0272	HM3	2.1680
Ar IV	1431.3240	451.8700	2.167557	10.533	10.0	1.0400	HM3	2.1680
Ne VI	1431.3830	401.1400	2.568288	12.028	5.9	0.1700	HM2	2.5683
Ne VI	1431.4636	401.1400	2.568489	12.406	18.1	0.1700	HM2	2.5683
N III	1431.5019	451.8690	2.167958	12.311	13.1	0.0272	HM3	2.1680

Table A.6: continued.

ion	λ_{obs} (Å)	λ_{rest} (Å)	z	log N	b (km/s)	f	model	z_{system}
Ar IV	1431.5051	451.8700	2.167958	12.056	11.3	1.0400	HM3	2.1680
O II	1433.9402	832.7572	0.721919	13.180	4.9	0.0700	HM	0.7222
O II	1434.0664	832.7572	0.722070	13.509	8.0	0.0700	HM	0.7222
O II	1434.1629	832.7572	0.722186	14.366	4.7	0.0700	HM	0.7222
O III	1434.2326	832.9270	0.721919	12.198	4.9	0.0998	HM	0.7222
O III	1434.3588	832.9270	0.722070	12.528	8.0	0.0998	HM	0.7222
O III	1434.4553	832.9270	0.722186	13.332	4.7	0.0998	HM	0.7222
N II	1434.6172	436.1072	2.289598	10.714	7.0	0.0381	HM3	2.2896
Ar IV	1434.6182	452.9100	2.167557	10.533	10.0	1.5600	HM3	2.1680
Ar IV	1434.7998	452.9100	2.167958	12.056	11.3	1.5600	HM3	2.1680
O II	1434.9255	833.3294	0.721919	13.180	4.9	0.1500	HM	0.7222
O II	1435.0518	833.3294	0.722070	13.509	8.0	0.1500	HM	0.7222
O II	1435.1483	833.3294	0.722186	14.366	4.7	0.1500	HM	0.7222
Ne VI	1435.3784	401.1400	2.578248	12.841	8.7	0.1700	HM3	2.5785
Ne VI	1435.5556	401.1400	2.578690	13.344	6.0	0.1700	HM3	2.5785
Ne VI	1435.6595	401.1400	2.578949	14.276	10.1	0.1700	HM3	2.5785
Ne VI	1435.9643	433.1760	2.314967	11.134	7.1	0.0310	HM3	2.3155
Ne VI	1436.1980	433.1760	2.315507	11.094	3.8	0.0310	HM3	2.3155
Ne VI	1436.3661	433.1760	2.315895	14.102	6.7	0.0310	HM3	2.3155
Ne VI	1436.5666	433.1760	2.316358	13.661	4.8	0.0310	HM3	2.3155
O II	1436.8817	834.4655	0.721919	13.180	4.9	0.2100	HM	0.7222
O II	1437.0083	834.4655	0.722070	13.509	8.0	0.2100	HM	0.7222
O II	1437.1049	834.4655	0.722186	14.366	4.7	0.2100	HM	0.7222
He I	1440.0630	506.2000	1.844850	13.486	8.8	0.0011	MF	1.8450
He I	1440.1629	506.2000	1.845047	14.047	10.9	0.0011	MF	1.8450
He I	1440.3681	506.2000	1.845452	13.792	12.7	0.0011	MF	1.8450
He I	1441.1173	506.5706	1.844850	13.486	8.8	0.0015	MF	1.8450
He I	1441.2173	506.5706	1.845047	14.047	10.9	0.0015	MF	1.8450
He I	1441.4226	506.5706	1.845452	13.792	12.7	0.0015	MF	1.8450
N II	1442.0167	529.3572	1.724090	12.099	13.3	0.0819	HM3	1.7241
He I	1442.5027	507.0576	1.844850	13.486	8.8	0.0020	MF	1.8450
He I	1442.6028	507.0576	1.845047	14.047	10.9	0.0020	MF	1.8450
He I	1442.8083	507.0576	1.845452	13.792	12.7	0.0020	MF	1.8450
O III	1443.4512	507.3910	1.844850	14.334	4.6	0.1850	MF	1.8450
O III	1443.5513	507.3910	1.845047	14.459	8.8	0.1850	MF	1.8450
O III	1443.7570	507.3910	1.845452	14.024	10.9	0.1850	MF	1.8450
He I	1444.3809	507.7178	1.844850	13.486	8.8	0.0027	MF	1.8450
He I	1444.4811	507.7178	1.845047	14.047	10.9	0.0027	MF	1.8450
He I	1444.6869	507.7178	1.845452	13.792	12.7	0.0027	MF	1.8450
Si II	1445.1814	1190.4158	0.214014	12.892	6.1	0.2500	HM2	0.2140
N II	1445.6812	436.1072	2.314967	12.960	7.6	0.0381	HM3	2.3155
N II	1445.9164	436.1072	2.315507	13.142	4.6	0.0381	HM3	2.3155
N II	1446.0856	436.1072	2.315895	10.605	7.5	0.0381	HM3	2.3155
N II	1446.2875	436.1072	2.316358	11.415	5.8	0.0381	HM3	2.3155
He I	1447.0132	508.6431	1.844850	13.486	8.8	0.0039	MF	1.8450
He I	1447.1136	508.6431	1.845047	14.047	10.9	0.0039	MF	1.8450
He I	1447.3198	508.6431	1.845452	13.792	12.7	0.0039	MF	1.8450
N II	1448.4196	671.4102	1.157280	13.289	9.0	0.0730	HMs0.1	1.1573
Si II	1448.6704	1193.2897	0.214014	12.892	6.1	0.4990	HM2	0.2140
Ar VI	1449.0940	457.4800	2.167557	10.692	10.0	0.9420	HM3	2.1680
Ar VI	1449.2773	457.4800	2.167958	12.003	11.3	0.9420	HM3	2.1680
He I	1450.8674	509.9979	1.844850	13.486	8.8	0.0054	MF	1.8450
He I	1450.9681	509.9979	1.845047	14.047	10.9	0.0054	MF	1.8450
He I	1451.1748	509.9979	1.845452	13.792	12.7	0.0054	MF	1.8450
O II	1453.0959	429.9180	2.379937	11.670	8.9	0.0540	HM3	2.3799
N II	1453.3290	533.5099	1.724090	12.099	13.3	0.2560	HM3	1.7241
O II	1453.5117	430.0410	2.379937	11.670	8.9	0.1080	HM3	2.3799
O II	1453.9713	430.1770	2.379937	11.670	8.9	0.1620	HM3	2.3799
N II	1454.1732	442.0520	2.289598	10.714	7.0	0.0461	HM3	2.2896
He I	1456.8425	512.0982	1.844850	13.486	8.8	0.0084	MF	1.8450
He I	1456.9436	512.0982	1.845047	14.047	10.9	0.0084	MF	1.8450
He I	1457.1511	512.0982	1.845452	13.792	12.7	0.0084	MF	1.8450
He I	1457.2575	584.3340	1.493878	13.384	15.4	0.2760	PL15	1.4941
He I	1457.3686	584.3340	1.494068	13.314	11.0	0.2760	PL15	1.4941
He I	1457.4681	584.3340	1.494238	12.543	10.4	0.2760	PL15	1.4941
Ar VII	1460.7888	585.7500	1.493878	10.572	12.6	1.2100	PL15	1.4941
Ar VII	1460.9002	585.7500	1.494068	11.131	5.8	1.2100	PL15	1.4941
S III	1462.0877	677.7460	1.157280	12.704	8.5	1.6400	HMs0.1	1.1573
He I	1462.9170	537.0296	1.724090	16.330	17.4	0.0734	HM3	1.7241

Table A.6: continued.

ion	λ_{obs} (Å)	λ_{rest} (Å)	z	log N	b (km/s)	f	model	z_{system}
Ne II	1464.0015	445.0397	2.289598	10.579	5.9	0.0203	HM3	2.2896
Ne VI	1464.1078	433.1760	2.379937	13.489	8.5	0.0310	HM3	2.3799
Si III	1464.7079	1206.5000	0.214014	12.622	6.1	1.6690	HM2	0.2140
N II	1465.3880	442.0520	2.314967	12.960	7.6	0.0461	HM3	2.3155
N II	1465.6265	442.0520	2.315507	13.142	4.6	0.0461	HM3	2.3155
N II	1465.7980	442.0520	2.315895	10.605	7.5	0.0461	HM3	2.3155
N II	1466.0026	442.0520	2.316358	11.415	5.8	0.0461	HM3	2.3155
S V	1466.0209	786.4800	0.864028	11.530	3.2	1.4600	SB	0.8643
S V	1466.2150	786.4800	0.864275	12.605	3.3	1.4600	SB	0.8643
S V	1466.4119	786.4800	0.864525	12.508	6.3	1.4600	SB	0.8643
S V	1466.4949	786.4800	0.864631	10.410	2.8	1.4600	SB	0.8643
S V	1466.5826	786.4800	0.864742	12.635	5.7	1.4600	SB	0.8643
S V	1466.7594	786.4800	0.864967	11.027	13.1	1.4600	SB	0.8643
He I	1466.8515	515.6165	1.844850	13.486	8.8	0.0155	MF	1.8450
He I	1466.9533	515.6165	1.845047	14.047	10.9	0.0155	MF	1.8450
Ar V	1467.1506	445.9970	2.289598	10.540	4.4	1.4000	HM3	2.2896
He I	1467.1623	515.6165	1.845452	13.792	12.7	0.0155	MF	1.8450
Ne II	1468.0013	446.2556	2.289598	10.579	5.9	0.1020	HM3	2.2896
O IV	1468.3155	787.7110	0.864028	12.984	4.2	0.1100	SB	0.8643
O IV	1468.5099	787.7110	0.864275	13.081	4.6	0.1100	SB	0.8643
O II	1468.5174	539.0855	1.724090	13.147	13.1	0.0560	HM3	1.7241
O IV	1468.7072	787.7110	0.864525	13.671	7.0	0.1100	SB	0.8643
O IV	1468.7903	787.7110	0.864631	11.861	4.0	0.1100	SB	0.8643
O IV	1468.8781	787.7110	0.864742	13.962	6.4	0.1100	SB	0.8643
O IV	1469.0552	787.7110	0.864967	12.557	13.3	0.1100	SB	0.8643
O II	1469.7798	539.5489	1.724090	13.147	13.1	0.0370	HM3	1.7241
O II	1470.6120	539.8544	1.724090	13.147	13.1	0.0190	HM3	1.7241
Ne VII	1473.6140	465.2210	2.167557	11.660	10.9	0.3890	HM3	2.1680
Ne VII	1473.8005	465.2210	2.167958	13.069	12.2	0.3890	HM3	2.1680
Ne IV	1474.0786	541.1270	1.724090	13.210	12.7	0.0560	HM3	1.7241
Ne II	1475.2921	445.0397	2.314967	13.538	7.1	0.0203	HM3	2.3155
O II	1475.4086	429.9180	2.431837	10.468	6.7	0.0540	HM3	2.4321
O II	1475.5226	429.9180	2.432102	11.081	15.5	0.0540	HM3	2.4321
Ne II	1475.5322	445.0397	2.315507	12.963	3.8	0.0203	HM3	2.3155
Ne II	1475.7049	445.0397	2.315895	11.719	6.7	0.0203	HM3	2.3155
O II	1475.7827	429.9180	2.432707	11.231	16.4	0.0540	HM3	2.4321
O II	1475.8307	430.0410	2.431837	10.468	6.7	0.1080	HM3	2.4321
H I	1475.8405	1215.6701	0.214014	15.053	10.3	0.4160	HM2	0.2140
Ne II	1475.9109	445.0397	2.316358	12.066	4.8	0.0203	HM3	2.3155
O II	1475.9334	429.9180	2.433058	12.764	8.8	0.0540	HM3	2.4331
O II	1475.9447	430.0410	2.432102	11.081	15.5	0.1080	HM3	2.4321
O II	1476.0930	429.9180	2.433429	12.701	12.8	0.0540	HM3	2.4331
O II	1476.1826	429.9180	2.433638	13.044	10.7	0.0540	HM3	2.4331
O II	1476.2049	430.0410	2.432707	11.231	16.4	0.1080	HM3	2.4321
O II	1476.2975	430.1770	2.431837	10.468	6.7	0.1620	HM3	2.4321
O II	1476.3557	430.0410	2.433058	12.764	8.8	0.1080	HM3	2.4331
O II	1476.4115	430.1770	2.432102	11.081	15.5	0.1620	HM3	2.4321
O II	1476.5153	430.0410	2.433429	12.701	12.8	0.1080	HM3	2.4331
O II	1476.6049	430.0410	2.433638	13.044	10.7	0.1080	HM3	2.4331
Ne IV	1476.6556	542.0730	1.724090	13.210	12.7	0.1100	HM3	1.7241
O II	1476.6717	430.1770	2.432707	11.231	16.4	0.1620	HM3	2.4321
O II	1476.8226	430.1770	2.433058	12.764	8.8	0.1620	HM3	2.4331
O II	1476.9823	430.1770	2.433429	12.701	12.8	0.1620	HM3	2.4331
O II	1477.0719	430.1770	2.433638	13.044	10.7	0.1620	HM3	2.4331
N III	1477.7280	684.9960	1.157280	13.091	9.0	0.1310	HMs0.1	1.1573
O II	1477.9702	429.9180	2.437796	10.511	7.6	0.0540	MF	2.4386
O II	1478.1858	429.9180	2.438297	11.492	13.0	0.0540	MF	2.4386
O II	1478.3266	429.9180	2.438625	10.485	7.4	0.0540	MF	2.4386
O II	1478.3931	430.0410	2.437796	10.511	7.6	0.1080	MF	2.4386
O II	1478.4208	429.9180	2.438844	10.984	5.5	0.0540	MF	2.4386
Ar V	1478.4655	445.9970	2.314967	12.104	6.6	1.4000	HM3	2.3155
O II	1478.6087	430.0410	2.438297	11.492	13.0	0.1080	MF	2.4386
Ar V	1478.7061	445.9970	2.315507	11.826	2.8	1.4000	HM3	2.3155
O II	1478.7496	430.0410	2.438625	10.485	7.4	0.1080	MF	2.4386
O II	1478.7988	429.9180	2.439723	11.656	15.6	0.0540	HM	2.4405
N III	1478.8433	685.5130	1.157280	13.091	9.0	0.2610	HMs0.1	1.1573
O II	1478.8438	430.0410	2.438844	10.984	5.5	0.1080	MF	2.4386
O II	1478.8606	430.1770	2.437796	10.511	7.6	0.1620	MF	2.4386
Ar V	1478.8792	445.9970	2.315895	12.234	5.7	1.4000	HM3	2.3155

Table A.6: continued.

ion	λ_{obs} (Å)	λ_{rest} (Å)	z	log N	b (km/s)	f	model	z_{system}
O II	1479.0763	430.1770	2.438297	11.492	13.0	0.1620	MF	2.4386
Ar V	1479.0856	445.9970	2.316358	12.410	3.4	1.4000	HM3	2.3155
O II	1479.1483	429.9180	2.440536	10.172	8.8	0.0540	HM	2.4405
O II	1479.2172	430.1770	2.438625	10.485	7.4	0.1620	MF	2.4386
O II	1479.2219	430.0410	2.439723	11.656	15.6	0.1080	HM	2.4405
O II	1479.3115	430.1770	2.438844	10.984	5.5	0.1620	MF	2.4386
Ne II	1479.3228	446.2556	2.314967	13.538	7.1	0.1020	HM3	2.3155
Ne II	1479.5635	446.2556	2.315507	12.963	3.8	0.1020	HM3	2.3155
O II	1479.5715	430.0410	2.440536	10.172	8.8	0.1080	HM	2.4405
O II	1479.6897	430.1770	2.439723	11.656	15.6	0.1620	HM	2.4405
Ne II	1479.7367	446.2556	2.315895	11.719	6.7	0.1020	HM3	2.3155
C II	1479.8810	543.2570	1.724090	12.734	13.6	0.0349	HM3	1.7241
Ne II	1479.9432	446.2556	2.316358	12.066	4.8	0.1020	HM3	2.3155
O II	1480.0394	430.1770	2.440536	10.172	8.8	0.1620	HM	2.4405
Ne IV	1481.6080	543.8910	1.724090	13.210	12.7	0.1700	HM3	1.7241
C II	1482.1646	687.0526	1.157280	13.820	9.2	0.2700	HMs0.1	1.1573
C II	1483.3584	594.8000	1.493878	12.134	13.4	0.1170	PL15	1.4941
C II	1483.4715	594.8000	1.494068	11.951	7.5	0.1170	PL15	1.4941
C II	1483.5728	594.8000	1.494238	11.529	7.9	0.1170	PL15	1.4941
Ar IV	1484.2664	451.2000	2.289598	10.729	4.4	0.5210	HM3	2.2896
He I	1485.6170	522.2128	1.844850	13.486	8.8	0.0302	MF	1.8450
He I	1485.7201	522.2128	1.845047	14.047	10.9	0.0302	MF	1.8450
He I	1485.9317	522.2128	1.845452	13.792	12.7	0.0302	MF	1.8450
N III	1486.4671	451.8690	2.289598	12.675	7.0	0.0272	HM3	2.2896
Ar IV	1486.4704	451.8700	2.289598	10.729	4.4	1.0400	HM3	2.2896
Ne VI	1486.5896	433.1760	2.431837	12.097	6.0	0.0310	HM3	2.4321
Ne VI	1486.7044	433.1760	2.432102	12.358	15.3	0.0310	HM3	2.4321
Ne VI	1486.9664	433.1760	2.432707	11.937	16.1	0.0310	HM3	2.4321
Ne VI	1487.1183	433.1760	2.433058	12.946	8.2	0.0310	HM3	2.4331
Ne VI	1487.2791	433.1760	2.433429	12.355	12.5	0.0310	HM3	2.4331
Ne VI	1487.3694	433.1760	2.433638	12.797	10.3	0.0310	HM3	2.4331
N II	1489.0001	452.6390	2.289598	10.714	7.0	0.0222	HM3	2.2896
Ne VI	1489.5296	433.1760	2.438625	12.598	7.0	0.0310	MF	2.4386
Ne VI	1489.6246	433.1760	2.438844	11.848	5.0	0.0310	MF	2.4386
Ar IV	1489.8916	452.9100	2.289598	10.729	4.4	1.5600	HM3	2.2896
Ne VI	1490.0055	433.1760	2.439723	11.739	15.4	0.0310	HM	2.4405
Ne VI	1490.3575	433.1760	2.440536	12.954	8.6	0.0310	HM	2.4405
N II	1490.9673	453.2370	2.289598	10.714	7.0	0.0625	HM3	2.2896
Ar IV	1495.7133	451.2000	2.314967	12.625	6.6	0.5210	HM3	2.3155
Ar IV	1495.9567	451.2000	2.315507	12.324	2.8	0.5210	HM3	2.3155
Ar IV	1496.1318	451.2000	2.315895	12.123	5.7	0.5210	HM3	2.3155
Ar IV	1496.3406	451.2000	2.316358	12.437	3.4	0.5210	HM3	2.3155
N II	1496.7646	436.1072	2.432102	10.230	15.7	0.0381	HM3	2.4321
N II	1497.0284	436.1072	2.432707	10.346	16.5	0.0381	HM3	2.4321
N II	1497.1813	436.1072	2.433058	10.532	9.2	0.0381	HM3	2.4331
N II	1497.3432	436.1072	2.433429	10.350	13.0	0.0381	HM3	2.4331
N II	1497.4341	436.1072	2.433638	10.440	11.0	0.0381	HM3	2.4331
N III	1497.9310	451.8690	2.314967	14.453	7.6	0.0272	HM3	2.3155
Ar IV	1497.9343	451.8700	2.314967	12.625	6.6	1.0400	HM3	2.3155
N III	1498.1748	451.8690	2.315507	14.741	4.6	0.0272	HM3	2.3155
Ar IV	1498.1781	451.8700	2.315507	12.324	2.8	1.0400	HM3	2.3155
N III	1498.3501	451.8690	2.315895	13.074	7.5	0.0272	HM3	2.3155
Ar IV	1498.3534	451.8700	2.315895	12.123	5.7	1.0400	HM3	2.3155
N III	1498.5593	451.8690	2.316358	13.755	5.8	0.0272	HM3	2.3155
Ar IV	1498.5626	451.8700	2.316358	12.437	3.4	1.0400	HM3	2.3155
N II	1500.4835	452.6390	2.314967	12.960	7.6	0.0222	HM3	2.3155
N II	1500.7277	452.6390	2.315507	13.142	4.6	0.0222	HM3	2.3155
N II	1500.9034	452.6390	2.315895	10.605	7.5	0.0222	HM3	2.3155
N II	1501.1129	452.6390	2.316358	11.415	5.8	0.0222	HM3	2.3155
Ar IV	1501.3819	452.9100	2.314967	12.625	6.6	1.5600	HM3	2.3155
Ar IV	1501.6262	452.9100	2.315507	12.324	2.8	1.5600	HM3	2.3155
Ar IV	1501.8020	452.9100	2.315895	12.123	5.7	1.5600	HM3	2.3155
Ar IV	1502.0116	452.9100	2.316358	12.437	3.4	1.5600	HM3	2.3155
N II	1502.4659	453.2370	2.314967	12.960	7.6	0.0625	HM3	2.3155
N II	1502.7104	453.2370	2.315507	13.142	4.6	0.0625	HM3	2.3155
N II	1502.8863	453.2370	2.315895	10.605	7.5	0.0625	HM3	2.3155
N II	1503.0961	453.2370	2.316358	11.415	5.8	0.0625	HM3	2.3155
O II	1503.6293	430.0410	2.496479	9.906	8.3	0.1080	HM3	2.4965
Ne II	1504.2063	445.0397	2.379937	11.353	8.5	0.0203	HM3	2.3155

Table A.6: continued.

ion	λ_{obs} (Å)	λ_{rest} (Å)	z	log N	b (km/s)	f	model	z_{system}
Ar VI	1504.9251	457.4800	2.289598	10.635	4.4	0.9420	HM3	2.2896
N II	1505.9417	529.3572	1.844850	10.802	4.9	0.0819	MF	1.8450
N II	1506.0462	529.3572	1.845047	12.770	8.9	0.0819	MF	1.8450
N II	1506.2608	529.3572	1.845452	12.529	11.0	0.0819	MF	1.8450
O IV	1507.3207	553.3300	1.724090	14.041	13.1	0.1100	HM3	1.7241
S III	1507.3582	698.7310	1.157280	12.704	8.5	0.7830	HMs0.1	1.1573
Ar V	1507.4419	445.9970	2.379937	11.405	7.8	1.4000	HM3	2.3799
Ne II	1508.3160	446.2556	2.379937	11.353	8.5	0.1020	HM3	2.3799
S IV	1509.2440	809.6680	0.864028	12.934	3.2	0.1040	SB	0.8643
O IV	1509.3502	554.0750	1.724090	14.041	13.1	0.2180	HM3	1.7241
S IV	1509.4438	809.6680	0.864275	13.683	3.3	0.1040	SB	0.8643
S IV	1509.6466	809.6680	0.864525	13.535	6.3	0.1040	SB	0.8643
S IV	1509.7320	809.6680	0.864631	12.497	2.8	0.1040	SB	0.8643
S IV	1509.8222	809.6680	0.864742	13.514	5.7	0.1040	SB	0.8643
S IV	1510.0043	809.6680	0.864967	12.748	13.1	0.1040	SB	0.8643
Ne VI	1514.5908	433.1760	2.496479	13.535	7.4	0.0310	HM3	2.4965
O III	1515.1266	702.3320	1.157280	13.648	8.9	0.1260	HMs0.1	1.1573
Ar VI	1516.5313	457.4800	2.314967	12.055	6.6	0.9420	HM3	2.3155
Ar VI	1516.7781	457.4800	2.315507	11.858	2.8	0.9420	HM3	2.3155
Ar VI	1516.9556	457.4800	2.315895	12.946	5.7	0.9420	HM3	2.3155
Ar VI	1517.1674	457.4800	2.316358	13.030	3.4	0.9420	HM3	2.3155
N II	1517.1677	442.0520	2.432102	10.230	15.7	0.0461	HM3	2.4321
O IV	1517.2701	608.3980	1.493878	13.819	13.1	0.0694	PL15	1.4941
O IV	1517.3859	608.3980	1.494068	13.940	7.0	0.0694	PL15	1.4941
N II	1517.4351	442.0520	2.432707	10.346	16.5	0.0461	HM3	2.4321
O IV	1517.4895	608.3980	1.494238	12.796	7.5	0.0694	PL15	1.4941
N II	1517.5902	442.0520	2.433058	10.532	9.2	0.0461	HM3	2.4331
N II	1517.7542	442.0520	2.433429	10.350	13.0	0.0461	HM3	2.4331
N II	1517.7555	533.5099	1.844850	10.802	4.9	0.2560	MF	1.8450
N II	1517.8464	442.0520	2.433638	10.440	11.0	0.0461	HM3	2.4331
N II	1517.8608	533.5099	1.845047	12.770	8.9	0.2560	MF	1.8450
N II	1518.0771	533.5099	1.845452	12.529	11.0	0.2560	MF	1.8450
Ne VI	1521.6494	558.5900	1.724090	12.950	12.7	0.1400	HM3	1.7241
Ne V	1521.7261	480.4100	2.167557	12.855	10.9	0.1050	HM3	2.1680
Ne V	1521.9186	480.4100	2.167958	14.159	12.2	0.1050	HM3	2.1680
Ar IV	1525.0278	451.2000	2.379937	11.380	7.8	0.5210	HM3	2.3799
C II	1526.1425	560.2394	1.724090	12.734	13.6	0.0571	HM3	1.7241
N III	1527.2889	451.8690	2.379937	12.078	9.1	0.0272	HM3	2.3799
Ar IV	1527.2923	451.8700	2.379937	11.380	7.8	1.0400	HM3	2.3799
Ne II	1527.6910	445.0397	2.432707	10.178	16.1	0.0203	HM3	2.4321
He I	1527.7686	537.0296	1.844850	13.486	8.8	0.0734	MF	1.8450
Ne II	1527.8471	445.0397	2.433058	11.867	8.2	0.0203	HM3	2.4331
He I	1527.8746	537.0296	1.845047	14.047	10.9	0.0734	MF	1.8450
Ne II	1528.0123	445.0397	2.433429	11.841	12.5	0.0203	HM3	2.4331
He I	1528.0922	537.0296	1.845452	13.792	12.7	0.0734	MF	1.8450
Ne II	1528.1050	445.0397	2.433638	12.189	10.3	0.0203	HM3	2.4331
Si II	1530.1701	1260.4221	0.214014	12.892	6.1	1.0100	HM2	0.2140
Ne II	1530.1787	445.0397	2.438297	10.406	12.8	0.0203	MF	2.4386
Ne VII	1530.3898	465.2210	2.289598	10.370	5.9	0.3890	HM3	2.2896
Ne II	1530.4220	445.0397	2.438844	10.009	5.0	0.0203	MF	2.4386
Ar V	1530.7074	445.9970	2.432102	10.437	14.8	1.4000	HM3	2.4321
Ar IV	1530.8074	452.9100	2.379937	11.380	7.8	1.5600	HM3	2.3799
Ar V	1530.9772	445.9970	2.432707	10.386	15.7	1.4000	HM3	2.4321
Ar V	1531.1336	445.9970	2.433058	11.567	7.0	1.4000	HM3	2.4331
Ar V	1531.2991	445.9970	2.433429	11.311	11.8	1.4000	HM3	2.4331
Ar V	1531.3921	445.9970	2.433638	11.694	9.5	1.4000	HM3	2.4331
Ne II	1531.8649	446.2556	2.432707	10.178	16.1	0.1020	HM3	2.4321
Ne II	1532.0214	446.2556	2.433058	11.867	8.2	0.1020	HM3	2.4331
Ne II	1532.1870	446.2556	2.433429	11.841	12.5	0.1020	HM3	2.4331
Ne II	1532.2800	446.2556	2.433638	12.189	10.3	0.1020	HM3	2.4331
Ar V	1533.6163	445.9970	2.438625	11.310	6.2	1.4000	MF	2.4386
O II	1533.6173	539.0855	1.844850	12.286	4.6	0.0560	MF	1.8450
Ar V	1533.7140	445.9970	2.438844	11.230	3.9	1.4000	MF	2.4386
O II	1533.7237	539.0855	1.845047	12.943	8.8	0.0560	MF	1.8450
O II	1533.9422	539.0855	1.845452	12.762	10.9	0.0560	MF	1.8450
O II	1534.0712	429.9180	2.568288	11.912	6.5	0.0540	HM2	2.5683
Ar V	1534.1061	445.9970	2.439723	10.125	15.0	1.4000	HM	2.4405
O II	1534.1576	429.9180	2.568489	11.507	18.3	0.0540	HM2	2.5683
Ne II	1534.3593	446.2556	2.438297	10.406	12.8	0.1020	MF	2.4386

Table A.6: continued.

ion	λ_{obs} (Å)	λ_{rest} (Å)	z	log N	b (km/s)	f	model	z_{system}
Ar V	1534.4686	445.9970	2.440536	10.972	8.3	1.4000	HM	2.4405
O II	1534.5101	430.0410	2.568288	11.912	6.5	0.1080	HM2	2.5683
O II	1534.5965	430.0410	2.568489	11.507	18.3	0.1080	HM2	2.5683
Ne II	1534.6033	446.2556	2.438844	10.009	5.0	0.1020	MF	2.4386
O II	1534.9356	539.5489	1.844850	12.286	4.6	0.0370	MF	1.8450
O II	1534.9953	430.1770	2.568288	11.912	6.5	0.1620	HM2	2.5683
O II	1535.0421	539.5489	1.845047	12.943	8.8	0.0370	MF	1.8450
O II	1535.0818	430.1770	2.568489	11.507	18.3	0.1620	HM2	2.5683
O II	1535.2608	539.5489	1.845452	12.762	10.9	0.0370	MF	1.8450
O II	1535.8047	539.8544	1.844850	12.286	4.6	0.0190	MF	1.8450
O II	1535.9112	539.8544	1.845047	12.943	8.8	0.0190	MF	1.8450
O II	1536.1301	539.8544	1.845452	12.762	10.9	0.0190	MF	1.8450
O II	1538.3532	429.9180	2.578248	11.766	9.3	0.0540	HM3	2.5785
O II	1538.5432	429.9180	2.578690	12.090	6.6	0.0540	HM3	2.5785
O II	1538.6545	429.9180	2.578949	11.665	10.5	0.0540	HM3	2.5785
O II	1538.7933	430.0410	2.578248	11.766	9.3	0.1080	HM3	2.5785
O II	1538.9833	430.0410	2.578690	12.090	6.6	0.1080	HM3	2.5785
O II	1539.0947	430.0410	2.578949	11.665	10.5	0.1080	HM3	2.5785
O II	1539.2800	430.1770	2.578248	11.766	9.3	0.1620	HM3	2.5785
Ne IV	1539.4250	541.1270	1.844850	14.118	4.1	0.0560	MF	1.8450
O II	1539.4700	430.1770	2.578690	12.090	6.6	0.1620	HM3	2.5785
Ne IV	1539.5319	541.1270	1.845047	13.721	8.7	0.0560	MF	1.8450
O II	1539.5814	430.1770	2.578949	11.665	10.5	0.1620	HM3	2.5785
Ne IV	1539.7512	541.1270	1.845452	13.033	10.8	0.0560	MF	1.8450
Ne IV	1542.1163	542.0730	1.844850	14.118	4.1	0.1100	MF	1.8450
Ne IV	1542.2233	542.0730	1.845047	13.721	8.7	0.1100	MF	1.8450
Ne IV	1542.4430	542.0730	1.845452	13.033	10.8	0.1100	MF	1.8450
Ne VII	1542.6239	465.2210	2.315895	12.860	6.7	0.3890	HM3	2.3155
Ne VII	1542.8393	465.2210	2.316358	12.236	4.8	0.3890	HM3	2.3155
C II	1545.4846	543.2570	1.844850	11.563	5.2	0.0349	MF	1.8450
C II	1545.5918	543.2570	1.845047	13.830	9.1	0.0349	MF	1.8450
Ne VI	1545.6966	433.1760	2.568288	12.028	5.9	0.0310	HM2	2.5683
Ne VI	1545.7837	433.1760	2.568489	12.406	18.1	0.0310	HM2	2.5683
C II	1545.8120	543.2570	1.845452	13.075	11.1	0.0349	MF	1.8450
Ne III	1546.1099	488.1080	2.167557	11.547	10.9	0.0630	HM3	2.1680
Ar VI	1546.2538	457.4800	2.379937	12.007	7.8	0.9420	HM3	2.3799
Ne III	1546.3055	488.1080	2.167958	14.349	12.2	0.0630	HM3	2.1680
Ne IV	1547.2882	543.8910	1.844850	14.118	4.1	0.1700	MF	1.8450
Ne IV	1547.3956	543.8910	1.845047	13.721	8.7	0.1700	MF	1.8450
Ne IV	1547.6160	543.8910	1.845452	13.033	10.8	0.1700	MF	1.8450
Ne V	1548.4272	568.4200	1.724090	13.240	12.7	0.0815	HM3	1.7241
Ar IV	1548.5646	451.2000	2.432102	10.368	14.8	0.5210	HM3	2.4321
Ar IV	1548.8375	451.2000	2.432707	10.435	15.7	0.5210	HM3	2.4321
Ar IV	1548.9958	451.2000	2.433058	11.706	7.0	0.5210	HM3	2.4331
Ar IV	1549.1633	451.2000	2.433429	11.524	11.8	0.5210	HM3	2.4331
Ar IV	1549.2573	451.2000	2.433638	11.890	9.5	0.5210	HM3	2.4331

A.3. H_2 lines towards HS 1700+6416

Table A.7: Considered H_2 lines in the FUSE spectrum of HS 1700+6416. For details of the modelling procedure see Chapter 5.

transition	λ_{rest}(Å)	f	λ_{obs}(Å)	log N	transition	λ_{rest}(Å)	f	λ_{obs}(Å)	log N
L (8 − 0) R (0)	1001.8207	0.0266	1001.668	16.0	L (5 − 0) P (3)	1043.5012	0.0107	1043.342	15.5
L (8 − 0) R (1)	1002.4531	0.0183	1002.300	17.8	L (4 − 0) R (0)	1049.3674	0.0233	1049.207	16.0
L (8 − 0) P (1)	1003.2993	0.0086	1003.146	17.8	L (4 − 0) R (1)	1049.9637	0.0154	1049.803	17.8
L (8 − 0) R (2)	1003.9838	0.0167	1003.831	14.7	L (4 − 0) P (1)	1051.0306	0.0077	1050.870	17.8
L (8 − 0) P (2)	1005.3917	0.0100	1005.238	14.7	L (4 − 0) R (2)	1051.4980	0.0139	1051.338	14.7
L (8 − 0) R (3)	1006.4127	0.0158	1006.259	15.5	L (4 − 0) P (2)	1053.2832	0.0090	1053.122	14.7
L (8 − 0) P (3)	1008.3854	0.0105	1008.232	15.5	L (4 − 0) R (3)	1053.9771	0.0133	1053.816	15.5
W (0 − 0) R (1)	1008.4970	0.0206	1008.343	17.8	L (4 − 0) P (3)	1056.4727	0.0096	1056.311	15.5
W (0 − 0) R (0)	1008.5560	0.0439	1008.402	16.0	L (3 − 0) R (0)	1062.8821	0.0178	1062.720	16.0
W (0 − 0) R (2)	1009.0233	0.0156	1008.869	14.7	L (3 − 0) R (1)	1063.4601	0.0119	1063.298	17.8
W (0 − 0) Q (1)	1009.7709	0.0245	1009.617	17.8	L (3 − 0) P (1)	1064.6056	0.0057	1064.443	17.8
W (0 − 0) R (3)	1010.1293	0.0138	1009.975	15.5	L (3 − 0) R (2)	1064.9935	0.0107	1064.831	14.7
W (0 − 0) Q (2)	1010.9380	0.0245	1010.784	14.7	L (3 − 0) P (2)	1066.8993	0.0071	1066.736	14.7
W (0 − 0) P (2)	1012.1700	0.0055	1012.016	14.7	L (3 − 0) R (3)	1067.4739	0.0101	1067.311	15.5
W (0 − 0) Q (3)	1012.6810	0.0246	1012.526	15.5	L (3 − 0) P (3)	1070.1383	0.0075	1069.975	15.5
L (7 − 0) R (0)	1012.8105	0.0295	1012.656	16.0	L (2 − 0) R (0)	1077.1399	0.0115	1076.975	16.0
L (7 − 0) R (1)	1013.4364	0.0205	1013.282	17.8	L (2 − 0) R (1)	1077.6967	0.0078	1077.532	17.8
L (7 − 0) P (1)	1014.3259	0.0087	1014.171	17.8	L (2 − 0) P (1)	1078.9231	0.0039	1078.758	17.8
W (0 − 0) P (3)	1014.5042	0.0083	1014.349	15.5	L (2 − 0) R (2)	1079.2263	0.0068	1079.062	14.7
L (7 − 0) R (2)	1014.9774	0.0190	1014.822	14.7	L (2 − 0) P (2)	1081.2670	0.0047	1081.102	14.7
L (7 − 0) P (2)	1016.4581	0.0102	1016.303	14.7	L (2 − 0) R (3)	1081.7125	0.0063	1081.547	15.5
L (7 − 0) R (3)	1017.4232	0.0184	1017.268	15.5	L (2 − 0) P (3)	1084.5618	0.0050	1084.396	15.5
L (7 − 0) P (3)	1019.5024	0.0105	1019.347	15.5	L (1 − 0) R (0)	1092.1949	0.0059	1092.028	16.0
L (6 − 0) R (0)	1024.3772	0.0288	1024.221	16.0	L (1 − 0) R (1)	1092.7323	0.0039	1092.566	17.8
L (6 − 0) R (1)	1024.9866	0.0197	1024.830	17.8	L (1 − 0) P (1)	1094.0521	0.0020	1093.885	17.8
L (6 − 0) P (1)	1025.9344	0.0089	1025.778	17.8	L (1 − 0) R (2)	1094.2440	0.0033	1094.077	14.7
L (6 − 0) R (2)	1026.5265	0.0179	1026.370	14.7	L (1 − 0) P (2)	1096.4385	0.0024	1096.271	14.7
L (6 − 0) P (2)	1028.1056	0.0105	1027.949	14.7	L (1 − 0) R (3)	1096.7252	0.0030	1096.558	15.5
L (6 − 0) R (3)	1028.9832	0.0173	1028.826	15.5	L (1 − 0) P (3)	1099.7861	0.0025	1099.618	15.5
L (6 − 0) P (3)	1031.1921	0.0112	1031.035	15.5	L (0 − 0) R (0)	1108.1271	0.0017	1107.958	16.0
L (5 − 0) R (0)	1036.5446	0.0271	1036.386	16.0	L (0 − 0) R (1)	1108.6329	0.0011	1108.464	17.8
L (5 − 0) R (1)	1037.1483	0.0180	1036.990	17.8	L (0 − 0) P (1)	1110.0626	0.0006	1109.893	17.8
L (5 − 0) P (1)	1038.1589	0.0086	1038.000	17.8	L (0 − 0) R (2)	1110.1195	0.0009	1109.950	14.7
L (5 − 0) R (2)	1038.6855	0.0165	1038.527	14.7	L (0 − 0) P (2)	1112.4955	0.0007	1112.326	14.7
L (5 − 0) P (2)	1040.3663	0.0097	1040.208	14.7	L (0 − 0) R (3)	1112.5830	0.0008	1112.413	15.5
L (5 − 0) R (3)	1041.1573	0.0159	1040.998	15.5	L (0 − 0) P (3)	1115.8949	0.0007	1115.725	15.5

A.4. Observed Lyα lines towards HS 1700+6416

Table A.8: Parameters of the observed Lyα forest towards HS 1700+6416. Errors of parameters that have been fixed during the fitting procedure are set to 0.000.

z	$\lambda_{\rm H\,I}$ (Å)	$\lambda_{\rm He\,II}$ (Å)	b (km/s)	$\log N_{\rm H\,I}$	$\log N_{\rm He\,II}$	$\log \eta$
2.2932692	4003.529 ± 0.136	1000.44	57.620 ± 8.925	12.652 ± 0.092	14.427 ± 0.282	1.775 ± 0.297
2.2936997	4004.052 ± 0.005	1000.57	21.255 ± 0.729	13.099 ± 0.024	12.781 ± 7.593	−0.318 ± 7.593
2.2969639	4008.020 ± 0.016	1001.56	21.598 ± 0.708	13.501 ± 0.061	14.388 ± 0.566	0.887 ± 0.569
2.2972877	4008.414 ± 0.080	1001.66	27.805 ± 3.775	13.166 ± 0.133	13.543 ± 2.772	0.377 ± 2.775
2.2983065	4009.653 ± 0.017	1001.97	37.677 ± 2.048	12.794 ± 0.021	14.053 ± 0.299	1.259 ± 0.300
2.3014393	4013.461 ± 0.017	1002.92	52.153 ± 1.931	13.056 ± 0.015	14.441 ± 0.181	1.385 ± 0.182
2.3044891	4017.169 ± 0.104	1003.84	27.0	<11.217	15.033 ± 0.444	>3.816
2.3053534	4018.219 ± 0.004	1004.11	33.448 ± 0.492	13.366 ± 0.007	13.889 ± 0.378	0.523 ± 0.378
2.3081048	4021.564 ± 0.014	1004.94	42.769 ± 0.862	17.189 ± 0.077	13.553 ± 1.243	−3.636 ± 1.245
2.3085747	4022.135 ± 3.111	1005.09	58.473 ± 62.372	14.313 ± 3.704	13.400 ± 0.000	−0.913 ± 0.000
2.3112931	4025.440 ± 0.021	1005.91	32.103 ± 2.010	12.868 ± 0.044	13.780 ± 0.505	0.912 ± 0.507
2.3136504	4028.306 ± 0.136	1006.63	27.0	<12.448	13.715 ± 0.199	>1.267
2.3147817	4029.681 ± 1.988	1006.97	56.159 ± 30.393	15.794 ± 3.025	14.309 ± 0.192	−1.485 ± 3.031
2.3154650	4030.512 ± 0.086	1007.18	38.402 ± 14.422	16.558 ± 1.058	13.979 0± .368	−2.579 ± 1.120
2.3161817	4031.383 ± 0.144	1007.40	27.0	<13.021	13.795 ± 0.197	>0.774
2.3170538	4032.443 ± 0.010	1007.66	32.007 ± 1.376	13.484 ± 0.018	14.133 ± 0.202	0.649 ± 0.203
2.3178902	4033.460 ± 0.016	1007.92	36.359 ± 1.736	13.166 ± 0.020	14.056 ± 0.209	0.890 ± 0.210
2.3187575	4034.514 ± 0.060	1008.18	18.440 ± 6.827	11.851 ± 0.141	13.394 ± 0.700	1.543 ± 0.714
2.3199220	4035.930 ± 0.011	1008.53	23.668 ± 1.184	12.797 ± 0.021	13.938 ± 0.247	1.141 ± 0.248
2.3209884	4037.226 ± 0.065	1008.86	51.310 ± 10.486	12.639 ± 0.063	7.856 ± 99815.	−4.783 ± 99815.
2.3219194	4038.358 ± 0.047	1009.14	29.469 ± 6.243	12.422 ± 0.165	13.986 ± 0.240	1.564 ± 0.291
2.3227687	4039.391 ± 0.441	1009.40	83.487 ± 37.738	12.402 ± 0.221	14.047 ± 0.276	1.645 ± 0.354
2.3286066	4046.488 ± 0.049	1011.17	48.383 ± 4.964	12.714 ± 0.042	14.314 ± 0.143	1.600 ± 0.149
2.3296070	4047.704 ± 0.013	1011.48	38.662 ± 1.291	13.138 ± 0.015	14.207 ± 0.151	1.069 ± 0.152
2.3325405	4051.270 ± 0.037	1012.37	63.439 ± 4.363	12.929 ± 0.029	14.231 ± 0.165	1.302 ± 0.168
2.3339231	4052.951 ± 0.002	1012.79	40.593 ± 0.242	14.400 ± 0.005	14.663 ± 0.136	0.263 ± 0.136
2.3350289	4054.295 ± 0.008	1013.12	21.245 ± 0.924	12.770 ± 0.018	14.309 ± 0.280	1.539 ± 0.281
2.3363101	4055.853 ± 0.002	1013.51	22.112 ± 0.285	13.721 ± 0.009	13.500 ± 0.000	−0.221 ± 0.000
2.3365347	4056.125 ± 0.076	1013.58	48.496 ± 4.437	12.748 ± 0.091	14.025 ± 0.219	1.277 ± 0.237
2.3382998	4058.271 ± 0.060	1014.12	27.0	<11.196	14.697 ± 0.232	>3.501
2.3410759	4061.646 ± 0.035	1014.96	28.803 ± 3.984	12.286 ± 0.062	13.200 ± 0.000	0.914 ± 0.000
2.3422129	4063.028 ± 0.008	1015.30	36.375 ± 0.937	13.181 ± 0.012	14.610 ± 0.137	1.429 ± 0.138
2.3428390	4063.789 ± 0.000	1015.49	27.0	<11.279	13.816 ± 0.255	>2.537
2.3434339	4064.513 ± 0.037	1015.68	41.113 ± 1.143	13.774 ± 0.049	14.108 ± 0.530	0.334 ± 0.532
2.3436847	4064.817 ± 0.005	1015.75	24.603 ± 0.778	13.916 ± 0.033	14.220 ± 0.354	0.304 ± 0.356
2.3448086	4066.184 ± 0.032	1016.09	48.647 ± 3.884	12.860 ± 0.036	14.256 ± 0.123	1.396 ± 0.128
2.3467796	4068.580 ± 0.060	1016.69	75.029 ± 7.335	12.808 ± 0.055	14.360 ± 0.149	1.552 ± 0.159
2.3470416	4068.898 ± 0.008	1016.77	19.724 ± 1.039	12.753 ± 0.030	14.069 ± 0.299	1.316 ± 0.301
2.3484893	4070.658 ± 0.056	1017.21	29.203 ± 3.109	12.965 ± 0.084	14.377 ± 0.159	1.412 ± 0.180
2.3489828	4071.258 ± 0.007	1017.36	26.956 ± 0.408	13.845 ± 0.012	14.335 ± 0.189	0.490 ± 0.189
2.3497748	4072.221 ± 0.132	1017.60	27.0	<11.248	14.000 ± 0.196	>2.752
2.3503101	4072.872 ± 0.001	1017.76	28.122 ± 0.159	14.143 ± 0.004	13.975 ± 0.710	−0.168 ± 0.710
2.3507690	4073.430 ± 0.120	1017.90	27.0	<11.393	14.165 ± 0.270	>2.772
2.3516626	4074.516 ± 0.006	1018.18	18.943 ± 0.700	13.006 ± 0.019	14.300 ± 0.163	1.294 ± 0.164
2.3527689	4075.861 ± 0.002	1018.51	27.642 ± 0.265	14.147 ± 0.006	15.711 ± 0.257	1.564 ± 0.257
2.3549130	4078.467 ± 0.045	1019.16	28.608 ± 5.624	12.243 ± 0.077	13.946 ± 0.170	1.703 ± 0.187
2.3561382	4079.957 ± 0.002	1019.54	26.318 ± 0.198	13.760 ± 0.004	15.681 ± 0.359	1.921 ± 0.359
2.3570836	4081.106 ± 0.004	1019.82	20.894 ± 0.387	13.197 ± 0.007	14.248 ± 0.154	1.051 ± 0.154
2.3578827	4082.078 ± 0.176	1020.07	27.0	<11.268	13.268 ± 0.198	>2.000
2.3593707	4083.886 ± 0.064	1020.52	27.0	<11.255	13.976 ± 0.116	>2.721
2.3604529	4085.202 ± 0.014	1020.85	20.314 ± 1.372	12.777 ± 0.029	14.878 ± 0.249	2.101 ± 0.251
2.3609509	4085.808 ± 0.012	1021.00	21.685 ± 1.194	12.896 ± 0.022	13.615 ± 0.400	0.719 ± 0.401
2.3615992	4086.596 ± 0.188	1021.19	27.0	<11.262	13.410 ± 0.180	>2.148
2.3623168	4087.468 ± 0.136	1021.41	27.0	<11.260	13.737 ± 0.143	>2.477
2.3629863	4088.282 ± 0.016	1021.62	34.359 ± 2.406	12.825 ± 0.024	14.507 ± 0.119	1.682 ± 0.121
2.3638363	4089.315 ± 0.007	1021.87	25.692 ± 0.772	13.046 ± 0.011	14.417 ± 0.144	1.371 ± 0.144
2.3651638	4090.929 ± 0.027	1022.28	54.354 ± 3.406	12.856 ± 0.024	14.625 ± 0.100	1.769 ± 0.103
2.3657668	4091.662 ± 0.300	1022.46	27.0	<11.237	13.640 ± 0.264	>2.403
2.3663456	4092.366 ± 0.002	1022.64	25.540 ± 0.237	14.022 ± 0.004	14.672 ± 0.232	0.650 ± 0.232
2.3670914	4093.272 ± 0.003	1022.86	27.181 ± 0.226	13.999 ± 0.004	14.585 ± 0.135	0.586 ± 0.135
2.3684988	4094.983 ± 0.076	1023.29	27.0	<11.266	13.739 ± 0.110	>2.473
2.3696377	4096.368 ± 0.200	1023.64	27.0	<11.271	13.213 ± 0.215	>1.942
2.3705003	4097.417 ± 0.184	1023.90	27.0	<11.317	13.564 ± 0.251	>2.247
2.3710568	4098.093 ± 0.059	1024.07	50.698 ± 7.181	12.643 ± 0.055	14.496 ± 0.143	1.853 ± 0.153

Table A.8: continued.

z	$\lambda_{\mathrm{H\,I}}$ (Å)	$\lambda_{\mathrm{He\,II}}$ (Å)	b (km/s)	$\log N_{\mathrm{H\,I}}$	$\log N_{\mathrm{He\,II}}$	$\log \eta$
2.3718646	4099.075 ± 0.012	1024.31	21.502 ± 1.339	13.013 ± 0.030	14.669 ± 1.417	1.656 ± 1.417
2.3722551	4099.550 ± 0.078	1024.43	14.961 ± 6.394	11.930 ± 0.257	14.348 ± 0.300	2.418 ± 0.395
2.3729448	4100.388 ± 0.021	1024.64	24.977 ± 2.443	12.385 ± 0.038	14.143 ± 0.205	1.758 ± 0.208
2.3733773	4100.914 ± 0.136	1024.77	27.0	<11.194	13.813 ± 0.167	>2.619
2.3858724	4116.104 ± 0.097	1028.57	42.027 ± 12.024	12.027 ± 0.146	13.264 ± 0.729	1.237 ± 0.743
2.3895700	4120.599 ± 0.144	1029.69	27.0	<11.213	13.304 ± 0.169	>2.091
2.3907743	4122.063 ± 0.003	1030.06	16.990 ± 0.297	13.187 ± 0.006	14.709 ± 0.195	1.522 ± 0.195
2.3926620	4124.358 ± 0.117	1030.63	53.498 ± 13.823	12.146 ± 0.122	13.862 ± 0.184	1.716 ± 0.221
2.3944483	4126.529 ± 0.044	1031.17	27.0	<11.293	15.276 ± 0.202	>3.983
2.3955731	4127.897 ± 0.004	1031.51	21.872 ± 0.528	13.794 ± 0.013	14.528 ± 0.127	0.734 ± 0.128
2.3963332	4128.821 ± 0.004	1031.75	24.201 ± 0.387	14.013 ± 0.010	12.939 ± 1.189	−1.074 ± 1.189
2.3979006	4130.726 ± 0.003	1032.22	21.232 ± 0.308	13.285 ± 0.006	16.471 ± 0.221	3.186 ± 0.221
2.3989058	4131.948 ± 0.055	1032.53	15.167 ± 6.171	11.694 ± 0.145	13.648 ± 0.217	1.954 ± 0.261
2.4000282	4133.312 ± 0.056	1032.87	27.0	<11.221	15.258 ± 0.260	>4.037
2.4009013	4134.374 ± 0.005	1033.13	18.173 ± 0.459	13.423 ± 0.019	14.214 ± 0.285	0.791 ± 0.286
2.4014597	4135.053 ± 0.008	1033.30	41.957 ± 0.518	13.962 ± 0.006	14.172 ± 0.204	0.210 ± 0.204
2.4018815	4135.565 ± 0.000	1033.43	27.0	<11.453	14.100 ± 0.000	>2.647
2.4039915	4138.131 ± 0.100	1034.07	27.0	<11.205	13.495 ± 0.122	>2.290
2.4048960	4139.230 ± 0.012	1034.35	28.487 ± 0.909	13.251 ± 0.016	14.677 ± 0.128	1.426 ± 0.129
2.4055312	4140.002 ± 0.005	1034.54	26.438 ± 0.630	13.658 ± 0.012	14.270 ± 0.220	0.612 ± 0.220
2.4061277	4140.728 ± 0.084	1034.72	27.0	<11.357	14.398 ± 0.252	>3.041
2.4077208	4142.664 ± 0.048	1035.20	27.0	<11.921	14.025 ± 0.095	>2.104
2.4088690	4144.060 ± 0.048	1035.55	37.730 ± 5.603	12.416 ± 0.053	14.100 ± 0.000	1.684 ± 0.000
2.4101009	4145.558 ± 0.036	1035.93	27.0	<11.187	18.988 ± 0.300	>7.801
2.4129813	4149.059 ± 0.096	1036.80	27.0	<11.335	13.569 ± 0.107	>2.234
2.4141040	4150.424 ± 0.136	1037.14	27.0	<11.135	13.324 ± 0.144	>2.189
2.4158101	4152.498 ± 0.015	1037.66	28.778 ± 1.551	12.584 ± 0.021	14.304 ± 0.087	1.720 ± 0.089
2.4169085	4153.833 ± 0.044	1038.00	27.0	<11.141	14.173 ± 0.119	>3.032
2.4200950	4157.707 ± 0.076	1038.96	27.0	<11.137	13.599 ± 0.098	>2.462
2.4235201	4161.871 ± 0.036	1040.00	21.810 ± 4.408	12.014 ± 0.094	14.200 ± 0.103	2.186 ± 0.139
2.4280875	4167.423 ± 0.104	1041.39	27.0	<11.131	13.398 ± 0.127	>2.267
2.4302599	4170.065 ± 0.045	1042.05	22.514 ± 1.582	13.248 ± 0.175	15.484 ± 0.238	2.236 ± 0.295
2.4305754	4170.448 ± 0.060	1042.15	27.490 ± 2.481	13.488 ± 0.102	14.500 ± 0.000	1.012 ± 0.00
2.4312742	4171.297 ± 0.000	1042.36	27.0	<11.640	15.635 ± 0.275	>3.995
2.4333057	4173.767 ± 0.001	1042.98	50.242 ± 9.364	16.453 ± 0.205	16.003 ± 0.159	−0.450 ± 0.259
2.4350693	4175.911 ± 0.002	1043.51	59.956 ± 11.387	15.101 ± 0.066	14.745 ± 0.110	−0.356 ± 0.128
2.4376934	4179.101 ± 0.000	1044.311	21.8	<12.106	14.584 ± 0.055	>2.478
2.4386029	4180.207 ± 0.000	1044.59	35.106 ± 3.486	15.667 ± 0.055	14.579 ± 0.254	−1.088 ± 0.260
2.4397273	4181.574 ± 0.000	1044.93	30.540 ± 3.612	15.552 ± 0.041	15.379 ± 0.225	−0.173 ± 0.229
2.4411495	4183.303 ± 0.000	1045.36	27.0	<11.430	15.695 ± 0.226	>4.265
2.4424334	4184.863 ± 0.000	1045.75	27.0	<11.191	13.954 ± 0.110	>2.763
2.4429662	4185.511 ± 0.002	1045.91	29.411 ± 0.176	13.677 ± 0.003	14.338 ± 0.105	0.661 ± 0.105
2.4443557	4187.200 ± 0.112	1046.33	27.0	<11.144	13.359 ± 0.129	>2.215
2.4456232	4188.741 ± 0.088	1046.72	27.0	<11.137	13.495 ± 0.109	>2.358
2.4467587	4190.122 ± 0.076	1047.06	27.0	<11.130	13.566 ± 0.103	>2.436
2.4486482	4192.418 ± 0.374	1047.64	68.854 ± 16.562	12.697 ± 0.236	14.836 ± 0.064	2.139 ± 0.245
2.4492674	4193.171 ± 0.096	1047.83	24.670 ± 6.139	12.740 ± 0.292	13.656 ± 0.505	0.916 ± 0.583
2.4501760	4194.276 ± 0.010	1048.10	22.476 ± 1.021	12.775 ± 0.025	13.356 ± 0.352	0.581 ± 0.353
2.4515486	4195.944 ± 0.034	1048.52	24.505 ± 3.640	12.074 ± 0.056	14.024 ± 0.145	1.950 ± 0.155
2.4541564	4199.115 ± 0.041	1049.31	20.614 ± 4.324	11.878 ± 0.077	15.554 ± 0.281	3.676 ± 0.291
2.4552255	4200.414 ± 0.088	1049.64	27.0	<11.098	13.565 ± 0.103	>2.467
2.4561620	4201.553 ± 0.064	1049.92	27.280 ± 6.563	11.920 ± 0.103	14.160 ± 0.125	2.240 ± 0.162
2.4575102	4203.192 ± 0.053	1050.33	66.198 ± 7.541	12.601 ± 0.039	14.592 ± 0.063	1.991 ± 0.074
2.4586728	4204.605 ± 0.004	1050.68	23.720 ± 0.469	13.093 ± 0.009	14.946 ± 0.193	1.853 ± 0.193
2.4597499	4205.915 ± 0.042	1051.01	44.192 ± 4.645	12.691 ± 0.042	14.437 ± 0.106	1.746 ± 0.114
2.4609671	4207.394 ± 0.002	1051.38	40.537 ± 0.248	14.585 ± 0.006	15.860 ± 0.182	1.275 ± 0.182
2.4625218	4209.284 ± 0.062	1051.85	51.890 ± 7.070	12.388 ± 0.052	13.982 ± 0.146	1.594 ± 0.155
2.4651504	4212.479 ± 0.220	1052.65	27.0	<11.101	13.047 ± 0.235	>1.946
2.4671617	4214.925 ± 0.156	1053.26	27.0	<11.105	13.221 ± 0.174	>2.116
2.4686501	4216.734 ± 0.002	1053.71	24.982 ± 0.197	13.588 ± 0.003	14.626 ± 0.134	1.038 ± 0.134
2.4696925	4218.001 ± 0.005	1054.03	18.813 ± 0.647	13.020 ± 0.013	15.400 ± 0.298	2.380 ± 0.298
2.4703574	4218.810 ± 0.002	1054.23	30.503 ± 0.248	13.761 ± 0.003	14.410 ± 0.134	0.649 ± 0.134
2.4717381	4220.488 ± 0.004	1054.65	36.580 ± 0.325	13.946 ± 0.004	14.722 ± 0.122	0.776 ± 0.122
2.4725440	4221.468 ± 0.003	1054.90	28.372 ± 0.221	14.084 ± 0.004	14.447 ± 0.132	0.363 ± 0.132
2.4731727	4222.232 ± 0.144	1055.09	27.0	<11.206	13.467 ± 0.155	>2.261
2.4747856	4224.193 ± 0.076	1055.58	27.0	<11.217	13.672 ± 0.102	>2.455
2.4754381	4224.986 ± 0.023	1055.78	13.086 ± 1.448	12.641 ± 0.081	14.196 ± 0.184	1.555 ± 0.201
2.4763083	4226.044 ± 0.017	1056.04	39.209 ± 2.083	13.177 ± 0.021	14.653 ± 0.083	1.476 ± 0.086
2.4777942	4227.851 ± 0.052	1056.49	27.0	<11.222	13.949 ± 0.097	>2.727

Table A.8: continued.

z	$\lambda_{\rm H\,I}$ (Å)	$\lambda_{\rm He\,II}$ (Å)	b (km/s)	$\log N_{\rm H\,I}$	$\log N_{\rm He\,II}$	$\log \eta$
2.4795668	4230.005 ± 0.118	1057.03	41.567 ± 7.475	12.728 ± 0.110	14.448 ± 0.090	1.720 ± 0.142
2.4800916	4230.643 ± 0.024	1057.19	23.727 ± 2.954	12.777 ± 0.130	13.424 ± 0.855	0.647 ± 0.865
2.4806619	4231.337 ± 0.040	1057.36	40.354 ± 2.749	13.064 ± 0.037	14.600 ± 0.090	1.536 ± 0.097
2.4823689	4233.412 ± 0.006	1057.88	23.359 ± 1.020	13.393 ± 0.061	16.170 ± 0.291	2.777 ± 0.297
2.4826272	4233.726 ± 0.051	1057.96	37.182 ± 1.482	13.343 ± 0.070	14.881 ± 0.181	1.538 ± 0.194
2.4843695	4235.844 ± 0.011	1058.49	22.866 ± 1.207	12.550 ± 0.020	14.322 ± 0.106	1.772 ± 0.108
2.4884045	4240.749 ± 0.040	1059.72	28.152 ± 4.399	12.175 ± 0.061	15.137 ± 0.171	2.962 ± 0.182
2.4893293	4241.873 ± 0.102	1060.00	32.056 ± 11.709	12.085 ± 0.152	14.243 ± 0.111	2.158 ± 0.188
2.4900737	4242.778 ± 0.136	1060.22	30.555 ± 13.720	11.941 ± 0.201	13.900 ± 0.160	1.959 ± 0.257
2.4907920	4243.652 ± 0.035	1060.44	12.943 ± 3.927	11.728 ± 0.108	13.663 ± 0.231	1.935 ± 0.255
2.4915285	4244.547 ± 0.016	1060.66	29.518 ± 1.750	12.639 ± 0.023	14.313 ± 0.104	1.674 ± 0.107
2.4925673	4245.809 ± 0.042	1060.98	41.630 ± 5.868	12.498 ± 0.053	14.312 ± 0.094	1.814 ± 0.108
2.4936314	4247.103 ± 0.045	1061.30	40.716 ± 4.719	12.483 ± 0.049	14.366 ± 0.086	1.883 ± 0.099
2.4952781	4249.105 ± 0.165	1061.80	44.338 ± 9.953	12.500 ± 0.179	14.341 ± 0.087	1.841 ± 0.199
2.4964230	4250.497 ± 0.003	1062.15	28.215 ± 0.546	14.536 ± 0.011	14.561 ± 0.110	0.025 ± 0.111
2.4971426	4251.372 ± 0.005	1062.37	21.713 ± 0.400	13.758 ± 0.014	14.016 ± 0.311	0.258 ± 0.311
2.4975386	4251.853 ± 0.112	1062.49	27.0	<11.273	13.918 ± 0.177	>2.645
2.4992042	4253.878 ± 0.064	1063.00	27.0	<11.111	14.006 ± 0.113	>2.895
2.4998393	4254.650 ± 0.068	1063.19	21.778 ± 7.247	11.699 ± 0.126	13.172 ± 0.840	1.473 ± 0.849
2.5050094	4260.935 ± 0.004	1064.76	23.183 ± 0.387	13.077 ± 0.007	14.500 ± 0.218	1.423 ± 0.218
2.5060139	4262.156 ± 0.015	1065.06	20.316 ± 0.808	13.149 ± 0.038	14.900 ± 0.298	1.751 ± 0.300
2.5064836	4262.727 ± 0.006	1065.21	27.218 ± 0.518	13.815 ± 0.009	14.600 ± 0.180	0.785 ± 0.180
2.5071969	4263.594 ± 0.003	1065.42	16.991 ± 0.436	13.081 ± 0.009	14.300 ± 0.162	1.219 ± 0.162
2.5076284	4264.119 ± 0.027	1065.56	10.658 ± 3.072	11.782 ± 0.098	13.300 ± 0.443	1.518 ± 0.454
2.5086329	4265.340 ± 0.105	1065.86	22.008 ± 11.873	11.519 ± 0.225	13.600 ± 0.280	2.081 ± 0.359
2.5093234	4266.180 ± 0.116	1066.07	27.0	<11.137	13.800 ± 0.143	>2.663
2.5100539	4267.068 ± 0.002	1066.29	35.076 ± 0.175	13.993 ± 0.002	14.600 ± 0.116	0.607 ± 0.116
2.5109098	4268.108 ± 0.010	1066.55	19.577 ± 1.086	12.623 ± 0.022	14.100 ± 0.143	1.477 ± 0.145
2.5123267	4269.831 ± 0.005	1066.98	26.445 ± 0.656	15.250 ± 0.061	15.900 ± 0.470	0.650 ± 0.474
2.5125432	4270.094 ± 0.015	1067.05	47.103 ± 0.629	14.240 ± 0.029	15.000 ± 0.209	0.760 ± 0.211
2.5141461	4272.042 ± 0.188	1067.54	27.0	<11.195	13.401 ± 0.211	>2.206
2.5145712	4272.559 ± 0.060	1067.66	31.550 ± 7.642	12.077 ± 0.133	13.700 ± 0.394	1.623 ± 0.416
2.5158017	4274.055 ± 0.196	1068.04	27.0	<11.184	13.300 ± 0.197	>2.116
2.5163667	4274.742 ± 0.116	1068.21	23.454 ± 13.082	11.598 ± 0.235	14.100 ± 0.151	2.502 ± 0.279
2.5180421	4276.779 ± 0.006	1068.72	23.193 ± 0.611	12.973 ± 0.011	14.400 ± 0.130	1.427 ± 0.130
2.5190320	4277.982 ± 0.018	1069.02	44.991 ± 2.095	12.883 ± 0.019	14.500 ± 0.086	1.617 ± 0.088
2.5215244	4281.012 ± 0.045	1069.78	30.738 ± 5.066	12.161 ± 0.070	14.100 ± 0.160	1.939 ± 0.175
2.5226157	4282.339 ± 0.002	1070.11	23.947 ± 0.182	13.615 ± 0.003	14.300 ± 0.133	0.685 ± 0.133
2.5235007	4283.414 ± 0.010	1070.38	31.434 ± 1.094	12.888 ± 0.013	14.300 ± 0.126	1.412 ± 0.127
2.5243475	4284.444 ± 0.416	1070.63	27.0	<11.153	13.600 ± 0.576	>2.447
2.5245266	4284.662 ± 0.035	1070.69	10.637 ± 3.971	11.613 ± 0.118	13.799 ± 1.430	2.186 ± 1.435
2.5250418	4285.288 ± 0.256	1070.84	27.0	<11.145	13.299 ± 0.272	>2.154
2.5260689	4286.537 ± 0.620	1071.16	27.0	<11.137	12.702 ± 0.599	>1.565
2.5271423	4287.841 ± 0.184	1071.48	27.0	<11.129	13.301 ± 0.195	>2.172
2.5280726	4288.972 ± 0.019	1071.77	33.628 ± 2.004	12.607 ± 0.024	14.400 ± 0.115	1.793 ± 0.117
2.5292625	4290.419 ± 0.027	1072.13	45.757 ± 3.098	12.638 ± 0.028	14.400 ± 0.105	1.762 ± 0.109
2.5311828	4292.753 ± 0.014	1072.71	30.252 ± 1.611	12.596 ± 0.023	14.400 ± 0.121	1.804 ± 0.123
2.5329354	4294.884 ± 0.040	1073.24	26.817 ± 4.666	12.088 ± 0.071	14.500 ± 0.127	2.412 ± 0.145
2.5335426	4295.622 ± 0.037	1073.43	11.482 ± 4.145	11.620 ± 0.123	13.701 ± 0.283	2.081 ± 0.309
2.5343657	4296.623 ± 0.006	1073.68	29.981 ± 0.676	12.976 ± 0.010	14.801 ± 0.138	1.825 ± 0.138
2.5358036	4298.371 ± 0.020	1074.11	26.943 ± 2.248	12.884 ± 0.086	14.400 ± 0.170	1.516 ± 0.191
2.5363781	4299.069 ± 0.012	1074.29	21.889 ± 1.957	13.078 ± 0.117	13.898 ± 5.187	0.820 ± 5.188
2.5368235	4299.611 ± 0.051	1074.42	43.032 ± 6.788	13.514 ± 0.200	15.099 ± 1.307	1.585 ± 1.322
2.5375869	4300.539 ± 0.513	1074.66	85.830 ± 35.569	13.408 ± 0.274	15.000 ± 0.156	1.592 ± 0.315
2.5390978	4302.375 ± 0.001	1075.11	30.926 ± 0.225	14.593 ± 0.008	15.000 ± 0.311	0.407 ± 0.311
2.5399241	4303.380 ± 0.396	1075.37	27.0	<11.111	13.100 ± 0.384	>1.989
2.5413597	4305.125 ± 0.064	1075.80	27.0	<11.118	14.200 ± 0.152	>3.082
2.5425117	4306.525 ± 4.830	1076.15	7.8	<11.095	14.101 ± *	>3.006
2.5432093	4307.374 ± 0.097	1076.36	34.111 ± 8.853	12.159 ± 0.114	14.400 ± 0.175	2.241 ± 0.209
2.5436735	4307.938 ± 0.026	1076.51	10.309 ± 3.913	11.848 ± 0.241	15.557 ± 12.40	3.709 ± 12.40
2.5440271	4308.368 ± 0.020	1076.61	31.481 ± 1.533	13.031 ± 0.024	14.900 ± 0.275	1.869 ± 0.276
2.5454447	4310.091 ± 0.080	1077.04	27.0	<11.105	15.900 ± 0.405	>4.795
2.5471518	4312.166 ± 0.003	1077.56	27.139 ± 0.360	13.281 ± 0.006	16.000 ± 0.428	2.719 ± 0.428
2.5483129	4313.578 ± 0.009	1077.91	48.879 ± 0.990	13.191 ± 0.009	15.400 ± 0.227	2.209 ± 0.227
2.5495992	4315.142 ±16.511	1078.31	7.7	<11.102	14.500 ± *	>3.398
2.5501101	4315.763 ± 0.002	1078.46	24.524 ± 0.245	13.323 ± 0.004	14.300 ± 0.321	0.977 ± 0.321
2.5510969	4316.962 ± 0.140	1078.76	27.0	<11.118	15.500 ± 0.633	>4.382
2.5523641	4318.503 ± 0.148	1079.15	27.0	<11.095	14.900 ± 0.530	>3.804
2.5532968	4319.637 ± 0.043	1079.43	32.250 ± 4.596	12.151 ± 0.059	14.400 ± 0.161	2.249 ± 0.171

Table A.8: continued.

z	$\lambda_{\mathrm{H\,I}}$ (Å)	$\lambda_{\mathrm{He\,II}}$ (Å)	b (km/s)	$\log N_{\mathrm{H\,I}}$	$\log N_{\mathrm{He\,II}}$	$\log \eta$
2.5540528	4320.556 ± 0.168	1079.66	27.0	<11.120	13.500 ± 0.186	>2.380
2.5551031	4321.833 ± 0.124	1079.98	27.0	<11.116	13.600 ± 0.151	>2.484
2.5561399	4323.093 ± 0.080	1080.29	27.0	<11.118	14.100 ± 0.161	>2.982
2.5570846	4324.241 ± 0.116	1080.58	27.0	<11.172	13.801 ± 0.142	>2.628
2.5581007	4325.476 ± 0.028	1080.89	20.714 ± 3.015	12.122 ± 0.054	15.601 ± 0.464	3.479 ± 0.467
2.5788765	4350.733 ± 0.002	1087.20	28.343 ± 1.112	15.648 ± 0.015	15.376 ± 0.213	−0.272 ± 0.214
2.5800376	4352.145 ± 0.031	1087.55	20.474 ± 3.763	12.308 ± 0.087	14.013 ± 0.191	1.705 ± 0.210
2.5805938	4352.821 ± 0.008	1087.72	26.845 ± 0.694	13.137 ± 0.012	14.407 ± 0.133	1.270 ± 0.134
2.5829947	4355.739 ± 0.041	1088.45	27.111 ± 2.548	12.561 ± 0.069	14.861 ± 0.228	2.300 ± 0.238
2.5835984	4356.473 ± 0.051	1088.63	33.241 ± 3.661	12.638 ± 0.062	14.405 ± 0.154	1.767 ± 0.166
2.5864747	4359.970 ± 0.086	1089.51	20.158 ± 9.379	11.502 ± 0.190	13.500 ± 0.000	1.998 ± 0.000
2.5891731	4363.250 ± 0.042	1090.33	82.893 ± 6.052	12.752 ± 0.046	14.862 ± 0.075	2.110 ± 0.088
2.5910180	4365.493 ± 0.016	1090.89	34.859 ± 1.782	12.651 ± 0.024	14.576 ± 0.132	1.925 ± 0.134
2.5919223	4366.592 ± 0.022	1091.16	20.116 ± 2.487	12.166 ± 0.060	14.043 ± 0.228	1.877 ± 0.236
2.5928106	4367.672 ± 0.001	1091.43	25.556 ± 0.143	13.857 ± 0.003	14.940 ± 0.449	1.083 ± 0.449
2.5948031	4370.094 ± 0.003	1092.04	21.960 ± 0.344	13.551 ± 0.010	15.500 ± 0.000	1.949 ± 0.000
2.5950332	4370.374 ± 0.057	1092.11	159.453 ± 3.664	13.938 ± 0.016	15.500 ± 0.000	1.562 ± 0.000
2.5960608	4371.623 ± 0.024	1092.42	65.898 ± 1.185	14.401 ± 0.018	14.300 ± 0.000	−0.101 ± 0.000
2.5965559	3497.783 ± 0.010	1092.57	30.470 ± 0.923	15.017 ± 0.090	14.839 ± 0.914	−0.178 ± 0.918
2.5976367	4373.539 ± 0.021	1092.90	11.406 ± 2.606	12.049 ± 0.130	14.500 ± 0.000	2.451 ± 0.000
2.5978971	4373.856 ± 0.000	1092.98	10.9	<11.101	14.600 ± 0.000	>3.499
2.5985947	4374.704 ± 0.004	1093.19	17.328 ± 0.271	13.397 ± 0.008	15.807 ± 1.362	2.410 ± 1.362
2.5990150	4375.215 ± 0.019	1093.32	20.035 ± 1.387	12.743 ± 0.036	14.674 ± 0.568	1.931 ± 0.569
2.5999146	4376.309 ± 0.000	1093.59	27.0	<11.139	14.616 ± 0.618	>3.477
2.6005642	4377.098 ± 0.010	1093.79	24.070 ± 1.101	12.655 ± 0.021	14.800 ± 0.000	2.145 ± 0.000
2.6013632	4378.069 ± 0.000	1094.03	27.0	<11.139	14.800 ± 0.000	>3.661
2.6022923	4379.199 ± 0.004	1094.31	40.807 ± 0.271	14.287 ± 0.003	15.200 ± 0.000	0.913 ± 0.000
2.6030738	4380.149 ± 0.005	1094.55	20.426 ± 0.504	13.488 ± 0.013	15.200 ± 0.000	1.712 ± 0.000
2.6038437	4381.085 ± 0.002	1094.78	29.332 ± 0.185	14.066 ± 0.003	15.202 ± 0.678	1.136 ± 0.678
2.6048479	4382.306 ± 0.002	1095.09	21.003 ± 0.227	13.306 ± 0.004	15.429 ± 0.864	2.123 ± 0.864
2.6062479	4384.008 ± 0.005	1095.51	20.812 ± 0.670	12.900 ± 0.019	14.283 ± 1.242	1.383 ± 1.242
2.6065371	4384.359 ± 0.033	1095.60	78.410 ± 3.488	13.064 ± 0.020	14.998 ± 0.215	1.934 ± 0.216
2.6073904	4385.396 ± 0.584	1095.86	27.0	<11.111	13.378 ± 0.785	>2.267
2.6085188	4386.768 ± 0.008	1096.20	39.137 ± 1.535	13.288 ± 0.018	15.161 ± 0.253	1.873 ± 0.254
2.6085415	4386.796 ± 0.010	1096.21	15.683 ± 1.777	12.577 ± 0.103	14.500 ± 0.000	1.923 ± 0.000
2.6097245	4388.234 ± 0.019	1096.57	48.209 ± 2.060	12.949 ± 0.018	15.019 ± 0.160	2.070 ± 0.161
2.6107447	4389.475 ± 0.248	1096.88	27.0	<11.087	13.627 ± 0.209	>2.540
2.6114328	4390.311 ± 0.083	1097.09	41.043 ± 4.445	12.960 ± 0.080	14.684 ± 0.188	1.724 ± 0.204
2.6118648	4390.836 ± 0.008	1097.22	21.865 ± 1.315	12.954 ± 0.074	12.724 ± 8.957	−0.230 ± 8.957
2.6132333	4392.500 ± 0.100	1097.64	27.0	<11.052	13.382 ± 0.116	>2.330
2.6148150	4394.422 ± 0.065	1098.12	52.647 ± 6.134	12.613 ± 0.054	14.724 ± 0.067	2.111 ± 0.086
2.6155276	4395.289 ± 0.039	1098.33	19.087 ± 3.160	12.511 ± 0.105	14.000 ± 0.000	1.489 ± 0.000
2.6159103	4395.754 ± 0.006	1098.45	16.711 ± 0.568	13.217 ± 0.019	16.202 ± 1.652	2.985 ± 1.652
2.6164465	4396.406 ± 0.003	1098.61	22.006 ± 0.298	13.394 ± 0.005	15.293 ± 4.594	1.899 ± 4.594
2.6172657	4397.402 ± 0.010	1098.86	26.854 ± 1.105	12.656 ± 0.017	14.464 ± 0.210	1.808 ± 0.211
2.6183748	4398.750 ± 0.022	1099.20	10.341 ± 2.919	11.776 ± 0.150	15.100 ± 0.000	3.324 ± 0.000
2.6188581	4399.338 ± 0.011	1099.34	32.376 ± 1.623	12.910 ± 0.018	16.762 ± 0.254	3.852 ± 0.255
2.6196856	4400.344 ± 0.004	1099.60	22.100 ± 0.462	13.030 ± 0.008	13.444 ± 1.602	0.414 ± 1.602
2.6203821	4401.190 ± 0.001	1099.81	19.712 ± 0.127	13.501 ± 0.002	15.531 ± 0.265	2.030 ± 0.265
2.6216619	4402.746 ± 0.012	1100.20	26.280 ± 1.244	12.526 ± 0.020	15.222 ± 0.150	2.696 ± 0.151
2.6225612	4403.840 ± 0.018	1100.47	23.016 ± 2.012	12.284 ± 0.033	14.076 ± 0.111	1.792 ± 0.116
2.6234348	4404.901 ± 0.076	1100.73	27.0	<12.125	13.922 ± 0.111	>1.797
2.6242597	4405.904 ± 0.019	1100.99	32.334 ± 1.911	12.629 ± 0.025	14.907 ± 0.119	2.278 ± 0.122
2.6265564	4408.696 ± 0.031	1101.68	29.738 ± 3.373	12.142 ± 0.050	14.509 ± 0.078	2.367 ± 0.093
2.6277764	4410.179 ± 0.003	1102.05	21.144 ± 0.346	12.927 ± 0.007	15.599 ± 0.191	2.672 ± 0.191
2.6287446	4411.356 ± 0.148	1102.35	27.0	<11.020	13.252 ± 0.144	>2.232
2.6296861	4412.501 ± 0.092	1102.63	27.0	<11.169	13.680 ± 0.098	>2.511
2.6304166	4413.389 ± 0.100	1102.86	27.0	<11.013	13.729 ± 0.098	>2.716
2.6313417	4414.514 ± 0.372	1103.14	27.0	<11.014	13.635 ± 0.530	>2.621
2.6315269	4414.739 ± 0.018	1103.19	14.097 ± 2.120	11.949 ± 0.062	13.177 ± 5.025	1.228 ± 5.025
2.6319439	4415.246 ± 0.120	1103.32	27.0	<11.278	13.629 ± 0.149	>2.351
2.6332018	4416.775 ± 0.216	1103.70	27.0	<11.021	13.420 ± 0.244	>2.399
2.6336806	4417.357 ± 0.029	1103.85	16.593 ± 3.337	11.984 ± 0.110	14.376 ± 0.384	2.392 ± 0.399
2.6346345	4418.516 ± 0.001	1104.14	30.598 ± 0.209	14.796 ± 0.010	14.963 ± 0.428	0.167 ± 0.428
2.6346512	4418.537 ± 0.067	1104.14	109.025 ± 11.161	13.039 ± 0.043	14.969 ± 0.078	1.930 ± 0.089
2.6375504	4422.061 ± 0.001	1105.02	25.925 ± 0.124	13.738 ± 0.002	14.965 ± 0.125	1.227 ± 0.125
2.6384692	4423.178 ± 0.011	1105.30	16.940 ± 1.285	12.338 ± 0.037	14.233 ± 0.126	1.895 ± 0.131
2.6392627	4424.143 ± 0.006	1105.54	26.762 ± 0.359	13.620 ± 0.006	15.128 ± 0.216	1.508 ± 0.216
2.6400616	4425.114 ± 0.029	1105.79	33.876 ± 4.959	12.653 ± 0.060	14.589 ± 0.136	1.936 ± 0.149

Table A.8: continued.

z	$\lambda_{\rm H\,I}$ (Å)	$\lambda_{\rm He\,II}$ (Å)	b (km/s)	$\log N_{\rm H\,I}$	$\log N_{\rm He\,II}$	$\log \eta$
2.6408179	4426.033 ± 0.035	1106.02	18.164 ± 4.371	12.467 ± 0.115	16.119 ± 1.526	3.652 ± 1.530
2.6413524	4426.683 ± 0.009	1106.18	19.932 ± 1.572	12.843 ± 0.033	13.989 ± 0.472	1.146 ± 0.473
2.6418223	4427.254 ± 0.046	1106.32	17.936 ± 4.437	12.128 ± 0.128	14.050 ± 0.871	1.922 ± 0.880
2.6419842	4427.451 ± 0.000	1106.37	27.0	<11.054	13.882 ± 0.408	>2.828
2.6425462	4428.134 ± 0.017	1106.54	30.398 ± 2.482	12.579 ± 0.036	14.529 ± 0.117	1.950 ± 0.122
2.6433675	4429.133 ± 0.030	1106.79	25.395 ± 3.345	12.219 ± 0.067	14.395 ± 0.099	2.176 ± 0.120
2.6444685	4430.472 ± 0.002	1107.12	28.787 ± 0.162	13.773 ± 0.003	15.317 ± 0.184	1.544 ± 0.184
2.6452637	4431.438 ± 0.009	1107.37	19.901 ± 0.974	12.611 ± 0.021	14.017 ± 0.448	1.406 ± 0.448
2.6457040	4431.973 ± 0.308	1107.50	27.0	<11.118	13.935 ± 0.202	>2.817
2.6460645	4432.412 ± 0.003	1107.61	19.350 ± 0.204	13.539 ± 0.005	13.940 ± 0.732	0.401 ± 0.732
2.6466806	4433.160 ± 0.002	1107.80	25.882 ± 0.181	13.861 ± 0.003	14.732 ± 0.174	0.871 ± 0.174
2.6489227	4435.886 ± 0.012	1108.48	89.256 ± 2.265	13.445 ± 0.010	15.606 ± 0.087	2.161 ± 0.088
2.6490242	4436.010 ± 0.002	1108.51	27.634 ± 0.268	13.604 ± 0.006	15.000 ± 0.000	1.396 ± 0.000
2.6508560	4438.236 ± 0.001	1109.06	21.416 ± 0.140	13.571 ± 0.003	14.614 ± 0.265	1.043 ± 0.265
2.6515074	4439.028 ± 0.164	1109.26	27.0	<11.094	13.900 ± 0.000	>2.806
2.6519043	4439.511 ± 0.069	1109.38	38.258 ± 3.297	13.245 ± 0.075	14.160 ± 0.358	0.915 ± 0.366
2.6524155	4440.132 ± 0.037	1109.54	30.063 ± 1.482	13.144 ± 0.093	14.577 ± 0.107	1.433 ± 0.142
2.6539502	4441.998 ± 0.000	1110.01	27.0	<11.027	13.891 ± 0.113	>2.864
2.6548357	4443.075 ± 0.020	1110.27	31.832 ± 2.158	12.411 ± 0.027	14.479 ± 0.082	2.068 ± 0.086
2.6561723	4444.699 ± 0.120	1110.68	27.0	<11.005	13.489 ± 0.116	>2.484
2.6566367	4445.264 ± 0.053	1110.82	14.884 ± 5.529	11.474 ± 0.133	13.674 ± 0.281	2.200 ± 0.311
2.6572356	4445.992 ± 0.156	1111.00	27.0	<10.998	13.336 ± 0.133	>2.338
2.6580215	4446.947 ± 0.045	1111.24	25.172 ± 3.654	12.127 ± 0.082	14.533 ± 0.123	2.406 ± 0.148
2.6587553	4447.839 ± 0.081	1111.46	38.074 ± 7.222	12.182 ± 0.080	14.410 ± 0.084	2.228 ± 0.116
2.6604545	4449.905 ± 0.080	1111.98	27.0	<10.974	13.554 ± 0.093	>2.580
2.6615427	4451.228 ± 0.002	1112.31	19.704 ± 0.201	13.126 ± 0.004	15.557 ± 0.280	2.431 ± 0.280
2.6622431	4452.080 ± 0.020	1112.52	20.415 ± 2.150	12.070 ± 0.038	14.019 ± 0.127	1.949 ± 0.133
2.6640956	4454.332 ± 0.084	1113.09	27.0	<10.952	13.850 ± 0.119	>2.898
2.6649318	4455.348 ± 0.004	1113.34	34.266 ± 0.461	13.075 ± 0.005	14.916 ± 0.121	1.841 ± 0.121
2.6666505	4457.438 ± 0.036	1113.86	39.597 ± 2.047	12.962 ± 0.037	15.432 ± 0.151	2.470 ± 0.155
2.6674607	4458.422 ± 0.007	1114.11	20.997 ± 1.881	12.809 ± 0.121	13.477 ± 3.219	0.668 ± 3.221
2.6678448	4458.889 ± 0.055	1114.23	47.249 ± 3.512	13.380 ± 0.049	14.852 ± 0.119	1.472 ± 0.129
2.6688948	4460.166 ± 0.019	1114.55	26.767 ± 2.222	12.636 ± 0.047	14.544 ± 0.168	1.908 ± 0.174
2.6695750	4460.993 ± 0.005	1114.75	28.974 ± 0.505	13.259 ± 0.008	14.910 ± 0.208	1.651 ± 0.208
2.6705847	4462.220 ± 0.006	1115.06	32.383 ± 0.715	12.894 ± 0.010	14.807 ± 0.102	1.913 ± 0.102
2.6721821	4464.162 ± 0.011	1115.54	23.188 ± 1.192	12.363 ± 0.023	14.436 ± 0.094	2.073 ± 0.097
2.6738172	4466.150 ± 0.029	1116.04	63.494 ± 3.729	12.593 ± 0.034	14.794 ± 0.051	2.201 ± 0.061
2.6751845	4467.812 ± 0.048	1116.46	16.586 ± 4.852	11.617 ± 0.132	13.708 ± 0.205	2.091 ± 0.244
2.6758981	4468.679 ± 0.015	1116.67	32.811 ± 2.232	12.586 ± 0.026	14.577 ± 0.085	1.991 ± 0.089
2.6766541	4469.598 ± 0.018	1116.90	20.674 ± 1.961	12.239 ± 0.044	14.352 ± 0.130	2.113 ± 0.137
2.6776977	4470.867 ± 0.014	1117.22	23.534 ± 1.921	12.486 ± 0.067	15.064 ± 0.775	2.578 ± 0.778
2.6779647	4471.192 ± 0.031	1117.30	57.128 ± 1.960	12.978 ± 0.028	15.057 ± 0.098	2.079 ± 0.102
2.6795719	4473.146 ± 0.006	1117.79	26.293 ± 0.636	12.830 ± 0.011	14.746 ± 0.132	1.916 ± 0.132
2.6803217	4474.057 ± 0.025	1118.02	21.935 ± 2.725	12.155 ± 0.059	14.520 ± 0.158	2.365 ± 0.169
2.6811860	4475.108 ± 0.002	1118.28	23.133 ± 0.379	13.718 ± 0.021	15.593 ± 0.633	1.875 ± 0.633
2.6817536	4475.798 ± 0.145	1118.45	46.135 ± 19.933	12.866 ± 0.208	14.697 ± 0.166	1.831 ± 0.266
2.6828461	4477.126 ± 0.002	1118.78	29.842 ± 0.310	14.590 ± 0.008	15.571 ± 0.235	0.981 ± 0.235
2.6840224	4478.556 ± 0.068	1119.14	26.697 ± 4.385	12.701 ± 0.109	14.559 ± 0.105	1.858 ± 0.151
2.6849439	4479.676 ± 0.109	1119.42	40.988 ± 12.134	11.985 ± 0.149	14.398 ± 0.073	2.413 ± 0.166
2.6873872	4482.646 ± 0.601	1120.16	46.990 ± 30.282	12.741 ± 0.536	17.064 ± 0.176	4.323 ± 0.564
2.6877871	4483.132 ± 0.006	1120.28	25.599 ± 2.425	13.210 ± 0.158	15.000 ± 0.000	1.790 ± 0.000
2.6885333	4484.040 ± 0.003	1120.51	19.342 ± 0.205	13.494 ± 0.008	15.503 ± 1.075	2.009 ± 1.075
2.6891139	4484.745 ± 0.018	1120.69	10.066 ± 2.151	11.731 ± 0.068	13.977 ± 0.595	2.246 ± 0.599
2.6895330	4485.255 ± 0.020	1120.81	14.448 ± 2.345	11.876 ± 0.057	15.317 ± 0.294	3.441 ± 0.299
2.6906180	4486.574 ± 0.011	1121.14	22.759 ± 1.207	12.392 ± 0.022	15.640 ± 0.183	3.248 ± 0.184
2.6936157	4490.218 ± 0.005	1122.05	30.915 ± 0.539	12.928 ± 0.008	18.369 ± 0.255	5.441 ± 0.255
2.6947005	4491.537 ± 0.003	1122.38	20.928 ± 0.319	12.901 ± 0.006	15.206 ± 0.357	2.305 ± 0.357
2.6956062	4492.638 ± 0.040	1122.66	18.795 ± 2.729	12.147 ± 0.112	14.585 ± 2.516	2.438 ± 2.518
2.6960900	4493.226 ± 0.037	1122.81	27.758 ± 2.800	12.531 ± 0.049	15.684 ± 9.621	3.153 ± 9.621
2.6970561	4494.401 ± 0.007	1123.10	22.797 ± 0.786	12.575 ± 0.014	15.604 ± 0.241	3.029 ± 0.241
2.6985049	4496.162 ± 0.014	1123.54	33.697 ± 1.557	12.515 ± 0.022	14.923 ± 0.093	2.408 ± 0.096
2.7001982	4498.220 ± 0.010	1124.05	29.936 ± 1.186	12.545 ± 0.018	15.656 ± 0.150	3.111 ± 0.151
2.7017324	4500.085 ± 0.001	1124.52	21.861 ± 0.074	13.866 ± 0.002	16.403 ± 0.344	2.537 ± 0.344
2.7027645	4501.340 ± 0.011	1124.83	26.469 ± 2.536	12.963 ± 0.179	14.089 ± 0.676	1.126 ± 0.699
2.7030649	4501.705 ± 0.282	1124.93	40.078 ± 7.859	12.707 ± 0.331	14.937 ± 0.119	2.230 ± 0.352
2.7044892	4503.437 ± 0.069	1125.36	31.868 ± 5.853	12.168 ± 0.083	14.513 ± 0.091	2.345 ± 0.123
2.7051132	4504.195 ± 0.018	1125.55	23.667 ± 1.302	12.523 ± 0.035	14.339 ± 0.141	1.816 ± 0.145
2.7057338	4504.950 ± 0.320	1125.74	27.0	<10.882	13.139 ± 0.202	>2.257
2.7065890	4505.990 ± 0.006	1126.00	16.637 ± 0.405	12.915 ± 0.013	16.511 ± 0.272	3.596 ± 0.272

Table A.8: continued.

z	$\lambda_{\mathrm{H\,I}}$ (Å)	$\lambda_{\mathrm{He\,II}}$ (Å)	b (km/s)	$\log N_{\mathrm{H\,I}}$	$\log N_{\mathrm{He\,II}}$	$\log \eta$
2.7075143	4507.114 ± 0.006	1126.28	19.500 ± 0.385	13.101 ± 0.011	14.828 ± 0.236	1.727 ± 0.236
2.7086225	4508.461 ± 0.004	1126.61	13.429 ± 0.446	12.522 ± 0.015	18.109 ± 0.756	5.587 ± 0.756
2.7097778	4509.866 ± 0.006	1126.96	75.110 ± 0.511	13.753 ± 0.003	15.547 ± 1.029	1.794 ± 1.029
2.7101498	4510.318 ± 0.001	1127.08	23.701 ± 0.102	13.896 ± 0.002	19.289 ± 2.777	5.393 ± 2.777
2.7115445	4512.014 ± 0.010	1127.50	11.613 ± 1.118	11.915 ± 0.034	13.849 ± 0.596	1.934 ± 0.597
2.7124672	4513.135 ± 0.002	1127.78	33.281 ± 0.237	13.385 ± 0.003	15.379 ± 0.236	1.994 ± 0.236
2.7133272	4514.181 ± 0.002	1128.04	25.811 ± 0.222	13.231 ± 0.004	14.815 ± 0.254	1.584 ± 0.254
2.7141280	4515.154 ± 0.128	1128.29	27.0	<10.838	13.728 ± 0.110	>2.890
2.7149665	4516.174 ± 0.007	1128.54	28.999 ± 0.893	12.597 ± 0.016	14.842 ± 0.120	2.245 ± 0.121
2.7164247	4517.946 ± 0.016	1128.98	37.231 ± 1.698	12.627 ± 0.022	15.223 ± 0.139	2.596 ± 0.141
2.7173650	4519.089 ± 0.012	1129.27	31.344 ± 1.200	13.002 ± 0.045	15.015 ± 0.428	2.013 ± 0.430
2.7181640	4520.061 ± 0.102	1129.51	53.687 ± 18.828	12.597 ± 0.169	14.576 ± 0.114	1.979 ± 0.204
2.7196455	4521.862 ± 0.231	1129.96	51.337 ± 20.934	12.718 ± 0.238	15.182 ± 0.160	2.464 ± 0.287
2.7202063	4522.544 ± 0.261	1130.13	24.519 ± 14.064	12.530 ± 0.705	13.600 ± 0.000	1.070 ± 0.000
2.7206967	4523.140 ± 1.396	1130.28	23.829 ± 55.512	12.788 ± 3.710	14.296 ± 1.736	1.508 ± 4.096
2.7210307	4523.546 ± 0.843	1130.38	23.297 ± 93.742	12.769 ± 5.135	15.009 ± 3.914	2.240 ± 6.457
2.7213542	4523.939 ± 0.284	1130.48	21.706 ± 5.646	12.987 ± 0.964	15.970 ± 0.530	2.983 ± 1.100
2.7223134	4525.105 ± 0.001	1130.77	28.565 ± 0.173	13.430 ± 0.003	14.507 ± 0.143	1.077 ± 0.143
2.7240102	4527.168 ± 0.074	1131.29	101.068 ± 6.453	12.923 ± 0.034	15.041 ± 0.065	2.118 ± 0.073
2.7245131	4527.779 ± 0.001	1131.44	24.079 ± 0.117	13.602 ± 0.003	14.543 ± 0.457	0.941 ± 0.457
2.7259982	4529.585 ± 0.023	1131.89	44.995 ± 3.154	12.707 ± 0.042	14.667 ± 0.087	1.960 ± 0.097
2.7269640	4530.759 ± 0.039	1132.19	27.166 ± 4.852	12.188 ± 0.101	14.198 ± 0.141	2.010 ± 0.173
2.7275660	4531.490 ± 0.034	1132.37	22.644 ± 3.126	12.174 ± 0.097	14.298 ± 0.155	2.124 ± 0.183
2.7284658	4532.584 ± 0.193	1132.64	125.020 ± 19.486	12.756 ± 0.073	14.495 ± 0.123	1.739 ± 0.143
2.7286713	4532.834 ± 0.240	1132.70	27.0	<10.849	13.131 ± 0.367	>2.282
2.7304845	4535.039 ± 0.015	1133.25	22.386 ± 1.788	12.135 ± 0.042	14.520 ± 0.115	2.385 ± 0.122
2.7316210	4536.420 ± 0.001	1133.60	34.025 ± 0.151	13.505 ± 0.002	15.043 ± 0.108	1.538 ± 0.108
2.7327309	4537.769 ± 0.001	1133.94	26.033 ± 0.098	13.582 ± 0.001	13.477 ± 0.365	−0.105 ± 0.365
2.7374113	4543.459 ± 0.112	1135.36	27.0	<10.910	13.383 ± 0.116	>2.473
2.7386026	4544.907 ± 0.002	1135.72	24.088 ± 0.244	13.058 ± 0.004	15.469 ± 0.195	2.411 ± 0.195
2.7398136	4546.379 ± 0.039	1136.09	36.963 ± 3.943	12.087 ± 0.045	14.578 ± 0.071	2.491 ± 0.084
2.7419567	4548.985 ± 0.177	1136.74	70.662 ± 17.116	12.046 ± 0.109	14.605 ± 0.057	2.559 ± 0.123
2.7437835	4551.206 ± 0.058	1137.29	26.610 ± 2.361	12.888 ± 0.128	15.779 ± 0.779	2.891 ± 0.789
2.7442510	4551.774 ± 0.011	1137.44	30.508 ± 0.491	13.808 ± 0.015	15.228 ± 4.044	1.420 ± 4.044
2.7445121	4552.091 ± 0.076	1137.52	90.713 ± 4.090	13.007 ± 0.034	15.166 ± 0.113	2.159 ± 0.118

A.5. Observed Lyα lines towards HE 2347-4342

Table A.9: Parameters of the observed Lyα forest towards HE 2347-4342. Errors of parameters that have been fixed during the fitting procedure are set to 0.000.

z	$\lambda_{\mathrm{H\,I}}$ (Å)	$\lambda_{\mathrm{He\,II}}$ (Å)	b (km/s)	$\log N_{\mathrm{H\,I}}$	$\log N_{\mathrm{He\,II}}$	$\log \eta$
2.2967753	4007.791 ± 0.005	1001.50	10.230 ± 0.716	12.439 ± 0.029	12.475 ± 7.853	0.036 ± 7.853
2.2972372	4008.353 ± 0.051	1001.64	79.782 ± 4.497	13.255 ± 0.026	14.478 ± 0.182	1.223 ± 0.184
2.2984388	4009.813 ± 0.052	1002.01	36.888 ± 21.185	12.864 ± 0.754	14.248 ± 0.204	1.384 ± 0.781
2.2999673	4011.672 ± 0.002	1002.47	20.969 ± 0.279	13.486 ± 0.009	13.922 ± 0.290	0.436 ± 0.290
2.3004909	4012.308 ± 0.039	1002.63	63.753 ± 3.201	13.142 ± 0.032	13.142 ± 0.000	0.000 ± 0.000
2.3018131	4013.916 ± 0.084	1003.03	27.0	<11.410	15.653 ± 0.382	>4.243
2.3042543	4016.883 ± 0.076	1003.77	27.0	<11.554	18.118 ± 0.554	>6.564
2.3059537	4018.949 ± 0.112	1004.29	27.0	<11.231	14.645 ± 0.244	>3.414
2.3065219	4019.640 ± 0.006	1004.46	23.417 ± 1.270	12.809 ± 0.038	13.967 ± 0.297	1.158 ± 0.299
2.3085642	4022.122 ± 0.009	1005.08	87.051 ± 1.216	14.026 ± 0.006	13.152 ± 1.668	−0.874 ± 1.668
2.3101330	4024.030 ± 0.004	1005.56	19.558 ± 0.301	14.142 ± 0.010	13.500 ± 0.000	−0.642 ± 0.000
2.3107216	4024.745 ± 0.080	1005.74	27.0	<11.496	15.079 ± 0.286	>3.583
2.3125725	4026.995 ± 0.144	1006.30	27.0	<12.714	14.281 ± 0.217	>1.567
2.3135438	4028.176 ± 0.012	1006.60	45.801 ± 4.658	15.666 ± 0.190	13.827 ± 0.379	−1.839 ± 0.424
2.3146448	4029.515 ± 0.062	1006.93	33.510 ± 1.990	13.829 ± 0.107	11.700 ± 0.000	−2.129 ± 0.000
2.3157673	4030.879 ± 0.036	1007.27	23.442 ± 3.964	12.283 ± 0.069	13.283 ± 0.000	1.000 ± 0.000
2.3162963	4031.522 ± 0.009	1007.43	21.819 ± 0.881	12.872 ± 0.018	14.813 ± 0.357	1.941 ± 0.357
2.3177655	4033.308 ± 0.038	1007.88	20.423 ± 3.674	12.200 ± 0.088	14.028 ± 0.269	1.828 ± 0.283
2.3183105	4033.971 ± 0.014	1008.04	26.571 ± 1.782	12.792 ± 0.025	14.075 ± 0.257	1.283 ± 0.258
2.3189695	4034.772 ± 0.021	1008.24	16.783 ± 2.452	12.122 ± 0.057	13.705 ± 0.405	1.583 ± 0.409
2.3197193	4035.683 ± 0.004	1008.47	27.710 ± 0.430	13.223 ± 0.006	14.430 ± 0.219	1.207 ± 0.219
2.3204603	4036.584 ± 0.002	1008.70	10.429 ± 0.220	13.231 ± 0.011	13.837 ± 0.373	0.606 ± 0.373
2.3236010	4040.402 ± 0.026	1009.65	23.706 ± 3.107	12.174 ± 0.057	13.506 ± 0.591	1.332 ± 0.594
2.3246295	4041.653 ± 0.032	1009.96	34.677 ± 2.817	12.752 ± 0.041	14.588 ± 0.207	1.836 ± 0.211
2.3251996	4042.346 ± 0.007	1010.14	19.520 ± 0.756	12.962 ± 0.021	13.864 ± 0.400	0.902 ± 0.401

Table A.9: continued.

z	$\lambda_{\rm H\,I}$ (Å)	$\lambda_{\rm He\,II}$ (Å)	b (km/s)	$\log N_{\rm H\,I}$	$\log N_{\rm He\,II}$	$\log \eta$
2.3262117	4043.576 ± 0.104	1010.44	27.0	<11.693	14.689 ± 0.264	>2.996
2.3268299	4044.328 ± 0.016	1010.63	76.477 ± 1.653	13.646 ± 0.011	13.542 ± 1.012	−0.104 ± 1.012
2.3283012	4046.116 ± 0.145	1011.08	24.121 ± 10.528	12.382 ± 0.263	14.102 ± 0.230	1.720 ± 0.349
2.3296773	4047.789 ± 0.116	1011.50	27.0	<11.740	14.485 ± 0.216	>2.745
2.3318107	4050.383 ± 0.011	1012.15	53.673 ± 0.380	15.223 ± 0.015	17.526 ± 0.298	2.303 ± 0.298
2.3340347	4053.086 ± 0.049	1012.82	18.425 ± 5.055	12.049 ± 0.119	14.284 ± 0.306	2.235 ± 0.328
2.3345015	4053.654 ± 0.264	1012.96	16.734 ± 10.059	12.526 ± 1.115	14.399 ± 2.069	1.873 ± 2.350
2.3347163	4053.915 ± 0.025	1013.03	18.329 ± 0.836	13.697 ± 0.075	15.582 ± 0.655	1.885 ± 0.659
2.3361516	4055.660 ± 0.035	1013.46	15.584 ± 3.234	12.090 ± 0.093	10.322 ± 681.6	−1.768 ± 681.6
2.3365307	4056.121 ± 0.014	1013.58	17.548 ± 1.338	12.568 ± 0.032	14.339 ± 0.251	1.771 ± 0.253
2.3372846	4057.037 ± 0.005	1013.81	14.365 ± 0.584	12.582 ± 0.014	14.309 ± 0.271	1.727 ± 0.271
2.3391678	4059.326 ± 0.071	1014.38	22.768 ± 6.717	12.108 ± 0.189	14.062 ± 0.244	1.954 ± 0.309
2.3397965	4060.091 ± 0.004	1014.57	36.467 ± 0.472	13.768 ± 0.005	14.337 ± 0.248	0.569 ± 0.248
2.3406682	4061.151 ± 0.053	1014.84	24.276 ± 5.678	12.005 ± 0.099	16.432 ± 1.255	4.427 ± 1.259
2.3414280	4062.074 ± 0.320	1015.07	27.0	<11.230	14.153 ± 0.482	>2.923
2.3432598	4064.301 ± 0.029	1015.62	49.893 ± 3.458	12.757 ± 0.029	14.519 ± 0.147	1.762 ± 0.150
2.3440886	4065.308 ± 0.005	1015.88	17.941 ± 0.491	13.782 ± 0.048	14.991 ± 1.271	1.209 ± 1.272
2.3443513	4065.628 ± 0.351	1015.95	27.636 ± 18.006	12.706 ± 0.614	15.052 ± 0.655	2.346 ± 0.898
2.3451602	4066.611 ± 0.127	1016.20	41.557 ± 11.964	12.309 ± 0.133	14.413 ± 0.204	2.104 ± 0.244
2.3463538	4068.062 ± 0.006	1016.56	25.279 ± 0.781	12.960 ± 0.012	16.846 ± 0.725	3.886 ± 0.725
2.3475647	4069.534 ± 0.008	1016.93	29.119 ± 0.384	15.959 ± 0.045	14.259 ± 0.191	−1.700 ± 0.196
2.3482533	4070.371 ± 0.118	1017.14	26.273 ± 4.426	13.571 ± 0.219	14.716 ± 0.252	1.145 ± 0.334
2.3489029	4071.161 ± 0.039	1017.34	13.370 ± 3.934	11.872 ± 0.139	13.979 ± 0.287	2.107 ± 0.319
2.3500476	4072.553 ± 0.028	1017.68	44.662 ± 2.547	12.764 ± 0.033	14.251 ± 0.338	1.487 ± 0.340
2.3503253	4072.890 ± 0.232	1017.77	27.0	<11.238	14.424 ± 0.431	>3.186
2.3513138	4074.092 ± 0.172	1018.07	73.528 ± 18.862	12.339 ± 0.118	14.676 ± 0.108	2.337 ± 0.160
2.3537621	4077.068 ± 0.032	1018.81	30.504 ± 3.763	12.241 ± 0.054	14.291 ± 0.141	2.050 ± 0.151
2.3549972	4078.570 ± 0.095	1019.19	37.687 ± 11.729	12.033 ± 0.121	14.320 ± 0.143	2.287 ± 0.187
2.3558171	4079.567 ± 0.024	1019.44	21.606 ± 2.701	12.290 ± 0.051	14.142 ± 0.198	1.852 ± 0.204
2.3570890	4081.113 ± 0.092	1019.82	53.842 ± 8.969	12.645 ± 0.074	14.732 ± 0.176	2.087 ± 0.191
2.3576536	4081.799 ± 0.003	1019.99	16.679 ± 0.415	13.127 ± 0.017	17.004 ± 1.803	3.877 ± 1.803
2.3584926	4082.819 ± 0.018	1020.25	33.919 ± 1.950	12.679 ± 0.025	14.405 ± 0.163	1.726 ± 0.165
2.3595538	4084.109 ± 0.010	1020.57	20.659 ± 1.251	12.781 ± 0.051	14.709 ± 0.385	1.928 ± 0.388
2.3605044	4085.265 ± 0.659	1020.86	54.193 ± 28.902	13.176 ± 0.577	14.942 ± 0.360	1.766 ± 0.680
2.3607559	4085.570 ± 0.008	1020.94	20.915 ± 1.184	13.682 ± 0.108	15.582 ± 0.000	1.900 ± 0.000
2.3609247	4085.776 ± 0.137	1020.99	32.227 ± 7.454	13.438 ± 0.379	15.438 ± 0.000	2.000 ± 0.000
2.3620079	4087.092 ± 0.046	1021.32	41.167 ± 4.991	12.939 ± 0.062	16.000 ± 0.000	3.061 ± 0.000
2.3630168	4088.319 ± 0.027	1021.62	36.056 ± 2.913	12.667 ± 0.036	14.798 ± 0.223	2.131 ± 0.226
2.3639956	4089.509 ± 0.050	1021.92	22.279 ± 5.722	11.990 ± 0.105	14.330 ± 0.223	2.340 ± 0.246
2.3646207	4090.269 ± 0.051	1022.11	26.531 ± 6.394	12.085 ± 0.090	13.338 ± 0.785	1.253 ± 0.790
2.3654537	4091.281 ± 0.002	1022.36	22.169 ± 0.260	13.706 ± 0.012	16.531 ± 0.673	2.825 ± 0.673
2.3660443	4091.999 ± 0.109	1022.54	47.010 ± 8.032	12.982 ± 0.050	14.771 ± 0.175	1.789 ± 0.182
2.3673623	4093.602 ± 0.080	1022.95	27.0	<11.208	14.596 ± 0.169	>3.388
2.3682356	4094.663 ± 0.027	1023.21	21.849 ± 3.121	12.086 ± 0.059	13.985 ± 0.199	1.899 ± 0.208
2.3690517	4095.656 ± 0.030	1023.46	23.513 ± 3.417	12.099 ± 0.059	14.783 ± 0.248	2.684 ± 0.255
2.3698559	4096.633 ± 0.048	1023.70	22.807 ± 5.870	11.917 ± 0.097	13.943 ± 0.243	2.026 ± 0.262
2.3705225	4097.443 ± 0.003	1023.91	22.110 ± 0.304	13.236 ± 0.005	15.171 ± 0.474	1.935 ± 0.474
2.3713014	4098.390 ± 0.002	1024.14	23.834 ± 0.244	13.329 ± 0.004	15.118 ± 0.315	1.789 ± 0.315
2.3731115	4100.591 ± 0.160	1024.69	22.951 ± 15.075	11.790 ± 0.405	13.539 ± 0.360	1.749 ± 0.542
2.3738699	4101.513 ± 0.006	1024.92	24.100 ± 1.305	13.283 ± 0.069	13.857 ± 0.415	0.574 ± 0.421
2.3741453	4101.847 ± 0.301	1025.01	47.989 ± 11.176	12.729 ± 0.290	14.237 ± 0.200	1.508 ± 0.352
2.3790903	4107.859 ± 0.109	1026.51	86.429 ± 16.103	12.489 ± 0.070	14.900 ± 0.077	2.411 ± 0.104
2.3812706	4110.510 ± 0.118	1027.17	64.388 ± 13.273	12.159 ± 0.091	13.601 ± 0.434	1.442 ± 0.443
2.3830225	4112.639 ± 0.031	1027.70	14.960 ± 3.520	11.744 ± 0.086	13.900 ± 0.292	2.156 ± 0.304
2.3834307	4113.136 ± 0.164	1027.83	27.0	<11.219	14.101 ± 0.194	>2.882
2.3856280	4115.807 ± 0.116	1028.49	17.120 ± 6.145	12.192 ± 0.364	15.527 ± 0.525	3.335 ± 0.639
2.3860035	4116.263 ± 0.010	1028.61	21.606 ± 2.292	13.265 ± 0.049	15.497 ± 3.508	2.232 ± 3.508
2.3864305	4116.782 ± 0.136	1028.74	17.576 ± 11.779	12.009 ± 0.436	14.101 ± 1.047	2.092 ± 1.134
2.3869324	4117.392 ± 0.038	1028.89	17.681 ± 5.994	12.044 ± 0.121	14.201 ± 0.216	2.157 ± 0.248
2.3886299	4119.456 ± 0.009	1029.41	27.227 ± 0.903	13.100 ± 0.014	14.001 ± 0.276	0.901 ± 0.276
2.3891983	4120.147 ± 0.027	1029.58	21.783 ± 3.934	12.451 ± 0.086	15.402 ± 0.571	2.951 ± 0.577
2.3898215	4120.905 ± 0.016	1029.77	25.992 ± 1.396	13.294 ± 0.039	14.000 ± 0.336	0.706 ± 0.338
2.3903153	4121.505 ± 0.126	1029.92	29.910 ± 7.870	12.571 ± 0.189	14.300 ± 0.161	1.729 ± 0.248
2.3912573	4122.650 ± 0.100	1030.20	23.398 ± 3.340	13.076 ± 0.268	14.001 ± 0.211	0.925 ± 0.341
2.3915405	4122.994 ± 0.248	1030.29	23.798 ± 7.662	12.707 ± 0.626	13.601 ± 0.470	0.894 ± 0.783
2.3934970	4125.373 ± 0.034	1030.88	47.603 ± 4.189	12.477 ± 0.041	14.200 ± 0.132	1.723 ± 0.138
2.3954725	4127.774 ± 0.010	1031.48	33.473 ± 1.084	13.056 ± 0.013	14.800 ± 0.157	1.744 ± 0.158
2.3960915	4128.527 ± 0.042	1031.67	15.767 ± 3.583	12.434 ± 0.113	14.000 ± 0.251	1.566 ± 0.275
2.3967943	4129.381 ± 0.013	1031.89	24.920 ± 0.871	13.501 ± 0.022	13.500 ± 0.405	−0.001 ± 0.406

Table A.9: continued.

z	$\lambda_{\mathrm{H\,I}}$ (Å)	$\lambda_{\mathrm{He\,II}}$ (Å)	b (km/s)	$\log N_{\mathrm{H\,I}}$	$\log N_{\mathrm{He\,II}}$	$\log \eta$
2.3971181	4129.775 ± 0.023	1031.98	16.186 ± 1.695	12.669 ± 0.130	13.299 ± 0.617	0.630 ± 0.631
2.3978417	4130.655 ± 0.005	1032.20	31.172 ± 0.542	13.522 ± 0.007	14.100 ± 0.163	0.578 ± 0.163
2.3984711	4131.420 ± 0.011	1032.40	23.302 ± 1.608	12.910 ± 0.034	13.994 ± 0.327	1.084 ± 0.329
2.3990097	4132.074 ± 0.009	1032.56	22.374 ± 0.762	12.979 ± 0.016	15.293 ± 0.833	2.314 ± 0.833
2.3999977	4133.276 ± 0.014	1032.86	31.106 ± 1.582	12.615 ± 0.020	15.602 ± 0.290	2.987 ± 0.291
2.4008906	4134.361 ± 0.022	1033.13	23.319 ± 2.475	12.217 ± 0.042	13.502 ± 0.427	1.285 ± 0.429
2.4023623	4136.150 ± 0.018	1033.58	30.840 ± 1.965	12.483 ± 0.026	14.300 ± 0.123	1.817 ± 0.126
2.4040225	4138.168 ± 0.032	1034.08	12.537 ± 3.665	11.681 ± 0.100	16.404 ± 0.538	4.723 ± 0.547
2.4052093	4139.611 ± 0.056	1034.44	27.0	<11.245	14.700 ± 0.147	>3.455
2.4062636	4140.893 ± 0.054	1034.76	17.991 ± 6.037	11.697 ± 0.130	15.099 ± 0.303	3.402 ± 0.330
2.4071782	4142.004 ± 0.072	1035.04	27.0	<11.257	14.400 ± 0.117	>3.143
2.4080064	4143.012 ± 0.070	1035.29	13.973 ± 7.941	11.390 ± 0.200	13.800 ± 0.219	2.410 ± 0.297
2.4090226	4144.247 ± 0.029	1035.60	27.941 ± 3.149	12.190 ± 0.045	15.502 ± 0.215	3.312 ± 0.220
2.4101193	4145.580 ± 0.042	1035.93	21.370 ± 4.532	11.860 ± 0.081	14.400 ± 0.148	2.540 ± 0.169
2.4115682	4147.341 ± 0.164	1036.37	18.075 ± 9.293	12.325 ± 0.406	15.023 ± 1.492	2.698 ± 1.546
2.4117439	4147.555 ± 0.079	1036.43	51.261 ± 7.713	12.439 ± 0.091	14.900 ± 0.131	2.461 ± 0.160
2.4117687	4147.585 ± 0.045	1036.44	11.270 ± 4.083	12.165 ± 0.527	14.663 ± 12.94	2.498 ± 12.95
2.4144297	4150.820 ± 0.120	1037.24	27.0	<11.292	14.200 ± 0.169	>2.908
2.4153669	4151.959 ± 0.037	1037.53	51.997 ± 4.336	12.705 ± 0.033	14.701 ± 0.106	1.996 ± 0.111
2.4162688	4153.056 ± 0.079	1037.80	23.071 ± 8.969	11.813 ± 0.182	13.901 ± 0.225	2.088 ± 0.289
2.4170921	4154.057 ± 0.055	1038.05	28.517 ± 6.935	12.023 ± 0.090	14.500 ± 0.146	2.477 ± 0.172
2.4178362	4154.961 ± 0.054	1038.28	18.815 ± 5.986	11.760 ± 0.124	14.800 ± 0.236	3.040 ± 0.267
2.4202600	4157.908 ± 0.091	1039.01	77.283 ± 12.200	12.463 ± 0.076	14.100 ± 0.142	1.637 ± 0.161
2.4214921	4159.406 ± 0.071	1039.39	20.623 ± 2.379	13.174 ± 0.190	14.797 ± 0.436	1.623 ± 0.476
2.4217429	4159.710 ± 0.040	1039.46	19.617 ± 1.261	13.340 ± 0.129	15.806 ± 0.926	2.466 ± 0.935
2.4224763	4160.602 ± 0.004	1039.69	20.159 ± 0.442	12.934 ± 0.009	14.400 ± 0.185	1.466 ± 0.185
2.4234045	4161.730 ± 0.020	1039.97	17.066 ± 2.308	12.057 ± 0.057	13.601 ± 0.261	1.544 ± 0.267
2.4244618	4163.016 ± 0.017	1040.29	34.474 ± 2.094	12.652 ± 0.027	14.600 ± 0.117	1.948 ± 0.120
2.4250531	4163.735 ± 0.039	1040.47	10.871 ± 4.508	11.805 ± 0.161	15.605 ± 0.925	3.800 ± 0.939
2.4258814	4164.742 ± 0.013	1040.72	40.409 ± 1.818	12.891 ± 0.019	14.400 ± 0.085	1.509 ± 0.087
2.4280422	4167.368 ± 0.670	1041.38	61.412 ± 39.947	12.574 ± 0.459	13.901 ± 0.317	1.327 ± 0.558
2.4281611	4167.513 ± 0.024	1041.41	13.017 ± 3.199	12.087 ± 0.230	14.200 ± 0.310	2.113 ± 0.386
2.4285376	4167.971 ± 0.017	1041.53	18.059 ± 4.479	12.419 ± 0.311	13.600 ± 0.348	1.181 ± 0.467
2.4292414	4168.826 ± 0.069	1041.74	31.228 ± 7.677	12.598 ± 0.171	14.300 ± 0.118	1.702 ± 0.208
2.4299259	4169.658 ± 0.025	1041.95	11.248 ± 3.317	11.829 ± 0.140	13.098 ± 0.696	1.269 ± 0.710
2.4305444	4170.410 ± 0.274	1042.14	25.593 ± 17.452	12.343 ± 0.522	13.602 ± 0.377	1.259 ± 0.644
2.4310079	4170.974 ± 0.022	1042.28	20.021 ± 1.445	13.281 ± 0.054	14.301 ± 0.284	1.020 ± 0.289
2.4320462	4172.236 ± 0.292	1042.59	97.880 ± 43.725	13.164 ± 0.215	14.900 ± 0.084	1.736 ± 0.231
2.4336700	4174.210 ± 0.033	1043.09	29.582 ± 1.762	13.950 ± 0.068	14.401 ± 0.154	0.451 ± 0.168
2.4345226	4175.246 ± 0.078	1043.35	28.214 ± 7.733	13.099 ± 0.307	13.501 ± 0.547	0.402 ± 0.627
2.4352100	4176.082 ± 0.840	1043.56	111.883 ±150.758	13.281 ± 0.645	14.301 ± 0.207	1.020 ± 0.677
2.4359317	4176.959 ± 0.100	1043.78	27.0	<11.260	14.300 ± 0.170	>3.040
2.4373219	4178.650 ± 7.204	1044.20	71.188 ±301.395	13.116 ± 5.395	14.600 ± 0.090	1.484 ± 5.396
2.4382770	4179.811 ± 0.049	1044.49	34.903 ± 4.218	14.624 ± 0.355	13.203 ± 1.649	−1.421 ± 1.687
2.4387662	4180.405 ± 0.112	1044.64	27.0	<11.755	14.500 ± 0.140	>2.745
2.4396522	4181.482 ± 0.018	1044.91	28.048 ± 2.231	14.114 ± 0.260	15.101 ± 0.325	0.987 ± 0.416
2.4398761	4181.754 ± 0.919	1044.97	35.479 ± 20.789	13.326 ± 1.613	14.001 ± 0.686	0.675 ± 1.753
2.4413321	4183.525 ± 0.027	1045.42	43.933 ± 2.782	12.993 ± 0.028	14.301 ± 0.119	1.308 ± 0.122
2.4421926	4184.571 ± 0.112	1045.68	30.954 ± 11.714	12.529 ± 0.216	15.101 ± 0.388	2.572 ± 0.444
2.4426124	4185.081 ± 0.012	1045.80	19.420 ± 1.434	12.960 ± 0.086	14.866 ± 2.173	1.906 ± 2.175
2.4431200	4185.698 ± 0.068	1045.96	38.857 ± 7.574	12.752 ± 0.089	14.599 ± 0.227	1.847 ± 0.244
2.4440317	4186.806 ± 0.019	1046.23	22.342 ± 1.027	13.478 ± 0.039	15.903 ± 1.239	2.425 ± 1.240
2.4443538	4187.198 ± 0.068	1046.33	19.171 ± 2.964	12.719 ± 0.212	14.602 ± 0.600	1.883 ± 0.636
2.4450314	4188.022 ± 0.043	1046.54	16.289 ± 5.354	11.821 ± 0.116	14.001 ± 0.159	2.180 ± 0.197
2.4473140	4190.797 ± 0.039	1047.23	32.840 ± 4.362	12.241 ± 0.057	14.401 ± 0.114	2.160 ± 0.127
2.4482968	4191.991 ± 0.022	1047.53	19.835 ± 2.431	12.171 ± 0.046	14.200 ± 0.149	2.029 ± 0.156
2.4493141	4193.228 ± 0.047	1047.84	41.962 ± 5.686	12.303 ± 0.052	14.400 ± 0.086	2.097 ± 0.100
2.4502785	4194.400 ± 0.005	1048.13	17.382 ± 0.487	12.780 ± 0.010	14.200 ± 0.145	1.420 ± 0.145
2.4528954	4197.582 ± 0.047	1048.93	19.974 ± 5.037	11.781 ± 0.094	13.201 ± 0.524	1.420 ± 0.532
2.4546604	4199.727 ± 0.001	1049.46	22.549 ± 0.097	14.381 ± 0.005	15.701 ± 0.361	1.320 ± 0.361
2.4555354	4200.791 ± 0.016	1049.73	20.602 ± 1.101	13.021 ± 0.033	15.002 ± 2.022	1.981 ± 2.022
2.4559162	4201.254 ± 0.026	1049.85	18.409 ± 2.544	12.664 ± 0.096	17.062 ± 71.29	4.398 ± 71.29
2.4561863	4201.583 ± 6.875	1049.93	27.0	<11.222	15.198 ± 15.20	>3.976
2.4564259	4201.874 ± 0.031	1050.00	29.926 ± 2.542	12.692 ± 0.039	12.239 ± 759.8	−0.453 ± 759.8
2.4572504	4202.876 ± 0.172	1050.25	27.0	<11.201	14.100 ± 0.225	>2.899
2.4616630	4208.240 ± 0.001	1051.59	23.255 ± 0.079	13.914 ± 0.002	15.150 ± 0.210	1.236 ± 0.210
2.4638708	4210.924 ± 0.013	1052.26	18.222 ± 1.398	12.292 ± 0.028	13.947 ± 0.162	1.655 ± 0.164
2.4649289	4212.210 ± 0.033	1052.58	23.078 ± 3.785	12.320 ± 0.068	13.738 ± 0.245	1.418 ± 0.254
2.4658620	4213.345 ± 0.023	1052.87	44.716 ± 3.058	12.732 ± 0.023	14.399 ± 0.111	1.667 ± 0.113

Table A.9: continued.

z	$\lambda_{\rm H\,I}$ (Å)	$\lambda_{\rm He\,II}$ (Å)	b (km/s)	$\log N_{\rm H\,I}$	$\log N_{\rm He\,II}$	$\log \eta$
2.4668183	4214.507 ± 0.014	1053.16	18.238 ± 1.456	12.345 ± 0.031	14.452 ± 0.194	2.107 ± 0.196
2.4697957	4218.127 ± 0.001	1054.06	31.337 ± 0.113	14.504 ± 0.004	15.208 ± 0.195	0.704 ± 0.195
2.4723732	4221.260 ± 0.013	1054.84	20.673 ± 1.346	12.376 ± 0.024	14.184 ± 0.170	1.808 ± 0.172
2.4746816	4224.067 ± 0.060	1055.55	24.142 ± 6.282	11.799 ± 0.098	13.432 ± 0.413	1.633 ± 0.424
2.4757209	4225.330 ± 0.029	1055.86	11.127 ± 3.213	11.758 ± 0.092	13.355 ± 0.411	1.597 ± 0.421
2.4765298	4226.313 ± 0.002	1056.11	22.600 ± 0.185	13.727 ± 0.005	13.815 ± 0.217	0.088 ± 0.217
2.4773748	4227.341 ± 0.749	1056.36	44.921 ± 91.250	12.029 ± 0.949	13.800 ± 0.283	1.771 ± 0.990
2.4779396	4228.027 ± 0.032	1056.54	23.642 ± 4.040	12.567 ± 0.215	14.127 ± 0.176	1.560 ± 0.278
2.4812427	4232.043 ± 0.752	1057.54	30.897 ± 26.315	12.453 ± 1.139	12.917 ± 2.074	0.464 ± 2.366
2.4815309	4232.393 ± 0.081	1057.63	22.598 ± 5.900	12.717 ± 0.617	13.698 ± 0.389	0.981 ± 0.729
2.4823041	4233.333 ± 0.001	1057.86	24.510 ± 0.101	14.107 ± 0.002	14.361 ± 0.140	0.254 ± 0.140
2.4846854	4236.228 ± 0.012	1058.58	30.246 ± 1.295	12.738 ± 0.016	13.883 ± 0.203	1.145 ± 0.204
2.4855001	4237.218 ± 0.002	1058.83	22.227 ± 0.168	13.769 ± 0.005	13.528 ± 0.608	−0.241 ± 0.608
2.4862518	4238.132 ± 0.011	1059.06	50.056 ± 2.194	13.407 ± 0.018	14.792 ± 0.139	1.385 ± 0.140
2.4876699	4239.856 ± 0.077	1059.49	50.556 ± 3.987	13.488 ± 0.105	14.605 ± 0.131	1.117 ± 0.168
2.4885669	4240.947 ± 0.003	1059.77	34.849 ± 0.672	14.861 ± 0.011	13.005 ± 4.391	−1.856 ± 4.391
2.4889445	4241.406 ± 0.327	1059.88	72.683 ± 10.662	13.707 ± 0.209	14.707 ± 0.000	1.000 ± 0.000
2.4908788	4243.757 ± 0.008	1060.47	22.780 ± 0.857	12.680 ± 0.015	13.965 ± 0.174	1.285 ± 0.175
2.4918003	4244.877 ± 0.006	1060.75	20.426 ± 0.313	13.604 ± 0.023	13.617 ± 0.478	0.013 ± 0.479
2.4921505	4245.303 ± 0.176	1060.85	27.629 ± 8.371	12.547 ± 0.266	14.221 ± 0.175	1.674 ± 0.318
2.4932964	4246.696 ± 0.003	1061.20	31.480 ± 0.337	13.314 ± 0.004	14.582 ± 0.133	1.268 ± 0.133
2.4943759	4248.008 ± 0.018	1061.53	27.073 ± 1.936	12.401 ± 0.027	14.297 ± 0.137	1.896 ± 0.140
2.4959908	4249.971 ± 0.009	1062.02	38.095 ± 0.951	13.060 ± 0.010	14.502 ± 0.112	1.442 ± 0.112
2.4971793	4251.416 ± 0.036	1062.38	41.183 ± 4.074	12.842 ± 0.041	14.127 ± 0.233	1.285 ± 0.237
2.4977949	4252.165 ± 0.006	1062.57	20.312 ± 0.819	13.053 ± 0.025	15.610 ± 0.845	2.557 ± 0.845
2.4983580	4252.849 ± 0.003	1062.74	23.248 ± 0.373	13.428 ± 0.006	16.195 ± 0.493	2.767 ± 0.493
2.5004594	4255.404 ± 0.002	1063.38	21.647 ± 0.166	13.443 ± 0.003	14.325 ± 0.155	0.882 ± 0.155
2.5057330	4261.815 ± 0.020	1064.98	21.969 ± 2.082	12.442 ± 0.035	15.223 ± 0.386	2.781 ± 0.388
2.5061495	4262.321 ± 0.027	1065.11	12.002 ± 3.119	11.934 ± 0.123	14.400 ± 0.000	2.466 ± 0.000
2.5066371	4262.914 ± 0.008	1065.25	24.534 ± 0.864	12.850 ± 0.012	14.853 ± 0.317	2.003 ± 0.317
2.5081475	4264.750 ± 0.088	1065.71	27.0	<11.309	14.410 ± 0.148	>3.101
2.5090733	4265.876 ± 0.389	1065.99	28.034 ± 20.306	12.039 ± 0.591	13.096 ± 4.182	1.057 ± 4.224
2.5095251	4266.425 ± 0.069	1066.13	25.303 ± 3.337	12.677 ± 0.135	15.828 ± 0.375	3.151 ± 0.399
2.5121994	4269.676 ± 0.052	1066.94	28.917 ± 4.349	12.789 ± 0.077	15.029 ± 0.279	2.240 ± 0.289
2.5126252	4270.193 ± 0.011	1067.07	17.898 ± 1.151	12.933 ± 0.054	16.040 ± 6.160	3.107 ± 6.160
2.5132136	4270.909 ± 0.122	1067.25	19.952 ± 5.222	12.791 ± 0.343	13.742 ± 12.20	0.951 ± 12.20
2.5134995	4271.256 ± 0.045	1067.34	20.510 ± 1.511	13.266 ± 0.112	15.174 ± 0.418	1.908 ± 0.433
2.5154173	4273.588 ± 0.026	1067.92	25.243 ± 2.663	12.209 ± 0.040	14.437 ± 0.167	2.228 ± 0.172
2.5179925	4276.718 ± 0.152	1068.70	27.0	<11.212	14.016 ± 0.189	>2.804
2.5195751	4278.642 ± 0.054	1069.18	51.846 ± 6.053	12.355 ± 0.046	14.347 ± 0.137	1.992 ± 0.145
2.5204494	4279.705 ± 0.324	1069.45	27.0	<11.245	14.254 ± 0.381	>3.009
2.5207727	4280.098 ± 0.006	1069.55	22.989 ± 0.397	13.350 ± 0.014	13.864 ± 1.015	0.514 ± 1.015
2.5215600	4281.055 ± 0.100	1069.79	38.697 ± 7.246	13.366 ± 0.118	14.853 ± 0.202	1.487 ± 0.234
2.5223854	4282.059 ± 0.125	1070.04	18.137 ± 12.368	12.059 ± 0.726	12.753 ± 3.148	0.694 ± 3.231
2.5231109	4282.941 ± 1.394	1070.26	44.080 ± 85.586	12.567 ± 1.560	14.546 ± 0.174	1.979 ± 1.570
2.5236192	4283.558 ± 0.264	1070.41	33.882 ± 10.129	12.759 ± 0.927	13.641 ± 0.704	0.882 ± 1.164
2.5251129	4285.374 ± 0.002	1070.87	25.793 ± 0.212	13.526 ± 0.003	14.331 ± 0.173	0.805 ± 0.173
2.5258632	4286.286 ± 0.001	1071.09	20.132 ± 0.133	14.151 ± 0.004	14.259 ± 0.233	0.108 ± 0.233
2.5267782	4287.399 ± 0.001	1071.37	26.740 ± 0.235	14.638 ± 0.010	15.108 ± 0.315	0.470 ± 0.315
2.5276358	4288.441 ± 0.002	1071.63	22.620 ± 0.137	13.842 ± 0.002	14.522 ± 0.221	0.680 ± 0.221
2.5289717	4290.065 ± 0.035	1072.04	18.329 ± 3.698	11.878 ± 0.076	13.794 ± 0.485	1.916 ± 0.491
2.5293922	4290.577 ± 0.312	1072.17	27.0	<11.227	14.169 ± 0.228	>2.942
2.5298812	4291.171 ± 0.003	1072.31	19.303 ± 0.275	13.322 ± 0.006	14.234 ± 0.311	0.912 ± 0.311
2.5303955	4291.796 ± 0.005	1072.47	21.625 ± 0.457	13.195 ± 0.008	13.951 ± 0.251	0.756 ± 0.251
2.5323799	4294.209 ± 0.029	1073.07	38.049 ± 3.075	12.457 ± 0.033	14.100 ± 0.206	1.643 ± 0.209
2.5335872	4295.676 ± 0.002	1073.44	21.620 ± 0.173	13.663 ± 0.003	13.899 ± 0.311	0.236 ± 0.311
2.5342009	4296.422 ± 0.003	1073.63	22.407 ± 0.336	13.528 ± 0.009	14.499 ± 0.278	0.971 ± 0.278
2.5348084	4297.161 ± 0.104	1073.81	39.929 ± 8.087	12.428 ± 0.103	13.899 ± 0.302	1.471 ± 0.319
2.5380981	4301.160 ± 0.025	1074.81	23.707 ± 2.681	12.150 ± 0.044	15.498 ± 0.509	3.348 ± 0.511
2.5388765	4302.106 ± 0.104	1075.05	27.0	<11.199	15.400 ± 0.000	>4.201
2.5411031	4304.813 ± 0.001	1075.72	25.590 ± 0.104	14.213 ± 0.003	14.694 ± 0.338	0.481 ± 0.338
2.5423033	4306.272 ± 0.001	1076.09	27.369 ± 0.109	14.289 ± 0.003	17.400 ± 1.009	3.111 ± 1.009
2.5436053	4307.855 ± 0.032	1076.48	59.424 ± 3.657	12.761 ± 0.025	13.598 ± 1.019	0.837 ± 1.019
2.5449123	4309.444 ± 0.228	1076.88	27.0	<11.252	14.400 ± 0.336	>3.148
2.5456052	4310.286 ± 0.014	1077.09	30.457 ± 1.481	12.634 ± 0.019	14.000 ± 0.417	1.366 ± 0.417
2.5476136	4312.728 ± 0.003	1077.70	24.242 ± 0.459	13.188 ± 0.012	17.699 ± 1.307	4.511 ± 1.307
2.5477641	4312.911 ± 0.052	1077.75	86.499 ± 6.113	13.005 ± 0.028	14.005 ± 0.000	1.000 ± 0.000
2.5487280	4314.082 ± 0.012	1078.04	21.043 ± 1.539	12.480 ± 0.043	14.899 ± 0.699	2.419 ± 0.700
2.5518415	4317.868 ± 0.002	1078.99	23.650 ± 0.164	13.428 ± 0.003	15.200 ± 0.516	1.772 ± 0.516

Table A.9: continued.

z	$\lambda_{\mathrm{H\,I}}$ (Å)	$\lambda_{\mathrm{He\,II}}$ (Å)	b (km/s)	$\log N_{\mathrm{H\,I}}$	$\log N_{\mathrm{He\,II}}$	$\log \eta$
2.5538113	4320.262 ± 0.001	1079.58	23.360 ± 0.142	13.789 ± 0.004	13.799 ± 0.668	0.010 ± 0.668
2.5541329	4320.653 ± 0.040	1079.68	74.794 ± 3.583	13.083 ± 0.018	14.200 ± 0.000	1.117 ± 0.000
2.5548117	4321.479 ± 0.200	1079.89	27.0	<11.195	14.599 ± 0.392	>3.404
2.5565581	4323.601 ± 0.042	1080.42	28.248 ± 2.193	12.812 ± 0.069	14.800 ± 0.455	1.988 ± 0.460
2.5570903	4324.248 ± 0.036	1080.58	30.590 ± 2.089	12.956 ± 0.050	14.400 ± 0.446	1.444 ± 0.449
2.5583949	4325.834 ± 0.021	1080.98	42.065 ± 2.881	12.832 ± 0.067	14.800 ± 0.369	1.968 ± 0.375
2.5596738	4327.389 ± 0.100	1081.36	92.784 ± 19.151	12.931 ± 0.083	14.899 ± 0.205	1.968 ± 0.221
2.5609851	4328.983 ± 0.018	1081.76	27.075 ± 2.445	12.549 ± 0.061	13.799 ± 0.709	1.250 ± 0.712
2.5619991	4330.216 ± 0.083	1082.07	25.246 ± 8.722	11.796 ± 0.157	13.800 ± 0.536	2.004 ± 0.559
2.5629711	4331.397 ± 0.015	1082.37	40.686 ± 2.157	12.929 ± 0.019	14.700 ± 0.316	1.771 ± 0.317
2.5638237	4332.434 ± 0.006	1082.63	25.236 ± 0.643	13.045 ± 0.012	16.099 ± 0.918	3.054 ± 0.918
2.5660379	4335.126 ± 0.004	1083.30	40.578 ± 0.708	13.714 ± 0.018	14.599 ± 0.856	0.885 ± 0.856
2.5663059	4335.451 ± 0.040	1083.38	93.673 ± 4.601	13.529 ± 0.024	14.929 ± 0.000	1.400 ± 0.000
2.5679011	4337.391 ± 0.012	1083.86	26.013 ± 1.270	12.908 ± 0.034	15.500 ± 0.000	2.592 ± 0.000
2.5686779	4338.335 ± 0.010	1084.10	41.376 ± 1.481	13.347 ± 0.015	15.305 ± 0.523	1.958 ± 0.523
2.5702140	4340.203 ± 0.275	1084.57	50.198 ± 16.240	13.158 ± 0.242	14.202 ± 0.286	1.044 ± 0.375
2.5717802	4342.106 ± 0.069	1085.04	45.523 ± 3.787	13.757 ± 0.066	14.600 ± 0.269	0.843 ± 0.277
2.5724273	4342.893 ± 0.004	1085.24	28.920 ± 0.476	15.029 ± 0.024	14.800 ± 0.487	−0.229 ± 0.488
2.5753806	4346.483 ± 0.208	1086.14	27.0	<11.246	14.300 ± 0.289	>3.054
2.5763152	4347.619 ± 0.016	1086.42	39.974 ± 1.642	12.804 ± 0.017	14.500 ± 0.106	1.696 ± 0.107
2.5777080	4349.313 ± 0.030	1086.84	56.136 ± 3.281	12.731 ± 0.024	14.600 ± 0.064	1.869 ± 0.068
2.5847220	4357.839 ± 0.042	1088.97	39.043 ± 4.399	12.228 ± 0.045	13.900 ± 0.123	1.672 ± 0.131
2.5859067	4359.280 ± 0.016	1089.33	24.734 ± 1.622	12.369 ± 0.025	14.300 ± 0.093	1.931 ± 0.096
2.5876944	4361.453 ± 0.042	1089.88	24.904 ± 3.542	12.333 ± 0.064	15.900 ± 0.270	3.567 ± 0.277
2.5882044	4362.073 ± 0.010	1090.03	19.040 ± 1.191	12.718 ± 0.034	14.718 ± 0.000	2.000 ± 0.000
2.5896604	4363.843 ± 0.108	1090.47	27.0	<11.207	14.200 ± 0.165	>2.993
2.5907321	4365.146 ± 0.231	1090.80	54.066 ± 23.419	11.967 ± 0.191	14.199 ± 0.098	2.232 ± 0.215
2.5921512	4366.871 ± 0.019	1091.23	24.610 ± 2.000	12.311 ± 0.034	14.400 ± 0.104	2.089 ± 0.109
2.5936606	4368.706 ± 0.014	1091.69	24.229 ± 1.526	12.597 ± 0.024	15.100 ± 0.156	2.503 ± 0.158
2.5950706	4370.420 ± 0.023	1092.12	36.483 ± 1.925	12.927 ± 0.025	14.700 ± 0.114	1.773 ± 0.117
2.5957680	4371.268 ± 0.003	1092.33	22.913 ± 0.356	13.761 ± 0.007	14.701 ± 0.415	0.940 ± 0.415
2.5962534	4371.858 ± 0.015	1092.48	18.384 ± 1.800	13.064 ± 0.068	13.912 ± 6.597	0.848 ± 6.597
2.5967252	4372.431 ± 0.004	1092.62	24.906 ± 0.493	13.930 ± 0.009	15.311 ± 15.89	1.381 ± 15.89
2.5971825	4372.987 ± 0.000	1092.76	27.0	<11.522	14.500 ± 0.000	>2.978
2.5975797	4373.470 ± 0.007	1092.88	33.891 ± 0.606	14.072 ± 0.010	17.634 ± 222.8	3.562 ± 222.8
2.5983822	4374.446 ± 0.018	1093.12	38.262 ± 2.189	13.914 ± 0.031	15.003 ± 6.729	1.089 ± 6.729
2.5986111	4374.724 ± 0.000	1093.19	27.0	<11.550	15.100 ± 0.000	>3.550
2.5988495	4375.014 ± 0.059	1093.27	21.487 ± 7.099	12.527 ± 0.506	13.519 ± 32.53	0.992 ± 32.53
2.5997238	4376.077 ± 0.072	1093.53	27.0	<11.236	14.200 ± 0.066	>2.964
2.6004946	4377.014 ± 0.025	1093.77	26.340 ± 2.567	12.292 ± 0.042	13.900 ± 0.102	1.608 ± 0.110
2.6016393	4378.405 ± 0.055	1094.11	49.665 ± 6.472	12.317 ± 0.056	13.999 ± 0.114	1.682 ± 0.127
2.6031473	4380.238 ± 0.022	1094.57	33.007 ± 2.363	12.413 ± 0.031	14.300 ± 0.075	1.887 ± 0.081
2.6045351	4381.926 ± 0.057	1094.99	34.414 ± 6.191	12.018 ± 0.080	14.000 ± 0.096	1.982 ± 0.125
2.6058507	4383.525 ± 0.056	1095.39	27.0	<11.279	14.200 ± 0.076	>2.921
2.6075506	4385.592 ± 0.024	1095.91	26.977 ± 2.497	12.321 ± 0.038	15.200 ± 0.118	2.879 ± 0.124
2.6086152	4386.886 ± 0.019	1096.23	20.610 ± 1.998	12.245 ± 0.037	14.500 ± 0.094	2.255 ± 0.101
2.6093462	4387.774 ± 0.056	1096.45	16.089 ± 5.431	11.770 ± 0.157	13.400 ± 0.408	1.630 ± 0.437
2.6099281	4388.482 ± 0.010	1096.63	29.847 ± 1.066	12.925 ± 0.014	15.000 ± 0.118	2.075 ± 0.119
2.6114225	4390.298 ± 0.022	1097.09	25.158 ± 2.229	12.374 ± 0.046	14.300 ± 0.082	1.926 ± 0.094
2.6124074	4391.496 ± 0.080	1097.39	56.606 ± 8.694	12.399 ± 0.064	14.300 ± 0.065	1.901 ± 0.091
2.6144323	4393.957 ± 0.002	1098.00	28.193 ± 0.195	13.697 ± 0.003	15.600 ± 0.187	1.903 ± 0.187
2.6152470	4394.948 ± 0.014	1098.25	29.897 ± 1.584	13.130 ± 0.026	14.300 ± 0.292	1.170 ± 0.293
2.6161027	4395.988 ± 0.002	1098.51	34.613 ± 0.361	14.252 ± 0.003	15.900 ± 0.185	1.648 ± 0.185
2.6183956	4398.775 ± 0.027	1099.20	29.510 ± 2.642	12.439 ± 0.037	14.600 ± 0.085	2.161 ± 0.093
2.6193323	4399.914 ± 0.072	1099.49	31.274 ± 2.002	13.703 ± 0.118	14.900 ± 0.105	1.197 ± 0.158
2.6216705	4402.757 ± 0.008	1100.20	22.177 ± 0.901	12.611 ± 0.016	14.299 ± 0.087	1.688 ± 0.088
2.6224942	4403.758 ± 0.016	1100.45	24.439 ± 1.701	12.378 ± 0.028	14.300 ± 0.078	1.922 ± 0.083
2.6238742	4405.435 ± 0.020	1100.87	45.663 ± 2.364	12.706 ± 0.022	14.500 ± 0.059	1.794 ± 0.063
2.6250005	4406.805 ± 0.039	1101.21	29.866 ± 4.214	12.160 ± 0.058	14.100 ± 0.087	1.940 ± 0.105
2.6265664	4408.708 ± 0.013	1101.69	44.309 ± 1.076	13.677 ± 0.042	15.600 ± 0.140	1.923 ± 0.146
2.6266482	4408.808 ± 0.007	1101.71	27.305 ± 1.181	13.468 ± 0.067	13.400 ± 0.000	−0.068 ± 0.000
2.6277139	4410.103 ± 0.019	1102.04	28.247 ± 2.696	12.598 ± 0.038	14.400 ± 0.147	1.802 ± 0.152
2.6285090	4411.070 ± 0.008	1102.28	25.096 ± 1.013	13.006 ± 0.016	15.300 ± 0.308	2.294 ± 0.308
2.6291351	4411.831 ± 0.026	1102.47	23.544 ± 3.000	12.435 ± 0.054	13.900 ± 0.182	1.465 ± 0.190
2.6298845	4412.742 ± 0.076	1102.69	24.128 ± 9.179	11.821 ± 0.152	13.700 ± 0.161	1.879 ± 0.221
2.6308823	4413.955 ± 0.026	1103.00	40.223 ± 3.087	12.849 ± 0.031	14.800 ± 0.081	1.951 ± 0.087
2.6317251	4414.980 ± 0.018	1103.25	30.443 ± 1.521	12.843 ± 0.027	14.400 ± 0.096	1.557 ± 0.100
2.6329296	4416.444 ± 0.010	1103.62	31.179 ± 0.702	13.475 ± 0.013	15.299 ± 0.159	1.824 ± 0.160
2.6334829	4417.117 ± 0.003	1103.79	21.156 ± 0.310	13.744 ± 0.010	15.300 ± 0.351	1.556 ± 0.351

Table A.9: continued.

z	$\lambda_{\rm H\,I}$ (Å)	$\lambda_{\rm He\,II}$ (Å)	b (km/s)	$\log N_{\rm H\,I}$	$\log N_{\rm He\,II}$	$\log \eta$
2.6347651	4418.675 ± 0.004	1104.18	54.426 ± 1.715	14.696 ± 0.038	14.500 ± 0.166	−0.196 ± 0.170
2.6353605	4419.399 ± 0.287	1104.36	84.076 ± 7.639	14.104 ± 0.168	15.004 ± 0.000	0.900 ± 0.000
2.6367342	4421.069 ± 0.068	1104.78	27.0	<11.219	14.400 ± 0.103	>3.181
2.6380751	4422.699 ± 0.092	1105.18	27.0	<11.311	14.705 ± 0.222	>3.394
2.6385803	4423.313 ± 0.004	1105.34	21.043 ± 0.687	13.484 ± 0.030	14.084 ± 0.000	0.600 ± 0.000
2.6387336	4423.500 ± 0.007	1105.38	50.309 ± 0.672	14.071 ± 0.006	14.571 ± 0.000	0.500 ± 0.000
2.6392822	4424.167 ± 0.232	1105.55	27.0	<11.356	14.599 ± 0.310	>3.243
2.6397574	4424.744 ± 0.009	1105.69	23.812 ± 0.983	13.082 ± 0.028	14.400 ± 0.000	1.318 ± 0.000
2.6405473	4425.704 ± 0.005	1105.93	40.383 ± 0.751	13.625 ± 0.007	15.701 ± 0.325	2.076 ± 0.325
2.6415126	4426.878 ± 0.003	1106.23	25.087 ± 0.269	13.500 ± 0.005	14.100 ± 0.173	0.600 ± 0.173
2.6427464	4428.378 ± 0.150	1106.60	68.471 ± 16.829	12.218 ± 0.102	13.800 ± 0.153	1.582 ± 0.184
2.6451180	4431.261 ± 0.104	1107.32	27.0	<11.217	13.800 ± 0.114	>2.583
2.6486428	4435.546 ± 0.001	1108.39	42.924 ± 0.174	15.866 ± 0.014	16.690 ± 0.109	0.824 ± 0.110
2.6506717	4438.012 ± 0.010	1109.01	23.403 ± 1.478	13.053 ± 0.093	15.181 ± 0.121	2.128 ± 0.153
2.6528244	4440.629 ± 0.031	1109.66	32.630 ± 3.270	12.383 ± 0.039	14.227 ± 0.074	1.844 ± 0.084
2.6536353	4441.615 ± 0.001	1109.91	23.775 ± 0.118	13.718 ± 0.002	14.934 ± 0.139	1.216 ± 0.139
2.6545808	4442.765 ± 0.018	1110.20	21.462 ± 1.796	12.270 ± 0.033	12.897 ± 0.718	0.627 ± 0.719
2.6557035	4444.130 ± 0.222	1110.54	46.699 ± 9.073	12.452 ± 0.200	14.459 ± 0.077	2.007 ± 0.214
2.6560814	4444.589 ± 0.022	1110.65	24.932 ± 3.622	12.485 ± 0.170	13.822 ± 0.261	1.337 ± 0.311
2.6574488	4446.251 ± 0.028	1111.07	16.799 ± 1.875	12.366 ± 0.088	14.295 ± 0.112	1.929 ± 0.142
2.6578755	4446.770 ± 0.027	1111.20	23.959 ± 2.793	12.651 ± 0.058	14.017 ± 0.112	1.366 ± 0.126
2.6587198	4447.796 ± 0.077	1111.45	40.250 ± 8.166	12.211 ± 0.084	13.166 ± 0.493	0.955 ± 0.500
2.6599572	4449.301 ± 0.001	1111.83	21.823 ± 0.130	13.576 ± 0.002	14.647 ± 0.108	1.071 ± 0.108
2.6607242	4450.233 ± 0.001	1112.06	21.554 ± 0.078	13.957 ± 0.002	14.299 ± 0.091	0.342 ± 0.091
2.6621575	4451.976 ± 0.005	1112.50	33.972 ± 0.320	13.708 ± 0.005	15.237 ± 0.141	1.529 ± 0.141
2.6632297	4453.279 ± 0.005	1112.82	40.554 ± 0.487	14.368 ± 0.005	14.363 ± 0.641	−0.005 ± 0.641
2.6640122	4454.230 ± 0.010	1113.06	29.770 ± 0.589	13.737 ± 0.017	17.926 ± 0.682	4.189 ± 0.682
2.6649153	4455.328 ± 0.001	1113.34	22.584 ± 0.092	14.023 ± 0.002	13.265 ± 3.422	−0.758 ± 3.422
2.6662416	4456.940 ± 0.024	1113.74	18.451 ± 2.327	12.253 ± 0.050	13.662 ± 0.160	1.409 ± 0.168
2.6667259	4457.529 ± 0.055	1113.89	17.510 ± 5.225	11.862 ± 0.120	12.912 ± 0.643	1.050 ± 0.654
2.6685412	4459.736 ± 0.001	1114.44	22.037 ± 0.098	13.746 ± 0.002	14.313 ± 0.076	0.567 ± 0.076
2.6695197	4460.925 ± 0.032	1114.73	16.879 ± 2.815	12.275 ± 0.071	13.998 ± 0.104	1.723 ± 0.126
2.6702106	4461.765 ± 0.062	1114.94	33.253 ± 10.347	12.271 ± 0.114	13.928 ± 0.099	1.657 ± 0.151
2.6728170	4464.934 ± 0.001	1115.74	24.369 ± 0.146	14.145 ± 0.003	13.000 ± 0.000	−1.145 ± 0.000
2.6729760	4465.127 ± 0.011	1115.79	59.649 ± 1.269	13.437 ± 0.014	15.276 ± 0.058	1.839 ± 0.060
2.6757822	4468.539 ± 0.053	1116.64	24.069 ± 4.644	12.145 ± 0.092	14.164 ± 0.090	2.019 ± 0.129
2.6765318	4469.450 ± 0.005	1116.86	33.569 ± 0.453	13.440 ± 0.005	14.667 ± 0.075	1.227 ± 0.075
2.6785860	4471.947 ± 0.032	1117.49	25.378 ± 1.554	13.097 ± 0.052	14.964 ± 0.136	1.867 ± 0.146
2.6790454	4472.506 ± 0.006	1117.63	23.493 ± 0.293	13.824 ± 0.010	14.353 ± 0.133	0.529 ± 0.133
2.6797893	4473.410 ± 0.006	1117.85	15.481 ± 0.690	12.596 ± 0.017	14.323 ± 0.118	1.727 ± 0.119
2.6805191	4474.297 ± 0.020	1118.08	29.106 ± 2.331	12.443 ± 0.036	14.172 ± 0.072	1.729 ± 0.080
2.6820159	4476.117 ± 0.034	1118.53	19.597 ± 2.202	12.510 ± 0.073	14.339 ± 0.101	1.829 ± 0.125
2.6825242	4476.735 ± 0.004	1118.69	22.762 ± 0.548	13.623 ± 0.014	14.083 ± 0.108	0.460 ± 0.109
2.6831911	4477.545 ± 0.014	1118.89	33.128 ± 3.803	13.239 ± 0.049	14.377 ± 0.081	1.138 ± 0.095
2.6837442	4478.218 ± 0.005	1119.06	18.201 ± 0.713	13.233 ± 0.031	13.938 ± 0.156	0.705 ± 0.159
2.6841967	4478.768 ± 0.036	1119.19	18.559 ± 2.946	12.327 ± 0.080	14.412 ± 0.114	2.085 ± 0.139
2.6851673	4479.948 ± 0.050	1119.49	39.712 ± 6.882	12.268 ± 0.077	14.445 ± 0.060	2.177 ± 0.098
2.6870513	4482.238 ± 0.006	1120.06	39.775 ± 0.272	14.379 ± 0.006	16.686 ± 0.169	2.307 ± 0.169
2.6879528	4483.334 ± 0.195	1120.33	34.364 ± 13.752	13.277 ± 0.260	14.593 ± 0.249	1.316 ± 0.360
2.6886315	4484.159 ± 0.052	1120.54	19.999 ± 3.044	12.476 ± 0.191	14.075 ± 0.131	1.599 ± 0.232
2.6896369	4485.381 ± 0.052	1120.85	35.377 ± 6.312	12.187 ± 0.077	14.090 ± 0.077	1.903 ± 0.109
2.6912489	4487.341 ± 0.002	1121.34	39.443 ± 0.260	15.486 ± 0.015	15.618 ± 0.112	0.132 ± 0.113
2.6924536	4488.806 ± 0.007	1121.70	28.250 ± 1.120	13.686 ± 0.023	14.352 ± 0.098	0.666 ± 0.101
2.6930387	4489.517 ± 0.035	1121.88	30.397 ± 1.636	13.164 ± 0.048	14.262 ± 0.082	1.098 ± 0.095
2.6947689	4491.620 ± 0.046	1122.41	27.976 ± 1.318	13.391 ± 0.102	15.057 ± 0.109	1.666 ± 0.149
2.6962159	4493.379 ± 0.002	1122.84	30.631 ± 0.182	13.703 ± 0.002	16.338 ± 0.212	2.635 ± 0.212
2.6977060	4495.191 ± 0.008	1123.30	43.545 ± 0.476	13.893 ± 0.007	14.571 ± 0.074	0.678 ± 0.074
2.6984847	4496.137 ± 0.007	1123.53	34.223 ± 0.436	13.700 ± 0.010	14.764 ± 0.101	1.064 ± 0.101
2.6995411	4497.422 ± 0.021	1123.85	25.167 ± 2.374	12.367 ± 0.035	14.477 ± 0.085	2.110 ± 0.092
2.7003858	4498.448 ± 0.028	1124.11	29.650 ± 2.981	12.325 ± 0.040	14.425 ± 0.070	2.100 ± 0.081
2.7024796	4500.994 ± 0.022	1124.75	24.928 ± 2.279	12.258 ± 0.037	14.481 ± 0.077	2.223 ± 0.085
2.7050898	4504.167 ± 0.017	1125.54	21.439 ± 1.907	12.344 ± 0.051	14.144 ± 0.000	1.800 ± 0.000
2.7060771	4505.367 ± 0.015	1125.84	62.092 ± 2.054	13.166 ± 0.012	16.185 ± 0.110	3.019 ± 0.111
2.7081940	4507.941 ± 0.011	1126.48	27.497 ± 1.506	13.404 ± 0.026	14.827 ± 0.000	1.423 ± 0.000
2.7090042	4508.925 ± 0.009	1126.73	33.812 ± 1.726	13.417 ± 0.024	26.894 ± 26.89	13.477 ± 26.89
2.7097602	4509.844 ± 0.010	1126.96	30.960 ± 0.861	13.416 ± 0.016	15.295 ± 0.000	1.879 ± 0.000
2.7109897	4511.339 ± 0.016	1127.33	41.137 ± 0.891	13.783 ± 0.017	15.793 ± 241929.	2.010 ± 241929.
2.7122233	4512.839 ± 0.005	1127.71	55.258 ± 0.610	14.709 ± 0.004	16.211 ± 0.242	1.502 ± 0.242
2.7132108	4514.039 ± 0.003	1128.01	14.362 ± 0.451	13.270 ± 0.022	14.270 ± 0.000	1.000 ± 0.000

Table A.9: continued.

z	$\lambda_{\mathrm{H\,I}}$ (Å)	$\lambda_{\mathrm{He\,II}}$ (Å)	b (km/s)	$\log N_{\mathrm{H\,I}}$	$\log N_{\mathrm{He\,II}}$	$\log \eta$
2.7147882	4515.957 ± 0.006	1128.49	35.809 ± 0.244	14.493 ± 0.008	16.583 ± 0.167	2.090 ± 0.167
2.7165601	4518.111 ± 0.025	1129.03	23.326 ± 2.653	12.139 ± 0.048	14.762 ± 0.113	2.623 ± 0.123
2.7174878	4519.239 ± 0.080	1129.31	27.0	<11.175	14.237 ± 0.082	>3.062
2.7183957	4520.342 ± 0.005	1129.58	25.314 ± 0.453	13.245 ± 0.008	14.966 ± 0.226	1.721 ± 0.226
2.7189417	4521.006 ± 0.033	1129.75	19.992 ± 2.465	12.274 ± 0.066	14.600 ± 0.162	2.326 ± 0.175
2.7202785	4522.631 ± 0.008	1130.15	27.065 ± 0.811	12.714 ± 0.012	15.960 ± 0.149	3.246 ± 0.149
2.7221003	4524.846 ± 0.015	1130.71	24.009 ± 1.477	12.344 ± 0.024	14.577 ± 0.086	2.233 ± 0.089
2.7262592	4529.902 ± 0.021	1131.97	33.099 ± 2.145	12.394 ± 0.027	14.432 ± 0.070	2.038 ± 0.075
2.7274470	4531.346 ± 0.014	1132.33	12.053 ± 1.813	11.995 ± 0.079	13.597 ± 1.592	1.602 ± 1.594
2.7278609	4531.849 ± 0.034	1132.46	48.822 ± 2.697	12.688 ± 0.031	14.988 ± 0.076	2.300 ± 0.082
2.7298658	4534.286 ± 0.022	1133.07	18.586 ± 2.540	11.993 ± 0.064	14.275 ± 0.096	2.282 ± 0.115
2.7307799	4535.398 ± 0.003	1133.34	20.763 ± 0.282	13.063 ± 0.006	15.555 ± 0.169	2.492 ± 0.169
2.7392588	4545.705 ± 0.010	1135.92	34.237 ± 0.380	16.566 ± 0.051	17.566 ± 0.000	1.000 ± 0.000
2.7412729	4548.154 ± 0.010	1136.53	36.787 ± 2.397	15.992 ± 0.180	16.992 ± 0.000	1.000 ± 0.000
2.7423732	4549.491 ± 0.174	1136.87	29.194 ± 7.278	13.259 ± 0.314	16.300 ± 0.000	3.041 ± 0.000
2.7436910	4551.093 ± 0.090	1137.27	42.700 ± 9.844	12.511 ± 0.227	16.195 ± 14.51	3.684 ± 14.51
2.7457402	4553.584 ± 0.001	1137.89	28.871 ± 0.137	14.375 ± 0.003	16.771 ± 46.69	2.396 ± 46.69
2.7457950	4553.651 ± 0.033	1137.91	84.745 ± 5.441	13.127 ± 0.031	15.700 ± 0.139	2.573 ± 0.142
2.7488499	4557.365 ± 0.088	1138.83	48.106 ± 4.884	12.931 ± 0.070	16.201 ± 0.294	3.270 ± 0.302
2.7507505	4559.675 ± 0.007	1139.41	28.205 ± 0.802	12.795 ± 0.014	16.902 ± 1.087	4.107 ± 1.087
2.7523170	4561.579 ± 0.070	1139.89	24.848 ± 1.381	14.019 ± 0.308	15.900 ± 1.665	1.881 ± 1.693
2.7526200	4561.948 ± 0.158	1139.98	28.475 ± 7.031	14.032 ± 0.356	16.603 ± 3.055	2.571 ± 3.076
2.7531824	4562.632 ± 0.614	1140.15	40.769 ± 27.547	13.054 ± 0.630	14.600 ± 1.340	1.546 ± 1.481
2.7539475	4563.562 ± 0.014	1140.38	12.789 ± 2.091	12.342 ± 0.119	14.500 ± 2.470	2.158 ± 2.473
2.7542710	4563.955 ± 0.038	1140.48	12.150 ± 3.101	11.905 ± 0.114	16.367 ± 88.86	4.462 ± 88.86
2.7546408	4564.405 ± 1.873	1140.59	27.0	<11.116	15.601 ± 6.890	>4.484
2.7559965	4566.053 ± 0.050	1141.01	33.576 ± 1.322	14.094 ± 0.071	15.200 ± 0.300	1.106 ± 0.308
2.7571869	4567.500 ± 0.042	1141.37	47.400 ± 3.825	13.262 ± 0.041	14.800 ± 0.102	1.538 ± 0.110
2.7582471	4568.789 ± 0.012	1141.69	27.778 ± 0.982	12.841 ± 0.022	15.200 ± 0.249	2.359 ± 0.250
2.7594068	4570.199 ± 0.013	1142.04	33.457 ± 0.801	13.359 ± 0.033	14.800 ± 0.158	1.441 ± 0.161
2.7602870	4571.268 ± 0.025	1142.31	54.702 ± 6.672	13.363 ± 0.053	14.800 ± 0.120	1.437 ± 0.131
2.7609861	4572.118 ± 0.014	1142.52	18.819 ± 2.247	12.454 ± 0.125	14.500 ± 0.361	2.046 ± 0.382
2.7617364	4573.030 ± 0.013	1142.75	36.644 ± 1.678	13.130 ± 0.021	14.600 ± 0.163	1.470 ± 0.164
2.7623737	4573.805 ± 0.008	1142.94	18.293 ± 0.834	12.724 ± 0.033	16.200 ± 2.624	3.476 ± 2.624
2.7630286	4574.601 ± 0.019	1143.14	34.980 ± 2.192	12.676 ± 0.027	15.400 ± 0.355	2.724 ± 0.356
2.7650819	4577.098 ± 0.036	1143.77	87.735 ± 7.026	12.958 ± 0.021	15.300 ± 0.000	2.342 ± 0.000
2.7651374	4577.165 ± 0.010	1143.78	24.679 ± 1.425	12.571 ± 0.043	14.423 ± 4.013	1.852 ± 4.013
2.7667975	4579.183 ± 0.017	1144.29	42.461 ± 1.615	12.757 ± 0.023	14.901 ± 0.138	2.144 ± 0.140
2.7679067	4580.531 ± 0.072	1144.62	27.0	<11.078	14.400 ± 0.097	>3.322
2.7693348	4582.268 ± 0.029	1145.06	46.244 ± 3.321	12.416 ± 0.036	14.001 ± 0.131	1.585 ± 0.136
2.7702570	4583.389 ± 0.076	1145.34	27.0	<11.086	15.100 ± 0.226	>4.014
2.7715838	4585.001 ± 0.932	1145.74	27.0	<11.106	15.901 ± 3.800	>4.795
2.7726357	4586.281 ± 0.020	1146.06	94.967 ± 2.186	13.276 ± 0.013	15.200 ± 0.000	1.924 ± 0.000
2.7729635	4586.679 ± 0.001	1146.16	26.920 ± 0.115	13.792 ± 0.002	15.635 ± 7.284	1.843 ± 7.284
2.7739370	4587.862 ± 2.681	1146.45	27.0	<11.115	14.816 ± 2.759	>3.701
2.7749109	4589.046 ± 0.051	1146.75	39.201 ± 4.579	12.487 ± 0.055	15.525 ± 7.054	3.038 ± 7.054
2.7757401	4590.054 ± 0.032	1147.00	28.263 ± 3.602	12.539 ± 0.078	16.002 ± 0.413	3.463 ± 0.420
2.7775354	4592.237 ± 0.062	1147.55	35.593 ± 7.966	12.227 ± 0.098	16.102 ± 0.343	3.875 ± 0.357
2.7782955	4593.161 ± 0.013	1147.78	15.341 ± 1.407	12.206 ± 0.045	14.901 ± 1.123	2.695 ± 1.124
2.7791290	4594.174 ± 0.004	1148.03	41.073 ± 0.602	13.266 ± 0.007	14.800 ± 0.119	1.534 ± 0.119
2.7803733	4595.687 ± 0.005	1148.41	32.046 ± 0.345	13.522 ± 0.007	15.201 ± 0.319	1.679 ± 0.319
2.7812042	4596.697 ± 0.009	1148.66	42.968 ± 0.754	13.476 ± 0.009	15.202 ± 0.498	1.726 ± 0.498
2.7825606	4598.346 ± 0.019	1149.07	37.681 ± 2.277	12.565 ± 0.033	15.299 ± 0.344	2.734 ± 0.346
2.7844810	4600.680 ± 0.012	1149.66	48.344 ± 0.498	14.307 ± 0.010	15.900 ± 0.325	1.593 ± 0.325
2.7853789	4601.772 ± 0.007	1149.93	37.158 ± 0.525	14.653 ± 0.010	15.701 ± 0.865	1.048 ± 0.865
2.7864115	4603.027 ± 0.010	1150.24	23.640 ± 1.522	13.266 ± 0.034	14.500 ± 0.226	1.234 ± 0.229
2.7871025	4603.867 ± 0.002	1150.45	24.657 ± 0.200	14.570 ± 0.007	14.600 ± 0.175	0.030 ± 0.175
2.7879734	4604.926 ± 0.012	1150.72	28.317 ± 1.136	12.860 ± 0.019	15.200 ± 0.181	2.340 ± 0.182
2.7891884	4606.403 ± 0.013	1151.09	16.880 ± 1.425	12.148 ± 0.037	15.900 ± 0.349	3.752 ± 0.351
2.7899437	4607.321 ± 0.004	1151.32	23.538 ± 0.421	12.909 ± 0.008	13.700 ± 0.695	0.791 ± 0.695
2.7903571	4607.824 ± 0.120	1151.44	27.0	<11.085	14.601 ± 0.165	>3.516
2.7910151	4608.624 ± 0.036	1151.64	12.079 ± 3.854	11.494 ± 0.125	13.303 ± 3.101	1.809 ± 3.104
2.7912619	4608.924 ± 0.404	1151.72	27.0	<11.071	14.300 ± 0.295	>3.229
2.7920711	4609.907 ± 0.246	1151.96	37.909 ± 7.587	12.943 ± 0.285	14.400 ± 0.375	1.457 ± 0.471
2.7924070	4610.316 ± 0.006	1152.07	25.718 ± 0.820	13.578 ± 0.065	15.100 ± 0.000	1.522 ± 0.000
2.7935109	4611.658 ± 0.005	1152.40	25.080 ± 0.593	12.806 ± 0.010	14.600 ± 0.000	1.794 ± 0.000
2.7940278	4612.286 ± 0.184	1152.56	27.0	<11.093	14.401 ± 0.175	>3.308
2.7947066	4613.111 ± 0.003	1152.76	35.970 ± 0.193	13.958 ± 0.003	14.300 ± 0.151	0.342 ± 0.151
2.7951653	4613.669 ± 0.005	1152.90	13.882 ± 0.648	12.751 ± 0.037	14.100 ± 0.355	1.349 ± 0.357

Table A.9: continued.

z	$\lambda_{\rm H\,I}$ (Å)	$\lambda_{\rm He\,II}$ (Å)	b (km/s)	$\log N_{\rm H\,I}$	$\log N_{\rm He\,II}$	$\log \eta$
2.7957063	4614.327 ± 0.168	1153.07	27.0	<11.036	14.700 ± 0.221	>3.664
2.7966061	4615.421 ± 0.057	1153.34	41.572 ± 4.849	12.430 ± 0.055	14.900 ± 0.210	2.470 ± 0.217
2.7972896	4616.251 ± 0.010	1153.55	21.688 ± 1.095	12.609 ± 0.033	14.400 ± 0.219	1.791 ± 0.221
2.7982254	4617.389 ± 0.009	1153.83	36.122 ± 0.877	13.382 ± 0.011	14.800 ± 0.127	1.418 ± 0.127
2.7989275	4618.243 ± 0.003	1154.05	23.622 ± 0.252	13.493 ± 0.006	14.998 ± 0.421	1.505 ± 0.421
2.7996926	4619.173 ± 0.000	1154.28	27.0	<11.020	14.499 ± 0.212	>3.479
2.8000779	4619.641 ± 0.000	1154.40	27.0	<11.016	14.200 ± 0.280	>3.184
2.8005438	4620.207 ± 0.018	1154.54	23.228 ± 1.940	12.119 ± 0.037	13.901 ± 0.278	1.782 ± 0.280
2.8012097	4621.017 ± 0.168	1154.74	27.0	<11.016	14.300 ± 0.164	>3.284
2.8016062	4621.499 ± 0.007	1154.86	19.362 ± 0.487	12.876 ± 0.014	14.200 ± 0.237	1.324 ± 0.237
2.8022957	4622.337 ± 0.017	1155.07	26.300 ± 0.851	13.747 ± 0.028	14.300 ± 0.292	0.553 ± 0.293
2.8027217	4622.855 ± 0.014	1155.20	23.311 ± 0.698	13.656 ± 0.039	15.096 ± 1.231	1.440 ± 1.232
2.8033228	4623.586 ± 0.033	1155.38	41.174 ± 1.951	13.131 ± 0.029	14.900 ± 0.181	1.769 ± 0.183
2.8044724	4624.983 ± 0.232	1155.73	27.0	<11.028	14.800 ± 0.506	>3.772
2.8049893	4625.612 ± 0.018	1155.89	46.727 ± 1.741	12.982 ± 0.017	14.700 ± 0.172	1.718 ± 0.173
2.8062265	4627.116 ± 0.027	1156.26	40.311 ± 0.784	13.564 ± 0.036	14.900 ± 0.249	1.336 ± 0.252
2.8064194	4627.350 ± 0.003	1156.32	23.962 ± 0.502	13.645 ± 0.029	14.800 ± 0.739	1.155 ± 0.740
2.8072906	4628.409 ± 0.002	1156.59	20.965 ± 0.188	13.361 ± 0.004	14.600 ± 0.238	1.239 ± 0.238
2.8079059	4629.157 ± 0.384	1156.77	27.0	<11.034	14.400 ± 0.363	>3.366
2.8082261	4629.547 ± 0.013	1156.87	25.971 ± 1.217	12.664 ± 0.020	13.501 ± 4.006	0.837 ± 4.006
2.8088894	4630.353 ± 0.016	1157.07	23.408 ± 1.879	12.586 ± 0.042	15.103 ± 0.542	2.517 ± 0.544
2.8095498	4631.156 ± 0.009	1157.27	31.254 ± 0.696	13.103 ± 0.010	15.100 ± 0.187	1.997 ± 0.187
2.8107312	4632.592 ± 0.008	1157.63	26.039 ± 0.829	12.583 ± 0.014	14.400 ± 0.088	1.817 ± 0.089
2.8130445	4635.404 ± 0.027	1158.33	21.513 ± 2.733	12.003 ± 0.050	14.100 ± 0.113	2.097 ± 0.124
2.8138671	4636.404 ± 0.007	1158.58	28.260 ± 0.866	12.805 ± 0.011	14.601 ± 0.094	1.796 ± 0.095
2.8148017	4637.540 ± 0.029	1158.87	33.344 ± 2.944	12.316 ± 0.034	13.701 ± 0.189	1.385 ± 0.192
2.8179989	4641.427 ± 0.021	1159.84	25.810 ± 2.264	12.088 ± 0.039	13.151 ± 0.534	1.063 ± 0.535
2.8202505	4644.164 ± 0.044	1160.52	31.812 ± 4.395	11.964 ± 0.062	14.210 ± 0.093	2.246 ± 0.112
2.8214877	4645.668 ± 0.009	1160.90	21.437 ± 0.890	12.456 ± 0.017	14.389 ± 0.106	1.933 ± 0.107
2.8236310	4648.274 ± 0.028	1161.55	45.580 ± 2.476	12.675 ± 0.028	15.153 ± 0.100	2.478 ± 0.104
2.8251860	4650.164 ± 0.011	1162.02	25.148 ± 0.919	12.765 ± 0.016	15.584 ± 0.378	2.819 ± 0.378
2.8257742	4650.879 ± 0.003	1162.20	20.416 ± 0.283	13.165 ± 0.007	16.800 ± 0.000	3.635 ± 0.000
2.8269448	4652.302 ± 0.013	1162.56	46.191 ± 0.843	13.235 ± 0.012	15.138 ± 0.314	1.903 ± 0.314
2.8282447	4653.883 ± 0.008	1162.95	33.439 ± 0.774	12.871 ± 0.010	15.095 ± 0.488	2.224 ± 0.488
2.8296411	4655.580 ± 0.001	1163.38	27.806 ± 0.099	13.992 ± 0.002	16.709 ± 1.604	2.717 ± 1.604
2.8306065	4656.754 ± 0.001	1163.67	35.834 ± 0.125	14.445 ± 0.002	14.800 ± 0.000	0.355 ± 0.000
2.8317075	4658.092 ± 0.032	1164.01	27.905 ± 2.903	12.187 ± 0.046	17.835 ± 9.259	5.648 ± 9.259
2.8332727	4659.995 ± 0.000	1164.48	27.0	<10.977	16.700 ± 0.000	>5.723
2.8346429	4661.661 ± 0.034	1164.90	19.358 ± 3.432	11.677 ± 0.069	17.800 ± 0.000	6.123 ± 0.000
2.8358524	4663.131 ± 0.008	1165.26	35.054 ± 0.602	13.102 ± 0.016	14.402 ± 2.355	1.300 ± 2.355
2.8373857	4664.995 ± 0.002	1165.73	26.884 ± 0.224	14.265 ± 0.007	15.800 ± 0.000	1.535 ± 0.000
2.8375404	4665.183 ± 0.059	1165.78	81.067 ± 4.916	13.545 ± 0.053	16.127 ± 2.274	2.582 ± 2.275
2.8382530	4666.049 ± 0.011	1165.99	20.502 ± 0.945	13.342 ± 0.050	15.500 ± 0.000	2.158 ± 0.000
2.8386276	4666.505 ± 0.049	1166.11	22.443 ± 1.928	12.868 ± 0.090	15.700 ± 0.000	2.832 ± 0.000
2.8394613	4667.519 ± 0.000	1166.36	27.0	<10.955	15.010 ± 6.587	>4.055
2.8406689	4668.986 ± 0.001	1166.73	33.997 ± 0.149	13.458 ± 0.002	16.394 ± 0.725	2.936 ± 0.725
2.8424442	4671.145 ± 0.036	1167.27	31.509 ± 3.831	12.011 ± 0.053	15.626 ± 0.591	3.615 ± 0.593
2.8434255	4672.337 ± 0.001	1167.56	24.222 ± 0.088	13.799 ± 0.002	15.500 ± 0.000	1.701 ± 0.000
2.8441687	4673.241 ± 0.000	1167.79	27.0	<10.963	15.200 ± 0.000	>4.237
2.8449287	4674.165 ± 0.030	1168.02	32.809 ± 3.397	12.062 ± 0.050	15.394 ± 0.332	3.332 ± 0.336
2.8499341	4680.250 ± 0.144	1169.54	30.770 ± 15.002	12.166 ± 0.276	15.600 ± 0.000	3.434 ± 0.000
2.8504927	4680.929 ± 0.026	1169.71	24.299 ± 1.431	12.737 ± 0.059	15.191 ± 11.27	2.454 ± 11.27
2.8517563	4682.465 ± 0.109	1170.09	57.067 ± 6.029	12.505 ± 0.078	15.497 ± 3.504	2.992 ± 3.505
2.8522248	4683.035 ± 0.001	1170.24	23.846 ± 0.160	13.551 ± 0.005	15.034 ± 15.21	1.483 ± 15.21
2.8530040	4683.982 ± 1.769	1170.47	27.0	<11.020	14.697 ± 1.425	>3.677
2.8536816	4684.806 ± 1.088	1170.68	27.0	<11.024	14.689 ± 1.190	>3.665
2.8559113	4687.516 ± 0.041	1171.36	111.333 ± 5.965	12.833 ± 0.038	15.900 ± 0.000	3.067 ± 0.000
2.8586557	4690.852 ± 0.002	1172.19	22.326 ± 0.203	13.069 ± 0.004	16.292 ± 2.378	3.223 ± 2.378
2.8594098	4691.769 ± 0.000	1172.42	27.0	<11.045	14.900 ± 0.000	>3.855
2.8602629	4692.806 ± 0.001	1172.68	20.371 ± 0.082	13.665 ± 0.002	16.000 ± 0.000	2.335 ± 0.000
2.8608811	4693.558 ± 0.026	1172.87	80.488 ± 1.866	13.264 ± 0.012	17.501 ± 1.505	4.237 ± 1.505
2.8623686	4695.366 ± 0.001	1173.32	35.223 ± 0.066	14.335 ± 0.001	16.202 ± 8.966	1.867 ± 8.966
2.8638594	4697.178 ± 0.001	1173.77	24.627 ± 0.125	13.355 ± 0.002	14.399 ± 0.211	1.044 ± 0.211
2.8681543	4702.399 ± 0.018	1175.08	21.317 ± 1.204	13.298 ± 0.152	14.501 ± 5.966	1.203 ± 5.968
2.8685174	4702.841 ± 0.121	1175.19	31.283 ± 14.731	13.156 ± 0.576	15.400 ± 4.526	2.244 ± 4.563
2.8691826	4703.650 ± 0.414	1175.39	51.858 ± 36.366	13.218 ± 0.421	15.000 ± 0.167	1.782 ± 0.453
2.8704588	4705.201 ± 0.065	1175.78	21.019 ± 4.577	12.996 ± 0.663	13.701 ± 4.171	0.705 ± 4.223
2.8713348	4706.266 ± 0.003	1176.04	46.089 ± 0.333	13.834 ± 0.004	15.600 ± 1.400	1.766 ± 1.400
2.8723600	4707.512 ± 0.000	1176.35	27.0	<10.964	14.700 ± 0.000	>3.736

Table A.9: continued.

z	$\lambda_{\mathrm{H\,I}}$ (Å)	$\lambda_{\mathrm{He\,II}}$ (Å)	b (km/s)	$\log N_{\mathrm{H\,I}}$	$\log N_{\mathrm{He\,II}}$	$\log \eta$
2.8739138	4709.401 ± 0.113	1176.83	87.529 ± 4.154	13.832 ± 0.051	15.600 ± 0.615	1.768 ± 0.617
2.8741393	4709.675 ± 0.008	1176.90	32.644 ± 0.327	14.397 ± 0.010	15.296 ± 199.6	0.899 ± 199.6
2.8747332	4710.397 ± 0.007	1177.07	21.560 ± 0.429	14.169 ± 0.018	16.691 ± 146.4	2.522 ± 146.4
2.8753357	4711.130 ± 0.000	1177.26	27.0	<10.998	14.900 ± 0.000	>3.902
2.8765733	4712.634 ± 0.000	1177.63	27.0	<10.949	15.500 ± 0.000	>4.551
2.8772581	4713.467 ± 0.000	1177.84	27.0	<10.960	15.500 ± 0.000	>4.540
2.8780391	4714.416 ± 0.007	1178.08	31.161 ± 2.112	13.800 ± 0.160	15.600 ± 0.678	1.800 ± 0.697
2.8799472	4716.736 ± 0.199	1178.66	64.906 ± 9.293	12.632 ± 0.074	15.400 ± 0.210	2.768 ± 0.223
2.8816526	4718.809 ± 0.000	1179.18	27.0	<10.930	15.000 ± 0.000	>4.070
2.8817549	4718.933 ± 0.000	1179.21	27.0	<10.930	15.600 ± 0.000	>4.670
2.8831439	4720.622 ± 0.000	1179.63	27.0	<10.940	15.300 ± 0.000	>4.360
2.8839190	4721.564 ± 0.134	1179.86	47.879 ± 10.551	12.107 ± 0.113	14.600 ± 0.185	2.493 ± 0.217
2.8848557	4722.703 ± 0.029	1180.15	33.690 ± 2.464	12.459 ± 0.044	14.800 ± 0.228	2.341 ± 0.232
2.8859546	4724.039 ± 0.005	1180.48	31.832 ± 0.496	12.924 ± 0.007	14.900 ± 0.194	1.976 ± 0.194
2.8871491	4725.491 ± 0.024	1180.85	20.985 ± 2.458	11.882 ± 0.051	15.500 ± 0.383	3.618 ± 0.386
2.8884504	4727.073 ± 0.092	1181.24	27.0	<10.976	15.600 ± 0.330	>4.624
2.8894806	4728.325 ± 0.001	1181.56	29.023 ± 0.084	14.029 ± 0.001	14.300 ± 0.209	0.271 ± 0.209
2.9040897	4746.085 ± 0.001	1186.00	29.500 ± 0.000	16.020 ± 0.000	16.900 ± 0.560	0.880 ± 0.560

References

Abel, T., Bryan, G. L., & Norman, M. L. 2002, Science, 295, 93

Abgrall, H., Roueff, E., Launay, F., Roncin, J. Y., & Subtil, J. L. 1993a, A&AS, 101, 273

Abgrall, H., Roueff, E., Launay, F., Roncin, J. Y., & Subtil, J. L. 1993b, A&AS, 101, 323

Adelberger, K. L., Shapley, A. E., Steidel, C. C., et al. 2005, ApJ, 629, 636

Adelberger, K. L., Steidel, C. C., Shapley, A. E., & Pettini, M. 2003, ApJ, 584, 45

Agafonova, I. I., Centurión, M., Levshakov, S. A., & Molaro, P. 2005, A&A, 441, 9

Aguirre, A., Schaye, J., Kim, T., et al. 2004, ApJ, 602, 38

Anderson, S. F., Hogan, C. J., Williams, B. F., & Carswell, R. F. 1999, AJ, 117, 56

Aracil, B., Petitjean, P., Pichon, C., & Bergeron, J. 2004, A&A, 419, 811

Bajtlik, S., Duncan, R. C., & Ostriker, J. P. 1988, ApJ, 327, 570

Ballester, P., Mondigliani, A., Boitquin, O., et al. 2000, ESO Messenger, 101, 31

Barkana, R. & Loeb, A. 2004, ApJ, 609, 474

Becker, R. H., Fan, X., White, R. L., et al. 2001, AJ, 122, 2850

Benson, A. J., Frenk, C. S., Baugh, C. M., Cole, S., & Lacey, C. G. 2003, MNRAS, 343, 679

Benson, A. J., Frenk, C. S., Lacey, C. G., Baugh, C. M., & Cole, S. 2002, MNRAS, 333, 177

Bernardi, M., Sheth, R. K., SubbaRao, M., et al. 2003, AJ, 125, 32

Bharadwaj, S. & Ali, S. S. 2005, MNRAS, 356, 1519

Bianchi, S., Cristiani, S., & Kim, T.-S. 2001, A&A, 376, 1

Boksenberg, A., Sargent, W. L. W., & Rauch, M. 2003, astro-ph/0307557

Bolton, J. S., Haehnelt, M. G., Viel, M., & Carswell, R. F. 2005, MNRAS, submitted, astro-ph/0508201

Bowen, D. V., Pettini, M., & Blades, J. C. 2002, ApJ, 580, 169

Bowman, J. D., Morales, M. F., & Hewitt, J. N. 2005, ApJ, submitted, astro-ph/0507357

Bromm, V., Coppi, P. S., & Larson, R. B. 2002, ApJ, 564, 23

Bruzual A., G. & Charlot, S. 1993, ApJ, 405, 538

Bunker, A. J., Stanway, E. R., Ellis, R. S., & McMahon, R. G. 2004, MNRAS, 355, 374

Burles, S., Nollett, K. M., & Turner, M. S. 2001, ApJ, 552, L1

Cardelli, J. A., Clayton, G. C., & Mathis, J. S. 1989, ApJ, 345, 245

Cen, R., Miralda-Escude, J., Ostriker, J. P., & Rauch, M. 1994, ApJ, 437, L9

Chen, X. & Kamionkowski, M. 2004, Phys. Rev. D, 70, 043502

Chieffi, A. & Limongi, M. 2004, ApJ, 608, 405

Choudhury, T. R. & Ferrara, A. 2005, MNRAS, 557

Ciardi, B. & Ferrara, A. 2005, Space Science Reviews, 116, 625

Ciardi, B., Stoehr, F., & White, S. D. M. 2003, MNRAS, 343, 1101

Clarke, C. & Oey, M. S. 2002, MNRAS, 337, 1299

Cooke, A. J., Espey, B., & Carswell, R. F. 1997, MNRAS, 284, 552

Cooray, A. & Yoshida, N. 2004, MNRAS, 351, L71

Cristiani, S., D'Odorico, S., Fontana, A., Giallongo, E., & Savaglio, S. 1995, MNRAS, 273, 1016

Croft, R. A. C. 2004, ApJ, 610, 642

Croft, R. A. C., Weinberg, D. H., Katz, N., & Hernquist, L. 1997, ApJ, 488, 532

Davé, R. 2003, in IAU Symposium, astro-ph/0311518

Davé, R., Hernquist, L., Katz, N., & Weinberg, D. H. 1999, ApJ, 511, 521

Davidsen, A. F., Kriss, G. A., & Zheng, W. 1996, Nature, 380, 47

Di Matteo, T., Perna, R., Abel, T., & Rees, M. J. 2002, ApJ, 564, 576

Dijkstra, M., Haiman, Z., & Loeb, A. 2004, ApJ, 613, 646

Ding, J., Charlton, J. C., Bond, N. A., Zonak, S. G., & Churchill, C. W. 2003, ApJ, 587, 551

Diplas, A. & Savage, B. D. 1994, ApJ, 427, 274

Dobrzycki, A. & Bechtold, J. 1991, ApJ, 377, L69

Erb, D. K., Shapley, A. E., Steidel, C. C., et al. 2003, ApJ, 591, 101

Fan, X., Narayanan, V. K., Lupton, R. H., et al. 2001, AJ, 122, 2833

Fan, X., Narayanan, V. K., Strauss, M. A., et al. 2002, AJ, 123, 1247

Fardal, M. A., Giroux, M. L., & Shull, J. M. 1998, AJ, 115, 2206

Fechner, C., Baade, R., & Reimers, D. 2004, A&A, 418, 857

Fechner, C. & Reimers, D. 2004, in Astrophysics in the Far Ultraviolet - Five Years of Discovery with FUSE, ed. G. Sonneborn, W. Moos, & B.-G. Andersson, astro-ph/0410622

Feigelson, E. D. & Nelson, P. I. 1985, ApJ, 293, 192

Ferland, G. 1997, A Brief Introduction to Cloudy, Internal Rep., Lexington: Univ. Kentucky

Ferland, G. J., Korista, K. T., Verner, D. A., et al. 1998, PASP, 110, 761

Fernández-Soto, A., Lanzetta, K. M., & Chen, H.-W. 2003, MNRAS, 342, 1215

Fox, A. J., Savage, B. D., & Wakker, B. P. 2005, AJ, 130, 2418

Franx, M., Illingworth, G. D., Kelson, D. D., van Dokkum, P. G., & Tran, K.-V. 1997, ApJ, 486, L75+

Fujita, A., Martin, C. L., Mac Low, M.-M., & Abel, T. 2003, ApJ, 599, 50

Furlanetto, S. R. & Oh, S. P. 2005, MNRAS, 873

Giallongo, E., Cristiani, S., D'Odorico, S., & Fontana, A. 2002, ApJ, 568, L9

Giallongo, E., Cristiani, S., D'Odorico, S., Fontana, A., & Savaglio, S. 1996, ApJ, 466, 46

Gleser, L., Nusser, A., Benson, A. J., Ohno, H., & Sugiyama, N. 2005, MNRAS, 361, 1399

Gnedin, N. Y. 2000, ApJ, 535, 530

Grevesse, N. & Sauval, A. J. 1998, Space Science Reviews, 85, 161

Gunn, J. E. & Peterson, B. A. 1965, ApJ, 142, 1633

Haardt, F. & Madau, P. 1996, ApJ, 461, 20

Haardt, F. & Madau, P. 2001, in Clusters of Galaxies and the High Redshift Universe Observed in X-rays, ed. D. M. Neumann & J. T. T. Van, 64

Haehnelt, M. G., Madau, P., Kudritzki, R., & Haardt, F. 2001, ApJ, 549, L151

Haehnelt, M. G. & Steinmetz, M. 1998, MNRAS, 298, L21

Haiman, Z. & Loeb, A. 1998, ApJ, 503, 505

Hansen, S. H. & Haiman, Z. 2004, ApJ, 600, 26

Heap, S. R., Williger, G. M., Smette, A., et al. 2000, ApJ, 534, 69

Heger, A. & Woosley, S. E. 2002, ApJ, 567, 532

Hernquist, L., Katz, N., Weinberg, D. H., & Miralda-Escudé, J. 1996, ApJ, 457, L51+

Hogan, C. J., Anderson, S. F., & Rugers, M. H. 1997, AJ, 113, 1495

Holweger, H. 2001, in AIP Conf. Proc. 598: Joint SOHO/ACE workshop "Solar and Galactic Composition", ed. R. F. Wimmer-Schweingruber, 23

Hu, E. M., Kim, T., Cowie, L. L., Songaila, A., & Rauch, M. 1995, AJ, 110, 1526

Hui, L. & Gnedin, N. Y. 1997, MNRAS, 292, 27

Hui, L. & Haiman, Z. 2003, ApJ, 596, 9

Hunt, M. P., Steidel, C. C., Adelberger, K. L., & Shapley, A. E. 2004, ApJ, 605, 625

Iliev, I. T., Scannapieco, E., & Shapiro, P. R. 2005, ApJ, 624, 491

Inoue, A. K., Iwata, I., Deharveng, J.-M., Buat, V., & Burgarella, D. 2005, A&A, 435, 471

Jakobsen, P., Boksenberg, A., Deharveng, J. M., et al. 1994, Nature, 370, 35

Jakobsen, P., Jansen, R. A., Wagner, S., & Reimers, D. 2003, A&A, 397, 891

Köhler, S., Reimers, D., & Wamsteker, W. 1996, A&A, 312, 33

Kassim, N. E., Lazio, T. J. W., Ray, P. S., et al. 2004, Planet. Space Sci., 52, 1343

Kim, T.-S., Carswell, R. F., Cristiani, S., D'Odorico, S., & Giallongo, E. 2002a, MNRAS, 335, 555

Kim, T.-S., Cristiani, S., & D'Odorico, S. 2001, A&A, 373, 757

Kim, T.-S., Cristiani, S., & D'Odorico, S. 2002b, A&A, 383, 747

Kirkman, D. & Tytler, D. 1997, ApJ, 484, 672

Kirkman, D., Tytler, D., Suzuki, N., et al. 2005, MNRAS, 360, 1373

Kogut, A., Spergel, D. N., Barnes, C., et al. 2003, ApJS, 148, 161

Koratkar, A. & Blaes, O. 1999, PASP, 111, 1

Kriss, G. A., Shull, J. M., Oegerle, W., et al. 2001, Science, 293, 1112

Lai, K., Lidz, A., Hernquist, L., & Zaldarriaga, M. 2005, ApJ, submitted, astro-ph/0510841

Lehnert, M. D. & Bremer, M. 2003, ApJ, 593, 630

Levshakov, S. A., Agafonova, I. I., Centurión, M., & Molaro, P. 2003, A&A, 397, 851

Liske, J. 2000, MNRAS, 319, 557

Liske, J. & Williger, G. M. 2001, MNRAS, 328, 653

Loeb, A. & Zaldarriaga, M. 2004, Physical Review Letters, 92, 211301

Lopez, S., Reimers, D., Rauch, M., Sargent, W. L. W., & Smette, A. 1999, ApJ, 513, 598

Lu, L., Sargent, W. L. W., Womble, D. S., & Takada-Hidai, M. 1996, ApJ, 472, 509

Madau, P., Haardt, F., & Rees, M. J. 1999, ApJ, 514, 648

Madau, P., Meiksin, A., & Rees, M. J. 1997, ApJ, 475, 429

Madau, P., Rees, M. J., Volonteri, M., Haardt, F., & Oh, S. P. 2004, ApJ, 604, 484

Magliocchetti, M., Salvaterra, R., & Ferrara, A. 2003, MNRAS, 342, L25

Malkan, M., Webb, W., & Konopacky, Q. 2003, ApJ, 598, 878

Mapelli, M. & Ferrara, A. 2005, MNRAS, accepted, astro-ph/0508413

Masiero, J. R., Charlton, J. C., Ding, J., Churchill, C. W., & Kacprzak, G. 2005, ApJ, 623, 57

Mathews, W. G. & Ferland, G. J. 1987, ApJ, 323, 456

McCandliss, S. R. 2003, PASP, 115, 651

Meiksin, A. 2005, MNRAS, 356, 596

Miniati, F., Ferrara, A., White, S. D. M., & Bianchi, S. 2004, MNRAS, 348, 964

Miralda-Escudé, J. 1993, MNRAS, 262, 273

Miralda-Escudé, J. 2003, Science, 300, 1904

Miralda-Escudé, J. 2005, ApJ, 620, L91

Miralda-Escudé, J., Haehnelt, M., & Rees, M. J. 2000, ApJ, 530, 1

Misawa, T. 2002, PhD thesis, University of Tokyo

Møller, P. & Jakobsen, P. 1990, A&A, 228, 299

Moos, H. W., Cash, W. C., Cowie, L. L., et al. 2000, ApJ, 538, L1

Morales, M. F. & Hewitt, J. 2004, ApJ, 615, 7

Oh, S. P. & Mack, K. J. 2003, MNRAS, 346, 871

Oh, S. P., Nollett, K. M., Madau, P., & Wasserburg, G. J. 2001, ApJ, 562, L1

Padmanabhan, N. & Finkbeiner, D. P. 2005, Phys. Rev. D, 72, 023508

Pei, Y. C. 1992, ApJ, 395, 130

Petitjean, P., Riediger, R., & Rauch, M. 1996, A&A, 307, 417

Pettini, M., Madau, P., Bolte, M., et al. 2003, ApJ, 594, 695

Pettini, M., Shapley, A. E., Steidel, C. C., et al. 2001, ApJ, 554, 981

Picard, A. & Jakobsen, P. 1993, A&A, 276, 331

Porciani, C. & Madau, P. 2005, ApJ, 625, L43

Press, W. H., Rybicki, G. B., & Schneider, D. P. 1993, ApJ, 414, 64

Press, W. H., Teukolsky, S. A., Vetterling, W. T., & Flannery, B. P. 1994, Numerical Recipes in C: the art of scientific computing, 2nd edn. (Cambridge: Cambridge University Press)

Prochaska, J. X. & Wolfe, A. M. 1996, ApJ, 470, 403

Qian, Y.-Z. & Wasserburg, G. J. 2005, ApJ, 623, 17

Rauch, M., Miralda-Escude, J., Sargent, W. L. W., et al. 1997, ApJ, 489, 7

Reimers, D., Bade, N., Schartel, N., et al. 1995, A&A, 296, L49

Reimers, D., Clavel, J., Groote, D., et al. 1989, A&A, 218, 71

Reimers, D., Fechner, C., Hagen, H.-J., et al. 2005a, A&A, 442, 63

Reimers, D., Fechner, C., Kriss, G., et al. 2004, in Astrophysics in the Far Ultraviolet - Five Years of Discovery with FUSE, ed. G. Sonneborn, W. Moos, & B.-G. Andersson, astro-ph/0410588

Reimers, D., Hagen, H.-J., Schramm, J., Kriss, G. A., & Shull, J. M. 2005b, A&A, 436, 465

Reimers, D., Janknecht, E., Fechner, C., et al. 2005c, A&A, 435, 17

Reimers, D., Köhler, S., Wisotzki, L., et al. 1997a, A&A, 327, 890

Reimers, D., Toussaint, F., Hagen, H.-J., Hippelein, H., & Meisenheimer, K. 1997b, A&A, 326, 489

Reimers, D., Vogel, S., Hagen, H.-J., et al. 1992, Nature, 360, 561

Richter, P., Sembach, K. R., Wakker, B. P., & Savage, B. D. 2001, ApJ, 562, L181

Richter, P., Wakker, B. P., Savage, B. D., & Sembach, K. R. 2003, ApJ, 586, 230

Ricotti, M., Gnedin, N. Y., & Shull, J. M. 2000, ApJ, 534, 41

Ricotti, M. & Ostriker, J. P. 2004a, MNRAS, 350, 539

Ricotti, M. & Ostriker, J. P. 2004b, MNRAS, 352, 547

Ricotti, M. & Shull, J. M. 2000, ApJ, 542, 548

Sahnow, D. J., Moos, H. W., Ake, T. B., et al. 2000, ApJ, 538, L7

Salvaterra, R. & Ferrara, A. 2003, MNRAS, 339, 973

Salvaterra, R., Haardt, F., & Ferrara, A. 2005, MNRAS, 362, L50

Savage, B. D. & Sembach, K. R. 1991, ApJ, 379, 245

Savaglio, S., Cristiani, S., D'Odorico, S., et al. 1997, A&A, 318, 347

Schaerer, D. 2002, A&A, 382, 28

Schaye, J. 2001, ApJ, 559, 507

Schaye, J. 2004, ApJ, submitted, astro-ph/0409137

Schaye, J., Aguirre, A., Kim, T., et al. 2003, ApJ, 596, 768

Schaye, J., Theuns, T., Leonard, A., & Efstathiou, G. 1999, MNRAS, 310, 57

Schaye, J., Theuns, T., Rauch, M., Efstathiou, G., & Sargent, W. L. W. 2000, MNRAS, 318, 817

Schirber, M., Miralda-Escudé, J., & McDonald, P. 2004, ApJ, 610, 105

Schlegel, D. J., Finkbeiner, D. P., & Davis, M. 1998, ApJ, 500, 525

Schmidt, M., Schneider, D. P., & Gunn, J. E. 1991, in ASP Conf. Ser. 21: The Space Distribution of Quasars, 109–114

Schneider, R. 2004, Memorie della Societa Astronomica Italiana Supplement, 5, 307

Schneider, R., Ferrara, A., Natarajan, P., & Omukai, K. 2002, ApJ, 571, 30

Schneider, R., Ferrara, A., Salvaterra, R., Omukai, K., & Bromm, V. 2003, Nature, 422, 869

Scott, J., Bechtold, J., Dobrzycki, A., & Kulkarni, V. P. 2000, ApJS, 130, 67

Scott, J., Bechtold, J., Morita, M., Dobrzycki, A., & Kulkarni, V. P. 2002, ApJ, 571, 665

Scott, J. E., Kriss, G. A., Brotherton, M., et al. 2004, ApJ, 615, 135

Shapley, A. E., Steidel, C. C., Erb, D. K., et al. 2005, ApJ, 626, 698

Shaver, P. A., Windhorst, R. A., Madau, P., & de Bruyn, A. G. 1999, A&A, 345, 380

Shull, J. M. 2004, in Astrophysics in the Far Ultraviolet - Five Years of Discovery with FUSE, ed. G. Sonneborn, W. Moos, & B.-G. Andersson, astro-ph/0410189

Shull, J. M., Tumlinson, J., Giroux, M. L., Kriss, G. A., & Reimers, D. 2004, ApJ, 600, 570

Simcoe, R. A., Sargent, W. L. W., & Rauch, M. 2002, ApJ, 578, 737

Simcoe, R. A., Sargent, W. L. W., & Rauch, M. 2004, ApJ, 606, 92

Simcoe, R. A., Sargent, W. L. W., Rauch, M., & Becker, G. D. 2005, ApJ, accepted, astro-ph/0508116

Smette, A., Heap, S. R., Williger, G. M., et al. 2002, ApJ, 564, 542

Sokasian, A., Abel, T., & Hernquist, L. 2002, MNRAS, 332, 601

Sokasian, A., Abel, T., & Hernquist, L. 2003, MNRAS, 340, 473

Songaila, A. 1998, AJ, 115, 2184

Songaila, A. 2001, ApJ, 561, L153

Songaila, A. 2004, AJ, 127, 2598

Songaila, A. 2005, AJ, accepted, astro-ph/0509821

Spergel, D. N., Verde, L., Peiris, H. V., et al. 2003, ApJS, 148, 175

Springel, V., White, S. D. M., Jenkins, A., et al. 2005, Nature, 435, 629

Steidel, C. C., Adelberger, K. L., Shapley, A. E., et al. 2005, ApJ, 626, 44

Steidel, C. C., Pettini, M., & Adelberger, K. L. 2001, ApJ, 546, 665

Telfer, R. C., Zheng, W., Kriss, G. A., & Davidsen, A. F. 2002, ApJ, 565, 773

Teplitz, H. I., Malkan, M., & McLean, I. S. 1998, ApJ, 506, 519

Theuns, T., Bernardi, M., Frieman, J., et al. 2002a, ApJ, 574, L111

Theuns, T., Schaye, J., Zaroubi, S., et al. 2002b, ApJ, 567, L103

Tripp, T. M., Lu, L., & Savage, B. D. 1997, ApJS, 112, 1

Tumlinson, J., Shull, J. M., & Venkatesan, A. 2003, ApJ, 584, 608

Umeda, H. & Nomoto, K. 2002, ApJ, 565, 385

Umeda, H. & Nomoto, K. 2005, ApJ, 619, 427

Venkatesan, A., Tumlinson, J., & Shull, J. M. 2003, ApJ, 584, 621

Verner, D. A., Barthel, P. D., & Tytler, D. 1994, A&AS, 108, 287

Vogel, S. & Reimers, D. 1993, A&A, 274, L5

Vogel, S. & Reimers, D. 1995, A&A, 294, 377

Warren, S. J., Hewett, P. C., & Osmer, P. S. 1994, ApJ, 421, 412

White, R. L., Becker, R. H., Fan, X., & Strauss, M. A. 2003, AJ, 126, 1

Williger, G. M., Baldwin, J. A., Carswell, R. F., et al. 1994, ApJ, 428, 574

Willott, C. J., Delfosse, X., Forveille, T., Delorme, P., & Gwyn, S. D. J. 2005, ApJ, in press, astro-ph/0507183

Wolfe, A. M., Gawiser, E., & Prochaska, J. X. 2005, ARA&A, 43, 861

Woosley, S. E. & Weaver, T. A. 1995, ApJS, 101, 181

Wyithe, J. S. B. & Loeb, A. 2003a, ApJ, 586, 693

Wyithe, J. S. B. & Loeb, A. 2003b, ApJ, 588, L69

Zaldarriaga, M., Furlanetto, S. R., & Hernquist, L. 2004, ApJ, 608, 622

Zhang, Y., Anninos, P., & Norman, M. L. 1995, ApJ, 453, L57

Zhang, Y., Anninos, P., Norman, M. L., & Meiksin, A. 1997, ApJ, 485, 496

Zheng, W., Chiu, K., Anderson, S. F., et al. 2004a, AJ, 127, 656

Zheng, W., Kriss, G. A., Deharveng, J.-M., et al. 2004b, ApJ, 605, 631

Zheng, W., Kriss, G. A., Telfer, R. C., Grimes, J. P., & Davidsen, A. F. 1997, ApJ, 475, 469

Zonak, S. G., Charlton, J. C., Ding, J., & Churchill, C. W. 2004, ApJ, 606, 196

Acknowledgements

Ich danke Herrn Prof. Dr. D. Reimers für die Betreuung dieser Arbeit.

Für die Bereitschaft, die Dissertation zu begutachten, gilt mein Dank Herrn Prof. Dr. L. Wisotzki.

Dr. R. Baade danke ich für das Korrekturlesen der Arbeit.

Desweiteren danke ich allen Mitarbeitern der Hamburger Sternwarte für die freundliche Unterstützung bei der Anfertigung dieser Arbeit.